N° d'ordre: 3358

THESE

PRESENTEE A

L'UNIVERSITE BORDEAUX I

PAR

Iyad SAADEDDIN

POUR OBTENIR LE GRADE DE

DOCTEUR

Spécialité: Physico-chimie de la matière condensée

PREPERATION AND CHARACTERIZATION OF NEW TRANSPARENT CONDUCTING OXIDES BASED ON SnO_2 AND In_2O_3:CERAMICS AND THIN FILMS

Soutenue le 30 mars 2007

MM. C. DELMAS	Directeur de Recherche	Président
M. SUBRAMANIAN	Professeur	Rapporteur
H. S. HILAL	Professeur	Rapporteur
H. CACHET	Directeur de Recherche	Examinateur
F. FAVERJON	Ingénieur R&D (HEF)	Examinateur
T. TOUPANCE	Professeur	Examinateur
B. PECQUENARD	Maître de Conférences	Examinateur
G. CAMPET	Directeur de Recherche	Examinateur

2007

This thesis is dedicated

To my wife Lubna

To my daughter Yasmine

To my family (mother, brothers, and sisters)

Acknowledgments

First of all, I would like to express my deepest sense of gratitude to my supervisors Dr. Guy CAMPET and Dr. Brigitte PECQUENARD for their patient guidance, encouragement, excellent advices, and the experience I got because of them throughout this study.

I would like to express my gratitude to my grant sponsor, the French Ministry of Foreign Affairs, for financing of my study. Also I would like to thank very much the French Consulate at Jerusalem, particularly Mr. Sébastien FAGART, for the help and the grant prolongations. Many thanks expressed to CROUS of Bordeaux, particularly Madame Christine LAOUE, for the many helps I got from them through this grant. Also I would like to thank the jury members for the efforts they made in order to review and judge this work.

My sincere thanks to Jean-Pierre MANAUD for the effective collaboration on sputtering deposition technique. His continuous guidance, advice and encouragement throughout this work make it possible for me to have a good experience on the sputtering deposition technique. I would like also to express my appreciation to Yves GARRABOS, and Carole LECOUTRE, from group 7, for the effective collaboration done concerning the applications related to this thesis.

My deep gratitude to Rodolphe DECOURT, Christine LABRUGERE and Michel LAHAYE for the effective discussions and the intensive measurements on the electronic properties, the composition of my material and the morphology done at their laboratories throughout this thesis. Many thanks to Annie SIMON, Mario MAGLIONE, and Régnault VON DER MÜHLL, from group 4, for allowing me intensively use their laboratory.

I am thankful to all the following people from the ICMCB for the help, experiments they did or the effective discussions: Eric LEBRAUD, Stanislav PECHEV, and Pierre GRAVEREAU, Dominique DENUX, François GUILLEN , Samir MATAR, Marie-Helene DELVILLE, Jean-marc HEINTZ, Bernard LESTIENNE and Michel GONZALEZ. I am also thankful to my friends at the ICMCB for the encouragements, help and support: Mathieu QUINTIN, Sandrine DULUARD, Bernard CLAVEL, Hamdi Ben YAHYA, Dae hoon PARK and Hyun JONG.

I would like also to thank the following people from outside the ICMCB for the collaboration done on some experiments: Elisabeth SELLIER for the SEM, Thierry

BUFFETEAU for IR spectroscopy, Abdeslam El MANSOURI for porosity measurements and Jacques MARCUS for Hall measurements done on the ceramics.

I would like to thank my Palestinian and Syrian friends in Bordeaux for the support and encouragements listed hereafter: Ali, Khaleel, Omar, Amjad, Jamal, Mohammed, Bashar, Abu Yazan, Saed, Abderrahman, Ismail, Zakwan, Shadi, Wasim, Adnan, Nayef and the wives of married friends.

I will take this opportunity to express my profound gratitude to my beloved family in Palestine (my mother, my brothers and my sisters) for the continuous support and encouragement.

Finally, I strongly express my profound gratitude to my dearly loved wife Lubna and my daughter Yasmine for the moral support and patience during my study.

Table of contents

General introduction:

Presentation of the topic

Transparent conducting oxides (TCOs), such as Sn-doped In_2O_3 (indium doped tin oxide, ITO), Al-doped ZnO (AZO), Sb-doped SnO_2 (ATO), and F-doped SnO_2 (FTO), have the unique feature of combining optical transparency in the visible region (colorless state) with metal type electrical conductivity. Therefore, they are widely applied as transparent electrodes for liquid crystal displays (LCDs), organic light-emitting diodes (OLEDs), solar cells, etc. (Fig. 1) [1-3]. A TCO is a semiconductor with a wide band-energy gap (≥ 3 eV), which confers the optical transparency. It has also quasi free electrons in its wide conduction band of s-character; the free electrons confer the metal type conductivity. These arise either from defects in the material or from extrinsic dopants which introduce electron donor centers that underlie the conduction band edge. During the last thirty to forty years, the dominant doped TCOs have been based on tin oxide (SnO_2), indium oxide (In_2O_3), and zinc oxide (ZnO) [1-4]. Fig. 2 shows the improvement of the electrical conductivity achieved for these three dominant families of TCO materials over the last 35 years. In spite of all these intensive investigations, there is still a need to have TCOs with better optimized opto-electronic properties. That is particularly needed (in our case) for the following applications: heat reflectors, transparent micro-furnaces and flexible electrochromic devices, that will be discussed later on in this thesis. That led us to carry out studies on the following TCOs, in both ceramic and thin film forms: (i) ATO and AZTO (tin dioxide co-doped with antimony and zinc) (ii) ITZO (indium trioxide co-doped with tin and zinc).

i) Tin dioxide doped with Sb^{5+} (ATO)

Doping SnO_2 with substitutional pentavalent cations such as Sb^{5+} with oxidation state higher than Sn^{4+} highly enhances the electronic n-type conductivity. This dopant behaves as ionized electron donor center liberating (quasi) free electron in the conduction band leading to a metal-type conductivity. The occurrence of the free electrons in the conduction band $xe^-_{C.B.}$ can be depicted as:

$$Sn^{4+}_{1-x} Sb^{5+}_{x} O^{2-}_{2} \left[xe^-_{C.B.} \right] \quad \text{(a)}$$

It is well known that ATO thin films are chemically stable [3, 5, 6]. They are also thermally stable with no alteration in opto-electronic properties upon heating in air up to 400 °C [7]. Numerous reports described ATO deposition using different techniques [8-12].

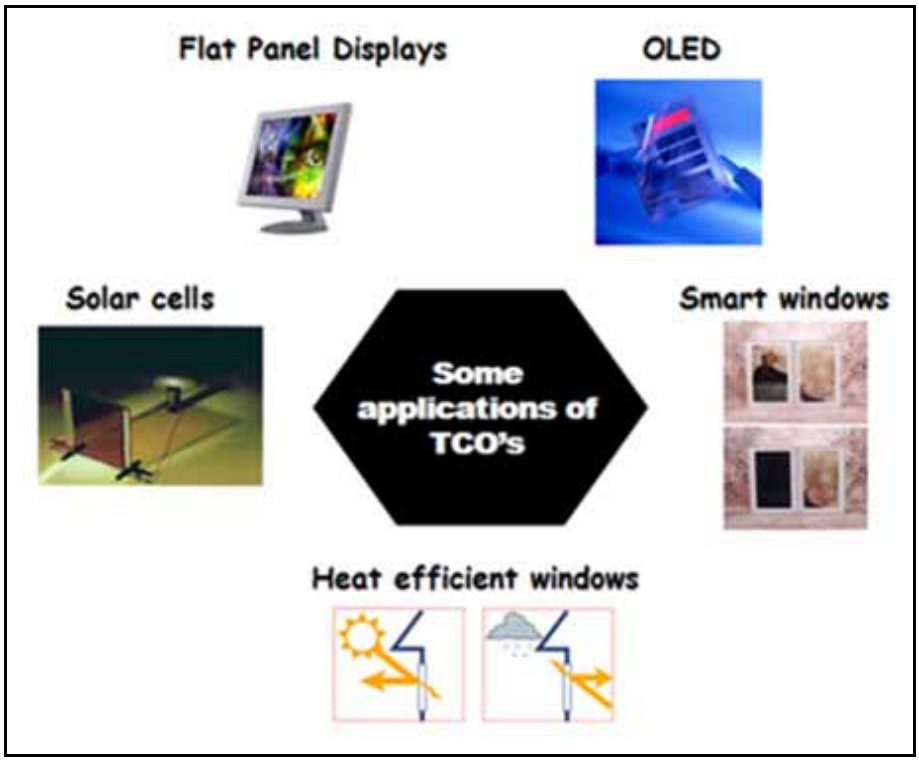

Fig. 1: Some applications of TCOs

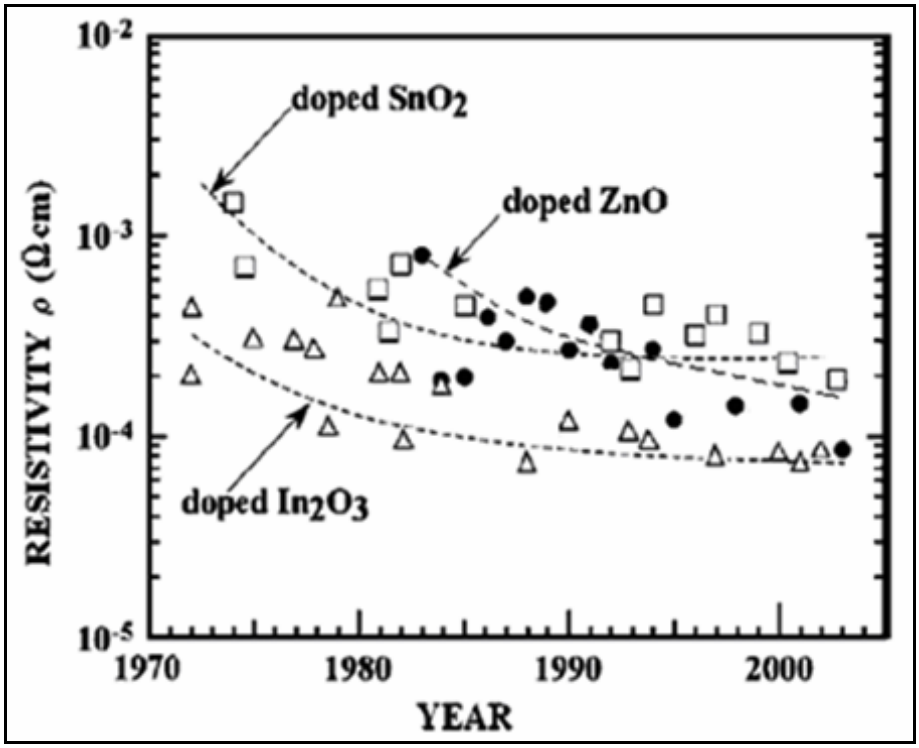

Fig. 2: Dominant TCOs development over the last 35 years [4].

It appears that the surface quality of the films deposited by physical vapor deposition (PVD) is generally higher (lower roughness, etc.). However, the commercial ATO electrodes are produced either by spray or chemical vapor deposition (CVD) but not by PVD such as RF or DC sputtering because, to our knowledge, no commercial ATO targets exist for RF or DC sputtering. The reason is presumably due to the ability of antimony to depart during sintering of ATO targets [13, 14]. In this thesis, the possibility to prepare ATO targets without antimony departure will be studied. Then ATO films will be prepared by sputtering from these targets, and their opto-electronic properties will be investigated. Their use as heat reflectors for high temperature supercritical fluid application will be presented.

ii) Tin dioxide co-doped with Sb^{5+} and Zn^{2+} (symbolized as AZTO).

To our knowledge, this is the first time that such co-doping is proposed for tin dioxide. This system has been investigated while keeping in mind two objectives:

1) Preparation of highly dense targets.

For undoped SnO_2 and ATO targets, sintered at high temperature, ~ 1300 °C, the reported relative bulk density $\rho_{exp.}/\ \rho_{theo}$ is around 0.6 [14, 15]. For industrial production of TCO films by sputtering it is necessary to produce targets as dense as possible in order to increase the film deposition rate and get dense homogeneous films [16]. According to literature [17-19], doping SnO_2 with substitutional divalent M^{2+} cations, such as Mn^{2+} or Cu^{2+} strongly enhances the ceramic density. Indeed, the presence of uncharged oxygen vacancies according to:

$$Sn_{1-x}^{4+} M_x^{2+} O_{2-x}^{2-} \square_x \qquad \text{(b)}$$

promotes mass transport at the grain boundaries resulting in ceramics with higher densities [17-19]. However, doping SnO_2 with d^5 or d^9 elements, such as Mn^{2+} or Cu^{2+}, introduces occupied energy states of d character which are located inside the band-energy gap of the oxide. Therefore, they will behave as color centers affecting the transparency in the visible [15]. That will not occur when SnO_2 is doped with Zn^{2+}. Indeed, Zn^{2+} is a d^{10} ion, like Sn^{4+}, and the Zn^{2+}:d^{10} energy sates underlie the O^{2-}:$2p^6$ valence band of SnO_2 [15]. Therefore, doping the oxide with Zn^{2+} will not affect its transparency. Moreover, Zn^{2+} is a

divalent element like Mn^{2+} or Cu^{2+}; Therefore it should similarly enhance the ceramic density.

2) Modulation of the mobile electron concentration into the films.

In addition, we expect that co-doping with Sb and Zn would allow a modulation of the mobile-electron concentration according to the following equation:

$$Sn^{4+}_{1-x-y-\delta} Sb^{5+}_{x} Zn^{2+}_{y+\delta} O^{2-}_{2-\delta} \square_{\delta} \left[(x-2y) e^{-}_{C.B.} \right] \quad \text{(c)}$$

This would lead to a better control of the electrical conductivity needed for specific applications such as transparent micro-furnaces.

iii) Indium oxide co-doped with Sn^{4+} and Zn^{2+} (symbolized as ITZO).

Similar tendency should be observed for indium oxide-based ceramics since Zn^{2+} has a lower oxidation state than In^{3+}. It may thus be possible to get new highly dense and conductive ITZO targets suitable for sputtering. In fact, co-doping with zinc may allow a straightforward target preparation by direct sintering of the powder in an appropriate mold, i.e. without using any cold or (expensive) hot pressing procedure. That will markedly reduce the manufacturing cost of ITO based targets, particularly those with large areas intended for industrial use.

Moreover, x-ray amorphous ITO films, exhibiting a high transparency, but unfortunately not a high enough conductivity, were recently deposited at room temperature by DC sputtering on polycarbonate-based plastic substrates. This was achieved by SOLEMS Company in the framework of the European project NANOEFFECT whose objective is to produce flexible electrochromic devices. Electrical conductivity enhancement might be expected for ITZO films, deposited on plastic substrates, insofar as Zn^{2+} ions occupy not only substitutional positions, but also interstitial positions leading to an overall increase of the electron carrier density and, therefore, of the electrical conductivity. Such results have been recently reported for x-ray amorphous IZO (Zinc Indium Oxide) films, deposited by sputtering at room temperature on glass substrates from IZO ceramic targets [20]. However, the solubility limits of zinc in well crystallized In_2O_3, as it occurs for IZO ceramic does not exceed 1% at. [21]. Consequently, due to this too low solubility of Zn in the bixbyite structure of In_2O_3, IZO ceramic targets might not be

prepared with the above mentioned procedure (direct sintering of the powder without pressing); that wouldn't be the case for ITZO ceramics.

Therefore, our research will be conducted as follows. We will first investigate how the doping elements influence the density, the structure and the electronic properties of conductive oxide based ceramics corresponding to the three systems described above. Then, using optimized ceramics as targets, we will prepare thin films by RF magnetron sputtering, either on glass or plastic substrates. We will study the influence of the deposition conditions and the doping contents on the deposition rate, the composition, the structure and the optical and electrical properties of our TCOs thin films. Meanwhile, the co-doped thin films will be investigated based on a comparative approach with their well known ATO (Antimony-doped Tin dioxide) and ITO (Tin-doped Indium trioxide) homologues. The following techniques will be employed to study the properties of the TCOs ceramics and thin films:

1) Four-probe method and Hall measurements to study electrical properties.
2) Optical transparency and reflectivity in both visible and infrared regions to investigate the optical properties of the thin films.
3) Electron Probe X-ray Microanalysis (EPMA), X-ray Photoelectron Spectroscopy (XPS) and Auger Electron Spectroscopy (AES) to assess the chemical composition.
4) Scanning Electron Microscopy (SEM) and Atomic Force Microscopy (AFM) to study the surface morphology of the thin films.
5) X-ray Diffraction (XRD) to analyze the structure.

The work described in this thesis is presented in 3 chapters, as follows:

The first chapter will include a general review of electrical and optical properties for mainly widespread TCO films. It will present also the basic properties of TCOs that we will consider to interpret our experimental data. Concerning electrical properties, different scattering mechanisms involved in the electrical transport phenomena will be described. The classical optical models, such as the Drude theory and Burstein-Moss effect, allowing the determination of important optical parameters will be presented. Finally, it will describe the sputtering method used in this thesis allowing the deposition of homogeneous and uniform thin films.

In chapter 2, the different results obtained on both ceramics and thin films of single-doped and co-doped tin oxide (ATO and AZTO) will be discussed. We will first optimize the ATO and AZTO ceramic target composition by modifying the doping content and we will study the effect of Sb^{5+} and Zn^{2+} on the ceramic properties (density, morphology, structure, and electrical properties). The optimized ceramics will be used to prepare corresponding thin films by sputtering. The influence of different sputtering parameters (power, total pressure, and oxygen partial pressure) on the opto-electronic properties of the film will be studied. Finally, the optimized films will be fully characterized and used as heat reflector and transparent micro-furnace for supercritical fluid related applications.

A similar strategy will be followed, in chapter 3, for co-doped tin and zinc indium oxide (ITZO) materials starting with optimization of the ceramics. In this case, some films will be deposited either on glass or PET (polyethylene terephthalate) substrates. The main objectives of this part is to easily prepare highly dense targets and high-performance ITZO thin films on plastic substrates.

The general conclusion and perspectives of this thesis will then be presented.

References

[1]. D. S. Ginley, C. Bright, *Mater. Res. Soc. Bull.* **25** (2000) 15.

[2] H. Hosono, D. S. Ginley, N. Ichinose, Y. Shigesato (eds.), *Thin Solid Films* **445** (2003) 155.

[3] R. G. Gordon in *MRS Bull*. **25** (2000) 52.

[4] T. Minami, *Semicond. Sci. Technol.* **20** (2005) S35.

[5] M. Kojima, F. Takahashi, K. Kinoshita, T. Nishibe, M. Ichidate, *Thin Solid Films*, **392** (2001) 349.

[6] M. Pourbaix, *Atlas d'Equilibres Electrochimiques*; Gauthier-Villars: Paris (1963).

[7] I. Saadeddin, G. Campet, B. Pecquenard, Y. Garabos, *private communication*.

[8] E. Kh. Shokr, M. M. Wakkad, H. A. Abd El-Ghanny, H. M. Ali, *J. Phys. Chem. Solids* **61** (2000) 75.

[9] K. S. Kim, S. Y. Yoon, W. J. Lee, K. H. Kim, *Surf. Coat. Tec.* **138** (2001) 229.

[10] A. G. Sabnis, A. G. Moldavan, *Appl. Phys. Lett.* **33** (1978) 885.

[11] A. Messad , J. Bruneaux, H. Cachet , M. Froment M, *J. Mater. Sci*. **29** (1994) 5095.

[12] H. Kima, A. Piqué, *Appl. Phys. Lett*. **84** (2004) 218.

[13] Handbook of Chemistry and Physics (72nd ed.). CRC Press, Inc., Boca Raton, USA, 1991.

[14] I. Saadeddin, H. S. Hilal, B. Pecquenard, J. Marcus, A. Mansouri, C. Labrugere, M. A. Subramanian, G. Campet, *Solid State Sciences* **8** (2006) 7.

[15] S. J. Wen, *Ph.D. Thesis,* Bordeaux 1 University, Bordeaux, France (1992).

[16] C. Marcel, *Ph.D. Thesis*, Bordeaux 1 University, Bordeaux, France (1998).

[17] J. Fayat, M. S. Castro, *J. Eur. Cera. Soc.* **23** (2003) 1585.

[18] D. Gouvêa, *Ph.D. Thesis*, Limoges University, Limoges, France (1995).

[19] O. Scarlat, S. Mihaiu, Gh. Aldica, J. Grozac, M. Zaharescu, *J. Eur. Cer. Soc.* **24** (2004) 1049.

[20] N. Ito, Y. Sato, P. K. Song, A. Kaijio, K. Inoue, Y. Shigesato, *Thin Solid Films* **496** (2006) 99.

[21] D. H. Park, K. Y. Son, J. H. Lee, J. J. Kim, J. S. Lee, *Solid State Ionics* **172** (2004) 431.

Chapter I

Basic properties of TCOs: general review

1. Introduction

Studies of transparent and conducting semiconducting oxide films have attracted the attention of many research workers due to their wide range of applications. TCOs have been known for nearly a century. Indeed, the first TCO film, cadmium oxide, was synthesized and characterized as early as 1907 [1-2]. The first TCO patents for undoped and doped tin oxide (SnO_2) films were filed respectively in 1931 [3] and 1942 [4]. Such films were employed as aircraft windshield deicers in World War II [5]. The following decades saw the development of In_2O_3- and ZnO-based TCOs. It included indium-tin oxide (ITO) [6] and the first Al-doped ZnO films [7], which was reported in the same year (1971) as the first ZnO-based varistor [8]. Since that time, there has been steady improvement in the deposition and properties of SnO_2, In_2O_3, and ZnO-based films. The last decade has seen the development of complex TCOs, including binary [9–11] and ternary [12, 13] oxides. All of the materials mentioned thus far exhibited the expected degenerate n-type conduction (metal-type conductivity). However, recently some p-type TCOs were reported, but the electron-acceptor states responsible for the p-type conductivity were not clearly identified [14-16]. Thin films (~100-200 Å) of metals such as Au, Ag, Cu, Fe, etc. have also been considered, but the films, in general, are not very stable and their opto-electronic properties change with time. On the other hand, the TCO coatings, based on above quoted degenerated n-type oxide materials, have wider applications, due to their superior stability and hardness, than thin metallic films.

As mentioned earlier, in the general introduction, TCOs are being used in a wide variety of applications, such as solar cells [17], gas sensors [18], window insulation and thermal insulation in lamps [19-21], production of heating layers for protecting vehicle windscreens from freezing and misting over [22], light transmitting electrodes in the development of opto-electronic devices [23-24], photocathodes in photoelectrochemical cells [25], antistatic surface layers on temperature control coatings in orbiting satellites [26] and surface layers in electroluminescent applications [27]. Materials commonly used as TCOs for these applications, are mainly based on doped tin oxide or ITO.

For these TCOs to act as transparent current collectors or as transparent hot-mirror coatings, the TCO films must possess a high metal-type conductivity and must be

transparent (colorless) in the visible. In addition, TCOs with high resistivities are required for some specific applications such as transparent micro-furnaces. These different characteristics are achievable by carefully controlling, *via* 'co-doping', both the electrical conductivity and the 'optical window' of the electrodes (Fig. 1).

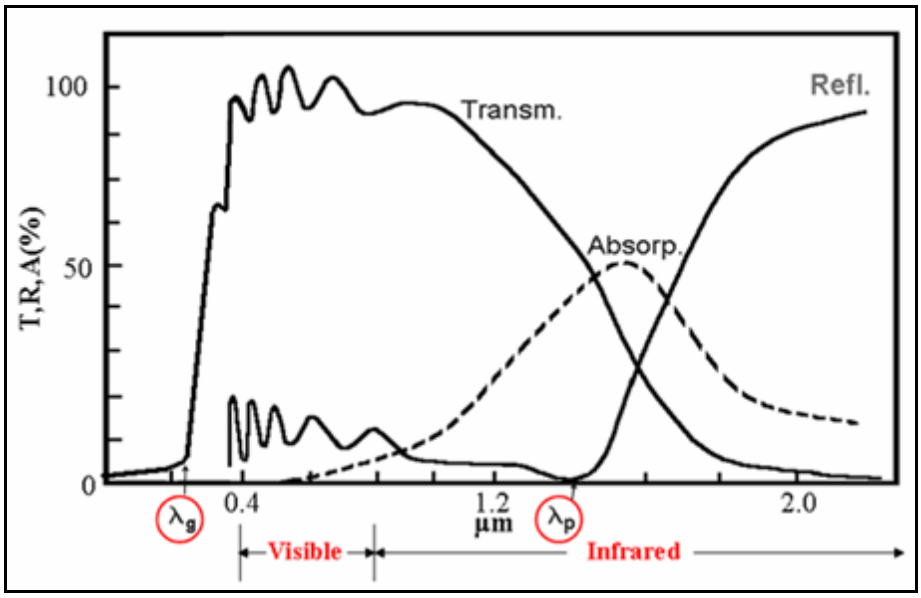

Fig. 1: Optical window schema for Transparent Conducting Oxides (TCOs)

As shown in Fig. 1, the optical window is delimited by two cutting wavelengths λ_g and λ_p. The first wavelength, λ_g, separates the absorption zone in the ultraviolet from the transparent zone in the visible. It corresponds to the threshold of inter-band absorptions and it is correlated to the optical band-gap, E_g, according to:

$$E_g = \frac{hc}{\lambda_g} \geq 3\text{eV} \qquad (1)$$

where h is Planck's constant, and c is the speed of light [28]. The second wavelength, λ_p (generally called plasma wavelength), corresponds to the front rise of the reflectivity in the IR and accounts for a metallic character of the TCO; it corresponds to intraband absorption in the conduction band of the electrode material, when resonance occurs between the incident electromagnetic radiation and the plasma oscillation of the (quasi) free electrons in the conduction band. λ_p depends on the concentration of these electrons in the conduction band (N)and on their mobility (μ) according to:

$$\lambda_p = 2\pi c(\varepsilon_0 \varepsilon_\infty \tau / Ne\mu)^{1/2} \qquad (2)$$

where τ is the carrier relaxation time; ε_0 is the permittivity of free space, and ε_∞ is the high frequency dielectric constant of the involved media [29]. In literature [9], various types of TCOs are reported. They are based either on: (i) non-stoichiometric binary compounds, such as In_2O_{3-x} (symbolized as IO), $Zn_{1+x}O$ (ZO), and SnO_{2-x} (TO), etc.; (ii) doped binary compounds, such as $In_{2-x}Sn_xO_3$ (ITO), $SnO_{2-x}F_x$ (FTO), Sn_{2-x} Sb_xO_2 (ATO), $Zn_{1-x}Al_xO$ (AZO), etc.; or (iii) non-stoichiometric ternary compounds such as Cd_2SnO_{4-x}, Zn_2SnO_{4-x}, $Zn_2In_2O_{5-x}$ and $ZnSnO_{3-x}$, etc.. In these formulas, x represents the deviation of the compound from stoichiometry, either by oxygen vacancy, interstitial cation, or addition of dopants, thereby creating electronic carriers in the first conduction band as illustrated in Fig. 2. All these oxides have their first conduction band of s character. Such a band is wide enough to allow the occurrence of metal-type conductivity [9]. As also illustrated in Fig. 2, the transparency in the visible, observed for all these oxides, occurs by virtue of:

i) their wide optical band-gap, $E_g \geq$ 3eV, which separates the top of the valence band of O^{2-}:$2p^6$ character from the bottom of the conduction band of **s** cationic character.

ii) the large energy separation, $E \geq$ 3eV, between the two first conduction bands [13, 30].

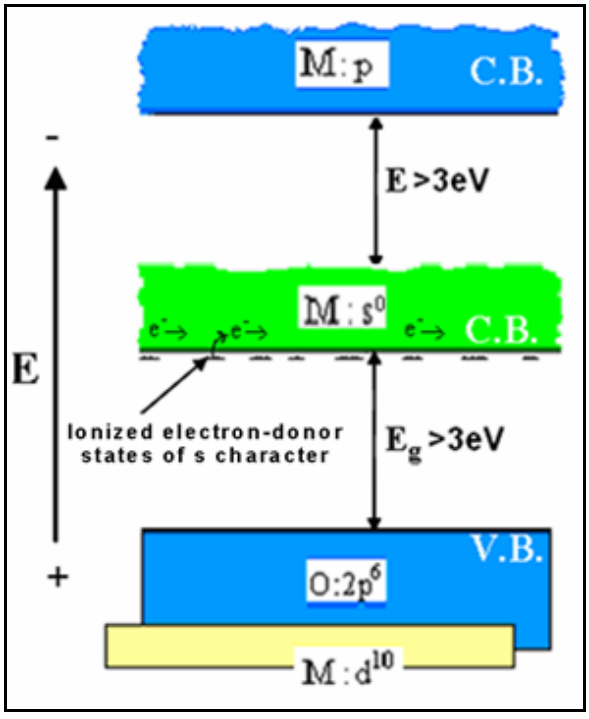

Fig. 2: Schematic diagram for TCO electronic bands (M = In^{3+}, Zn^{2+}, Sn^{4+}, etc.).

The metal-type conductivity of the TCO results from the non-stoichiometry or from the doping with appropriate foreign elements. As it occurs for the above quoted examples,

the non-stoichiometry and the doping with foreign elements generate electron-donor energy states, of **s** character, that are located at the immediate vicinity of the wide conduction band of **s** character as well (Fig. 2). Therefore, the electron-donor centers are (quasi) spontaneously ionized, liberating (quasi) free electrons in the conduction band, leading to the metal-type conductivity. For instance, in ATO and ITO, the occurrence of ($xe^{-}_{C.B.}$) free electrons in the conduction band can be depicted respectively as:

$$Sn^{4+}_{1-x} Sb^{5+}_{x} O^{2-}_{2} \left[xe^{-}_{C.B.} \right] \qquad \text{(a)}$$

and

$$In^{3+}_{2-x} Sn^{4+}_{x} O^{2-}_{3} \left[xe^{-}_{C.B.} \right] \qquad \text{(b)}$$

where x represents the mole fraction of added dopants which generate xe^{-}_{CB} . It is commonly observed that the donor ionization energy decreases linearly with increasing donor concentration. Fig. 3 illustrates this linear evolution for non stoichiometric indium oxide and tin oxide.

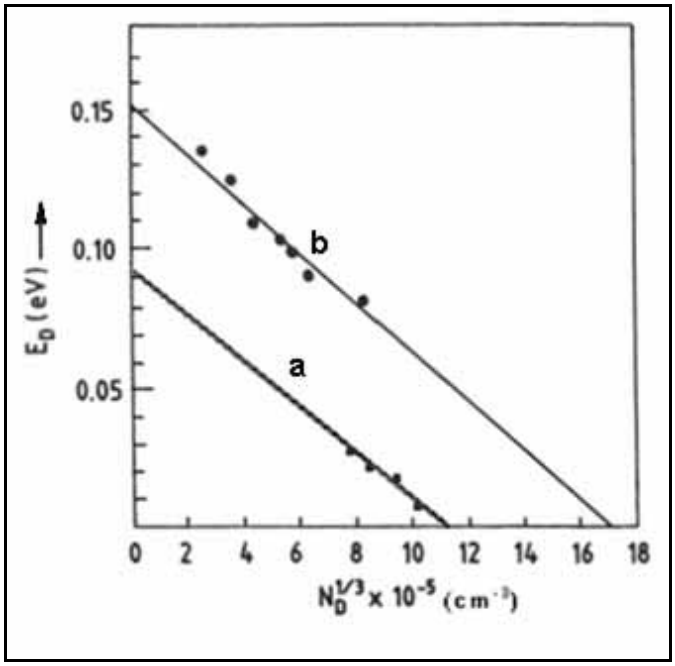

Fig. 3: Donor ionization energy in (a) In_2O_{3-x} and (b) SnO_{2-x} as a function of donor concentration [30-31].

Pearson and Bardeen [31] suggested a model for the decrease of ionization energy with donor concentration by considering the electrostatic attraction between electrons and ionized donors, which decreases with donor concentration. The model shows that:

$$E_D = E_{D0} - \beta N_D^{1/3} \tag{3}$$

where E_D is the donor ionization energy for a given donor concentration N_D, E_{D0} is the donor ionization energy as donor concentration approaches zero, and β is a constant. Such a variation of E_D with N_D has been observed by many workers [32-34] for different TCOs.

The main commercial TCOs include fluorine- or antimony-doped tin oxide (FTO and ATO), tin-doped indium oxide (ITO) and aluminum-doped zinc oxide (AZO) [35]. However, as already described in the general introduction, for specific applications, further optimizations of the opto-electronic properties of TCOs are desirable. The work on the growth and characterization of TCOs films has been reviewed by many workers at various periods [5, 19, 29, 36-46]. For instance, Holland [37] reviewed the work carried out up to 1955. Vossen [39], Haacke [38] and Jarzebski and Marton [36] gave comprehensive reviews of experimental work reported up to the mid-1970s. Manifacier [43], Jarzebski [41], Chopra *et al* [44] and Dawar and Joshi [45] reported detailed surveys of the work in this area up to the early 1980s. Hamberg and Granqvist [29] reviewed the work on indium tin oxide films in detail, particularly from an application point of view. Gordon [5] gives as well an extensive overview of TCO applications. More recently, Ingram *et al* [46] reviewed the chemical and structural factors governing transparent conductivity in oxides including TCOs. In addition to these reviews, many other works have been done on electrical and optical properties of the main TCOs; for sake of clarity, they are reported and commented in detail in the Annex 1.

A brief description of the basic theory sustaining the electrical and the optical properties of the TCOs, which will be needed in our study, is presented hereafter.

2. TCOs Electrical properties

The early work on the electrical properties of TCO films has been reviewed by many workers [39, 41, 44-45]. For sake of clarity, this section starts with a brief introduction to the basic theory of electrical transport phenomena in semiconductor thin films. Afterwards, the specific electrical properties of TCO films are discussed more in detail.

Transport phenomenon is the term applied to the motion of charge carriers under the action of internal or external field. In the absence of an electric field, the electron gas in a semiconductor is in an equilibrium state, which is established as a result of the interaction of electrons with lattice defects. Such defects especially include lattice imperfections in the crystallites, grain boundaries, impurity atoms, thermal vibrations of the lattice (phonons). If an electric field E is applied to a material, an electrical current will flow, whose density J, usually expressed in A/m^2, is given by

$$\boldsymbol{J} = \sigma \boldsymbol{E} \tag{4}$$

where σ is called the electrical conductivity of the material usually expressed in Siemens per cm (S.cm^{-1}). The reciprocal of electrical conductivity is known as electrical resistivity ρ (in Ω.cm), and can be expressed by:

$$\rho = \frac{V}{I}\frac{\pi t}{\ln 2} = 4.53t\frac{V}{I} \tag{5}$$

where t represents the film thickness. The resistivity, ρ, is correlated to the so-called parameter 'sheet resistance (R_s)' by

$$R_s = \rho / t \tag{6}$$

The accessibility for ρ is reported in Annex 2.

The current density can be also expressed as:

$$\boldsymbol{J} = Ne\boldsymbol{v}_d \tag{7}$$

where e is the electron charge, N is the carrier density (i.e. the density of the mobile electrons in the conduction band), $\mathbf{v}_d$ is the drift velocity[1] of the carriers. Combining equations (4) and (7) yields to:

$$\boldsymbol{v}_d = \{\sigma/Ne\}\boldsymbol{E}. \tag{8}$$

The σ/Ne proportionality factor here is called the mobility (μ) of charge carriers, i.e.

$$\mu = \sigma / Ne\,. \tag{9}$$

The charge carrier mobility (μ), normally measured in $cm^2/V{\cdot}s$, is related to the relaxation time (τ) and the effective mass of the charge carriers (m^*) according to:

$$\mu = \frac{e\tau}{m^*}. \tag{10}$$

"τ" is the carrier life time between two collisions and the effective mass "m^*" is defined by the mass that charge carrier seems to carry, usually stated in units of the ordinary mass of an electron m_e (9.11×10^{-31} kg). The electrical carrier mobility, μ, of the TCOs is usually deduced from electrical resistivity and carrier concentration obtained from Hall-effect measurements (Annex 3). These parameters: τ, μ, and m^* will be often used to interpret the electronic properties of our materials, in relation with the texture, structure and composition. The expression for mobility of charge carriers, equation (10), depends on the relaxation time, which in turn depends on the drift velocity and the mean free path of the charge carriers. These parameters depend on the mechanisms by which the carriers are scattered by lattice imperfections, such as lattice scattering, ionized impurity scattering, neutral impurity scattering, electron–electron scattering, electron–impurity scattering. On the other hand, grain boundary scattering plays an important role in polycrystalline thin films having small grain size. Hence, the total mobility μ_t is written as:

[1] Under the influence of an electric field, the electrons begin to move in a specific direction and such directional motion is termed drift. The average velocity of this motion is known as drift velocity, $\mathbf{v}_d$.

$$\frac{1}{\mu_t} = \sum_i \frac{1}{\mu_i} \tag{11}$$

where μ_i is related to the ith scattering mechanism.

The interpretation of the electronic properties of our materials and of their evolution when physical parameters (such as sintering temperature) or chemical parameters (such as change in chemical composition) were modified need a clear preliminary understanding of the electrical conduction occurring in 'microcrystalline', 'nanocrystalline' and 'amorphous' materials. The conduction mechanisms which occur in these different types of materials are overviewed in Annex 4.

3. TCOs Optical properties

The optical properties of TCO thin films provide a powerful tool to study energy band structure, impurity levels, localized defects, lattice vibrations etc. In such study, we first measure reflectivity and transmission spectra of the films. Afterwards, from these measurements we estimate the main optical constants as will be shown hereafter. The optical properties of TCO films, and therefore the optical constants, strongly depend on the deposition parameters, microstructure, level of impurities and growth technique. Brief reviews have been given by various workers in this area [29, 39, 41, 43-45]. Here we will discuss the determination of the main optical constants, and then, the optical properties of TCOs thin films.

Let us consider the typical case of a TCO thin film having a complex index $n^* = n - ik$ deposited on a transparent substrate of index $n_1^* = n_1 - ik_1$ (Fig. 4). Knowing the thickness of the film (t), by measuring its reflectance (R) and its transmittance (T) at normal incidence, it is then possible, at least in principle, to deduce the optical parameters, namely refractive index n , extinction coefficient k, optical band-gap E_g etc., of the film. The reflectance R and transmittance T expressions of such a thin film layer reported by Heavense [47] and Swanepoel [48] are detailed in Annex 5.

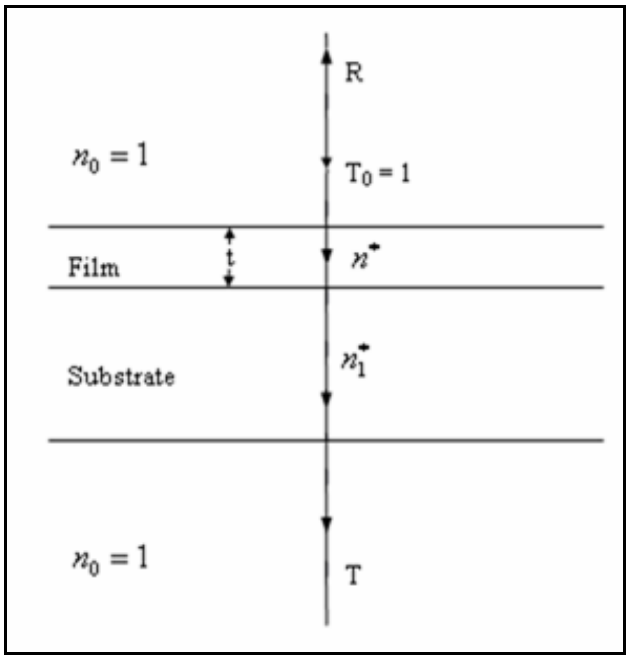

Fig. 4: System made of an absorbing thin film on a thick finite transparent substrate.

Let us consider a non absorbing thick transparent substrate alone (absorption coefficient $\alpha_1 = 0$, so that $k_1 = \alpha_1 \lambda / 4\pi = 0$ and hence $n_1^* = n_1$ is real). Then, the interference-free transmission T_s of the substrate is given by [49]

$$T_s = 1 - R_s$$

where

$$R_s = \frac{(n_1 - 1)^2}{n_1^2 + 1}$$

is the reflection from the substrate. Therefore, the transmission of the substrate is given by:

$$T_s = \frac{2n_1}{n_1^2 + 1} \tag{12}$$

Then the substrate reflective index can be calculated using

$$n_1 = \frac{1}{(1 - R_s)} + \left(\frac{1}{(1 - R_s)^2} - 1 \right)^{1/2} = \frac{1}{T_s} + \left(\frac{1}{T_s^2} - 1 \right)^{1/2} \tag{13}$$

3-1. *n* and *k* determination in the strong absorption and interference transmission regions

In the case of TCO thin films on a transparent substrate, two regions can be distinguished in the UV-visible range: a strong absorption region and interference absorption region (Fig. 5).

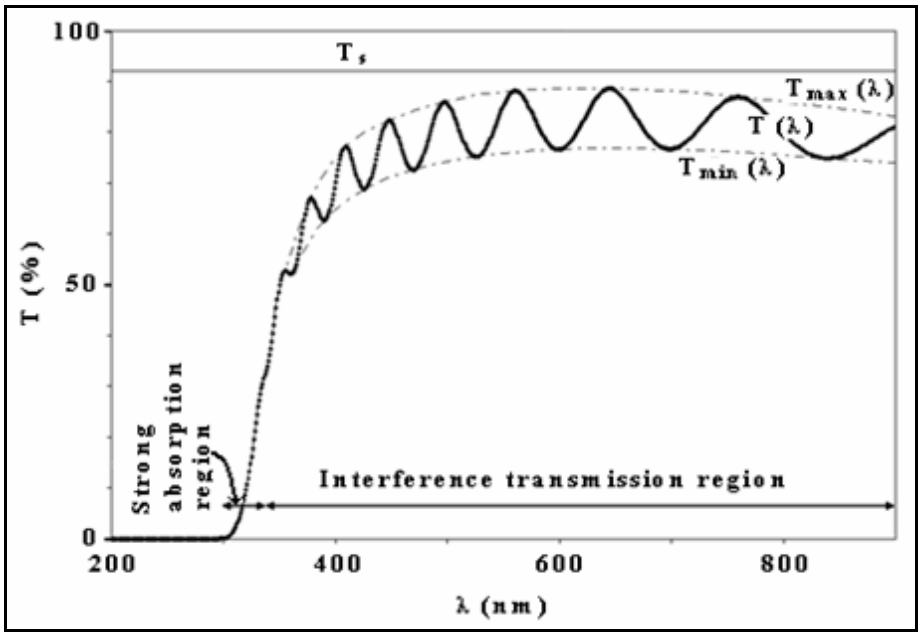

Fig. 5: Typical transmission spectrum for a uniform TCO thin film.

3-1-a. Strong (fundamental) absorption region.

One can define the transmission T by the following relation [50, 51]

$$T = A' \exp(-\alpha t) \tag{14}$$

With the approximation $A' \approx 1$ [52] in the fundamental absorption region, equation (14) becomes

$$T = \exp(-\alpha t) \tag{15}$$

Thus using the data from the transmission spectra T of the film and knowing the thickness t value, absorption coefficient (α) can be directly calculated, and hence k value since $k = \alpha\lambda / 4\pi$.

3-1-b. Interference transmission region.

For weakly and medium absorbing films, the measurement of transmission of light through a film in the region of transparency is sufficient to determine the real and imaginary parts of the complex refractive index $n^* = n - ik$. A simple method was developed to calculate these constants [48, 53]. The maxima and minima of *T(λ)* shown in Fig. 5 occur for

$$2nd = m\lambda \tag{16}$$

where *m* (the order number) is an integer for maxima and half integer for minima. The real part of the complex refractive index is expressed by the following equation:

$$n = \left[F + (F^2 - n_0^2 n_1^2)^{1/2}\right]^{1/2} \tag{17}$$

where

$$F = \frac{n_0^2 + n_1^2}{2} + 2n_0 n_1 \frac{T_{\max} - T_{\min}}{T_{\max} T_{\min}}.$$

with n_0 and n_1 which are respectively the real part of the refractive index of the air and substrate. Equation (17) shows that n is explicitly determined from $T_{\max}$, $T_{\min}$ (shown on Fig. 5), with n_1 and n_0 being measured at the same wavelength. Knowing *n,* one can also find the film thickness, which can be calculated from the two successive maxima or minima using the relation (16), and is given by

$$t = \frac{\lambda_1 \lambda_2}{2[n(\lambda_1)\lambda_2 - n(\lambda_2)\lambda_1]} \tag{18}$$

where λ_1 and λ_2 are the wavelengths of two successive maxima or minima. Knowing *t*, then the extension coefficient *k* can be calculated using the equation

$$x = \exp\frac{-4\pi kt}{\lambda} = \exp -\alpha t \tag{19}$$

With

$$x = \frac{C1\left[1-(T_{max}/T_{min})^{1/2}\right]}{C_2\left[1+(T_{max}/T_{min})^{1/2}\right]} \quad (20)$$

where $C_1 = (n+n_0)(n_1+n), C_2 = (n-n_0)(n_1-n)$.

More details for the above equations (17-20) are given in Annex 6.

3-2. Band-gap determination in the strong (fundamental) absorption region; influence of carrier concentration

In band-energy gap (or optical band-gap) determination, the strong absorption region (Fig.5) must obviously be considered. TCOs, as described earlier, have large band-energy gaps, in the range 3 to 4 eV, which correspond to photon wavelength range of 300–400 nm (near-ultraviolet region). While they are absorbed, these photons induce electronic transitions from the valence band to the empty energy states in the conduction band (Fig. 2). In this region, one can estimate the value of the optical band-gap using the relation [54, 55]:

$$\alpha h\nu \propto (h\nu - E_g)^{\eta} \quad (21)$$

where α is the absorption coefficient, $h\nu$ is the photon energy, E_g is the band-gap at the same wave number, and η is a constant taking the values 1/2 and 2, depending on whether the optical transitions are respectively direct allowed or indirect allowed. For the direct allowed transition, extrapolating for the linear part of the curve $(\alpha h\nu)^2$ versus $h\nu$, gives the value of E_g. For the indirect allowed transitions, the curve which has to be drawn and extrapolated to zero in order to determine the E_g, is $(\alpha h\nu)^{1/2}$ versus $h\nu$ [54, 55]. For TCOs, the optical transitions from occupied valence-band states to empty conduction-band states are obviously affected by free carrier concentration (i.e. mobile electrons) in the conduction-band. Indeed, the latter partially occupy the conduction band; i.e. the states at the bottom of the conduction band are filled with the electrons and the Fermi level has thereby moved into the conduction band. This means that the energy required to activate an electron from the valence band to the empty conduction band states in TCOs is more than the fundamental band-gap, and this energy enhancement is more pronounced with higher carrier concentrations (Fig. 6).

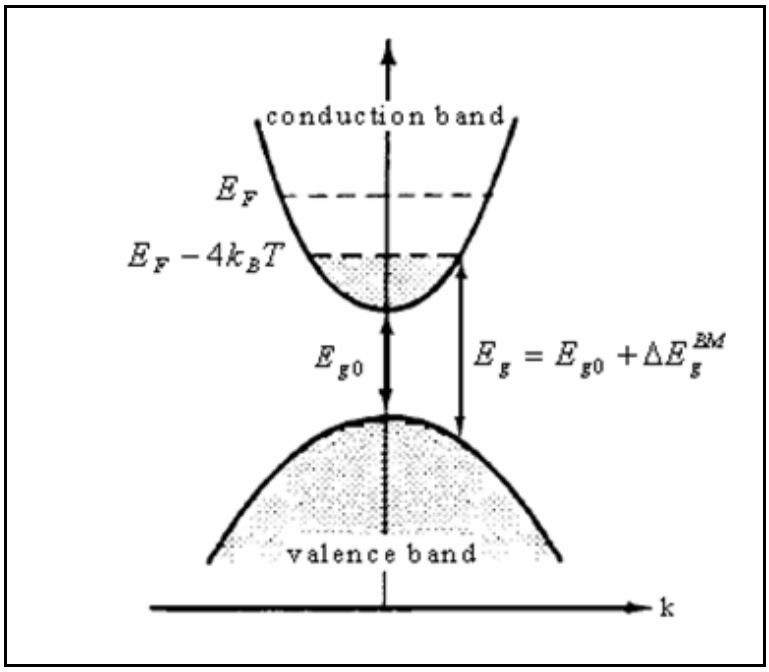

Fig. 6: Diagram showing the Burstein-Moss shift in the fundamental absorption edge, of a n-type semiconductor, to higher energy by heavy doping (after [56, 57]).

This is the well-known Burstein-Moss effect [56, 57]. According to these authors, the increase in energy required for a transition in a degenerate semiconductor may be expressed as

$$\Delta E_g^{BM} = \frac{\hbar^2 k_F^2}{2m_{CV}^*} \tag{22}$$

where $\hbar$ is the Planck's constant divided by 2π, and k_F is the Fermi wave vector, given by

$$k_F = (3\pi^2 N)^{1/3} \tag{23}$$

and m_{CV}^* is the reduced effective mass given by

$$\frac{1}{m_{CV}^*} = \frac{1}{m_C^*} + \frac{1}{m_V^*} \tag{24}$$

where m_C^* and m_V^* are respectively the electron and hole effective mass. These formulas assume that conduction and valence bands are parabolic.

We see then that the optical band-gap may be considered as the fundamental energy gap plus an energy that depends on the degeneracy and hence the carrier concentration. Quantitatively the optical band-gap is given by

$$E_g = E_{g0} + \Delta E_g^{BM} \tag{25}$$

where E_{g0} is the band-gap of the undoped semiconductor.

3-3. *n* and *k* determination in the infrared region: correlation between optical and electrical properties

In the infrared region, reflection occurs in the TCOs because of the plasma edge, and light cannot be transmitted (Fig. 1). This optical phenomenon can be understood on the basis of Drude's Model which characterizes the free electrons in metals and also in degenerate n-type semiconductors such as TCOs. This model is based on the classical equations of motion of an electron in an optical electric field, and gives the simplest theory which uses the optical constants. It assumes that the material contains immobile positive ions (in this work the positive ions are obviously the ionized donor centers) and an "electron gas" of density *N* whose motion is damped by a frictional force, due to collisions of the electrons with the ions. Their motion is thereby characterized by a relaxation time τ. In its simplest form, the Drude model describes the electrical current density *J* under an applied electric field *E*, and is given by

$$J = \frac{Ne^2 \tau E}{m^*} = \sigma E \tag{26}$$

where *e* is the charge of the electron, and m^* its effective mass, and σ is the dc conductivity. The Drude model also predicts the current as a response to a sinusoidal time-dependent electric field, with angular frequency ω. In this case, the conductivity can be derived to be

$$\sigma(\omega) = \frac{Ne^2 \tau / m^*}{1 - i\omega\tau} = \frac{Ne^2 \tau / m^*}{1 - \omega^2 \tau^2}(1 + i\omega\tau) \tag{27}$$

The interaction of free electrons with an electromagnetic field may lead to polarization of the field within a material and thereby influence the complex dielectric function $\varepsilon(\omega)$. The dielectric function and optical conductivity are introduced, through the Maxwell's equations of electromagnetic waves in solids, by the relation

$$\varepsilon(\omega) = (n + ik)^2 = \varepsilon_\infty + i\frac{\sigma(\omega)}{\varepsilon_0 \omega} = \varepsilon_1 + i\varepsilon_2 \tag{28}$$

This relation correlates the *n* and *k* optical constants with carrier concentration N through the term $\sigma(\omega)$. The real and imaginary parts of dielectric constant $\varepsilon(\omega)$ can then be written as follows

$$\varepsilon_1 = n^2 - k^2 = \varepsilon_\infty \left(1 - \frac{\omega_P^2}{\omega^2 + \gamma^2}\right) \tag{29}$$

and

$$\varepsilon_2 = 2nk = \varepsilon_\infty \frac{\omega_P^2 \gamma}{\omega(\omega^2 + \gamma^2)}. \tag{30}$$

The plasma resonance frequency ω_P is given by

$$\omega_P = (Ne^2 / \varepsilon_0 \varepsilon_\infty m_e^*)^{1/2} = \frac{2\pi c}{\lambda_P} \tag{31}$$

where ε_∞ and ε_0 represent the high frequency and free space dielectric constants, respectively. m_e^* is the effective mass of the charge carriers (in our case the mobile electrons in the conduction band). *N* is the carrier concentration, and λ_P is the plasma wavelength. γ is equal to *1/τ*, which is assumed to be independent of frequency and is related to mobility as

$$\gamma = \frac{1}{\tau} = \frac{e}{m_e^* \mu} \tag{32}$$

Three different frequency regions can be distinguished for the free carriers:

i) $0 < \omega << 1/\tau$ (absorbing region)

In this region, the imaginary part ε_2 (equation (30)) is much larger than the real part ε_1 (equation (29)), so that the films are strongly reflecting. In this case equations (29) and (30) become

$$\varepsilon_1 = \varepsilon_\infty \left(1 - \omega_P^2 \tau^2\right) \tag{33}$$

$$\varepsilon_2 = \varepsilon_\infty \frac{\omega_P^2 \tau}{\omega} >> 1 \tag{34}$$

This leads to the Hagen-Ruben relation [58]

$$n^2 = k^2 \frac{\varepsilon_\infty \omega_P^2 \tau}{2\omega} \tag{35}$$

When the thickness of the layer is greater than the skin depth $\delta(\lambda/4\pi k)$, the layer reflectivity is given by

$$R = \frac{(n-1)^2 + k^2}{(n+1)^2 + k^2} \tag{36}$$

Combining equations (35) and (36) gives

$$R = 1 - 2\left(\frac{2\omega}{\varepsilon_\infty \omega_P^2 \tau}\right)^{1/2} \tag{37}$$

ii) $1/\tau < \omega < \omega_P$ (reflecting region)

This is the relaxation region in which $\omega^2\tau^2 >> 1$ and the absorption coefficient falls rapidly. In this region, the real part ε_1 (relation (29)) is negative and we have almost total reflection. In this case equations (29) and (30) take the form

$$\varepsilon_1 = \varepsilon_\infty \left[1 - \left(\frac{\omega_P}{\omega}\right)^2\right] < 0 \tag{38}$$

$$\varepsilon_2 = \varepsilon_\infty \frac{\omega_P^2}{\omega^3 \tau} > 1 \tag{39}$$

This results in

$$n = \frac{\omega_P \varepsilon_\infty^{1/2}}{2\omega^2 \tau} \tag{40}$$

and

$$k = \sqrt{\left(\frac{\omega_P}{\omega}\right)^2 - 1} \cong \frac{\omega_P}{\omega} \varepsilon_\infty^{1/2} \tag{41}$$

When layer thickness is greater than the skin depth δ, the reflectivity is then given by

$$R = 1 - \frac{2}{\omega_P \tau \varepsilon_\infty^{1/2}} \tag{42}$$

iii) $\omega > \omega_P$ (transparent region)

In this region, the real part ε_1 (equation (29)) becomes positive and the reflection power becomes minimum; the films become transparent. In this case, equations (29) and (30) become

$$\varepsilon_1 = \varepsilon_\infty \left(1 - \left(\frac{\omega_P}{\omega}\right)^2\right) \tag{43}$$

$$\varepsilon_2 = \varepsilon_\infty \frac{\omega_P^2}{\omega^3 \tau} << 1 \tag{44}$$

This leads to

$$n \cong \varepsilon_\infty^{1/2} \sqrt{1 - \left(\frac{\omega_P}{\omega}\right)^2} \cong \varepsilon_\infty^{1/2} \tag{45}$$

and

$$k = \varepsilon_{\infty}^{1/2} \frac{\omega_P^2}{2\omega^3 \tau} \cong 0. \tag{46}$$

Fig. 7 shows the variation of n and k with wavelength for a typical TCO film. For $\lambda < \lambda_P$, the plasma resonance wavelength, the n value is almost constant ($\cong \varepsilon_{\infty}^{1/2}$). As we approach λ_P, the value of n approaches unity, which implies a very low reflectance. For $\lambda > \lambda_P$, both n and k increase rapidly, which leads to high reflectivity.

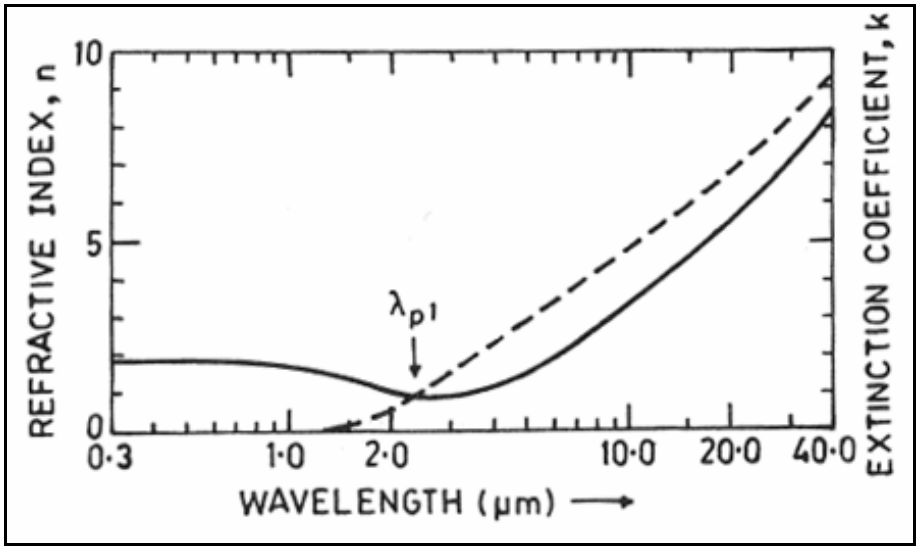

Fig. 7: typical curve for n and k for SnO_2 film (—) n and (----) k (from [32]).

The effect of carrier concentration N is two-fold. First, N determines the plasma wavelength in accordance with relation (31); the higher the carrier concentration, the lower will be the plasma wavelength; the plasma wavelength is not directly influenced by the change in value of mobility. Second, *N and μ (via τ)* governs the maximum achievable reflectivity in the infrared region in accordance with relation (42).

Knowing the values of n and k in the plasma resonance region from optical data, and N and μ from electrical data helps in estimating the values of m^* with the use of equations (30)-(32). In addition, Drude's approach is useful for computing the dielectric function in transparent conducting films in order to estimate the electron density and mobility from optical data. These data can be fruitfully compared with electrical data as shown hereafter.

The validity of Drude's theory has been tested by various workers [28, 29, 58, 59-65] for different TCO films having metal type conductivity. It was observed that in

general the experimental results for transmittance and reflectance in these films fit well with Drude's theory. We will obviously test this model for our TCO thin films.

4. Thin film growth techniques

Various TCO film growth techniques have been intensively investigated during the recent past. The growth technique plays a significant role in governing the film properties, because the same material deposited by two different techniques usually yields different physical properties. This is due to the fact that the electrical and optical properties of these films strongly depend on the structure, morphology and nature of impurities that are present. Hence, the properties can be tailored by controlling the deposition parameters. Therefore, it is essential to make a detailed investigation of the relationship between film properties and deposition method.

There are various methods to produce TCO thin films growth including chemical vapor deposition (CVD) [66, 67], hydrolysis or spray [68, 69], vacuum evaporation [70], ion assisted deposition techniques [71-78], and sputtering [79-81]. General comparison of different growth techniques, in relation to various deposition parameters and characteristics of transparent conducting oxide films, is shown in Table 1.

Deposition technique	**CVD**	**Spray**	**Sputtering**	**Ion plating**	**Evaporation**
Substrate temperature	High	High	Low	Room	High
Rate of growth	High	High	Low	Low	High
Uniformity	High	Poor	Excellent	Excellent	Moderate
Reproducibility	High	Moderate	Excellent	Excellent	Moderate
Cost	Moderate	Low	High	High	Moderate
Electrical conductivity	Moderate-excellent	Moderate-excellent	Excellent	Excellent	Moderate-excellent
Transmission	Moderate-excellent	Moderate-excellent	Excellent	Excellent	Moderate

Table 1: Comparison of various growth techniques employed for the deposition of semiconducting transparent thin films.

The important features related to various techniques are as follows:

i) Spray pyrolysis can be employed for the growth of low-cost films for large-area applications where uniformity is not the primary requirement.

ii) The ion-assisted growth technique is particularly suitable for deposition on polystyrene-like materials where substrate heating is not possible.

iii) For the growth of reproducible device quality films, sputtering and CVD have been extensively used in one form or another. However, deposition rates of CVD methods are usually greater than those of sputtering techniques. The sputtering deposition technique, although more complex and more expensive, is preferred as it permits better control of film homogeneity and thickness in addition to its high quality. In addition, sputtering technique is less toxic than CVD.

In this study, we have only used the sputtering technique to prepare our TCO thin films. Indeed, sputtering is chosen in order to have high quality, homogeneous composition, and a controlled morphology. Sputtering is one of the most versatile techniques used for the deposition of transparent conductors when device quality films are required. Compared with other deposition techniques, the sputtering process produces films with higher purity and better-controlled composition, provides films with greater adhesive strength and homogeneity and permits better control of film thickness. The sputtering process involves the creation of gas plasma (usually an inert gas such as argon) by applying voltage between a cathode and an anode. The cathode is used as a target holder and the anode is used as a substrate holder. Source material is subjected to intense bombardment by argon ions. By momentum transfer, particles are ejected from the surface of the cathode and they diffuse away from it, depositing a thin film onto a substrate. Sputtering is normally performed at a pressure of 10^{-2}-10^{-3} Torr.

Normally there are two modes of powering the sputtering system. In a DC sputtering system, a direct voltage is applied between the cathode and the anode. This process is restricted to conducting targets, such as tin or indium. In RF sputtering (Fig. 8), which is suitable for both conducting and insulating targets, a high frequency generator (13.56 MHz) is connected between the electrodes. The use of an alternative current allows the alternation of the target polarity. During the negative alternation, the cathode attracts the ions which allows its sputtering and inducing a positive charge on its surface. During the positive alternation, the target attracts the electrons to ensure its

neutralization. Therefore, the RF sputtering is convenient for deposition of insulating materials. Recently, however, use of magnetron sputtering is raised (Fig. 9). Magnetron sputtering is particularly useful where high deposition rates and low substrate temperature are required.

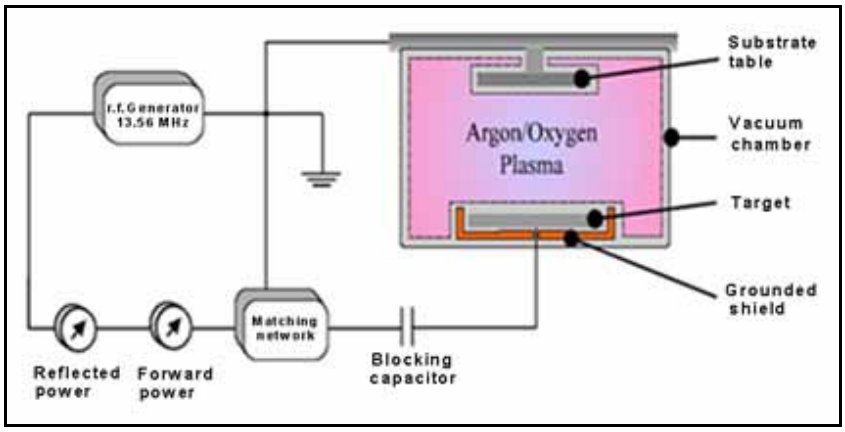

Fig. 8: Schematic of the RF sputtering chamber [82].

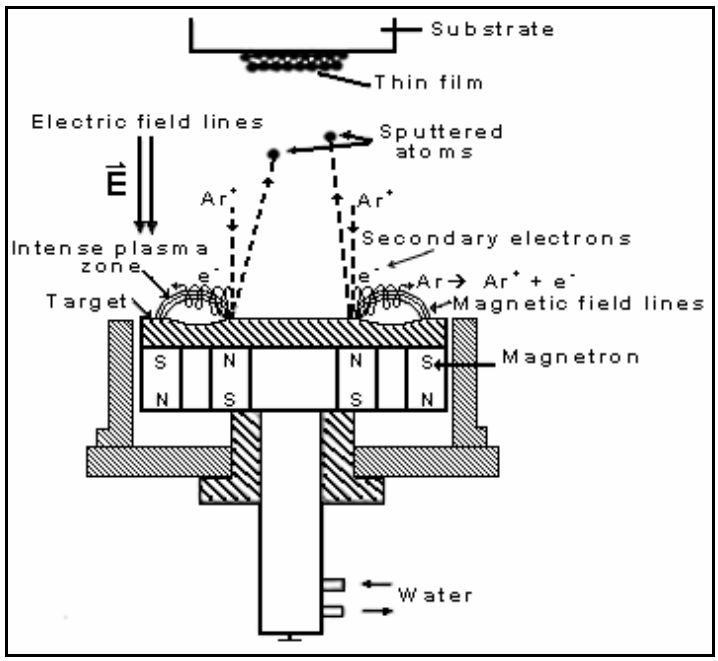

Fig. 9: Schematic presentation of Principles of the RF magnetron sputtering [83].

4. References.

[1] K. Badeker, *Ann. Phys. (Leipzig)* **22** (1907) 749.

[2] F. Streintz, *Ann. Phys. (Leipzig)* **9** (1902) 854.

[3] J. T. Littleton, *U.S. Patent 2* **118** (1938) 795.

[4] H. A. McMaster, *U.S. Patent 2* **429** (1947) 420.

[5] R.G. Gordon, *MRS Bull*. **25** (2000) 52.

[6] M. J. Zunick, *U.S. Patent 2* **516** (1947) 663.

[7] K. Wasa, S. Hayakawa, S. Shooji, S. Takata, *Jpn. J. Appl. Phys*. **10** (1971) 1732.

[8] M. Matsuoka, *Jpn. J. Appl. Phys*. **10** (1971) 736.

[9] T. Minami, *MRS Bull*. **25** (2000) 38.

[10] R .J. Cava, J.M. Phillips, J. Kwo, G. A. Thomas, R. B. van Dover, S. A. Carter, J. J. Krajewski, W. F. Peck, Jr., J. H. Marshall, D. H. Rapkine, *Appl. Phys. Lett*. **64** (1994) 2071.

[11] J .M. Phillips, R .J. Cava, G. A. Thomas, S. A. Carter, J. Kwo, T. Siegrist, J. J. Krajewski, J. H. Marshall, W. F. Peck, Jr., D. H. Rapkine, *Appl. Phys. Lett*. **67** (1995) 2246.

[12] D. D. Edwards, T. O. Mason, F. Goutenoire, and K. R. Poeppelmeier, *Appl. Phys. Lett*. **70** (1997) 1706.

[13] A. J. Freeman, K. R. Poeppelmeier, T. O. Mason, R. P. H. Chang, and T. J. Marks, *MRS Bull*. **25** (2000) 45.

[14] H. Kawazoe, M. Yasukawa, H. Hyodo, M. Kurita, H. Yanagi, H. Hosono, *Nature* **398** (1997) 939.

[15] K. Hayashi, S. Matsuishi, T. Kamiya, M. Hirano H. Hosono, *Nature*, **419** (2002) 462.

[16] H. Kawazoe, H.Y anagi, K. Ueda, H. Hosono, *MRS Bull*. **25** (2000) 28.

[17] N. Senoussaoui, T. Repmann, T. Brammer, H. Stiebig, H. Wagner, *Rev. Energ. Ren.* **3** (2000) 49.

[18] K. Zakrzewska, *thin solid films* **391** (2001) 229.

[19] C. M. Lampert, *Sol. Energy Mater* **6** (1981) 1.

[20] G. Frank, E. Kauer H. Kostlin, *Thin Solid Films* **77** (1981)107.

[21] C. G. Granqvist, *Thin Solid Films* **193/194** (1990) 730.

[22] H. Yoshida, H. Furubayashi, Y. Inque, T. Tonomura, *J. Vac. Soc. Japan* **19 (**1976) 13.

[23] R. Latz, K. Michael M. Scherer, *Japan. J. Appl. Phys*. **30** (1991) L149.

[24] H. Kim, C. M. Gilmore, *J. Appl. Phys.* **68** (1999) 6451.

[25] H. T. Tien J. Higgins, *J. Electrochem. Soc*. **127** (1980) 1475.

[26] G. Hass, J. B. Heaney A. R. Toft, *Appl. Opt.* **18** (1979) 1488.

[27] N. Miura, T. Ishikawa, T. Sasaki, T. Oka, H. Ohata, H. Matsumoto R. Nakano, *Japan. J. Appl. Phys.* **31** (1992) L46.

[28] F. Simonis, M. V. Leij, C. J. Hoogendoorn, *Solar Energy Mater.* **1** (1979) 221.

[29] I. Hamberg, C. G. Graqvist, *J. Appl. Phys.* **60** (1986) R123.

[30] K. C. Mishra, K. H. Johnson, P. C. Schmidt, *Phys. Rev. B* **51** (1995) 13972.

[31] G. L. Pearson, J. Bardeen, *Phys. Rev.* **75** (1949) 865.

[32] C. G. Fonstad, R. H. Rediker, *J. Appl Phys.* **42** (1971) 2911.

[33] J. A. Marley, R. C. Dockerty, *Phys. Rev. A* **140** (1965) 304.

[34] R. L. Weiher, *J. Appl. Phys.* **33** (1962) 2834.

[35] C. G. Granqvist, *Appl. Phys. A* **57** (1993) 19.

[36] M. Jarzebski, J. P. Marton, *J. Electrochem. Soc.* **123** (1976) 199C, 299C, 333C.

[37] L. Holland, *Vacuum Deposition of Thin Films,* New York: Wiley (1958) 492.

[38] G. Haacke, *Ann. Rev. Mater. Sci.* **7** (1977) 73.

[39] J. L. Vossen, *Phys. Thin Films* **9** (1977) 1.

[40] C. G. Granqvist, *Appl. Opt.* **20** (1981) 2606.

[41] M. Jarzebski, *Phys. Status Solidi* a **71** (1982) 13.

[42] H. Kostlin, *Festkorperprobleme* **22** (1982) 229.

[43] J. C. Manifacier, *Thin Solid Films* **90** (1982) 297.

[44] K. L. Chopra, S. Major, D. K. Pandya, *Thin Solid Films* **102** (1983) 1.

[45] A. L. Dawar, J. C.Joshi, *J. Mater. Sci.* **19** (1984) 1.

[46] B. J. Ingram, G .B. Gonzalez, D .R. Kammler, M. I. Bertoni, T.O. Mason, *J. Electroceramics*, **13 (**2004) 167.

[47] O. S. Heavens, *Optical Properties of Thin Solid Films*, London, Butterworth 1955.

[48] R. Swanepoel, *J. phys. E: Sci. Instrum*. **16** (1983) 1214.

[49] W. Jacob, A. Keudell, T. S. Selinger, *Braz. J. Phys*. **30** (2000) 508.

[50] A. Sarkar, S. Ghosh, S. Chaudhury, A. K. Pal, *Thin Solid Films* **204** (1991) 255.

[51] S. Shanthi, C. Subramanian, P. Ramasamy, *Cryst. Res. Technol.* **34** (1999) 1037.

[52] J. C. Manifacier, M. De Murcia, I. Fillard, E. Vicario, *Thin Solid Films* **41** (1977) 127.

[53] J. C. Manifacier, J. Gasiot, J. Fillard, *J. Phys. E: Sci. Instrum.* **9** (1976) 1002.

[54] F. Wooten, *Optical Properties of solids*, Academic, New York, 1981.

[55] R. A. Smith, *Semiconductors*, Cambridge University Press, Cambridge, 1978.

[56] E. Burstein, *Phys. Rev.* **93** (1954) 632.

[57] T. S. Moss, *Proc. Phys. Soc. London Sect. B* **67** (1954) 775.

[58] E. Hagen, R. Rubens, *Ann. Phys.* **11** (1903) 873.

[59] J. R. Bellingham, W. A. Phillips, C. J. Adkins, *Thin Solid Films* **195** (1991) 23.

[60] C. Geoffroy, G. Campet, J. Portier, J. Salardenne, G. Couturier, M. Baourrel, J. M. Chabagno, D. Ferry, C. Ouet, *Thin Solid Films* **202** (1991) 77.

[61] J. Hu, R. G. Gordon, *J. Appl. Phys.* **71** (1992) 880.

[62] I. Hamberg, A. Hjortsberg, C. G. Granqvist, *Appl. Phys. Lett.* **40** (1982) 362.

[63] S. Yoshida, *Appl. Opt.* **17** (1978) 145.

[64] J. C. C. Fan, F. J. Bachner, *J. Electrochem. Soc.* **122** (1975) 1719.

[65] J. C. C. Fan, F. J. Bachner, *Appl. Opt.* **15** (1976) 1012.

[66] Sundaram KB and Bhagavat GK 1981 *Thin Solid Films* **78** 35

[67] K. B. Sundaram, G. K. Bhagavat, *Thin Solid Films* **78** (1981) 35.

[68] J. B. Mooney, S. B. Reading, *Ann. Rev. Mater. Sci.* **12** (1982) 81.

[69] J. B. Mooney, S. B. Reading, *Ann. Rev. Mater. Sci.* **12** (1982) 81.

[70] P. Nath, R. F. Bunshah, *Thin Solid Films* **69** (1980) 63.

[71] R. P. Howson, M. I. Ridge, *Thin Solid Films* **77** (1981) 119.

[72] R. F. Bunshah, *J. Vac. Sci. Technol. A* **3** (1985) 553.

[73] J. A. Thornton, *Thin Solid Films* **107** (1983) 3.

[74] A. Matthews, *J. Vac. Sci. Technol.* A **3** (1985) 2354.

[75] M. I. Ridge, M. Stentake, R. P. Howson, C. A. Bishop, *Thin Solid Films* **80** (1981) 31.

[76] J. C. C. Fan, *Appl. Phys. Lett.* **34** (1979) 515.

[77] J. J. Cuomo in: R. F. Hochman (ed.), Synthesis by reactive ion-beam deposition, *Proc. Conf. on the Applications of Ion-Plating and Implantation to Materials* (1985), American Society for Metals, 1986, p 25.

[78] J. C. C. Fan, *Appl. Phys. Leu.* **34** (1979) 515.

[79] J. F. Smith, A. J. Aronson, D. Chen, W.H. Class, *Thin Solid Films* **72** (1980) 469.

[80] M. Matsuoka, Y. Hoshi, M. Naoe, J. *Vac. Sci. Technol. A* **5** (1987) 52.

[81] S. Onishi, M. Eschwel, W. C. Wang, *Appl. Phys. Lett.* **38** (1981) 419.

[82] S. A. Bashar, *Ph. D. thesis*, University of London, London, United Kingdom, 1998.

[83] C. Marcel, *Ph. D. Thesis*, Bordeaux 1 University, Bordeaux, France, 1998.

Chapter II

Synthesis and characterization of SnO_2 doped with Sb and/or Zn:

ceramics and thin films

As already quoted in the general introduction, despite the large number of studies done on ATO thin films, the commercial ATO thin films are only produced either by spray or chemical vapor deposition (CVD). Although the surface quality is better for thin films deposited by physical vapor deposition (PVD), they are not commercialized. This is mainly due to the absence of commercial large scale target on the market probably due to the difficulty to keep the antimony into the material during sintering at high temperature. In this chapter, we will show how it is possible to prepare ATO targets for PVD without antimony departure, even upon sintering at high temperature (1300 °C). Moreover, ATO ceramic targets, pelletized by cold pressing technique (and not prepared by using the expensive hot pressing technique), suffer from a low densification even after sintering [1]. For industrial production of ATO films by sputtering, it is necessary to produce highly dense targets to increase the film deposition rate and to get dense homogeneous films. In this study, we will show that doping SnO_2 with Zn^{2+} greatly enhances the ceramic target density without affecting the transparency of the films. We will also show that co-doping SnO_2 with Zn^{2+} and Sb^{5+} (forming AZTO ceramic) allowed us to produce highly dense and conductive ceramic targets.

In this work, both ATO and AZTO ceramics were prepared with different compositions; ZTO (zinc doped tin oxide) and SnO_2 ceramics were also prepared for sake of comparison. ATO and AZTO thin films have then been deposited by sputtering using the optimized ceramic targets. The influence of different sputtering conditions, on the opto-electronic properties of the film, has been investigated. Finally, original applications of the ATO and new AZTO films will be presented.

1. Ceramics

1-1. Preparation

SnO_2 (99.9%, Aldrich), Sb_2O_3 (>99%, Prolabo) and ZnO (99.9%, Aldrich) powders, were used to prepare the SnO_2 based ceramics. Appropriate amounts of the selected oxides were ball mixed for 30 min in an agate bowl containing agate balls and ethanol. The alcohol was then evaporated at 110 °C for 6 hours. Afterwards, the powder was ground in an agate mortar, and cold pressed in a mold at 184 MPa (1.88 ton/cm^2) to form cylindrical pellets, ~ 3 mm thick and 13 mm in diameter. The pellets were finally sintered at 1300 °C

under air for 12 hours. The sintering temperature was chosen to minimize the oxygen departure [2, 3]. The pellet dimensions of were measured with a digital caliper vernier, and the pellets were weighed using an analytical balance. These measurements were used to estimate the bulk densities of the pellets. For some samples, the bulk densities were also determined precisely from mercury displacement method using an AutoPore IV 9500 mercury porosimeter. The latter was also used to determine the pore size distribution.

1-2. Chemical composition and bulk density

1-2-a. SnO_2

Consistent with literature [2-4], no significant macroscopic shrinkage was observed for undoped ceramics (prepared using commercial SnO_2 powder) by sintering at 1300 °C. The bulk density (4.12 g/cm^3 as shown in table 1), corresponds to 58 % of the theoretical value (6.95 g/cm^3), as shown in Table 1. It should be noted that the n-type conductivity, normally observed in undoped SnO_2, is mainly due to the existence of oxygen vacancies (□) producing shallow donor levels [5]. Therefore, the *n*-type conduction in undoped SnO_2 can be reasonably depicted with the following formula:

$$SnO_2 \Leftrightarrow Sn^{4+} O_{2-\delta}^{2-} \square_{\delta} \left[2\delta \, e_{C.B.}^{-} \right] + \frac{\delta}{2} O_2 \uparrow \qquad \text{(a)}$$

where $e_{C.B.}^{-}$ represents the mobile electrons in the lattice. In this work, the ceramics, white in color, have a rather low electrical conductivity (<10^{-6} S.cm^{-1}). Such a low value of n-type conductivity indicates that δ, depicted in formula (a), is lower than 10^{-4} [6]. Consequently, it can possibly be asserted that practically no oxygen departs from the SnO_2 lattice at temperature up to 1300 °C, in agreement with literature [2, 3]. This was confirmed by TGA analysis (Fig. 1 (a)). Only a small weight loss (~ 0.4 %) takes place in the temperature range 25-500 °C. Such weight loss is due to minor adsorbed water removal and structural water removal from Sn-OH moieties present at the grain surface [7, 8]. In the temperature range 500-1300°C, almost no weight loss is observed.

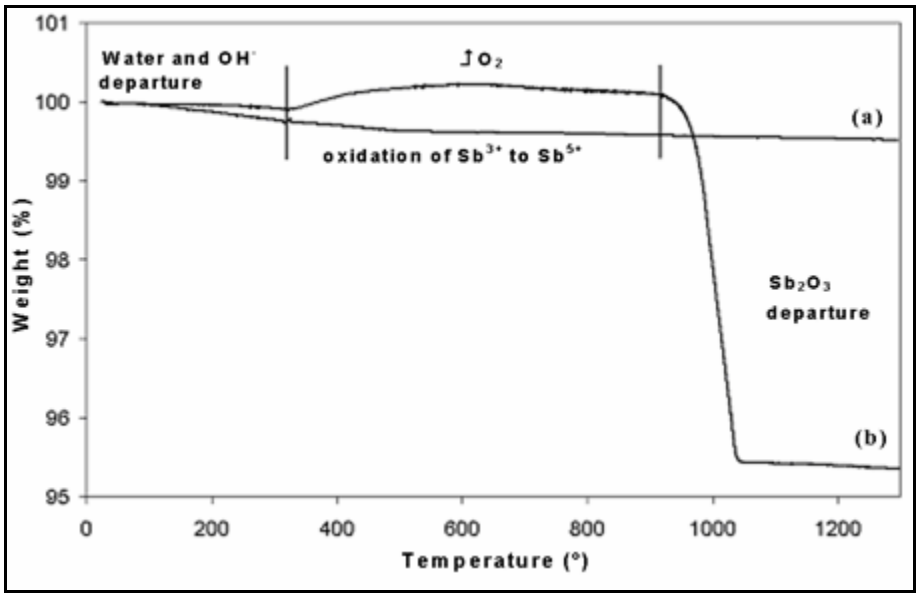

Fig. 1: TGA data for a) SnO_2, b) SnO_2:$Sb_{0.06}$ (nominal composition).

Sample identification	Starting Mixture	Ceramic composition determined by EPMA ± 0.005	Bulk density (g/cm^3) ± 0.05	Weight loss (%) ± 0.1
SnO_2	SnO_2	SnO_2	4.12	0.4
SnO_2:$Sb_{0.01}$	$(SnO_2)_{0.988}$+$(Sb_2O_3)_{0.006}$	$Sn_{0.989}Sb_{0.010}O_2$	4.09	0.4
SnO_2:$Sb_{0.02}$	$(SnO_2)_{0.980}$+$(Sb_2O_3)_{0.010}$	$Sn_{0.989}Sb_{0.011}O_2$	4.06	1.2
SnO_2:$Sb_{0.04}$	$(SnO_2)_{0.960}$+$(Sb_2O_3)_{0.020}$	$Sn_{0.987}Sb_{0.013}O_2$	4.02	3.0
SnO_2:$Sb_{0.06}$	$(SnO_2)_{0.940}$+$(Sb_2O_3)_{0.030}$	$Sn_{0.988}Sb_{0.012}O_2$	3.79	5.0
SnO_2:$Sb_{0.10}$	$(SnO_2)_{0.900}$+$(Sb_2O_3)_{0.050}$	$Sn_{0.987}Sb_{0.013}O_2$	3.47	8.9

Table 1: Ceramic chemical composition determined by EPMA, bulk density, and weight loss of SnO_2:Sb_x (ATO) ceramics with $0 \le x \le 0.10$. The reported bulk densities were deduced by measuring pellet dimensions and weights.

1-2-b. ATO (SnO_2:Sb)

The compositions of the ceramics have been determined by Electron Probe X-ray Microanalysis (EPMA), using a CAMECA SX100 spectrometer. The results for final compositions after ceramic sintering as well as nominal compositions are summarized in Table 1. It has been found that whatever the nominal antimony amount is, the final antimony composition always reaches only ~ 0.01 atoms (at.) per formula unit. This composition is found to be quite homogeneous over thickness using Auger Electron Spectroscopy (AES) analysis (Fig. 2), which was carried out with a VG MICROLAB 310

F spectrometer. Consequently, regarding the final antimony composition of the ceramic, the significant weight loss reported in Table 1, increasing with the Sb_2O_3 content in the starting mixture, accounts for antimony oxide departure at high temperature (T > 900°C) during ceramic sintering (see Fig. 1). Moreover, the bulk density values of the Sb-doped ceramics (from 4.1 to 3.5 g/cm^3) are lower than their undoped counterparts (Table 1). This is presumably a consequence of antimony departure during sintering. A closer look at the TGA curve on Fig. 1(b), we first observe a minor weight loss (~0.1%) at temperatures up to 340°C that can be assigned to the release of water (adsorbed water and hydroxyl groups) as it occurred for undoped SnO_2. The weight gain observed above ~340 °C is due to the oxidation of Sb^{3+} to Sb^{5+} when Sb^{5+} enters the structure (in substitutional position) as it will be confirmed hereafter by X-ray Photoelectron Spectroscopy (XPS) analysis. Finally, the weight loss that occurs above ~940 °C is due to unreacted antimony oxide (Sb_2O_3) departure.

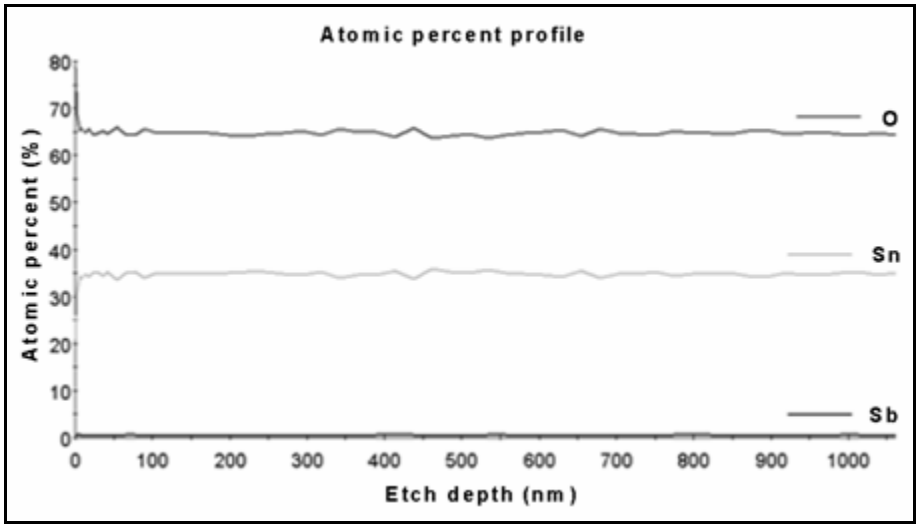

Fig. 2: Atomic percentage profile for ATO ceramic using AES analysis.

To better define the ATO composition, we have also investigated the formal oxidation state for antimony ions on ceramic targets (all tin ions being present as Sn^{4+}) by XPS. The XPS measurements were carried out using a VG 220i-XL Escalab spectrometer with a monochromatized Al K_α source (hν = 1486.6 eV), a 250 µm spot size and a 20 eV pass energy was used to get high-resolution spectra. Energy calibration was done using silver. Fresh samples were fractured and quickly transferred to the ultra-high vacuum system. As a preliminary step, several reference compounds have been characterized: Sb_2O_5, Sb_2O_4 and Sb_2O_3. The binding energies for the different reference compounds and all data for ceramics are reported on Table 2.

References	Sb^{5+} $4d_{5/2-3/2}$ (eV)	Sb^{4+} $4d_{5/2-3/2}$ (eV)	Sb^{3+} $4d_{5/2-3/2}$ (eV)
Sb_2O_5	35.0-36.2 (2.20) 100%		
Sb_2O_4		34.7-35.9 (1.96) 100 %	
Sb_2O_3			34.5-35.7 (1.57) 100%
Ceramics			
ATO ($Sn_{0.988}Sb_{0.012}O_2$)	34.9-36.2 (1.35) 69 %		34.3-35.6 (1.25) 31 %
AZTO($Sn_{0.892}Sb_{0.053}Zn_{0.055}O_{2-\delta}$)	35.0-36.2 (1.35) 100 %		

Table 2: XPS Sb^{5+}, Sb^{4+} and Sb^{3+} $4d_{5/2-3/2}$ binding energies (eV) as well as the full width at half maximum (in parentheses) for reference compounds and ceramics used for the targets. ATO and AZTO compositions are determined by EPMA (from Tables 1 and 3).

Note that for reference compounds, the shift in energy between Sb^{3+} and Sb^{5+} is only 0.5 eV. We have selected the Sb4d peak because the Sb3d is overlapped with a peak of Sn3d. The XPS spectrum of the Sb4d core peaks for ATO ceramic target is shown in Fig. 3.

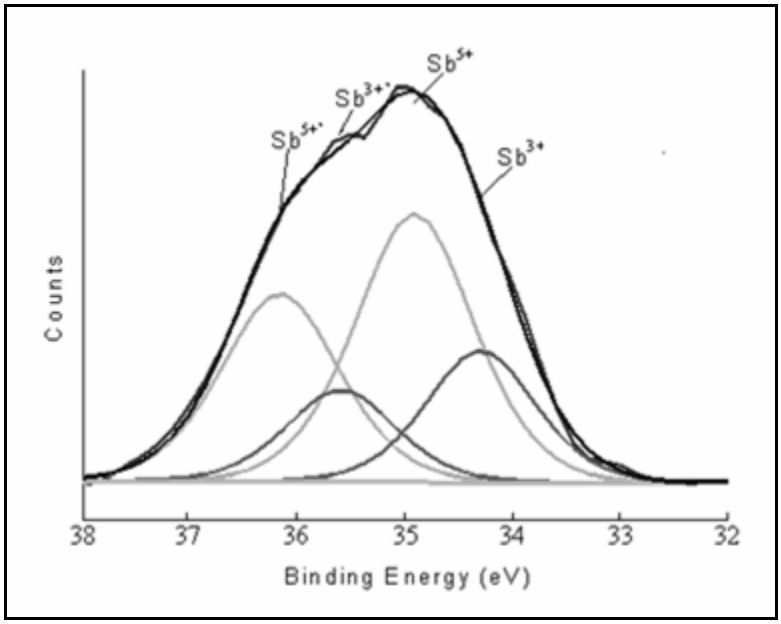

Fig. 3: XPS Sb 4d core peak for ATO ceramic pellet. The presence of both Sb^{5+} and Sb^{3+} is detected.

The presence of both Sb^{5+} and Sb^{3+} is detected with a deduced ratio Sb^{3+}/Sb^{5+} equal to ~ 30/70. Thus by assuming that both Sb^{3+} and Sb^{5+} substitute Sn^{4+} in the SnO_2 lattice, the formula of the ATO ceramic must be expressed as:

$$Sn_{1-x-y}^{4+} Sb_x^{5+} Sb_y^{3+} O_2^{2-} \left[(x-y) e_{C.B.}^- \right]. \quad \text{(b)}$$

From the ATO ceramic composition (Table 1) we have $x+y \approx 0.012$, and from XPS results, we have $x/y = 7/3$. This implies that ~0.008 out of 0.012 Sb exists as Sb^{5+} in the ATO ceramic, and the rest of antimony exists as Sb^{3+} state (~0.004). According to this, formula (b) should be more accurately expressed as:

$$Sn_{0.988}^{4+} Sb_{0.008}^{5+} Sb_{0.004}^{3+} O_2^{2-} \left[0.004 e_{C.B.}^- \right]. \quad \text{(c)}$$

The occurrence of ~0.004 $e_{C.B.}^-$ per formula unit of oxide will be confirmed later on.

1-2-c. ZTO (SnO_2:Zn)

According to literature [9-11], and as we have already described in the general introduction, doping SnO_2 with substitutional cations, having lower oxidation states than Sn^{4+}, such as Mn^{2+}or Cu^{2+}, strongly enhances the ceramic density. However, these d^5 or d^9 elements behave as color centers which affect the transparency [12]. Therefore, the later have to be avoided in TCOs. That will not occur when SnO_2 is doped with the divalent element Zn^{2+}. Indeed, Zn^{2+} is a d^{10} element, like Sn^{4+}, and the Zn^{2+}:d^{10} energy states will underlie the O^{2-}:$2p^6$ valence band of SnO_2. Therefore, doping SnO_2 with Zn^{2+} should not affect its transparency. But, as expected, Zn^{2+} has the same effect as than Mn^{2+} or Cu^{2+}; it greatly enhances the relative ceramic bulk density (d/d_0), where d is the measured bulk density and d_0 is the SnO_2 theoretical density (6.95 g/cm^3). Hence, the relative bulk density increased up to 95%, when SnO_2 is doped with 0.06 at. of Zn, which corresponds to the solubility limit of zinc in the rutile structure of SnO_2 [13]. We have correlated this event with the presence of Zn^{2+} in substitutional positions, leading to the formation of neutral oxygen vacancies [1] according to $Sn_{1-y}^{4+} Zn_y^{2+} O_{2-y}^{2-} \square_y$. Indeed, the presence of neutral oxygen vacancies, would promote mass transport at the grain boundary yielding high density ceramics. Let us quote that the presence of some Zn^{2+} in interstitial positions, leading to n-type conductivity according to:

$$Sn_{1-y}^{4+} Zn_y^{2+} Zn_\varepsilon^{2+} O_{2-y}^{2-} \square_y \left[2\varepsilon\, e_{C.B.}^- \right] \quad \text{(d)}$$

can be reasonably neglected regarding the high value of the resistivity reported in Fig. 4.

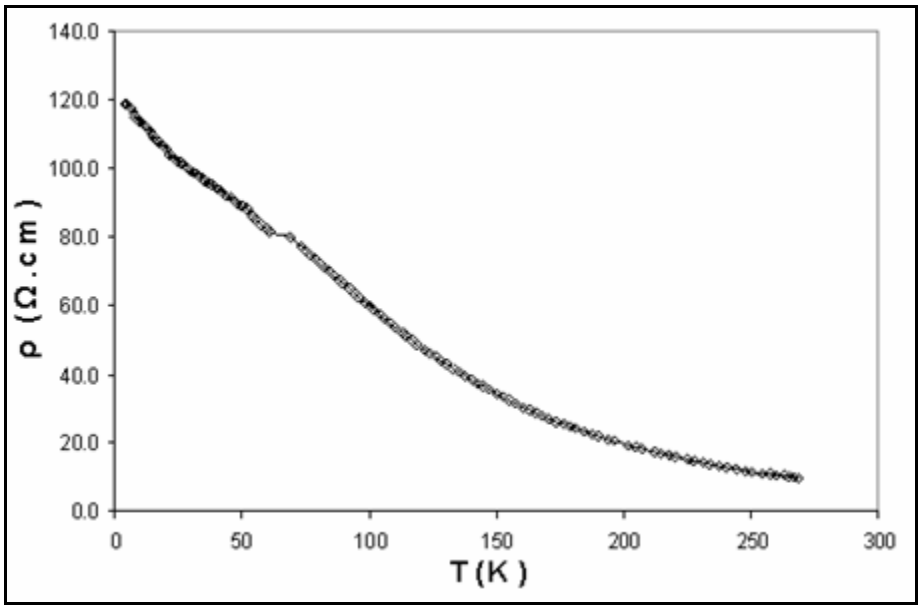

Fig. 4: Resistivity evolution with temperature for SnO_2 doped with 0.06 at. of Zn.

1-2-d. AZTO (SnO_2:Sb:Zn)

As we have mentioned in the previous paragraph, the solubility limit of Zn into SnO_2 is 0.06 at. (note that this value will be also confirmed by x-ray measurements for AZTO). After many trials, we found that a high densification associated with a high conductivity can be achieved only when the Zn content is at least equal to Sb content. In addition, to have the highest value of carrier concentration, we need to have high Sb contents. For all these reasons we decided, for sake of clarity, to detail only the results that we obtained on the peculiar nominal composition $[SnO_2:Sb_{0.06}]:Zn_y$. Note that this simplified sample identification is emphasizing the influence of Zn doping into ATO (see also Table 3).

The EPMA results reported on Table 3 show that the sintered AZTO ceramics have an antimony amount (reaching ~ 0.053) which is approximately 5 times higher than the solubility limit (~ 0.01 at.) previously observed for the ATO counterparts (see Table 1). The ceramic composition is homogeneous all over the thickness (Fig. 5). The main origin of this solubility difference can reasonably be attributed to the isovalent substitution of three Sn^{4+} by two Sb^{5+} and one Zn^{2+}, thereby maintaining charge neutrality as well as structural integrity. In addition, the ceramic shrinkage due to Zn doping, which causes density enhancement, Table 3, may also prevent antimony departure in AZTO.

Sample identification	Starting mixture	Ceramic composition determined by EPMA ± 0.005	Bulk density (g/cm^3) ± 0.05	Weight loss[a] (%) ± 0.1
SnO_2	SnO_2	SnO_2	4.12	0.4
$[SnO_2:Sb_{0.06}]:Zn_{0.02}$	$[(SnO_2)_{0.94}+(Sb_2O_3)_{0.03}]_{0.98}+(ZnO)_{0.02}$	$Sn_{0.948}Sb_{0.035}Zn_{0.017}O_{2-\delta}$	4.51	1.2
$[SnO_2:Sb_{0.06}]:Zn_{0.06}$	$[(SnO_2)_{0.94}+(Sb_2O_3)_{0.03}]_{0.94}+(ZnO)_{0.06}$	$Sn_{0.892}Sb_{0.053}Zn_{0.055}O_{2-\delta}$	6.42	~
$[SnO_2:Sb_{0.06}]:Zn_{0.10}$	$[(SnO_2)_{0.94}+(Sb_2O_3)_{0.03}]_{0.90}+(ZnO)_{0.10}$	$Sn_{0.865}Sb_{0.053}Zn_{0.082}O_{2-\delta}$	6.24	~
$[SnO_2:Sb_{0.06}]:Zn_{0.14}$	$[(SnO_2)_{0.94}+(Sb_2O_3)_{0.03}]_{0.86}+(ZnO)_{0.14}$	$Sn_{0.810}Sb_{0.052}Zn_{0.138}O_{2-\delta}$	6.07	~

Table 3: Ceramic chemical composition, bulk density, and weight loss of $[SnO_2:Sb_{0.06}]:Zn_y$, $0 \leq y \leq 0.14$. The reported bulk densities were deduced by measuring pellet dimensions and weights. [a] ~ indicates negligible weight loss. SnO_2 data were given here only for comparison. δ indicates the neutral oxygen vacancy, created by doping with Zn, which varies with Zn content.

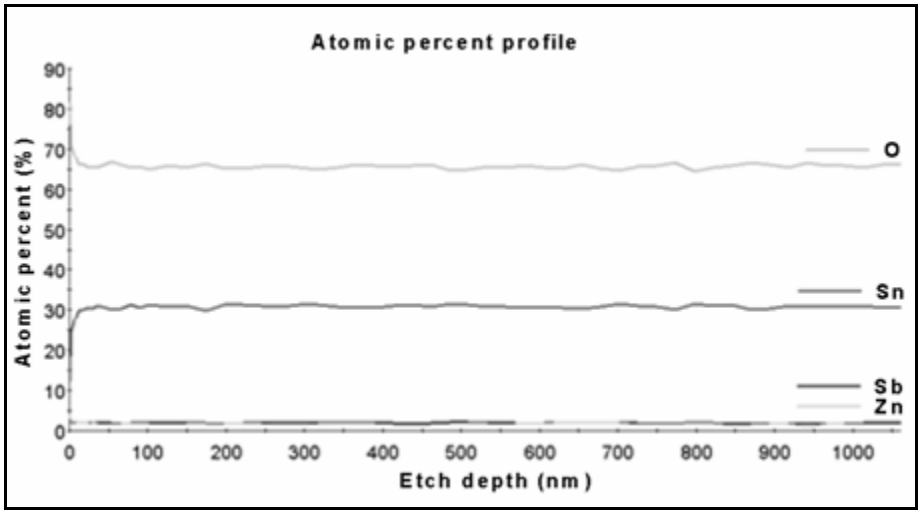

Fig. 5: AES analysis for AZTO ceramic ($[SnO_2:Sb_{0.06}]:Zn_{0.06}$) showing atomic percentage profile.

Due to this, a negligible weight loss, with almost no antimony departure, is observed for ceramics containing Zn amounts higher than 0.05 [Table 3 and Fig. 6(b)]. For lower amount of Zn such as in $[SnO_2:Sb_{0.06}]:Zn_{0.02}$ ceramic (nominal composition), a small weight loss is observed (~1.2%) due to Sb_2O_3 departure [Table 3 and Fig. 6(a)]. As in the case of ATO, AZTO showed weight gain in the temperature range 340-940 °C, which is due to the oxidation of Sb^{3+} into Sb^{5+} while entering the structure. As shown in Table 3 and Fig. 7, the highest bulk density (6.42 g/cm^3) is obtained for the nominal composition $[SnO_2:Sb_{0.06}]:Zn_{0.06}$. For low nominal Zn amount (0.02), only a small density enhancement (4.51 g/cm^3) is observed and for nominal contents higher than 0.06, the value of density is higher than 6 g/cm^3 but slightly decreases (this point will be discussed in paragraph 1-3-b).

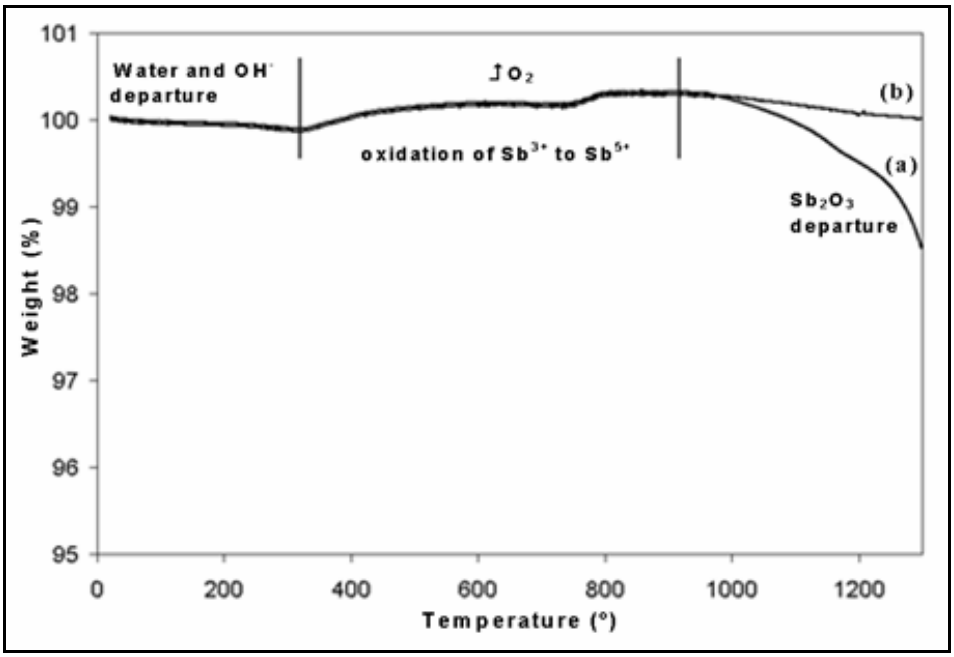

Fig. 6: TGA data for a) $[SnO_2:Sb_{0.06}]:Zn_{0.02}$ and b) $[SnO_2:Sb_{0.06}]:Zn_{0.06}$ (nominal composition).

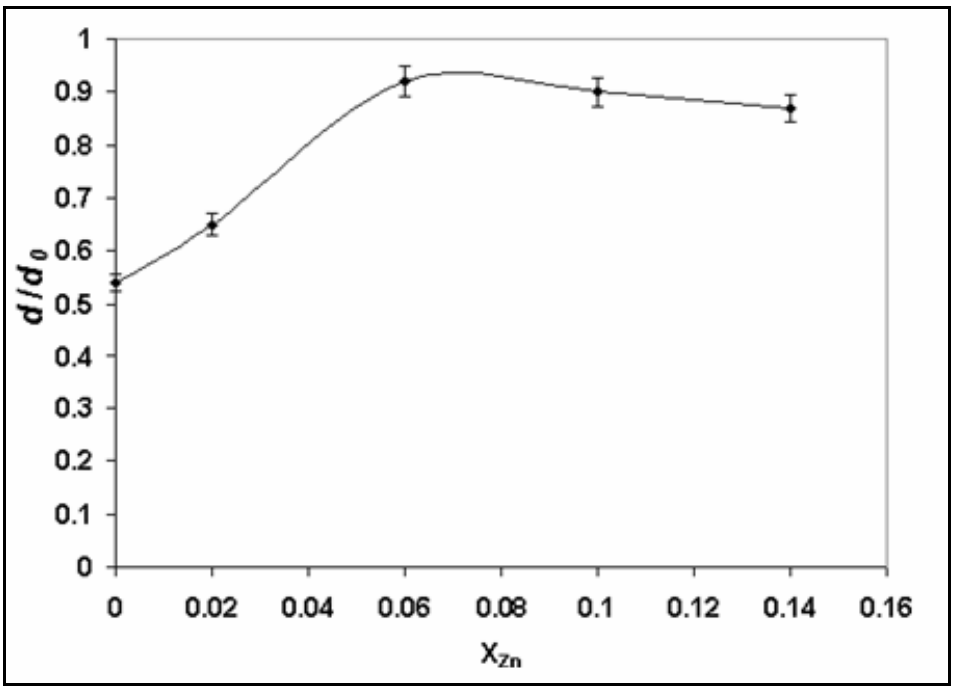

Fig. 7: Relative bulk density (d/d_0) variation with Zn content (X_{Zn}) for AZTO ceramics.

XPS measurements were performed on $[SnO_2:Sb_{0.06}]:Zn_{0.06}$ ceramic that has the highest density (Table 3). Only one component with a pronounced maximum around 35.0 eV, corresponding to Sb^{5+} is present (Fig. 8 and Table 2).Thus, all antimony present in the final ceramic composition has a formal oxidation state of 5+ in accordance with TGA results [Fig. 6 (b)]. Hence, the corresponding formula of the above ceramic can be written as:

$$Sn_{1-x-y-\delta}^{4+} Sb_x^{5+} Zn_{y+\delta}^{2+} O_{2-\delta}^{2-} \square_\delta \left[(x-2y)e_{C.B.}^-\right] \quad \text{(e)}$$

with $x \cong 0.053$, $y+\delta \cong 0.055$. The determination of the different parameters (x, y, δ) will be given later. In the expression of the formula we take into account that the y part of Zn^{2+} reduces the carrier concentration produced by Sb^{5+} and the δ part goes to create the neutral oxygen vacancies necessary for densification process.

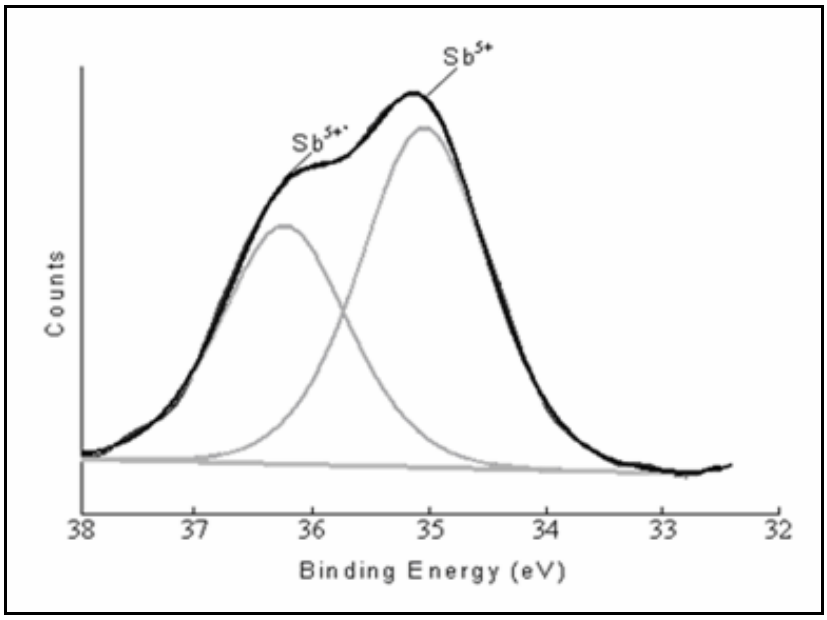

Fig. 8: XPS Sb 4d core peaks for AZTO ceramic target having the chemical composition $Sn_{0.892}Sb_{0.053}Zn_{0.055}O_{2-\delta}$. Only one doublet corresponding to Sb^{5+} is present.

1-3. Structural characterization

Tin (IV) dioxide (II) or SnO_2 has only one stable phase, the so-called cassiterite (mineral form) or rutile (material structure). It crystallizes in the tetragonal rutile structure with space group $D_{4h}^{14}(P4_2/mnm)$ [14]. Its unit cell contains six atoms (two tin atoms and four oxygens). Tin atoms occupy the center of a surrounding core composed of six oxygen atoms placed at the corners of a quasi-regular octahedron (Fig. 9). The metal atoms (Sn^{4+} cations) are located at (0,0,0) and (½,½,½) positions in the unit cell, and the oxygen atoms (O^{2-} anions) at ±(u,u,0) and ±(½+ u,½- u,½), where the internal parameter u, takes the value 0.307. Lattice parameters are: $a = b = 4.737$ Å and $c = 3.186$ Å [15].

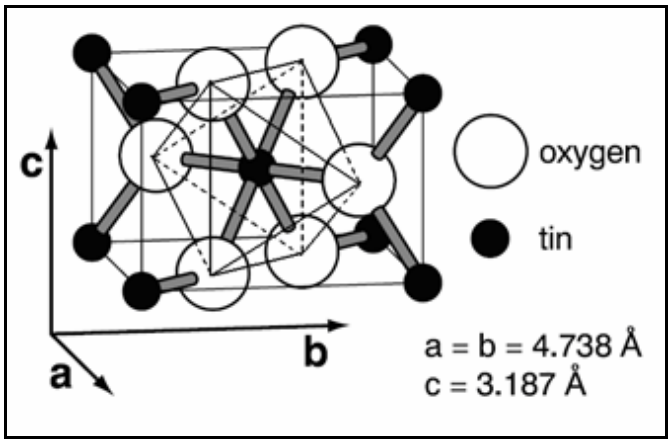

Fig. 9: Bulk unit cell of SnO_2.

SnO_2 is a n-type, wide band-gap semiconductor. The origin of the n-type behavior is the native non-stoichiometry caused by oxygen vacancies. The electrical resistivity, varies from 10 to 10^6 Ω.cm, depending on the temperature and the stoichiometry of the oxide [16-19]. SnO_2 has a direct band-energy gap of ≈ 3.6 eV (Fig. 10). The conduction band minimum is a 90 % tin s-like state and the valence band maximum consists mainly of oxygen p-like states (Fig. 10-b).

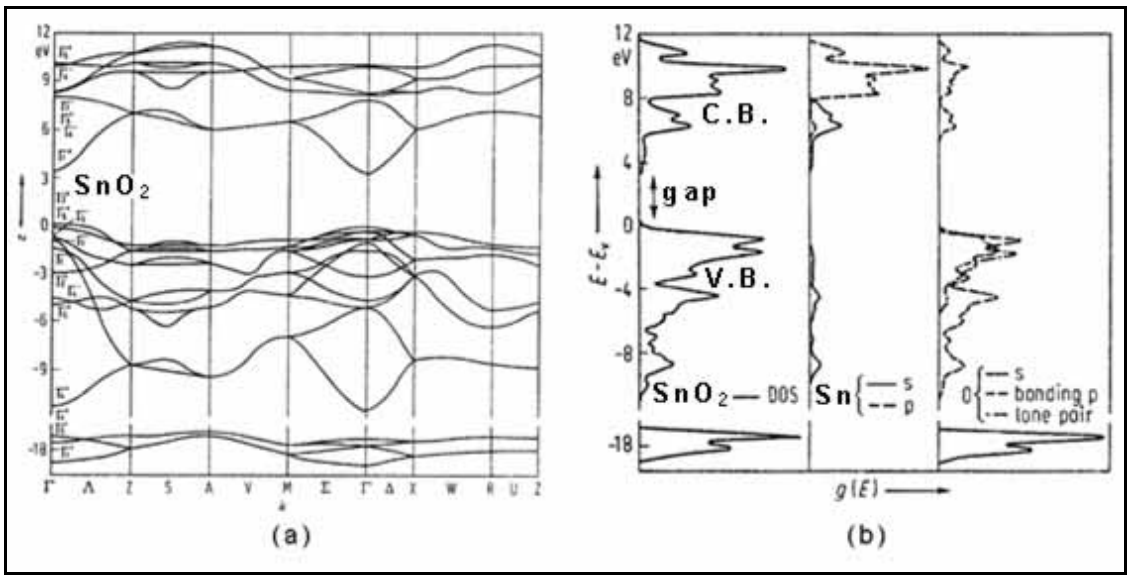

Fig. 10: Presentation of (a) energy band diagram of SnO_2 and (b) density of states (DOS) projection for SnO_2, Sn and O [20].

1-3-a. ATO (SnO_2:Sb)

X-Ray Diffraction (XRD) patterns for SnO_2 and ATO powders annealed at 1300°C (Fig. 11) were acquired on a Philips PW1820 vertical goniometer in a Bragg Brentano geometry with CuKα radiation (λ = 1.5406Å). As expected, there is no evidence of the

presence of extra phases such as antimony oxides (Sb_2O_3 or Sb_2O_5), in addition to the peaks characteristic of the rutile polycrystalline structure of SnO_2 (JCPDS reference pattern 41-1445), suggesting the formation of a solid solution. Moreover, the molar ratio of Sb may be too low (~ 0.012) to be detected. In addition, we have noted a slight shift of the main diffraction peaks towards lower angles compared to pure SnO_2, which implies a slight increase in the cell parameters ('a' from 4.738 to 4.745 Å and 'c' from 3.187 to 3.196 Å) (Fig.11). This evolution should be attributed to the existence of Sb^{3+} in substitutional position, which is consistent with XPS results showing the existence of Sb^{3+} and Sb^{5+} into ATO ceramics (see formula (b) : $Sn^{4+}_{1-x-y} Sb^{5+}_{x} Sb^{3+}_{y} O^{2-}_{2} \left[(x-y)e^{-}_{C.B.}\right]$). Indeed, the ionic radius for the 6-coordinated Sn^{4+} (0.69 Å) is smaller than that of Sb^{3+} (0.76 Å) and larger than Sb^{5+} (0.62 Å) [21]. However, one must consider that Sb^{3+} behaves as a non-ionized donor center having its $5s^2$ electrons stabilized below the conduction band edge. It means that Sb^{3+} should have a somewhat different structural environment than Sb^{5+} which behaves as an ionized donor centers. Hence, Sb^{3+} was assumed by Messad et al. [22] to segregate at the grain surface and also at grain boundaries forming planar defects.

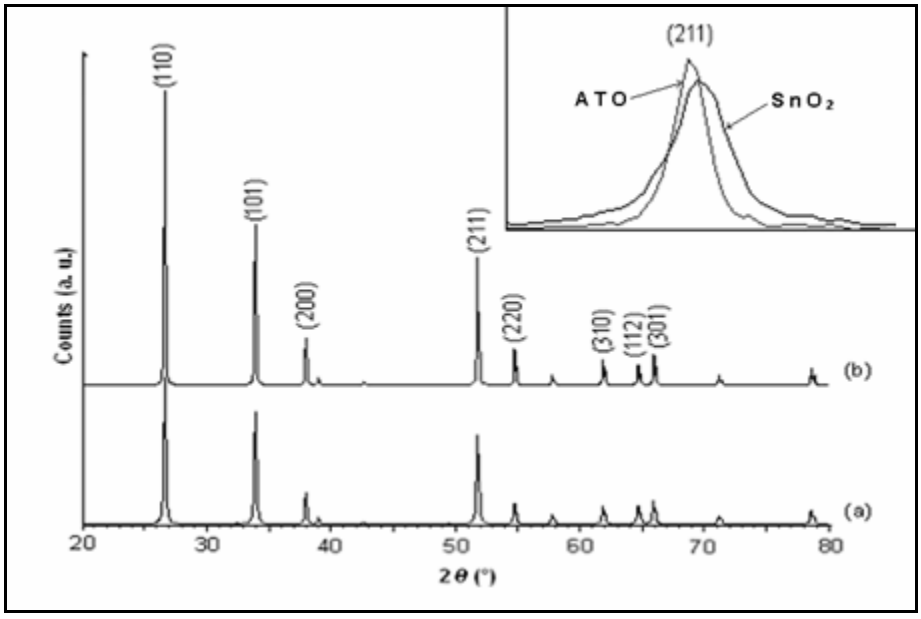

Fig.11: XRD data for (a) undoped SnO_2 and (b) SnO_2:Sb_x (ATO) powders annealed at 1300 °C. The shift of the (211) peak position is shown in the insert.

Finally, the only difference between SnO_2 and ATO powder comes from a decrease of the FWHM (full width at half maximum) for ATO powder indicating an enhancement of the crystallinity for doped SnO_2. By using the Scherrer law [23], the crystallite size was evaluated to be 65 nm for SnO_2 and 155 nm for ATO.

The morphology of some ATO samples has been studied by Scanning Electron Microscopy (SEM). The SEM micrographs were obtained using a JEOL JSM-6360 microscope. To avoid any charging of the sample by the electron beam during the observation, the samples were coated with a thin gold film. Fig. 12 shows that ATO ceramic samples consist of agglomerated particles, with rather regular sizes of micrometer order. This creates macropores responsible for the low density values as reported previously in Table 1. The presence of macropores was also evidenced from porosity measurements using a mercury porosimeter (collaboration with A. MANSOURI from the Institut Européen des Membranes (IEM), Montpellier, France). Main data deduced from porosity measurements are listed in Table 4.

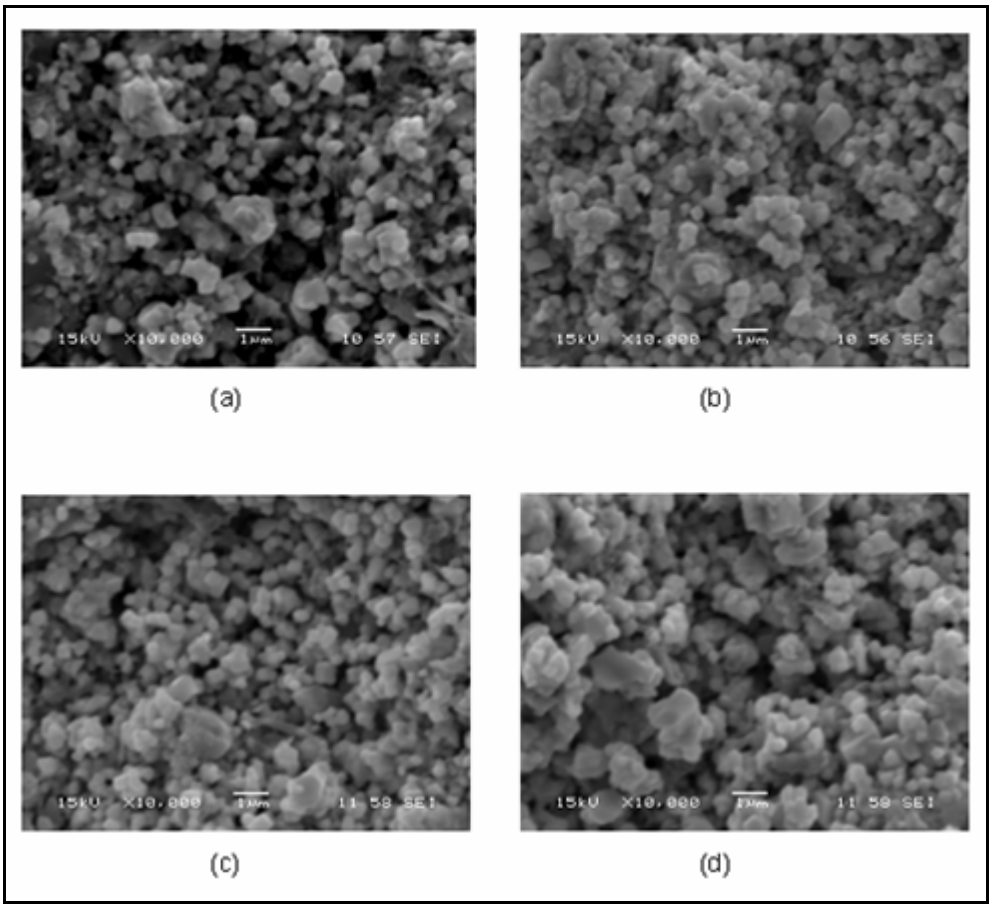

Fig. 12: SEM micrograph for ATO ceramics; a) $SnO_2Sb_{0.02}$, b) SnO_2:$Sb_{0.04}$, c) SnO_2:$Sb_{0.06}$, and d) SnO_2:$Sb_{0.10}$ (nominal composition).

Fig. 13 shows the variation of the differential intrusion of mercury versus pore size for doped SnO_2:Sb_x samples. Moreover, Fig. 13 and Table 4 indicates that as the nominal antimony content increases, the total pore volume and average pore size (diameter) slightly increases. In addition, the bulk density decreases while the nominal antimony content

increases, due to the antimony departure. As expected, there is a good accordance between the bulk density values deduced from porosity measurements, reported on Table 4, and those previously reported in Table 1 (deduced by measuring pellets dimensions and weights). Nevertheless, the porosity measurements lead to more accurate values of density, and confirm its tendency to decrease with nominal antimony content.

Sample identification	Total pore volume (cm^3/g)	Average pore diameter (µm)	Bulk density[a] (g/cm^3) ± 0.05
$SnO_2:Sb_{0.04}$	0.079	0.887	4.25
$SnO_2:Sb_{0.06}$	0.102	0.941	3.81
$SnO_2:Sb_{0.10}$	0.105	1.342	3.44

Table 4: Main data deduced from porosity measurements for $SnO_2:Sb_x$ ceramics.
[a]The deduced bulk density values are close to those listed in Table 1.

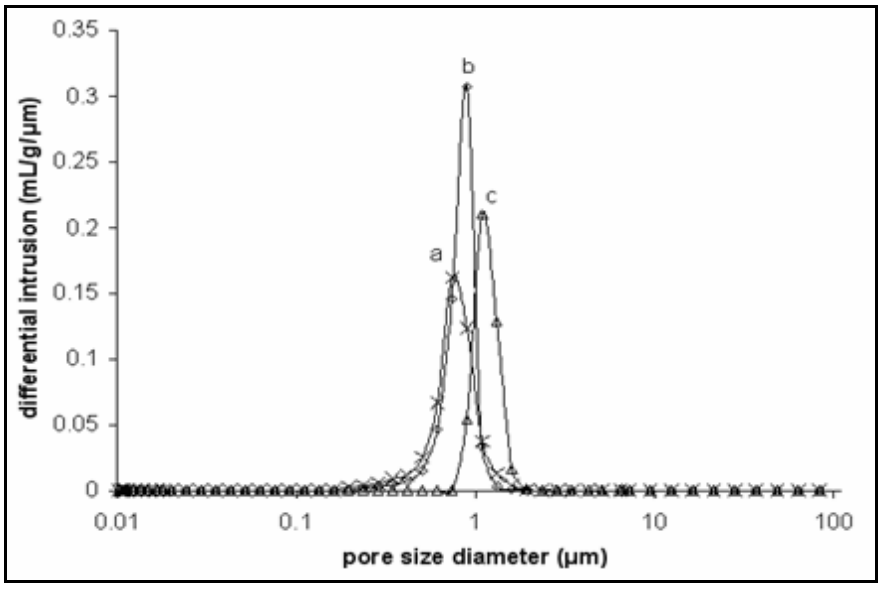

Fig. 13: Pore size diameter variation with Sb variation in ATO ceramics, a) $SnO_2:Sb_{0.04}$, b) $SnO_2:Sb_{0.06}$, and c) $SnO_2:Sb_{0.10}$ (nominal compositions).

1-3-b. AZTO (SnO_2:Sb:Zn)

XRD patterns for AZTO powders annealed at 1300 °C (Fig. 14) show that up to a nominal Zn content equal to 0.06 at., the diagram is characteristics of the SnO_2 structure. Indeed, we can assume the formation of a solid state solution. As previously observed for ATO ceramics, we note an enhancement of crystallinity for AZTO compared to SnO_2 one (the crystallite size was evaluated to be 175 nm for $[SnO_2:Sb_{0.06}]:Zn_{0.06}$ ceramic compared

to 65 nm for SnO_2). For Zn content higher than 0.06, some additional peaks are present with an intensity that increases with Zn content. These peaks account for the formation of the inverse spinel phase Zn_2SnO_4 [JCPDS reference pattern 24-1470] [1, 24].

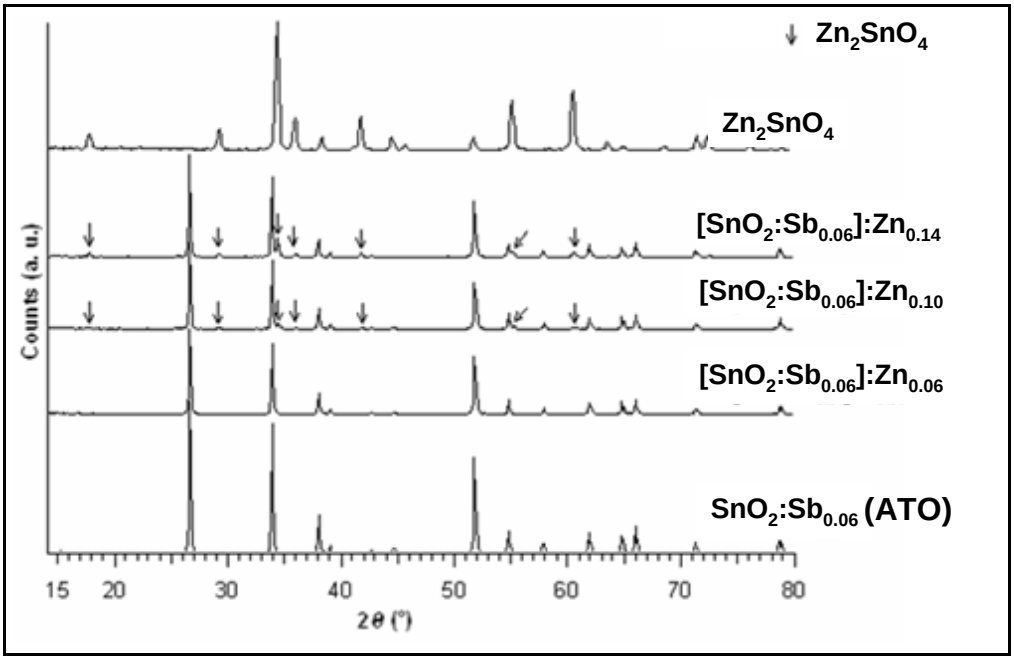

Fig. 14: XRD for SnO_2:$Sb_{0.06}$, [SnO_2:$Sb_{0.06}$]:$Zn_{0.06}$, [SnO_2:$Sb_{0.06}$]:$Zn_{0.10}$, and [SnO_2:$Sb_{0.06}$]:$Zn_{0.14}$ (Table 3). (↓) indicates peaks which correspond to the inverse spinel phase Zn_2SnO_4.

Moreover, the existence of this phase beside the rutile SnO_2 could be responsible for the density decrease observed earlier (paragraph 1-2-d) for AZTO ceramics when Zn content is higher than 0.06 (see Fig. 7).

A strong grain percolation is observed on the SEM micrograph (Fig. 15) for the

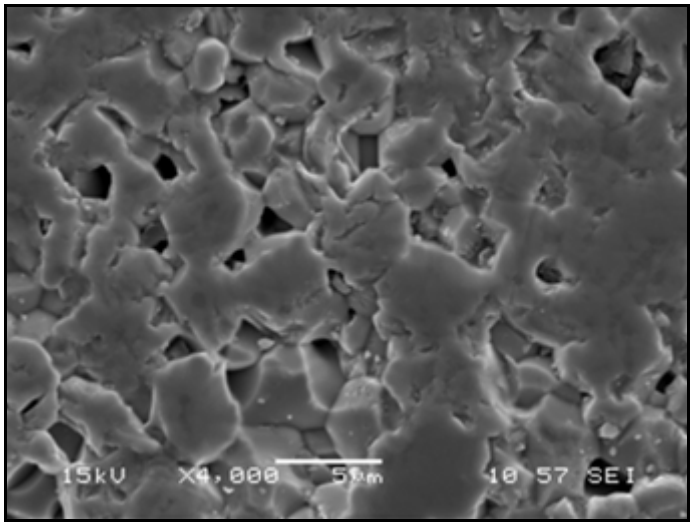

Fig. 15: SEM micrograph for AZTO ([SnO_2:$Sb_{0.06}$]:$Zn_{0.06}$) ceramic (see Table 3).

[SnO_2:$Sb_{0.06}$]:$Zn_{0.06}$ ceramic having the highest density. As we have already explained, co-doping with Zn leads to the presence of neutral oxygen vacancies according to $Sn^{4+}_{1-x-y-\delta}Sb^{5+}_{x}Zn^{2+}_{y+\delta}O^{2-}_{2-\delta}\square_{\delta}\left[(x-2y)e^{-}_{C.B.}\right]$ [formula (e)]. These allow mass transfer at the grain boundary and hence grain percolation, resulting in ceramic density enhancement.

1-4. Electrical measurements

Resistivity measurements were carried out as a function of the temperature, from 4.2 K to room temperature using a standard four probe configuration set-up with direct current (in collaboration with Rodolph Decourt from service de "Mesures de Transport Electronique" de l'ICMCB).

1-4-a. ATO (SnO_2:Sb)

Doping SnO_2 with different nominal amounts of Sb significantly lowers the resistivity from more than10^6 Ω.cm (for undoped SnO_2 ceramic) to around 0.03-0.04 Ω.cm (Fig. 16). The resistivity lowering is due to the introduction of free electrons in the conduction band according to the previously quoted formula (c) ($Sn^{4+}_{0.988}Sb^{5+}_{0.008}Sb^{3+}_{0.004}O^{2-}_{2}\left[0.004e^{-}_{C.B.}\right]$). Let us recall that in formula (c), Sb^{5+} behaves as an ionized electron donor center, the non-ionized center being normally Sb^{4+}. However, the energy of the Sb^{4+}:$5s^1$, is located at the immediate vicinity of the conduction band edge [25]; therefore Sb^{4+} is spontaneously ionized into Sb^{5+} (the Sb^{4+} was not evidenced by XPS measurements). Moreover, as already described before, Sb^{3+} behaves, as well, as a non-ionized donor center but having its $5s^2$ electron stabilized below the conduction band edge; it was assumed by Messad et al. [22] to segregate at the grain boundaries. On Fig. 16, we note some slight differences concerning the values of resistivity, even if the final compositions determined by EPMA, are similar for all these materials. This is due to the difference in ceramic density. The lowest resistivity is observed for SnO_2:$Sb_{0.02}$ (nominal composition) ceramic that has highest density. In addition, we have deduced the carrier concentration from Hall measurements (in collaboration work with J. Marcus, from Laboratoire d'Etudes des Propriétés Electroniques des Solides (CNRS- UPR11), Grenoble, France).

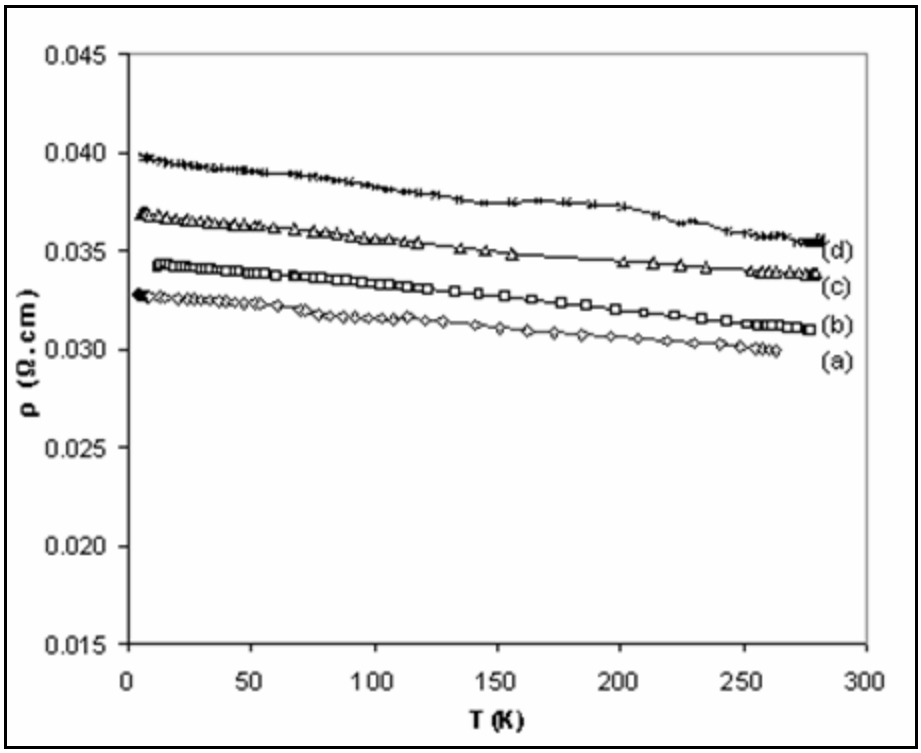

Fig. 16: Resistivity evolution with temperature for ATO ceramics having nominal composition of a) SnO_2:$Sb_{0.02}$, b) SnO_2:$Sb_{0.04}$, c) SnO_2:$Sb_{0.06}$, and d) SnO_2:$Sb_{0.10}$.

The values of electronic carrier concentration are around 1.2×10^{20} e^-.cm^{-3} (Table 5), thus leading to a carrier concentration per formula unit (Sb^{5+} responsible for electronic conductivity) equal to 0.004, which is in a full agreement with the following formula (formula (c): $Sn_{0.988}^{4+}Sb_{0.008}^{5+}Sb_{0.004}^{3+}O_2^{2-}\left[0.004e_{C.B.}^-\right]$) deduced from EPMA and XPS results. From the carrier concentration determined from Hall measurements and the resistivity values, the carrier mobilities (μ) were deduced from the well-known relation $1/\rho = n\mu e$. The mean mobility is estimated to be ~ 1.5 $cm^2V^{-1}s^{-1}$ (Table 5). This value is about ten times smaller than that occurring in dense thin films, for similar carrier concentrations [26, 27]. In fact, for the ceramics the mobility is limited by a textural effect as shown below.

Sample identification	**Carrier concentration (10^{20} e^- cm^{-3}) ± 5%**	**Carrier mobility (cm^2V^{-1} s^{-1}) ± 5%**	**Resistivity (10^{-2} Ω.cm) ± 5%**
SnO_2:$Sb_{0.02}$	1.22	1.71	3.00
SnO_2:$Sb_{0.04}$	1.26	1.61	3.09
SnO_2:$Sb_{0.06}$	1.25	1.48	3.38

Table 5: Electrical measurements conducted at room temperature for ATO (SnO_2:Sb_x) ceramics.

X-ray diffractogram shows that the crystallite mean size is estimated to be ~ 155 nm. This value is more than 400 times higher than the electron mean free path. The electron mean free path, *l*, can be roughly estimated from the classical relation:

$$l = v\tau \quad (1)$$

where $v = (3k_B T / m^*)^{1/2}$ is the electron velocity, m^* is the electron effective mass and $\tau = \mu m^* / e$ is the relaxation time. By assuming an intrinsic mobility μ ~ 10 $cm^2V^{-1}s^{-1}$, and taking m^* ~ 0.19-0.33 m_o [28], then *l is* ~ 0.29-0.38 nm. Consequently, the electron mean free path can be neglected in comparison with the average crystallite size. Therefore, the observed low carrier mobility, μ ~ 1.5 $cm^2V^{-1}s^{-1}$ (Table 5), cannot be a priori justified using a straightforward carrier-scattering occurring at the crystallite interfaces [6, 29]. However, this assertion does not take into account textural effects, such as effect of inefficient grain percolation and/or the presence of pores. An inefficient grain percolation and/or the presence of pores in the ceramics will also cause a drop of the carrier mobility and, therefore, a drop of the conductivity [30].

1-4-b. AZTO (SnO_2:Sb:Zn)

AZTO ceramics show lower electrical resistivity compared to the ATO counterparts (Fig. 17). The lowest resistivity (~ $1.4x10^{-2}$ Ω.cm at 273 K) is reached for the ceramic doped with 0.06 atomic content of Zn. Most interestingly, the resistivity remains nearly stable over the whole temperature range indicating a quasi-metallic behavior. For higher Zn content, a slight increase of the resistivity has been noticed (insert of Fig. 17). This can be correlated with the formation of the insulating inverse spinel phase Zn_2SnO_4 [1, 24], previously observed on the x-ray diffractogram (Fig. 14).

The carrier mobility, calculated from resistivity and Hall measurements, was found to be significantly enhanced for the AZTO ceramics up to around three times compared with ATO counterparts (Table 6). Nevertheless, the carrier concentrations are quite similar for both types of ceramics. We just notice a slight decrease when the Zn amount increases. So, the conductivity enhancement for AZTO ceramics is mainly due to the increase of carrier mobility.

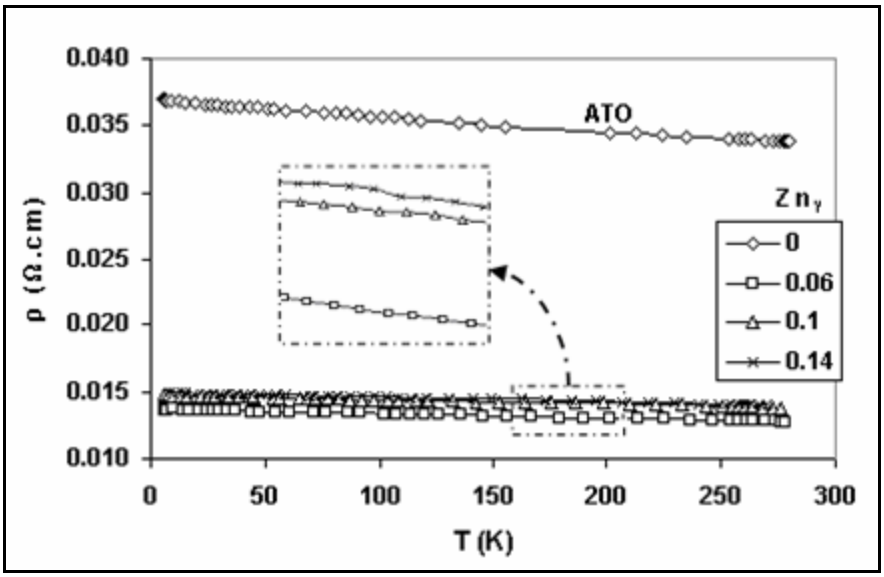

Fig. 17: Resistivity evolution with temperature for different nominal Zn contents (Zn_y) in the AZTO ($[SnO_2:Sb_{0.06}]:Zn_y$) ceramic with $0 \leq y \leq 0.14$. The evolution of resistivity for ATO is given for comparison.

Sample identification	**Carrier concentration (10^{20} e^- cm^{-3}) ± 5%**	**Carrier mobility (cm^2V^{-1} s^{-1}) ± 5%**	**Resistivity (10^{-2} Ω.cm) ± 5%**
$SnO_2:Sb_{0.06}$	1.25	1.48	3.38
$[SnO_2:Sb_{0.06}]:Zn_{0.06}$	1.15	4.26	1.28
$[SnO_2:Sb_{0.06}]:Zn_{0.10}$	0.97	4.69	1.37
$[SnO_2:Sb_{0.06}]:Zn_{0.14}$	0.95	4.71	1.40

Table 6: Electrical measurements conducted at room temperature for AZTO ($[SnO_2:Sb_{0.06}]:Zn_y$) ceramics. ATO is added as reference.

As previously shown, from the EPMA measurements, the chemical final composition of the ceramic having the highest density and conductivity is $Sn_{0.892}Sb_{0.053}Zn_{0.055}O_{2-\delta}$. Moreover, as already found by XPS analysis for AZTO ceramic, all antimony ions exist in the formal oxidation state 5+ (~0.053), which is far from the deduced carrier concentration from Hall measurements (~0.004). Finally, to calculate the accurate final formula for the above AZTO ceramic (according to the previously established formula (e) $Sn^{4+}_{1-x-y-\delta}Sb^{5+}_{x}Zn^{2+}_{y+\delta}O^{2-}_{2-\delta}\square_{\delta}\left[(x-2y)e^{-}_{C.B.}\right]$), we have considered:

i) from Hall measurements, $x\text{-}2y \approx 0.004$.

ii) from EPMA measurements and XPS analysis, $x \approx 0.053$

iii) from EPMA measurements, $y+\delta \approx 0.055$

So, we get $y \approx 0.024$ and therefore we can deduce the molar ratio of neutral oxygen vacancies; $\delta \approx 0.031$. Hence, the formula can be expressed as:

$$Sn^{4+}_{0.892} Sb^{5+}_{0.053} Zn^{2+}_{0.055} O^{2-}_{1.969} \square_{0.031} \left[0.004\, e^{-}_{C.B.}\right] \quad \text{(f)}$$

This means that part of Zn^{2+} goes to compensate the carrier concentration produced by doping with Sb^{5+}. The other remaining part of Zn^{2+} is responsible of producing neutral oxygen vacancy necessary for densification process. Consequently the enhancement of the conductivity for AZTO ceramic is mainly due to the enhancement of the carrier mobility.

1-5. Conclusions

According to the above results and discussion, we can establish the following conclusions.

1-5-a. ATO (SnO_2:Sb)

(i) Whatever the nominal Sb content in the starting mixture, the final antimony content, for ATO ceramic sintered at 1300 °C, always reaches only ~ 0.012 at. per formula unit. This implies that the Sb solubility within SnO_2 lattice is limited to ~1% in agreement with literature [22]. Hence, to prepare ATO ceramic without Sb departure, the Sb concentration in the starting mixture should not exceed 0.012 mole per formula unit.

(ii) Both Sb^{5+} and Sb^{3+} exist in ATO ceramic. Part of Sb introduced in the crystal lattice plays a role in the conduction mechanism, according to the formula $Sn^{4+}_{1-x-y} Sb^{5+}_{x} Sb^{3+}_{y} O^{2-}_{2} \left[(x-y) e^{-}_{C.B.}\right]$; Sb^{5+} is responsible for electron generation and hence induces the resistivity decreasing.

(iii) Doping SnO_2 with Sb slightly decreases the ceramic density compared to undoped SnO_2. As Sb content in the starting mixture increases, the porosity is slightly enhanced.

(iv) The lowest resistivity is observed for the ceramic having the following composition $Sn^{4+}_{0.988} Sb^{5+}_{0.008} Sb^{3+}_{0.004} O^{2-}_{2} \left[0.004\, e^{-}_{C.B.}\right]$.

The starting mixture leading to the final ceramic composition mentioned above is the following:

$[(SnO_2)_{0.988}+(Sb_2O_3)_{0.006}]$.

We will use this mixture for target preparation needed for thin film deposition. Indeed, the corresponding ceramics have the lowest resistivity with a soundly good density as well. Finally they undergo the lowest weight loss (corresponding to Sb departure) during sintering.

1-5-b. AZTO (SnO_2:Sb:Zn)

(i) AZTO ceramic was found to have higher solubility limit of Sb than ATO. This was attributed to the isovalent substitution of three Sn^{4+} by two Sb^{5+} and one Zn^{2+}.

(ii) All Sb exists in the AZTO ceramic as Sb^{5+}. The electrons produced by Sb^{5+} doping are compensated by Zn^{2+} leading to (x-$2y$) free electrons according to the formula $Sn_{1-x-y-\delta}^{4+} Sb_x^{5+} Zn_{y+\delta}^{2+} O_{2-\delta}^{2-} \square_\delta \left[(x-2y)e_{C.B.}^-\right]$.

(iii) Doping with Zn^{2+} strongly enhances the ceramic density. The presence of neutral oxygen vacancy ($\square_\delta$) due to Sn^{4+} substitution by Zn^{2+} promotes mass transport at the grain boundary and thereby enhances the density.

(iv) Co-doping with Sb^{5+} and Zn^{2+} highly decreases the ceramic resistivity. This was attributed to mobility enhancement due to grain percolation. The lowest resistivity and density were observed for AZTO ceramic having the final composition of $Sn_{0.892}^{4+} Sb_{0.053}^{5+} Zn_{0.055}^{2+} O_{1.969}^{2-} \square_{0.031} \left[0.004 e_{C.B.}^-\right]$. The starting mixture for this composition is $[(SnO_2)_{0.94} + (Sb_2O_3)_{0.03}]_{0.94} + (ZnO)_{0.06}$.

We will use this mixture for target preparation needed for thin film deposition

2. Thin films

In this work, the sputtering technique was used to deposit our ATO and AZTO thin films, from the corresponding previously optimized ceramic starting mixtures. Indeed, sputtering is one of the most versatile techniques used for the deposition of transparent conductors when device-quality films are required. Compared with other deposition techniques, the sputtering process produces films with high purity, provides films with greater adhesion strength and homogeneity, and permits better control of film thickness. Fig. 18 shows the RF magnetron sputtering machine and the sputtering chamber used to deposit our films (in collaboration with J. P. MANAUD, Centre de Ressources Couches Minces de l'ICMCB).

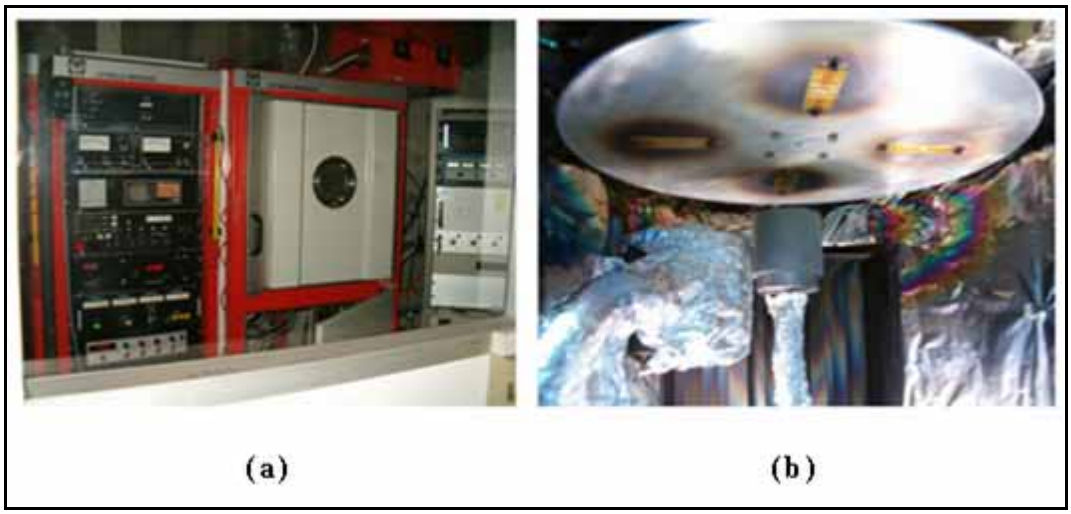

Fig. 18: Photographs of (a) the Leybold L560 rf magnetron sputtering machine and (b) sputtering chamber showing the substrate holders and magnetron sputtering head.

2-1. Preparation of target

ATO and AZTO ceramic targets having a diameter of 50 mm have been prepared. They have respectively the previously optimized chemical final compositions $Sn^{4+}_{0.988}Sb^{5+}_{0.008}Sb^{3+}_{0.004}O^{2-}_{2}\left[0.004\,e^{-}_{C.B.}\right]$ and $Sn^{4+}_{0.892}Sb^{5+}_{0.053}Zn^{2+}_{0.055}O^{2-}_{1.969}\,\square_{0.031}\left[0.004\,e^{-}_{C.B.}\right]$. Appropriate amounts of the selected oxides were first ball milled for 3 h in agate bowl containing agate balls and ethanol. Then, after evaporating the ethanol, the targets were prepared by cold pressing of 50 g powder at 37 tons (1.88 tons/cm^2) followed by sintering at 1300 °C under air for 12h.

2-2. Sputtering parameters optimization

ATO and AZTO thin films were prepared by RF magnetron sputtering in a turbo-pumped sputtering chamber (Leybold L560) using the optimized targets [31]. Prior to each deposition, vacuum was applied into the chamber until the pressure was about 5-9×10^{-5} Pa. All the thin films were deposited at room temperature with no intentional heating of the substrate. The nominal RF power density was varied from 1 W/cm^2 to 3 W/cm^2. Before deposition, a pre-sputtering has been achieved systematically for 20 min in order to clean the target surface. The films were deposited at a total gas pressure varying from 0.4 Pa to 1 Pa under a mixture of argon (99.999 %) and oxygen (99.99 %); the oxygen partial pressure varying between 0-4 %. The thin films were deposited on glass substrates and during various deposition times.

Optimization of sputtering conditions is necessary in order to have films with high deposition rate and good opto-electronic properties. The influence of different sputtering parameters (power density (P), oxygen partial pressure (p_{O_2}) and total pressure (p_{tot}) on ATO thin films deposition rate, optical and electrical properties, has been studied as illustrated on Fig. 19 [31]. In order to have the highest sputtering rate and to have a high energy sputtered particles (that could induce a better crystallization), the target to substrate distance (d_{t-s}) was fixed at 5 cm which is the allowed minimum distance in this sputtering chamber. Note that main optimizations have been done for ATO thin films.

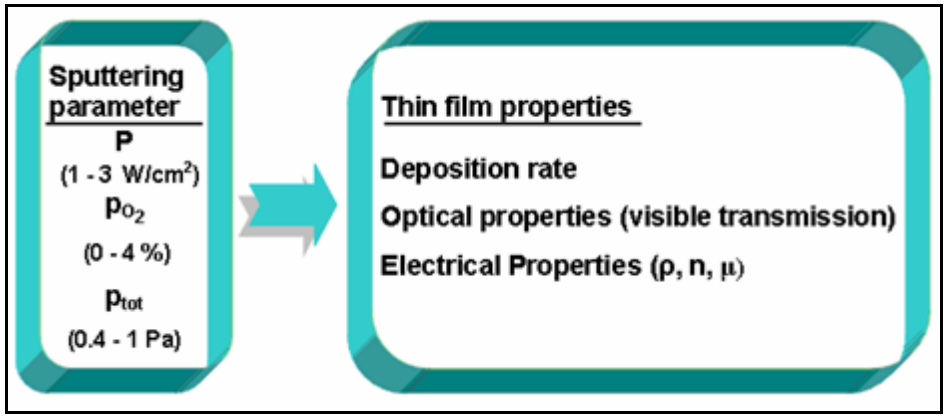

Fig. 19: Schematic diagram showing the influence of some sputtering parameters on different thin film properties that need to be optimized.

2-2-a. Influence of the sputtering parameters on the deposition rate

The deposition rate was determined by depositing a film for a certain period of time and then measuring the film thickness using a TENCOR 100 profilometer. The film thickness (t) was also calculated using the thin films interference transmission spectra in the visible according to equation (18), chapter I ($t = \frac{\lambda_1 \lambda_2}{2[n(\lambda_1)\lambda_2 - n(\lambda_2)\lambda_1]}$), where λ_1 and λ_2 are the wavelengths of two successive maxima or minima and *n* is the refractive index of the TCO thin film at a given wavelength.

It was found that the deposition rate increases gradually with the applied sputtering power density between 1 and 3 W/cm^2 due to higher plasma density and momentum transfer to the target. When the power density was increased from 1 to 3 W/cm^2 (Fig. 20), the deposition rate was almost multiplied by 4. We didn't exceed 3 W/cm^2 because some small cracks were appearing at the target surface with higher power density.

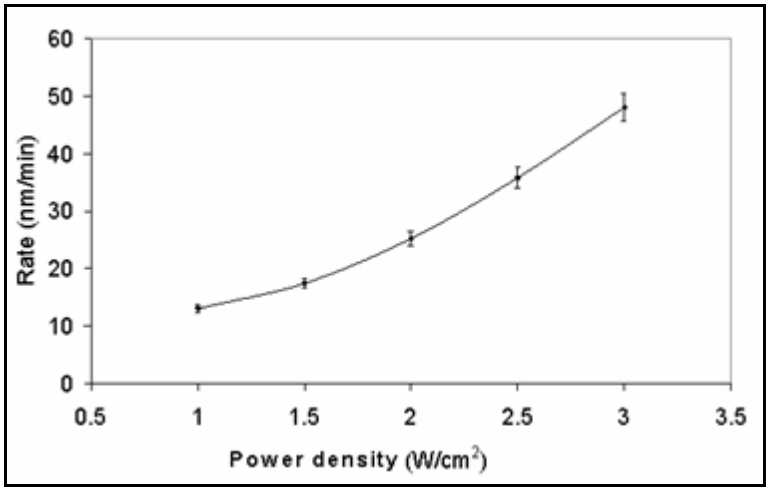

Fig. 20: Influence of the sputtering power density on deposition rate of ATO thin films (p_{O_2} = 2 %, p_{tot} = 1 Pa).

An increase in the deposition rate is also observed when the total pressure increases from 0.4 Pa to 1 Pa (Fig. 21). In fact, two opposite phenomena have to be considered when the total pressure is increased:

i) first, the number of argon ions that reach the target is higher. Consequently, the number of ejected particles per time unit is more important.

ii) second, the mean free path of sputtered particles becomes smaller (it is inversely proportional to the total pressure). So, the probability for these particles to sustain collisions will be more important, this induces a decrease in the number of particles that reach the substrate. In our conditions, the first phenomenon seems to be preponderant.

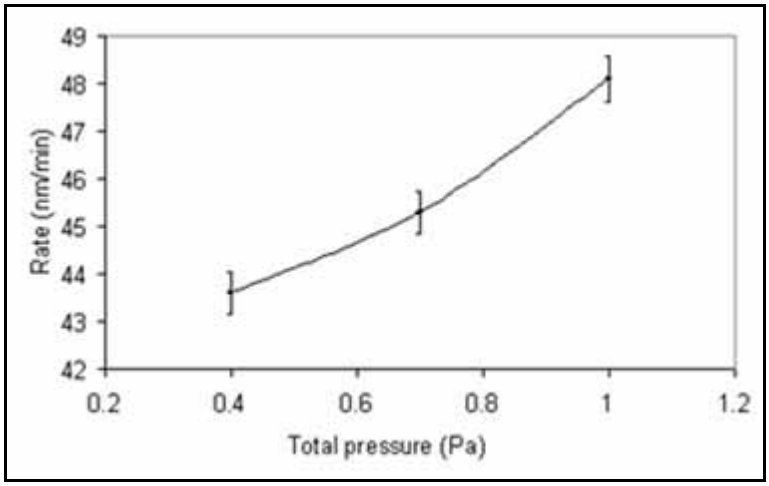

Fig. 21: Influence of the total pressure on the deposition rate of ATO thin films (P = 3 W/cm^2, p_{O_2} = 2 %.)

The presence of even small amounts of oxygen in the plasma has an effect on the deposition rate (Fig. 22). Indeed, the deposition rate decreases slowly with the initial addition of oxygen to the discharge gas.

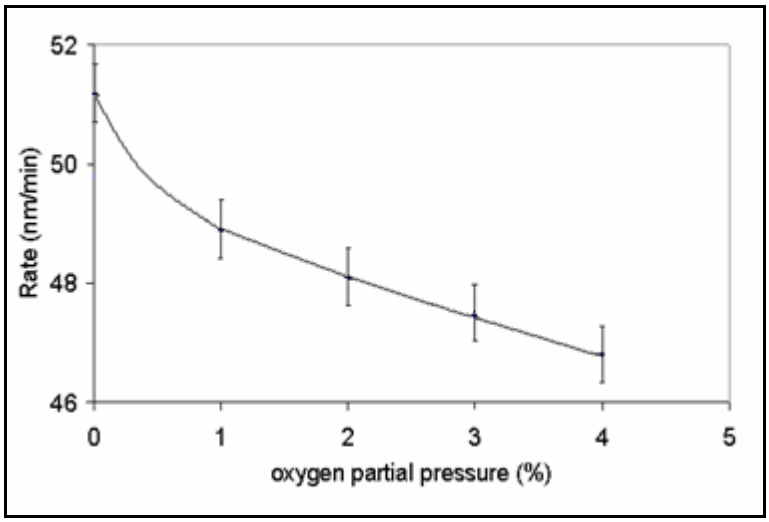

Fig. 22: Influence of the oxygen partial pressure on the deposition rate of ATO thin films (P = 3 W/cm^2, p_{tot} = 1 Pa).

This phenomenon can be related to the nature of the species present in the plasma (molecular ions present in a mixed plasma that have a lower mean free path inducing a lower probability for particles to reach the substrate) or to the composition of the target surface that varies according to the nature of plasma and can influence the deposition rate.

2-2-b. Influence of the sputtering parameters on the optical properties

The transmission spectra of the doped tin oxide films in the UV-visible-NIR region have been recorded using a Carry 5000 spectrometer. The IR spectra were collected using a Nicolet 870 Nexus Fourier Transform infrared (FT-IR) spectrometer.

Visible transparency of the ATO thin films (Fig. 23), deposited on glass substrate at different power densities, was found to be almost the same. The transparency of all samples reached around 90%. The same result was also observed when the total pressure in the sputtering was changed from 1 to 4 Pa.

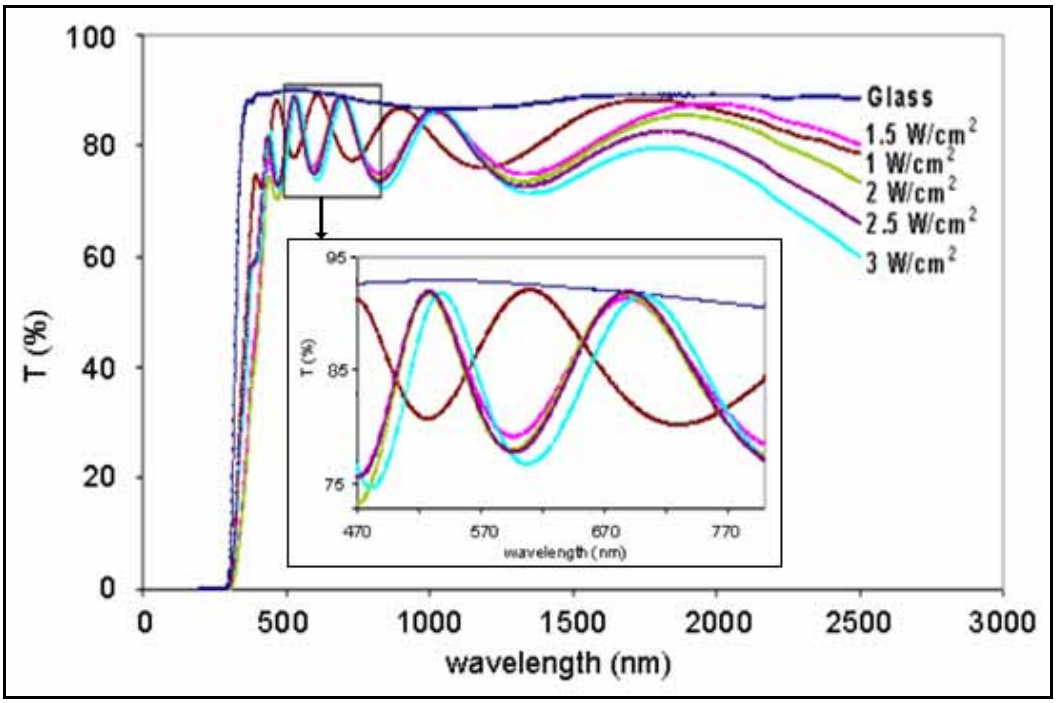

Fig. 23: Transparency spectrum for ATO thin films deposited at different power densities. (p_{O_2} = 4 %, p_{tot} = 1 Pa.). Inset shows the expanded visible region showing the transparency.

Finally, we have studied the influence of the oxygen partial pressure. The latter has a strong influence on the transmission in the visible part. For p_{O_2} = 1 %, the best

transmission reaches 80 % whereas it goes to 90 % for an oxygen partial pressure of 4 % (Fig. 24). Indeed, at low oxygen partial pressure, the films have brown color and are nearly colorless for p_{O_2} = 4 % (with only a slight difference between 2 and 4 %).

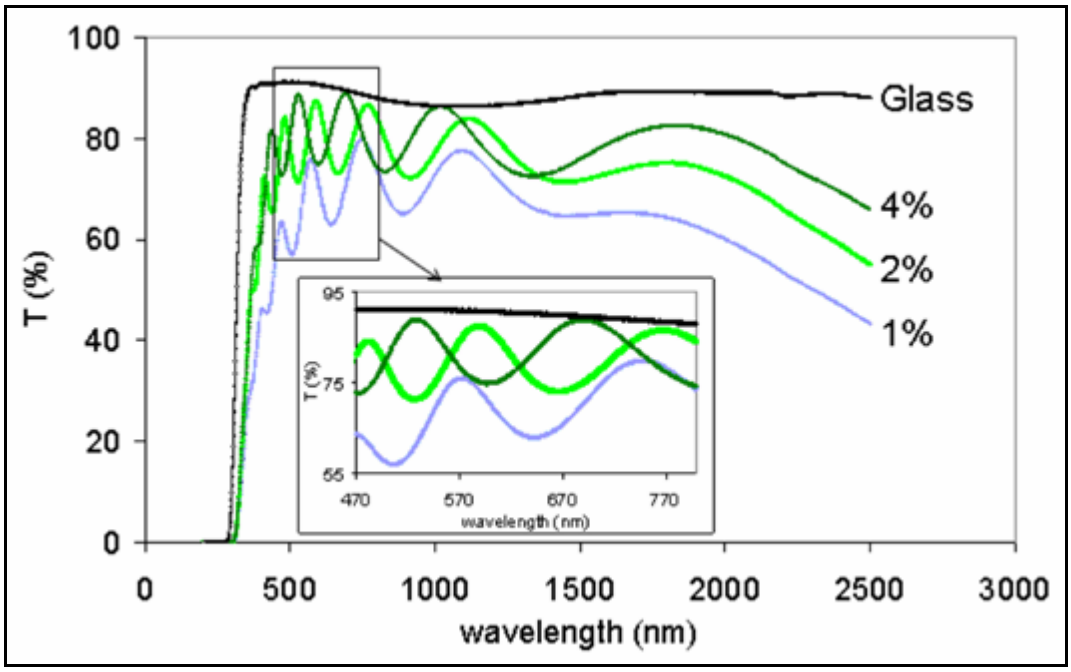

Fig. 24: Optical transmission for different ATO thin films prepared under various oxygen partial pressures from 1 to 4 % as a function of wavelength (P = 3 W/cm^2, p_{tot} = 1 Pa). Inset shows the expanded visible region showing the transparency.

2-2-c. Influence of the sputtering parameters on the electrical properties

Resistivity measurements were carried out as a function of the temperature, from 4.2 K to room temperature using a standard four probe configuration set-up with direct current. The resistivity was found to gradually decrease when the power density was increased up to 3 W/cm^2 (Fig. 25). The decrease of resistivity was attributed to a better crystallinity as shown in the XRD pattern (Fig. 26). Indeed, if the power density increases, the energy of particles arriving on the substrate is higher allowing a better crystallization of the material. The intensity of all the diffraction peaks (Fig. 26) is greatly increased and the FWHM is reduced when the power density increased from 1 to 3 W/cm^2. If we consider the peaks (110) and (211), by using the Scherrer law, we have deduced the crystallite sizes. The latter respectively increases from 7 to 17 nm for (110), and from 10 to 22 nm for (211)

when the power density rises from 1 to 3 W/cm^2. In addition, the resistivity also gradually decreases when the total pressure is increased up to 1 Pa (Fig. 27).

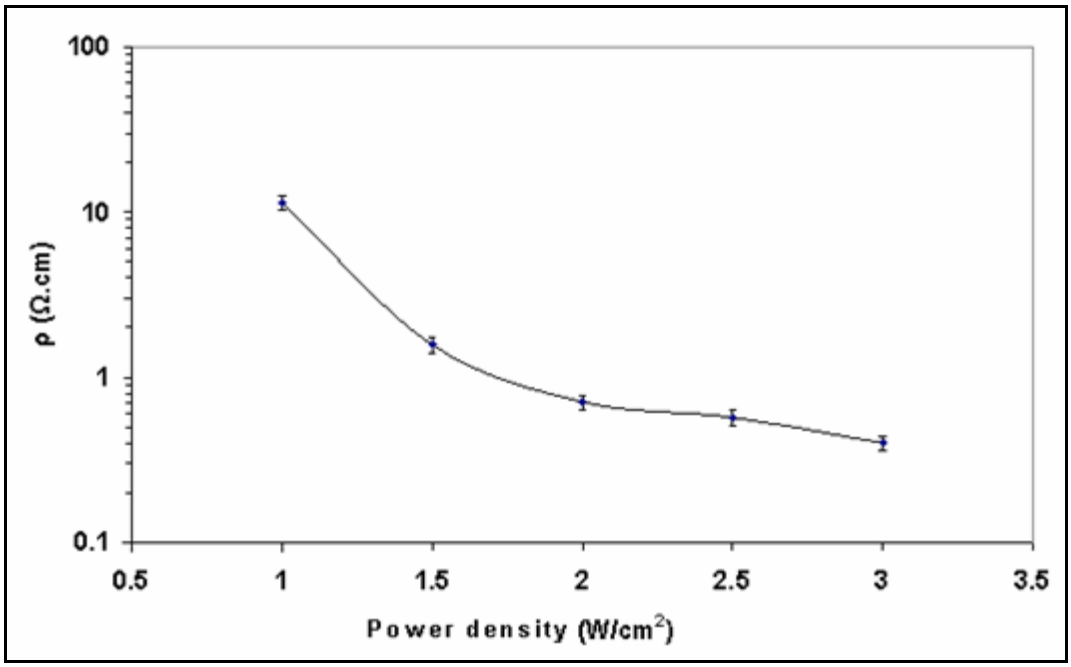

Fig. 25: Evolution of resistivity with power density (p_{O_2} = 4 %, P_{tot} = 1 Pa).

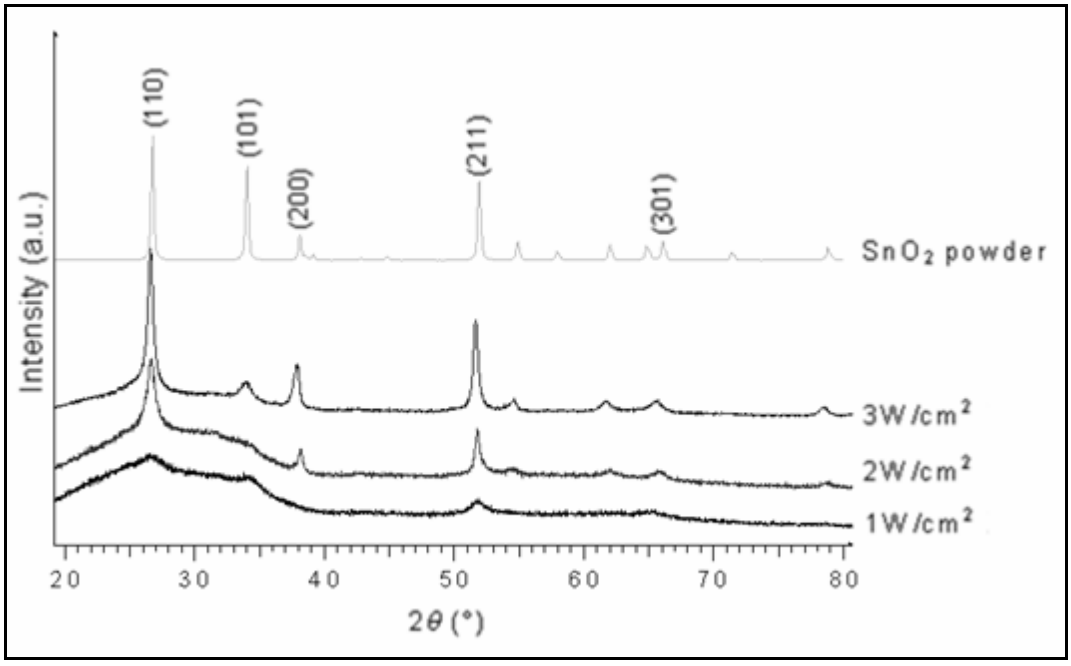

Fig. 26: X-ray diffraction patterns of ATO thin films deposited at different power densities. The pattern of SnO_2 powder is given for comparison.

Finally, we have followed the evolution of the resistivity as a function of the oxygen partial pressure for ATO thin films (Fig. 28). The lowest value of resistivity is obtained for an oxygen partial pressure equal to 2 %.

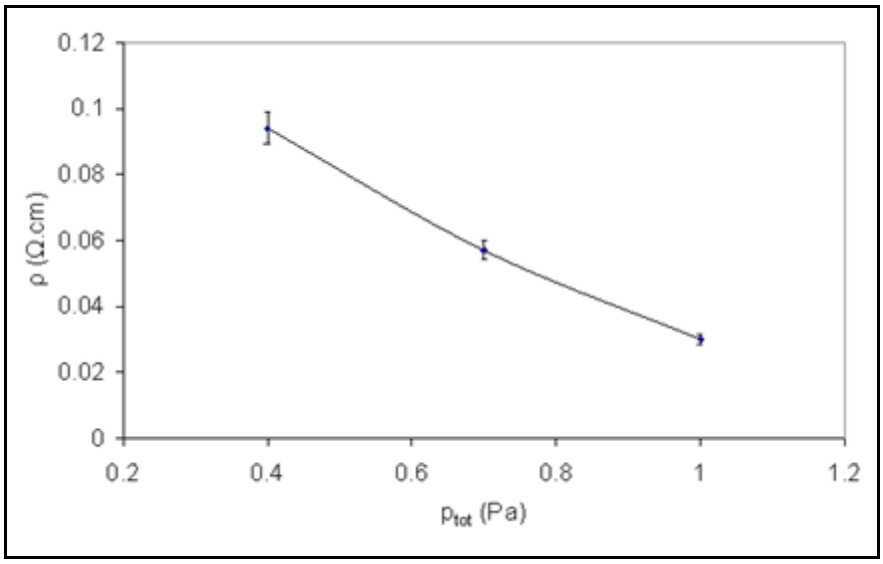

Fig. 27: Evolution of resistivity with total pressure (P = 3 W/cm^2, p_{O_2} = 2 %).

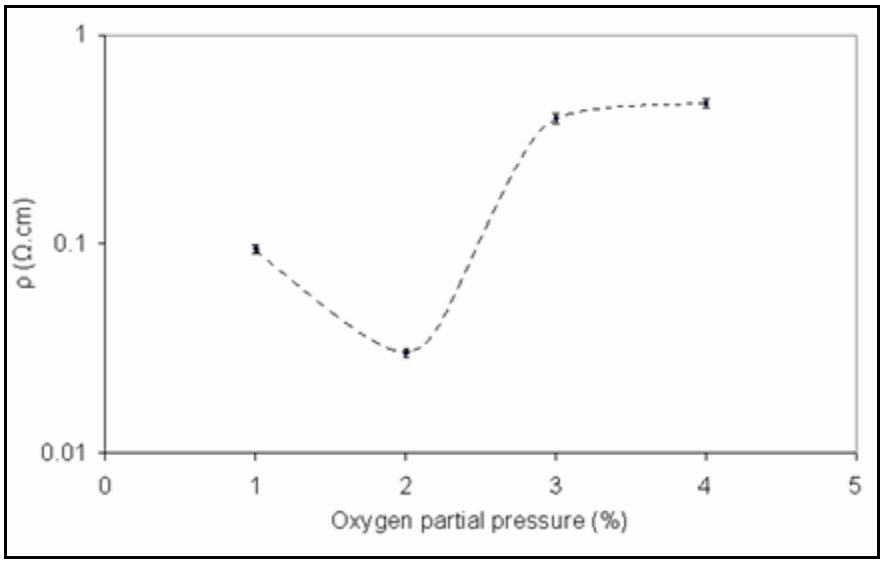

Fig. 28: Evolution of the resistivity as a function of the oxygen partial pressure for ATO thin films (P = 3 W/cm^2, p_{tot} = 1 Pa).

Taking into account all the results concerning the influence of the sputtering parameters on the thin films, we can conclude that:

i) The highest deposition rate, the lowest resistivity and the highest transparency were observed for thin film deposited at sputtering power density (P) of 3 W/cm^2, with a total pressure (p_{tot}) of 1 Pa.

ii) Changing the oxygen partial pressures (p_{O2}) in the range 1-4 % showed no significant effect on deposition rate (~ 2 nm/min). The highest transparency (~ 90 %) was observed for films deposited at p_{O_2} = 2 % or 4 %, with only a very

slight difference (~ 2 % lower for p_{O_2} = 2 %). Finally, the lowest resistivity was obtained for films deposited at p_{O_2} = 2 % (~ 1 order of magnitude lower than others).

As it is clearly observed, the oxygen partial pressure is the most important sputtering parameter because it has a great effect on both film transparency and resistivity.

Similar evolutions have been observed for AZTO thin films. Nevertheless, whatever the sputtering conditions the deposition rate is always higher, for AZTO thin films compared to ATO thin films (Fig. 29), from about 15-25 % (depending on the sputtering conditions). This is due to the higher density of the corresponding AZTO target: 6.42 g/cm^3 instead of 3.79 g/cm^3 for ATO target. This result is in full agreement with literature indicating that target density has a drastic effect on the deposition rate [32].

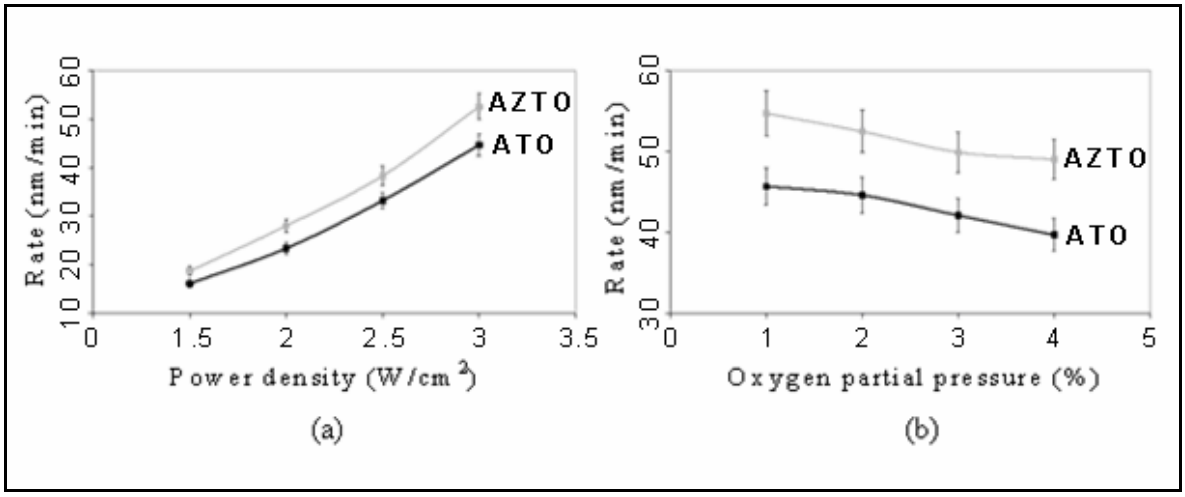

Fig.29: Comparison between deposition rates of ATO and AZTO thin films deposited at (a) different sputtering power density, with p_{O_2} = 2 %, and p_{tot} = 1 Pa and (b) different oxygen partial pressure, with P = 3 W/cm^2 and p_{tot} = 1 Pa.

In summary, the optimized sputtering conditions for both ATO and AZTO thin films leading to a high deposition rate, a high transparency and a low resistivity are the following [31]:

P = 3 W/cm^2, p_{tot} = 1 Pa, p_{O_2} = 2% and d_{t-s} = 5 cm.

2-3. ATO thin films

After the optimization of the sputtering conditions, we have thoroughly studied the composition, the structure, the roughness, the morphology as well as the optical and the electrical properties of our thin films. In addition, we have followed the influence of the post deposition (PD)-annealing treatment (done at 250 °C or 500 °C under vacuum at ~ 4×10^{-4} Pa) and the film thickness on their opto-electronic properties.

2-3-a. Chemical composition and oxidation states

Thin film composition was determined by EPMA. The composition of the ATO thin films deposited under optimized sputtering conditions (see end of part II. 2) as well as the composition of the ceramic target used for deposition are indicated in Table 7. There is a rather good accordance between the composition of both forms (Table 7). Note that thin film compositions for as-deposited and PD-annealed films (either at 250 °C or 500 °C) are equivalent [31]. AES analysis also shows that the chemical composition is quite homogeneous over the whole thin film thickness (Fig. 30).

Ceramic and thin film identification	Starting mixture	Ceramic final composition	Thin film composition
(ATO)	$(SnO_2)_{0.98} + (Sb_2O_3)_{0.01}$	$Sn_{0.988}Sb_{0.012}O_2$	$Sn_{0.985}Sb_{0.015}O_2$

Table 7: ATO ceramic and thin film compositions determined by EPMA.

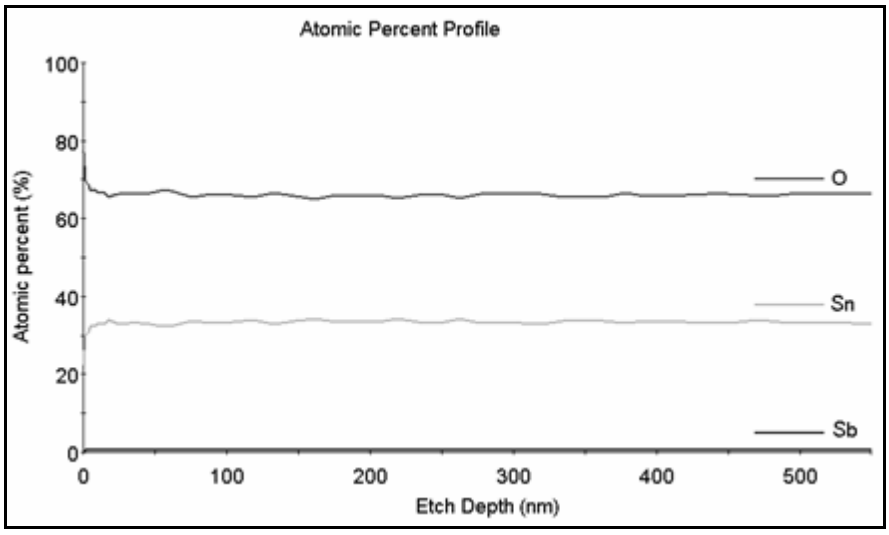

Fig. 30: AES analysis for ATO thin film showing atomic percentage profiles.

Considering the XPS measurements for ATO thin films, no reliable results have been obtained. This is due to the fact that it is a thin film and it contains a very low content of antimony (1.5 % as indicated above in Table 7) which corresponds to the limit of XPS-signal detection. However, one can reasonably assume that Sb^{5+} and Sb^{3+} coexist in ATO films, as it occurred for corresponding ceramics, both Sb^{5+} and Sb^{3+} substituting Sn^{4+} in SnO_2 according to formula (b) ($Sn_{1-x-y}^{4+} Sb_x^{5+} Sb_y^{3+} O_2 \left[(x-y) e_{C.B.}^- \right]$).

As we will see in the electrical part (see part 2-3-d), the proportion of Sb^{5+} deduced from Hall measurements is higher for PD-annealed films showing that part of Sb^{3+} is oxidized during PD-annealing. Since PD-annealing occurs under vacuum, one may assume that the Sb^{3+} species have been oxidized either directly by giving electrons as:

$$Sb^{3+} \rightarrow Sb^{5+} + 2e^- \qquad \text{(g)}$$

or by chemisorbed OH^- species present on the film surface. This is confirmed by infrared transmittance spectra for ATO thin films (Fig. 31). The intensity of the hydroxyl group bands at ~ 2800 and 3700 nm are decreased after PD-annealing. These results are in agreement with those obtained by V. Geraldoa et al. [33] for ATO films deposited via sol-gel. The OH^- species, which are strongly attached to the film surface, usually begins to be desorbed around 250°C [7, 33].

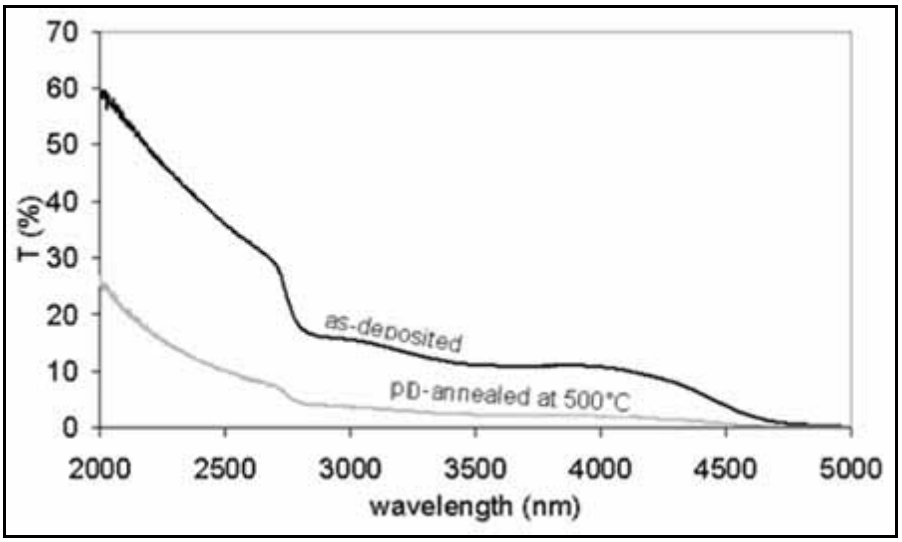

Fig. 31: Infrared transmittance spectra for as-deposited and post deposition (PD)-annealed at 500°C ATO thin films.

2-3-b. Structure and morphology

The thin film surfaces were observed by Field Emission Scanning Electron Microscopy (FESEM) using a JEOL JSM-6700F microscope. The surface morphologies were also examined using a VEECO Dimension 3100 atomic force microscope (AFM) under tapping mode.

The morphology is dense with a smooth surface (Fig. 32) even after PD-annealed treatment. From AFM, it can be seen that by increasing the PD-annealing temperature, the roughness is increased (Fig. 33). Indeed, the Ra, which is the arithmetic average deviation from the mean line within the assessment length, increases from 0.45 nm (as-deposited) to 0.50 nm (PD-annealed at 500°C).

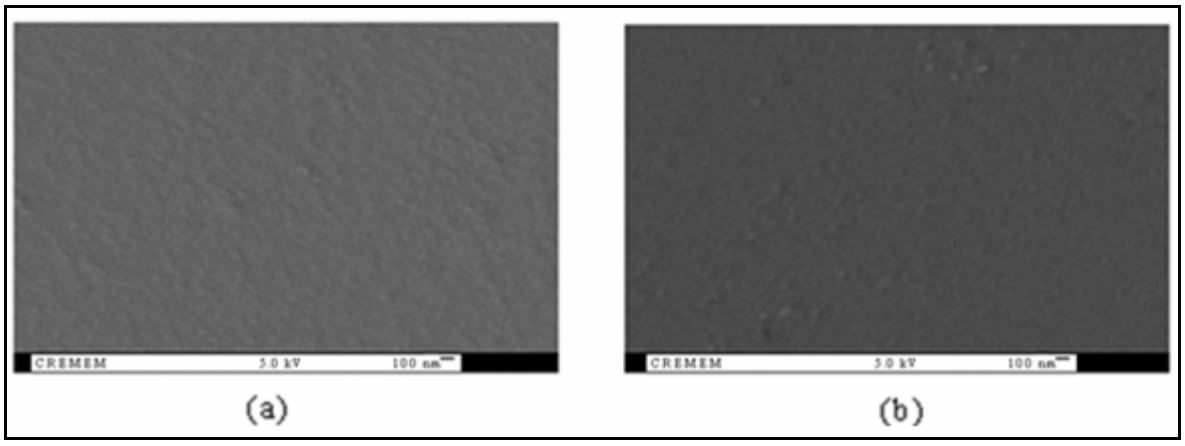

Fig. 32: SEM micrographs of ATO thin films (a) as-deposited and (b) PD -annealed at 500°C under vacuum.

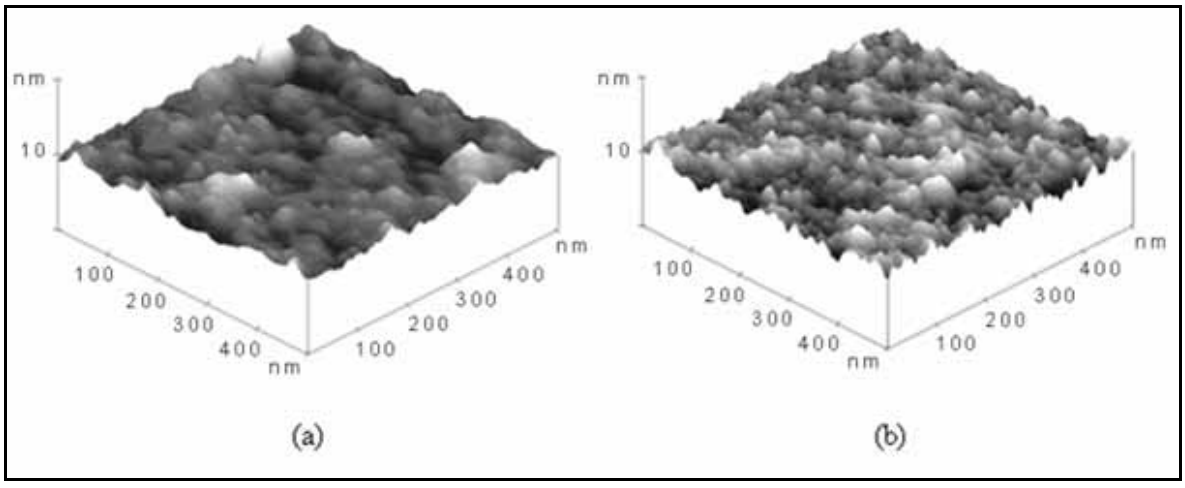

Fig. 33: AFM images obtained in the tapping mode for (a) as-deposited and (b) PD-annealed at 500°C under vacuum ATO thin films.

Fig. 34 shows the x-ray diffraction spectra for ATO thin films deposited on glass substrates. The (110), (101), (211) and (301) diffraction peaks are mainly observed. The films are polycrystalline and retained the rutile structure (JCPDS file 41-1445). As expected, there is no evidence of the presence of extra phases such as antimony oxides (Sb_2O_3 or Sb_2O_5) suggesting the formation of a solid solution. Moreover, the amount of Sb is too low to be detected. However, some authors have proposed that Sn^{4+} ions in the SnO_2 lattice are partly replaced not only by Sb^{5+} ions, but also by Sb^{3+} ions [31, 34]. This is also in agreement with formula (c) ($Sn^{4+}_{0.988}Sb^{5+}_{0.008}Sb^{3+}_{0.004}O^{2-}_{2}\left[0.004e^{-}_{C.B.}\right]$) previously obtained on the ceramic. Moreover, the substitution of Sn^{4+} by Sb^{3+} accounts for the slight shift of the main diffraction peaks towards lower angles compared to pure SnO_2 (Fig. 34), which induces an increase of the cell parameters (Table 8). Indeed, the ionic radius for the 6-coordinated Sn^{4+} (0.69 Å) is smaller than that of Sb^{3+} (0.76 Å) [21]. However, one must also consider that Sb^{3+} behaves as a non-ionized donor center having its $5s^2$ electron stabilized below the conduction band edge. It means that Sb^{3+} should have a somewhat different structural environment than Sb^{5+} species which behave as ionized donor centers.

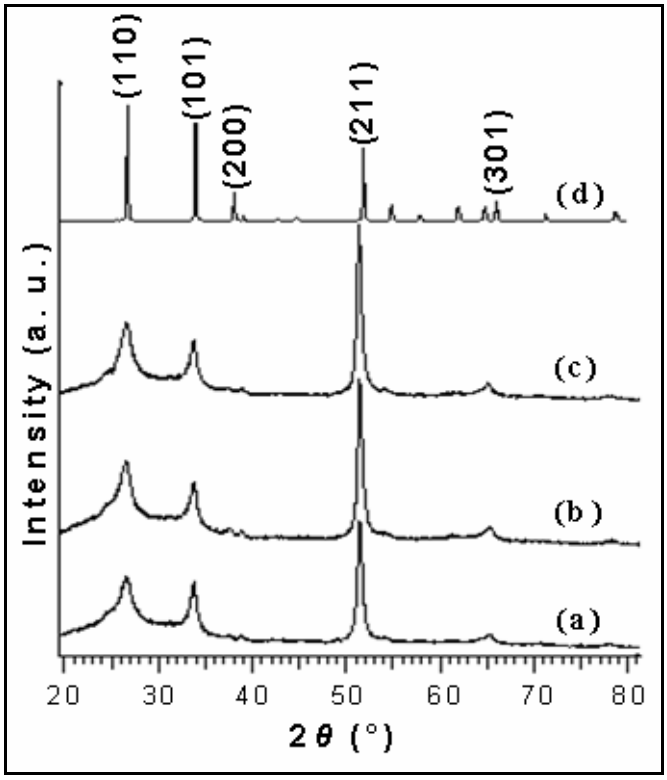

Fig. 34: X-ray diffraction patterns of ATO thin films (a) as-deposited, (b) PD-annealed at 250°C and (c) 500°C under vacuum. (d) The pattern of SnO_2 powder is given for comparison.

Hence, Sb^{3+} was assumed by Messad et al. to segregate at the grain surfaces and also at grain boundaries forming planar defects [22]. Contrary to what we can expect, the enhancement of the cell parameters is emphasized for thin film PD-annealed at 500 °C whereas the Sb^{5+} content is more important (Table 8). So this behavior could be related to the enhancement of the electronic carrier concentration. The intensity of the (211) peak increases with the PD-annealing temperature, showing the existence of a preferential orientation (note that this preferential orientation is strongly influenced by the oxygen partial pressure). The crystallite sizes for the different samples have been determined by the well-known Scherrer equation [23] from diffraction lines 110 (the broadest one) and 211 (the narrowest one).For both orientations, we observe an increase in the crystallite size with the PD-annealing temperature (from room temperature to 500 °C) from 7 to 9 nm for (110) and from 26 to 31 nm for (211).

Sample	a (Å)	c (Å)
SnO_2 powder (JCPDS file 41-1445)	4.738	3.187
ATO film (as-deposited)	4.76	3.21
ATO film (PD-annealed at 500 °C)	4.80	3.23

Table 8: Cell parameters for different ATO thin films. SnO_2 powder cell parameters are given for comparison.

2-3-c. Optical properties

For a 500 nm thickness thin film, we notice almost similar optical results for as-deposited and PD-annealed thin films in the visible part (Fig. 35). In the IR domain, the transparency decreases and the reflectivity increases with PD-annealing temperature (reflectivity reaches 60 % for films PD-annealed at 500°C). Note that the properties of the thin films PD-annealed at 250°C are close to those obtained for the as-deposited one. On Fig. 35, the shift observed for the plasma wavelength (λ_P) towards lower wavelengths when the PD-annealed temperature is increased can be described on the basis of Drude model according to the following equation (equation 31, chapter I) considering the plasma frequency: $\omega_P = (Ne^2 / \varepsilon_0 \varepsilon_\infty m_e^*)^{1/2} = \frac{2\pi c}{\lambda_P}$, where ε_∞ and ε_0 represent the high

frequency and free space dielectric constants, respectively. m_e^* is the effective mass of the charge carriers (in our case the mobile electrons in the conduction band), N is the carrier concentration, and λ_P is the plasma wavelength. Hence, we should expect an increase of the carrier concentration with the PD-annealing temperature. In addition, we can observe on Fig. 35 an increase in the IR reflectivity, R, as the PD-annealing temperature increases; the latter must be correlated to the increase of the plasma frequency (ω_P) according to the equation $R = 1 - \frac{2}{\omega_P \tau \varepsilon_\infty^{1/2}}$ (equation 42, chapter I). A slight increase of the reflectivity is also observed when the thickness is increased from 520 to 960 nm (Fig. 36). Nevertheless, as expected a decrease of the transparency is also noticed in the visible part for thicker film [31].

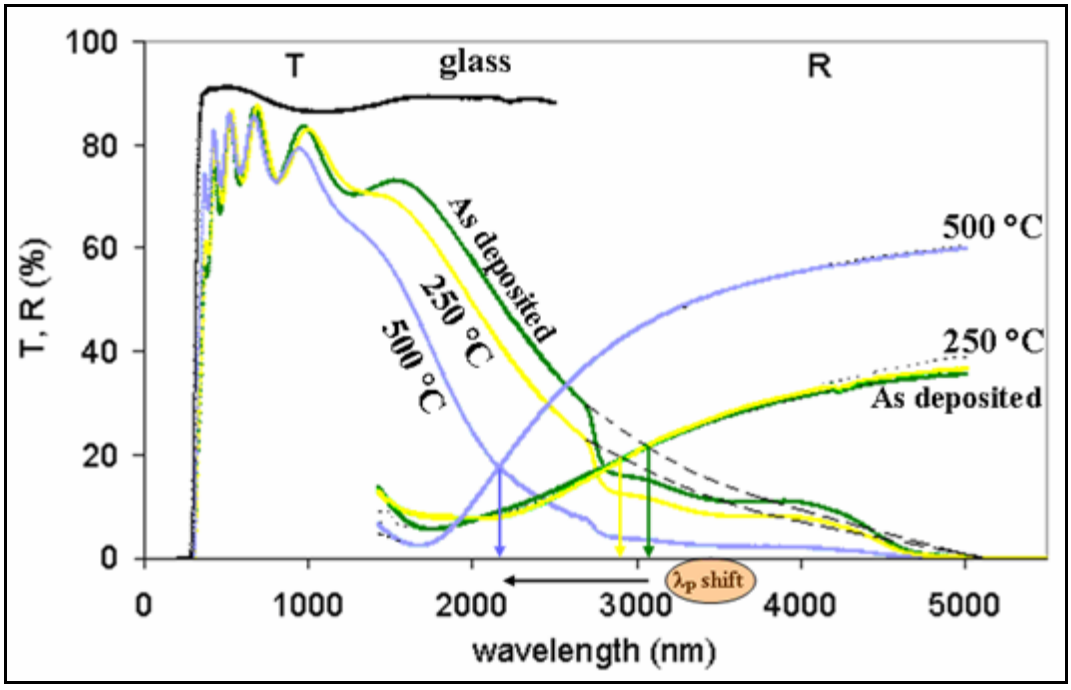

Fig. 35: Comparison of transmittance and reflectance spectra as a function of wavelength for ATO thin films (~520 nm) PD-annealed at 250 °C or 500 °C under vacuum. On reflectivity spectra, full lines represent the experimental data and dotted lines represent simulated data. λ_P is the plasma wavelength.

By using the Drude model, we have fitted the reflectivity curve in order to determine the values of important parameters such as the optical mobility and the carrier concentration. Indeed, the calculations of the optical parameters of degenerate TCOs in the longer-wavelength region (IR reflective region), where plasma edge occurs, are based on Maxwell's equations and Drude's model, previously described in Chapter I (equations 29-

32). From these equations, one can calculate n and k values from the plasma resonance frequency ω_p, and then deduce the carrier concentration (N, in e^- cm^{-3}) and the optical mobility (μ, in $cm^2V^{-1}s^{-1}$) by assuming a carrier effective mass of 0.25 m_e. As expected, regarding the shift of λ_P (Fig. 35) and the reflectivity increase, the carrier concentration was for PD-annealed film at 500 °C as well as mobility (see electrical properties part).

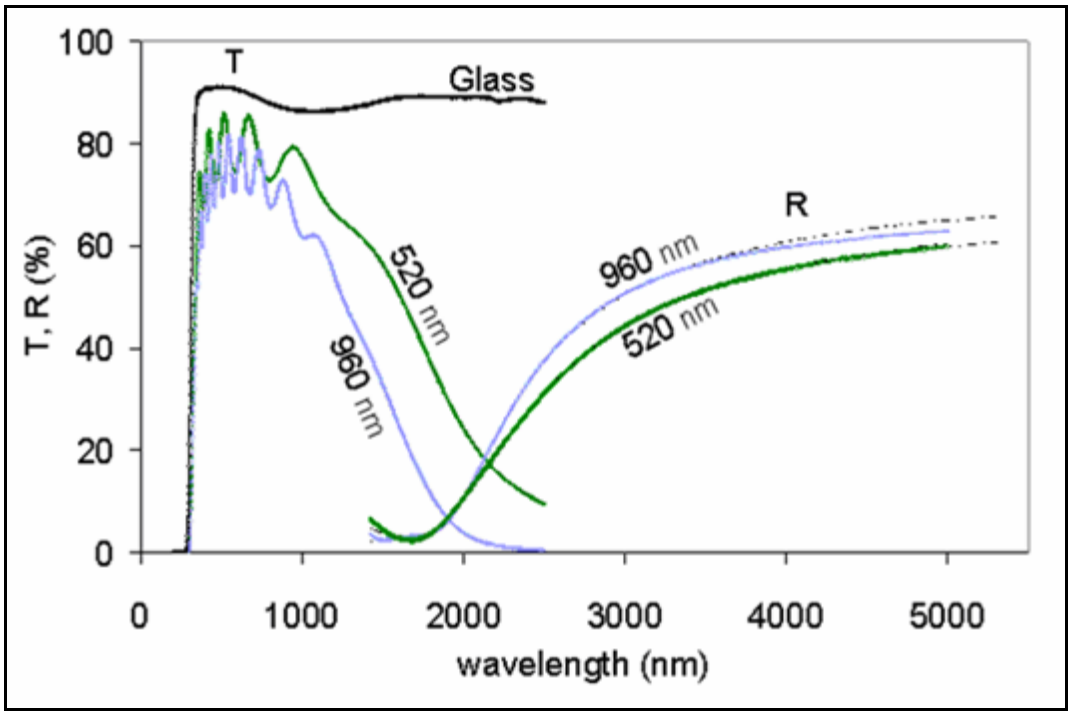

Fig. 36: Transmittance and reflectance spectra for thin films, annealed at 500 °C under vacuum, having a thickness of 520 nm or 960 nm.

We have also determined the direct optical band-gap for different thin films (as-deposited or PD-annealed). The fundamental absorption which corresponds to electron excitation from the valence band to the conduction band can be used to determine the value of the optical band-gap. For all studied samples, the $\alpha(h\nu)$ curves correspond to the case of a crystalline material with direct allowed transitions (direct gap) according to the following equation :

$$\alpha h\nu = A^*(h\nu - E_g)^{1/2} \qquad (2)$$

Where α is the absorption coefficient, A^* is a constant depending on the material and E_g is the direct optical band-gap. Eg is determined by extrapolating the linear portion of the plotted curves (Fig. 37) to zero absorption. The optical gap varies between ~ 3.85 (for as-deposited) and ~ 3.95 eV (for film PD-annealed at 500 °C). This variation can be explained

by the Burstein-Moss effect [35, 36]. It shows that for the transparent thin film E_g increases with the carrier concentration. E_g values reported in the literature vary between 3.7 and 4.5 eV depending on the nature of dopants and preparation methods used [31, 37-40].

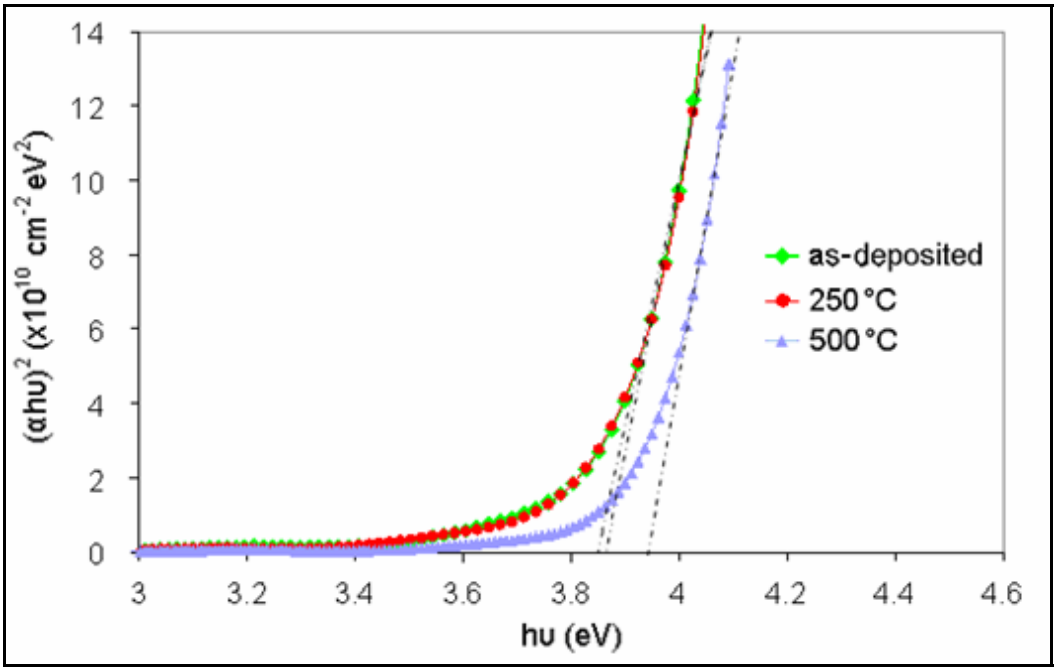

Fig. 37: Determination of the direct gap for ATO thin film as-deposited, PD-annealed at 250°C and 500°C under vacuum.

2-3-d. Electrical properties

The temperature dependence of the carrier concentration, Hall mobility, and the resistivity for as-deposited and PD-annealed at 500 °C under vacuum ATO thin films, has been studied (Fig. 38). Whatever the measurement temperature, we have clearly noticed an increase of the mobility (from 2.5 to 11.1 $cm^2\ v^{-1}\ s^{-1}$) and of the carrier concentration (from 6.76×10^{19} to 2.65×10^{20} e^-cm^{-3}) from as-deposited to PD-annealed at 500 °C (Fig. 38). Usually when the carrier concentration increases, the mobility decreases. In fact the increase of the carrier mobility must be the consequence of the improvement of crystallinity previously observed (Fig. 34). Indeed, by increasing the size of the crystallites upon PD-annealing, we decrease the density of structural defects at the grain surface and, therefore, the density of scattering centers. Consequently, the mobility increases. The simultaneous increase of carrier concentration and mobility leads to a significant decrease in the resistivity from 3.6×10^{-2} Ω.cm (observed for as-deposited film) to 2.1×10^{-3} Ω.cm

(for 500°C PD-annealed sample), corresponding to values of sheet resistances respectively equal to 691 Ω/□ and 38 Ω/□.

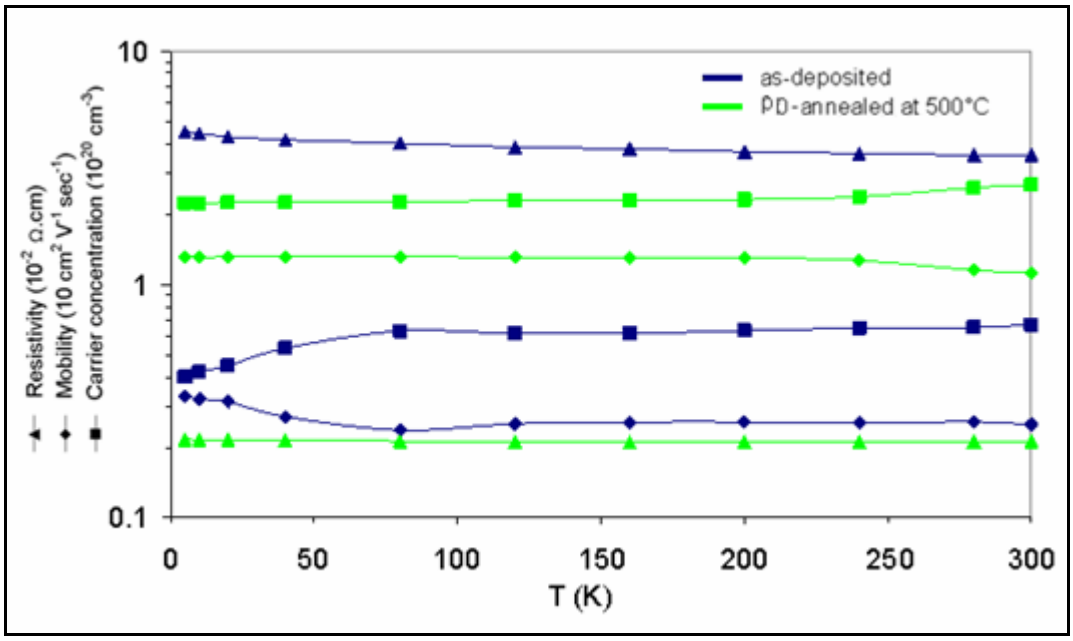

Fig. 38: Evolution of resistivity, Hall mobility and carrier concentration as a function of temperature for as-deposited and PD-annealed at 500°C under vacuum ATO thin films.

The Hall measurements were done using the PPMS (Physical Properties Measurements System) from Quantum Design, by varying the temperature from 4.2 to 300 K and the magnetic field from 0 to 9 Tesla for each specific temperature. The Hall and resistivity measurements were done in collaboration with Rodolph Decourt from service de "Mesures de Transport Electronique" de l'ICMCB. Note that this facility (Hall measurements) being not available at the ICMCB at the beginning of this Ph.D., R. Decourt greatly helped me to set up this experiment.

All the results of mobility, carrier concentration and resistivity, obtained at room temperature using experimental data (Hall and resistivity measurements) and calculated data from optical measurements (by fitting reflectivity spectrum using Drude model and assuming an effective mass of 0.25 m_e), are summarized in Table 9. For all samples we found a negative sign of the Hall coefficient that accounts for the n-type conductivity. There is a good agreement between calculation and experiment except for as-deposited ATO film. Indeed, for this compound the slight decrease of the resistivity when the temperature increases (Fig. 38) indicates that it corresponds to the limit of the Drude model validity.

ATO thin films ($Sn_{0.985}Sb_{0.015}O_2$)	Mobility ($cm^2/V.s$) ± 5%		Carrier conc. ($e^- cm^{-3}$) ± 5%		E_g (eV)	Resistivity (Ω.cm) ± 5%	
	deduced from optical	deduced from Hall	deduced from optical	deduced from Hall		deduced from optical	measured
as-deposited	5.7	2.5	2.2×10^{20}	6.76×10^{19}	3.85	4.9×10^{-3}	3.6×10^{-2}
PD-annealed at 250°C	6.2	5.7	2.1×10^{20}	1.83×10^{20}	3.87	4.7×10^{-3}	6.0×10^{-3}
PD-annealed at 500°C	11.5	11.1	2.7×10^{20}	2.65×10^{20}	3.95	2.0×10^{-3}	2.1×10^{-3}

Table 9: Mobility, carrier concentration, direct optical band-gap (E_g) and resistivity for different ATO thin films. Note that for calculated values deduced from optical measurements, the effective mass (m^*) is considered to be equal to 0.25 m_e.

If we suppose the existence of both Sb^{3+} and Sb^{5+} in thin films as it occurs for ceramic according to formula (b) ($Sn^{4+}_{1-x-y}Sb^{5+}_{x}Sb^{3+}_{y}O_2\left[(x-y)e^-_{C.B.}\right]$), we can calculate the accurate final formula for

1) <u>as-deposited thin film</u>:

i) from Hall measurements, x-y = 0.002.

ii) from final composition determined by EPMA ($Sn_{0.985}Sb_{0.015}O_2$), $x + y = 0.015$

Then the final formula for as-deposited ATO film is:

$$Sn^{4+}_{0.985}Sb^{5+}_{0.0085}Sb^{3+}_{0.0065}O^{2-}_{2}\left[(0.002)e^-_{C.B.}\right] \quad \text{(h)}$$

2) <u>post deposition (PD)-annealed at 500 °C thin film</u>:

i) from Hall measurements, x-y = 0.010.

ii) from final composition determined by EPMA ($Sn_{0.985}Sb_{0.015}O_2$), $x + y = 0.015$

The final formula for PD-annealed at 500 °C ATO film is:

$$Sn^{4+}_{0.985}Sb^{5+}_{0.0125}Sb^{3+}_{0.0025}O^{2-}_{2}\left[(0.010)e^-_{C.B.}\right]. \quad \text{(i)}$$

Consequently, PD-annealing causes an increase of the Sb^{5+} content into the film by oxidizing Sb^{3+}, that results in higher carrier concentration and hence lower resistivity (Fig. 38).

2-4. AZTO thin films

2-4-a. Chemical composition and oxidation states

The AZTO thin films have been deposited under the same optimized sputtering conditions than ATO. Their composition is indicated in Table 10 as well as the composition of the ceramic used as target. There is a quite good accordance between the compositions of ceramic and thin film. Note that thin film compositions for as-deposited and PD-annealed films are equivalent [31]. The chemical composition was found to be homogeneous all over the thin film thickness as shown by AES analyses (Fig. 39).

Ceramic and thin film identification	Starting mixture	Ceramic final composition	Thin film composition
(AZTO)	$[(SnO_2)_{0.94} + (Sb_2O_3)_{0.03}]_{0.94} + (ZnO)_{0.06}$	$Sn_{0.892}Sb_{0.053}Zn_{0.055}O_{2-\delta}$	$Sn_{0.888}Sb_{0.060}Zn_{0.052}O_{2-\delta}$

Table 10: AZTO ceramic and thin film compositions determined by EPMA.

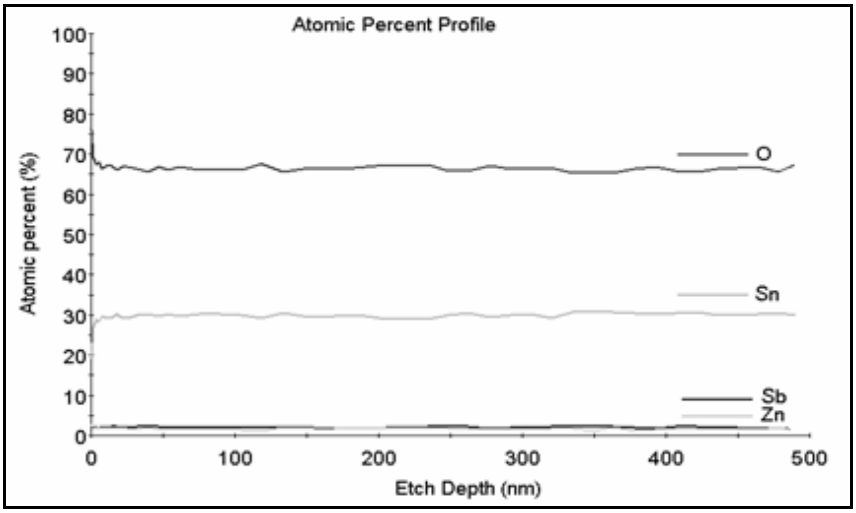

Fig 39: AES analysis for AZTO thin films showing atomic percentage profile.

The investigation of the formal oxidation state for antimony ions (all tin ions being present as Sn^{4+}) was done using XPS measurements. The Sb4d core peak present two components (Fig. 40):

i) the most important, located at lower binding energy corresponds to antimony ions in a formal oxidation state +3.

ii) the other component located at the higher energy side is attributed to antimony ions in a formal oxidation state +5.

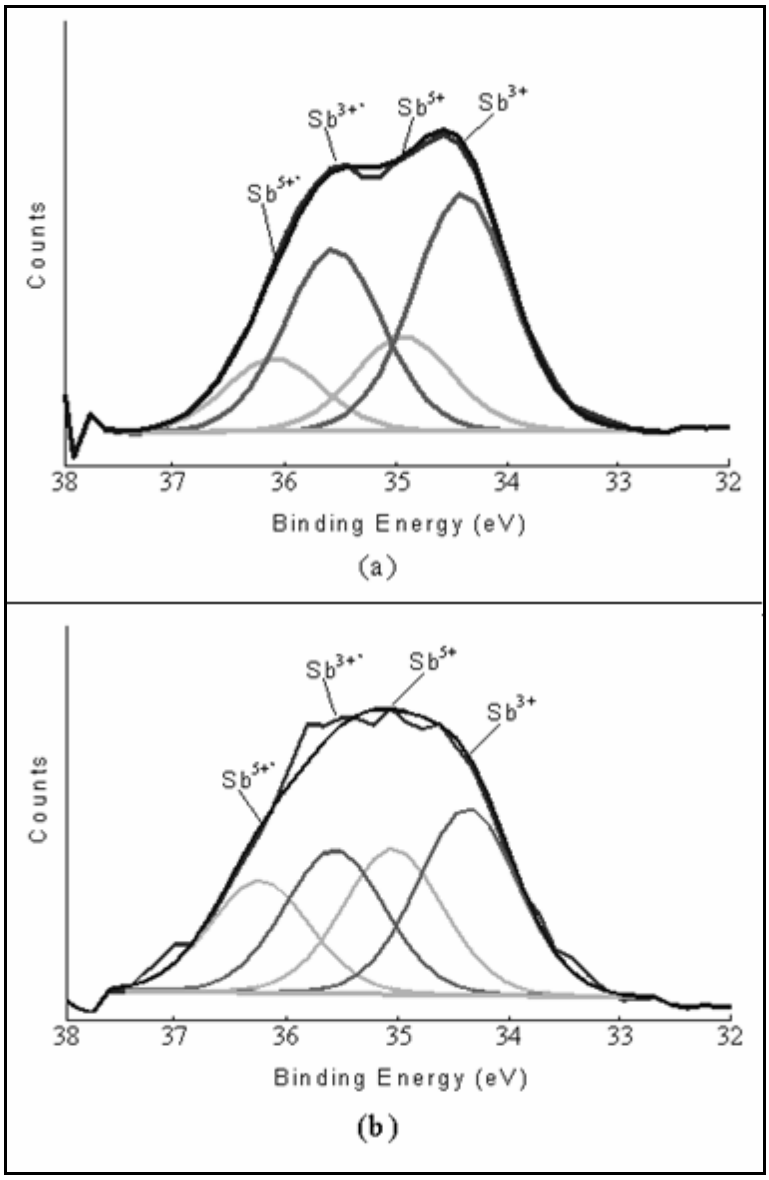

Fig. 40: XPS Sb 4d core peaks for as-deposited (a) and PD-annealed under vacuum at 500°C (b) AZTO thin films.

As we have seen previously, all the antimony ions present in the ceramic target have a 5+ formal oxidation state whereas XPS measurements have evidenced the existence of Sb^{3+} and Sb^{5+} into thin films. This difference is probably due to partial reduction of the AZTO target surface under the argon ions bombardment during sputtering. As the thin films are deposited under a low oxygen partial pressure, the reduced antimony species can not be re-oxidized in the sputtering chamber. Taking into account the above XPS results for AZTO thin film, it is assumed that Sn^{4+} is partially substituted not only by Sb^{5+}, but by the other

species Zn^{2+} and Sb^{3+} as well. The latter would reduce the carrier concentration produced by Sb^{5+} according to:

$$Sn_{1-x-z-y-\delta}^{4+} Sb_x^{5+} Sb_z^{3+} Zn_{y+\delta}^{2+} O_{2-\delta}^{2-} \square_\delta \left[(x - z - 2y) e_{C.B.}^- \right] \quad \text{(j)}$$

PD-annealed films show an enhancement of the Sb^{5+} amount from 29 % to 44 % (see Table 11 and Fig. 40), meaning that a part of Sb^{3+} is oxidized into Sb^{5+}during PD-annealing. Nevertheless, for as-deposited and PD-annealed thin films, XPS always shows higher amounts of Sb^{3+} than Sb^{5+}, So $z > x$. This should induce a negative carrier concentration according to formula (j) that would account for p-type conductivity. However, as we will see later (part 2-4-d) Hall measurements evidence n-type conductivity. Consequently, not all Sb^{3+} substitute Sn^{4+} in the lattice; probably part of it segregates at the grain boundary in an amorphous Sb_2O_3 form. Due to this, we may have difficulties in calculating the AZTO film final formula.

References	**Sb^{5+} $4d_{5/2-3/2}$ (eV)**	**Sb^{4+} $4d_{5/2-3/2}$ (eV)**	**Sb^{3+} $4d_{5/2-3/2}$ (eV)**
Sb_2O_5	35.0-36.2 (2.20) 100%		
Sb_2O_4		34.7-35.9 (1.96) 100 %	
Sb_2O_3			34.5-35.7 (1.57) 100%
Thin films			
as-deposited AZTO	35.0-36.2 (1.10) 29 %		34.4-35.6 (1.10) 71 %
PD-annealed AZTO	34.9-36.1 (1.10) 44 %		34.3-35.5 (1.10) 56 %

Table 11: XPS Sb^{5+}, Sb^{4+} and Sb^{3+} $4d_{5/2-3/2}$ binding energies (eV) as well as the full width at half maximum (in parentheses) for reference compounds and deposited thin films.

2-4-b. Structure and morphology

From AFM, it can be seen that by increasing the PD-annealing temperature, the roughness is increased (Fig. 41). Indeed, R_a (arithmetic average deviation from the mean line within the assessment length) was found to increase from 0.69 nm (as-deposited) to 0.86 nm (PD-annealed at 500°C).

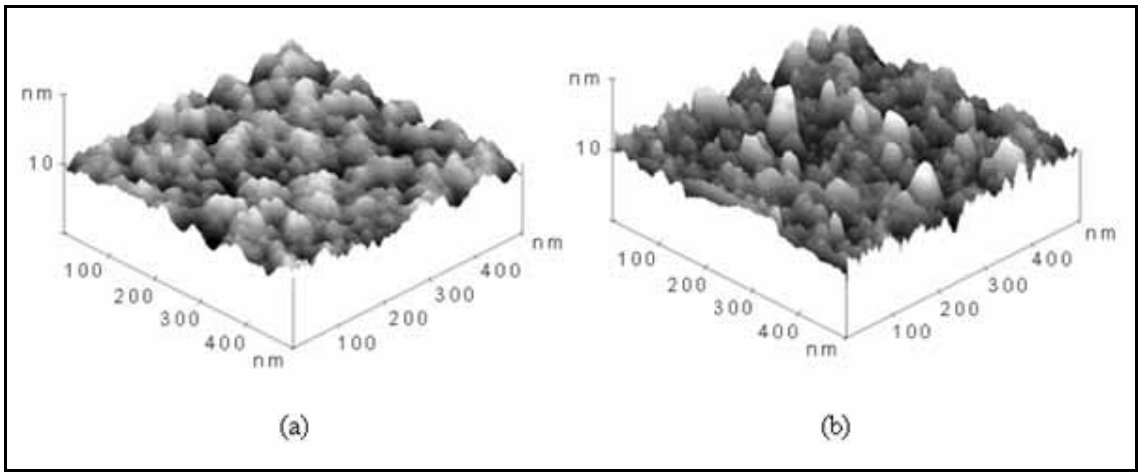

Fig. 41: AFM images obtained in the tapping mode for AZTO thin films as-deposited (a) and PD-annealed at 500°C under vacuum (b).

Fig. 42 shows the x-ray diffraction spectra for AZTO thin films deposited on glass substrates. The (110), (101), (211) and (301) diffraction peaks are mainly observed. The films are polycrystalline and retained the rutile structure. The crystallite size has been determined using Scherrer equation [23] from diffraction line 110. The latter is slightly enhanced by PD-annealing treatment form 7 nm (for as-deposited) to 9 nm (for PD-annealed at 500 °C films). In addition, a slight shift of the peaks towards lower angle

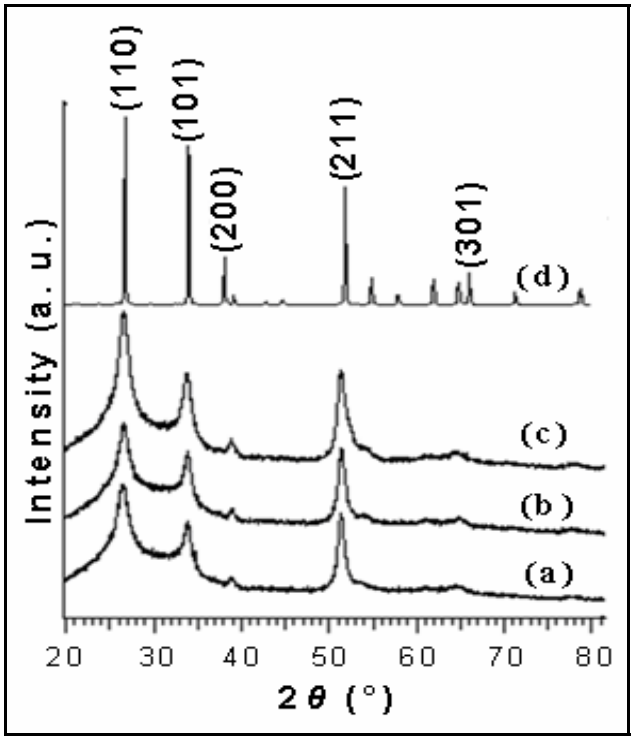

Fig. 42: X-ray diffraction patterns of AZTO thin films (a) as-deposited, (b) PD-annealed at 250°C and (c) 500°C under vacuum. (d) The pattern of SnO_2 powder is given for comparison.

compared to SnO_2 is observed for the as-deposited AZTO thin films. This accompanied an increase in the cell parameters a and c, from 4.738 to 4.76 Å, and from 3.187 to 3.21 Å respectively. As it occurs for ATO thin film, a more pronounced shift towards lower angle is observed upon PD-annealing to 500 °C leading to a and c values equal to 4.78 Å and 3.22 Å respectively. The evolution of the cell parameters tends to prove the existence of Sb^{3+} in substitutional position according to $Sn^{4+}_{1-x-z-y-\delta}Sb^{5+}_{x}Sb^{3+}_{z}Zn^{2+}_{y+\delta}O^{2-}_{2-\delta}\square_{\delta}\left[(x-z-2y)e^{-}\right]$ (formula (j)), the size of Sb^{3+} being larger than for Sn^{4+}. Finally, the AZTO film peaks are broader than those observed for ATO thin films indicating that the structure is more disordered.

2-4-c. Optical properties

The transparency in the visible part is similar to the one obtained for ATO thin films prepared in similar sputtering conditions (inset of Fig. 43).

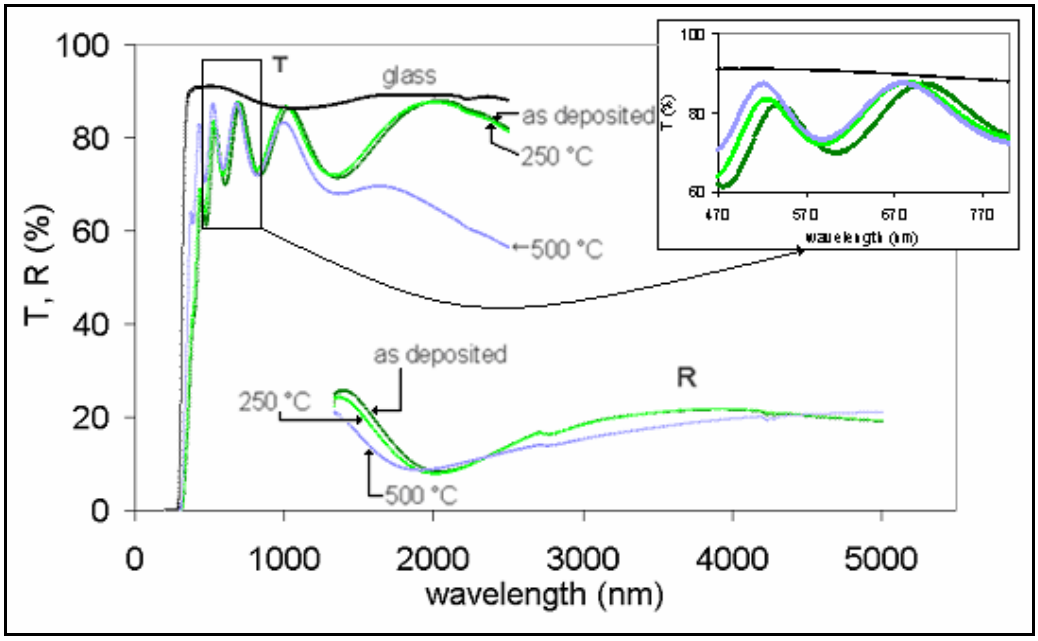

Fig. 43: Transmittance and reflectance spectra for as-deposited and PD-annealed AZTO thin films.

However, a very weak reflectivity is observed whatever the PD-annealing temperature (around 20 %). As these AZTO thin films do not have a metallic behavior (rather a semiconductor behavior), the Drude model was not applicable to fit the reflectivity evolution. The direct band-gap Eg varies from ~3.61 to ~ 3.78 eV (Fig. 44). It is thus lower than that for ATO thin films, indicating that the carrier concentration must be lowered, according to Burstein- Moss effect [35, 36].

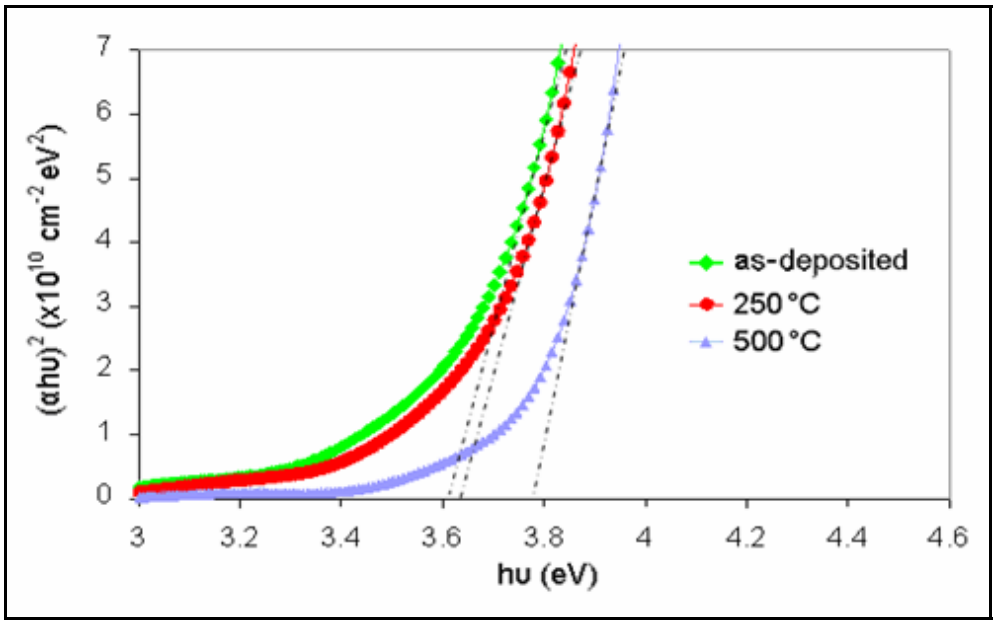

Fig. 44: Determination of the direct gap for AZTO thin film as-deposited, PD-annealed at 250°C and 500°C under vacuum.

2-4-d. Electrical properties

First, the mobility is lower for AZTO than for ATO films (Table 12). This can be explained by the higher disorder in AZTO films that induces more structural defects at the grain surface, which are responsible for a lower mobility. Moreover, as expected the carrier concentration increases while the mobility decreases when the PD-annealing temperature is increased (Table 12 and Fig. 45). This yields a resistivity decrease. Nevertheless, if we compare the performances of AZTO and ATO thin films, the low values of mobility combined with a carrier concentration, one order of magnitude lower, induces higher resistivity for AZTO thin films compared to ATO ones (Fig. 46).

Sample	Mobility ($cm^2/V.s$)		Carrier conc. ($e^- cm^{-3}$)		E_g (eV)	Resistivity (Ω.cm)	
	AZTO	ATO	AZTO	ATO	AZTO	AZTO	ATO
as-deposited	2.3	2.5	1.62×10^{18}	6.76×10^{19}	3.61	1.50	3.6×10^{-2}
PD-annealed at 250°C	1.8	5.7	1.26×10^{19}	1.83×10^{20}	3.64	0.27	6.0×10^{-3}
PD-annealed at 500°C	0.9	11.1	3.68×10^{19}	2.65×10^{20}	3.78	0.17	2.1×10^{-3}

Table 12: Values of mobility, carrier concentration, direct gap (E_g) and resistivity for different AZTO thin films. The carrier concentration was deduced using Hall measurements. The relative values for ATO are reported for comparison.

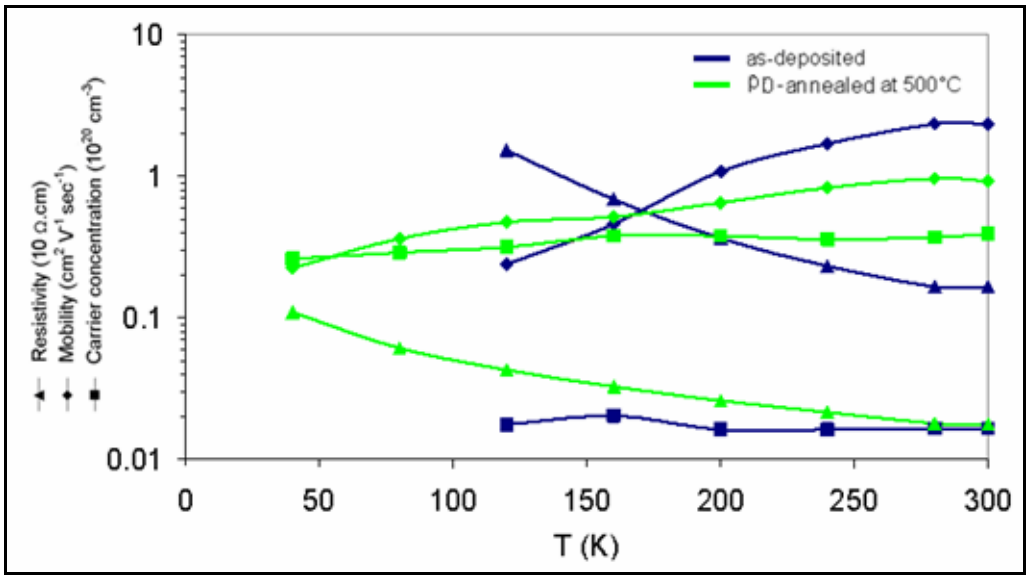

Fig. 45: Evolution of resistivity, Hall mobility and carrier concentration as a function of temperature for as-deposited and PD-annealed (at 500°C under vacuum) AZTO thin films.

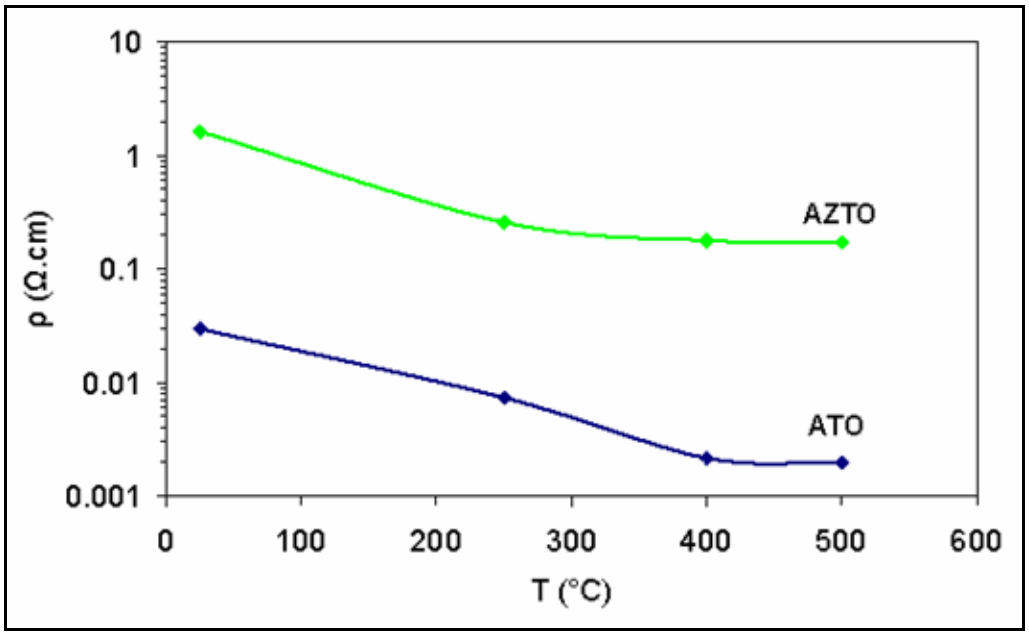

Fig. 46: Plots of resistivity (measured at room temperature) versus PD-annealing temperature for ATO and AZTO thin films.

This lower value of carrier concentration for AZTO is attributed to Zn^{2+} and Sb^{3+} species in cationic substitutional position, which reduce the carrier concentration (formula j: $Sn^{4+}_{1-x-z-y-\delta} Sb^{5+}_{x} Sb^{3+}_{z} Zn^{2+}_{y+\delta} O^{2-}_{2-\delta} \square_{\delta} \left[(x-z-2y)e^{-}\right]$). Taking into account Hall measurements for AZTO thin films, we can deduce *x-z-2y* in formula (j) for:

1) as-deposited thin film: $x-z-2y = 0.00006$.
2) PD-annealed at 500 °C thin film: $x-z-2y = 0.0013$.

Therefore, the PD-annealing provokes oxidation of Sb^{3+} to Sb^{5+}, that results in higher carrier concentration (electrons) and hence lower resistivity (Fig. 45).

2-5. Applications

The prepared ATO and AZTO thin films have been successfully used for the first time as transparent layers, deposited on sapphire substrates, in experimental cells for fluid studies at near critical point in the DECLIC (**D**ispositif pour l'**E**tude de la **C**roissance des **Li**quides **C**ritiques) device. This study was achieved in collaboration with Y. Garrabos and C. Lecoutre-Chabot from the ICMCB-CNRS. ATO was used as transparent heat reflector (transparent in the visible and reflective in the infrared) in high temperature insert (HTI) cell, to study materials having high critical temperature points (water). As for AZTO, it was used as transparent micro-furnace in Alice like insert (ALI) cell, to study the materials having near ambient critical points (like CO_2 and SF_6).

i) Transparent heat reflectors (ATO) to reduce HTI cell temperature gradient

For high temperature fluid studies, a problem of temperature losses through the transparent windows, which are adapted in the HTI cell for fluid observations, is encountered by the researchers. Due to this, there was a need for a transparent heat reflector, which is chemically stable at high temperature, to be deposited onto these observation windows, in order to reduce the temperature losses and hence reduce the temperature gradient inside the HTI cell (Fig. 47).

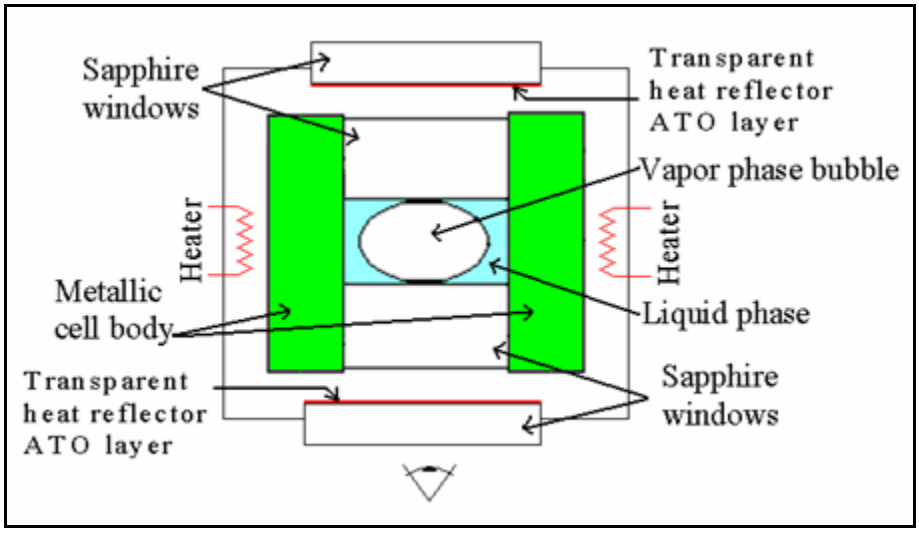

Fig. 47: Scheme of the HTI cell for fluid studies near critical point.

Due to the chemical stability at high temperature of our ATO thin films (1000 nm in thickness) their sheet resistances (~25 Ω/□) were found to be stable even after annealing many times in air at temperatures as high as 400 °C; that is not the case for ITO which is readily oxidized at this temperature. Most interestingly, the ATO film reflectivity was found to have a value of ~ 65% (Fig. 48) at a wavelength of 5000 nm. Due to this, our ATO films, presently tested, would be efficient to reduce the temperature gradient inside the HTI cell while allowing the direct observation of the fluid through the transparent windows.

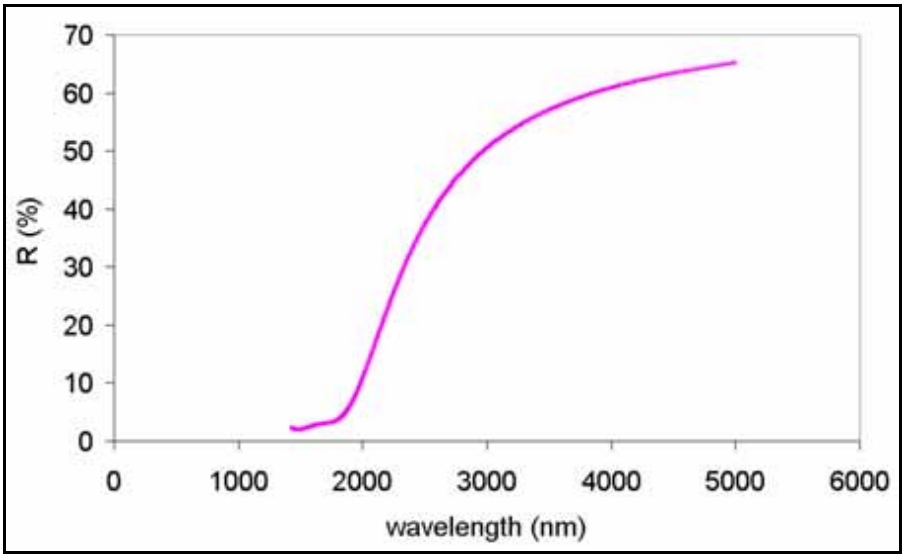

Fig. 48: Reflectivity of ATO film deposited on sapphire and PD-annealed at 500 °C.

ii) Transparent resistive layer (AZTO) for heating the ALI cell.

Boiling is a very efficient way to transfer heat from solid to liquid. Nevertheless, some aspects of the growth of a vapor bubble attached to a solid heater remain misunderstood. The most important one is the 'boiling crisis', a transition from nucleate boiling (where vapor bubbles nucleate on the heater) to film boiling (where the heater is covered by a continuous vapor film). Recently, some boiling experiments have been conducted by the group of Y. Garrabos (ICMCB) under microgravity in the proximity of the critical point. Microgravity (as in MIR space station) which cancels buoyancy forces is a powerful tool for studying the phenomena near the vapor - liquid - solid contact line (Fig. 49). These researchers have used the following optical cell (Fig. 50) under pressure, filled with a pure fluid (SF_6) at the critical density to study the drying of the liquid film and to observe the deformation of the interface gas-liquid due to the recoil force. The dedicated cell to observe the liquid film drying is composed of:

1) a spherical face of a sapphire window to center in zero gravity the vapor bubble in the observation field

2) a resistive film heated by Joule effect based on AZTO thin film deposited on the second sapphire window

3) a system of three thermistors to control the distribution of the temperature near the interface during the heating of the resistive thin film.

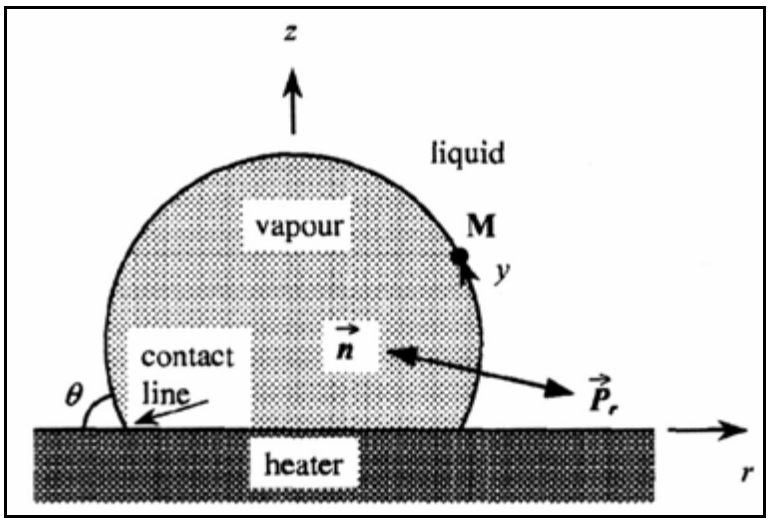

Fig.49: Nucleate boiling: a vapor bubble on the heating surface surrounded by liquid.

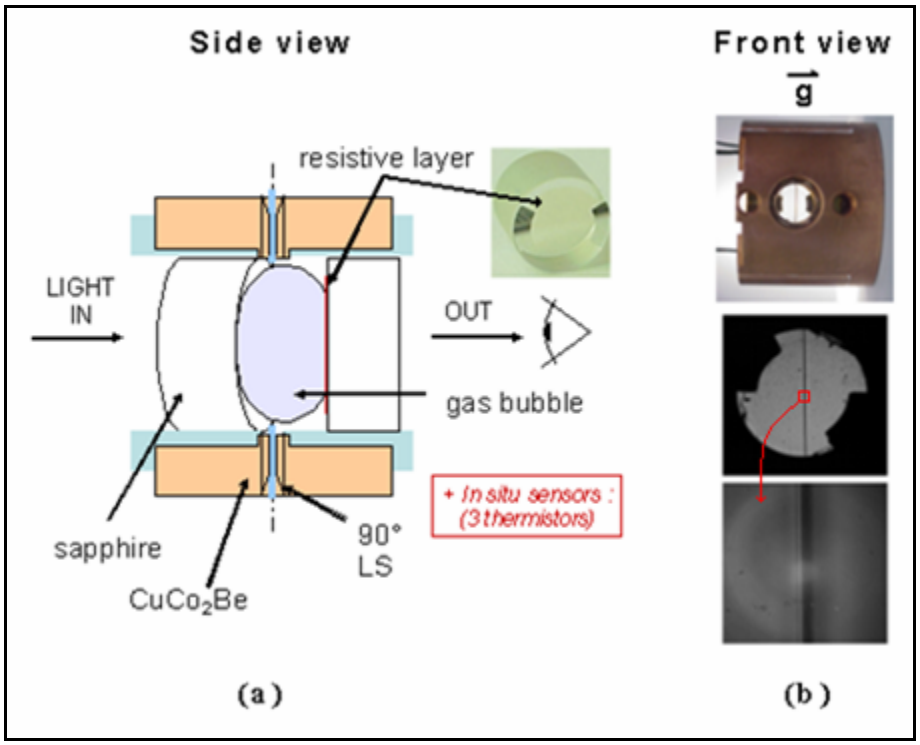

Fig. 50: Optical cell under pressure used for the observation of the liquid film drying; (a) scheme under microgravity force and (b) photographs under gravity force.

Our AZTO thin films were well-adapted to all the requirements imposed by this specific application, i.e. a transparent thin film, stable under pressure with a sheet resistance around 200-300 Ω/□ (280 Ω/□ in this case). This resistive layer is needed to allow a direct heating by Joule effect. AZTO was successfully tested in the laboratory under gravity force [Fig. 50 (b)]. It will allow Y. Garrabos and his group to do observations on the cell and to record the different images using a high resolution camera in the ISS (International Space Station).

2-6. Conclusions

Two types of thin films have been prepared by sputtering: ATO (antimony doped tin oxide) having the composition $Sn_{0.985}Sb_{0.015}O_2$ and AZTO (antimony and zinc doped tin oxide) having the composition $Sn_{0.888}Sb_{0.060}Zn_{0.052}O_{2-\delta}$ using the corresponding ceramic targets. We have first optimized the sputtering conditions for the thin films deposition by varying the power density (P), the oxygen partial pressure (p_{O_2}) and the total gas pressure (p_{tot}). The best performances in term of opto-electronic properties were obtained with the following parameters:

$$P = 3\ W/cm^2,\ p_{O_2} = 2\ \%,\ \text{and}\ p_{tot} = 1\ Pa$$

Note that for AZTO thin films, the deposition rate was always higher due to higher density ceramic target.

A good accordance between thin films and the corresponding ceramic targets compositions is observed. However, XPS analysis has allowed us to access the oxidation state of Sb in these films. Indeed, it shows the presence of both Sb^{3+} and Sb^{5+}. The morphology of thin films is dense with a smooth surface and they are polycrystalline with the rutile structure typical for SnO_2. However, cell parameters are increased due to the substitution of Sn^{4+} by Sb^{3+} and/or Zn^{2+}.

For both thin films, deposited with optimized sputtering conditions, the transmission reaches ~ 90% in the visible range. The reflectivity (R) for ATO thin film is found to increase up to ~ 60% with PD-annealing treatment at 500 °C, which accounts for the metal-like behavior. Due to this, Drude model was applicable to ATO thin films and allows us to assess the mobility, the carrier concentration and the resistivity. For AZTO

films, the reflectivity only reaches 20% (poor reflectivity) even after PD-annealing treatment, which accounts for the semiconducting behavior of the film. In term of electrical resistivity, lowest value of resistivity was obtained for ATO thin films, which is found to decrease with increasing PD-annealing temperature. A good accordance is found between calculated values of mobility, carrier concentration and resistivity with those measured by electrical measurements (Hall technique and four-probe resistivity). Indeed, lower values of resistivity for ATO can be explained by a higher carrier concentration and a higher mobility.

According to all measurements conducted on the thin films, the ATO films composition can be expresses by

$Sn_{0.985}^{4+} Sb_{0.0085}^{5+} Sb_{0.0065}^{3+} O_2 \left[(0.002) e_{C.B.}^{-}\right]$ for as-deposited films

and

$Sn_{0.985}^{4+} Sb_{0.0125}^{5+} Sb_{0.0025}^{3+} O_2 \left[(0.010) e_{C.B.}^{-}\right]$ for PD-annealed film at 500 °C.

Whereas for AZTO films, the composition can be expresses by:

$$Sn_{1-x-z-y-\delta}^{4+} Sb_x^{5+} Sb_z^{3+} Zn_{y+\delta}^{2+} O_{2-\delta}^{2-} \square_{\delta} \left[(x-z-2y) e_{C.B.}^{-}\right]$$

Sb^{3+}/Sb^{5+} ratio determined by XPS seems to be not enough precise because of the low amount of Sb into thin film. Mössbauer may be a better technique to control the accurate ratio and to have informations on the environment of Sb^{3+} and Sb^{5+} (substitutional, interstitial ...).

Although we have higher amount of Sb for AZTO films, their carrier concentrations are lower than for ATO counterparts because of Sb^{3+} and Zn^{2+} substitution to Sn^{4+}, which compensate for the charge carriers created by Sb^{5+} doping. Moreover, the existence of Sb^{3+} creates more structural defects at the grain surface and consequently lowers the film mobility.

Both types of thin films were successfully used for specific applications.

3. References

[1] I. Saadeddin, H. S. Hilal, B. Pecquenard , J. Marcus, A. Mansouri, C. Labrugere, M. A. Subramanian, G. Campet, *Solid state Sci.* **8** (2006) 7.

[2] J. A. Varela, L. A. Perazolli, J. A. Cerri, E. R. Leite, E. Longo, *Cerâmica* **47** (2001) 117.

[3] E. R. Leite, J. A. Cerri, E. Longo, J. A. Varela, C. A. Paskocima, *J. Eur. Cer. Soc.* **21** (2001) 669.

[4] E. R. Leite1, J. A. Cerri1, E. Longo1, J. A. Varela, *Cerâmica* **49** (2003) 87.

[5] C. Kilic, A. Zunger, *Phys. Rev. Lett.* **88** (2002) 95501.

[6] C. Marcel, *Ph.D. thesis*, Bordeaux 1 University, Bordeaux, France (1998).

[7] S. D. Han, S. Y. Huang, G. Campet, M. A. Kennard, *Act. Pass. Elec. Comp.* **18** (1995) 53.

[8] A. Gamard, O. Babot, B. Jousseaume, M.C. Rascle, T. Toupance, G. Campet , *Chem. Mater.* **12** (2000) 3419.

[9] J. Fayat, M.S. Castro, *J. Eur. Cera. Soc.* **23** (2003) 1585.

[10] D. Gouvêa, Ph.D. thesis, Limoges University, Limoges, France (1995).

[11] O. Scarlat, S. Mihaiu, Gh. Aldica, J. Grozac, M. Zaharescu, *J. Eur. Cer. Soc.* **24** (2004) 1049.

[12] S. J. Wen, *Ph.D. Thesis,* Bordeaux 1 University, Bordeaux, France (1992).

[13] G. B. Palmer, K. R. Poeppelmeier, *Solid State Sciences* **4** (2002) 317.

[14] Z. M. Jarzebski, *J. Electrochem. Soc.* **123** (1976) 199.

[15] G. McCarthy, J. Welton, *Powder Diffraction* **4** (1989) 156.

[16] E. E. Kohnke, *J. Phys. Chem. Solids* **23** (1962) 1557.

[17] C. G. Fonstad, R. H. Rediker, *J. Appl. Phys.* **42** (1971) 2911.

[18] M. Nagasawa,S. Shionya, *J. Phys. Soc. Jpn.* **30** (1971) 1213.

[19] Z. M. Jarzebski, J. P. Marton, *J. Electrochem. Soc.***123** (1976) 299.

[20] J. P. Joly, L. Gonszalez-Cruz, Y. Arnaud, *Bull. Soc. chim. Fr.* **1** (1986) 11.

[21] R D. Shannon, *Acta Cryst. A* **32** (1976) 751.

[22] A. Messad , J. Bruneaux, H. Cachet , M. Froment M, *J. Mater. Sci* **29** (1994) 5095.

[23] P. Scherrer, *Gottin Nachricht* **2** (1918) 98.

[24] Natl. Bur. Stand. (U.S.) Monogr. **25** (1972) 62.

[25] C.G. Fonstad, R. H. Rediker, *J. Appl. Phys.* **42** (1971) 2911.

[26] H. L. Ma, X. T. Hao, J. Ma, Y. G. Yang, J. Huang, D. H. Zhang, X. G. Xu, *Appl. Surf. Sci.* **191** (2002) 313.

[27] B. Thangaraju, *Thin Solid Films* **402** (2002) 71.

[28] E. Elangovan, K. Ramamurthi, *Cryst. Res. Technol.* **38** (2003) 779.

[29] T. Nutz, M. Haase, *J. Phys. Chem. B* **104** (2000) 8430.

[30] D. Maestre, A. Cremades, J. Piqueras, *Semicond. Sci. Technol*. **19** (2004) 1236.

[31] I. Saadeddin, B. Pecquenard, J.P. Manaud, R. Decourt, C. Labrugère, T. Buffeteau, G. Campet, *Applied Surface Science,* article in press.

[32] Y. Hamon, A. Douard, F. Sabary, C. Marcel, P. Vinatier, B. Pecquenard, A. Levasseur, *Solid State Ionics* **177** (2006) 257.

[33] V. Geraldoa, L. V. de Andrade Scalvib, E. A. de Moraisa, C. V. Santillic, S. H. Pulcinellic, *Mat. Res.* **6** (2003) 451.

[34] H. Miao, C. Ding , H. Luo, *Microelectronic Engineering* **66** (2003) 142.

[35] E. Burstein, *Phys. Rev.* **93** (1954) 632.

[36] T. S. Moss, *Proc. Phys. Soc. London Sect.* B **67** (1954) 775.

[37] E. Shanthi, V. Dutta, A. Banerjee, K. L. Chopra, *J. Appl. Phys*. **5** (1980) 6243.

[38] B. Stjerna, E. Olsson, C. G. Granqvist, *J Appl. Phys.* **76** (1994) 3797.

[39] E. Shanthi, A. Banerjee, V. Dutta, K. L. Chopra, *J. Appl. Phys.* **53** (1982) 1615.

[40] A. De, S. Ray, *J. Phys. D: Appl. Phys.* **24** (1991) 719.

Chapter III

Synthesis and characterization of In_2O_3 doped with Sn and Zn: ceramics and thin films

Sn-doped In_2O_3 (known as ITO) is a well known TCO, testifying to more than 50 years of intensive scientific investigations and technical applications. In a thin film, ITO exhibits a remarkable combination of optical and electrical transport properties [1–11]: (i) low electrical resistivity (~ 1-2×10^{-4} Ω.cm) and (ii) high optical transparency (>80%) in the visible part of the solar spectrum. However, to achieve such properties, the films must be deposited or post deposition-annealed at a temperature equal or higher to ~ 200 °C. Nowadays, the emphasis is put in processing TCO layers having high electronic and optical performances at low deposition temperatures (≤ 80°C), in order to be compatible with emerging organic related technologies, such as flexible OLED, polymer-based photovoltaic solar cells etc., for which low cost plastic substrates are used. For this reason, amorphous indium zinc oxide (IZO) thin films deposited at low temperature are increasingly being studied [12-22]. In addition to the high optical transparency in the visible, these X-ray amorphous IZO films have typically low resistivities (3-6×10^{-4} Ω.cm), i.e. lower than those measured for the amorphous ITO homologues (7-10×10^{-4} Ω.cm) [10, 18].

The binary In_2O_3-ZnO phase diagram includes a series of homologous IZO compounds having the chemical formula $Zn_kIn_2O_{3+k}$ (k= 2-9, 11, 13, 15); these oxides exhibit hexagonal layered structures and not a cubic bixbyite structure because the Zn content exceeds solubility limit in the bixbyite structure of In_2O_3 [15, 23, 24]. The solubility limit of ZnO into In_2O_3 has been found by D. H. Park et al. to be ~ 1-2 mol. % [24]. However, the solubility limit of Zn^{2+} into In_2O_3 ceramics was found to drastically increase up to 40 mol. % when In^{3+} is co-substituted with Zn^{2+} and Sn^{4+} [25]. Unfortunately, the reported Zn^{2+}-Sn^{4+}co-substituted In_2O_3 ceramics were found to have low bulk densities (≤ 60% of theoretical density) and higher resistivities than their ITO homologues [25-27].

A few works were reported for TCO films deposited by sputtering using ZnO-In_2O_3-SnO_2 [28-30] powder mixtures as targets. In order to approach the conductivity of ITO, the films were deposited on glass substrates at temperatures ≥ 160 °C; therefore, heat sensitive substrates (plastic) could not be used. In addition, ternary $Zn_2In_2O_5$ compound and multicomponent $Zn_2In_2O_5$-$ZnSnO_3$ films were prepared using such powder mixture-based targets.

In this Chapter, the objective is to follow a strategy similar to that of ATO, established in Chapter II. Here, it involves co-doping In_2O_3 with Sn^{4+} and Zn^{2+} (ITZO), forming a solid solution, in such a way to prepare new highly dense and conductive ITZO ceramics. In fact, we will show that co-doping with zinc will allow us to prepare a highly dense and conductive large area ceramic target suitable for both DC and RF sputtering. The synthesis of such target will be done by direct sintering of the powder mixture disposed in an appropriate container without using any cold or (expensive) hot pressing procedure. ITZO thin films deposited on glass and plastic substrates will then be deposited at room temperature using the ceramic target with optimized composition. The influence of the sputtering conditions on the opto-electronic properties of the films will also be investigated.

1. Ceramics

1-1. Preparation

In_2O_3 (99.99%, Aldrich), SnO_2 (99.9%, Aldrich), and ZnO (99.9%, Aldrich) powders, were used to prepare ITZO ceramics. Appropriate amounts of the selected oxides were ball milled for 30 min in an agate bowl containing agate balls and ethanol. The alcohol was then evaporated at 110 °C for 6 hours. After drying, the powder was ground in an agate mortar, and filled in a 16 mm diameter cylindrical alumina crucible, and then hand-pressed. The mixed powder, filled in the crucible, was finally sintered at 1300 °C under air for 12 hours. The dimensions of the resulting pellets were measured with a digital caliper vernier, and the pellets were weighed using an analytical balance, these measurements allowing an estimation of the pellet bulk densities.

1-2. Chemical composition and bulk density

According to literature [11, 28, 31-35], the best conductivity results have been obtained for an amount of Sn^{4+} that varies from ~ 6-10 mol. % in In_2O_3, depending on the synthesis conditions. The Sn^{4+}content in our ceramics was fixed to 10 mol. %, and to vary the initial Zn^{2+} content in the co-doped ceramic from 0-10 mol. %. For the sake of clarity, we have adopted a simplified sample identification (Table 1) emphasizing the influence of Zn doping into ITO.

The EPMA results, reported in Table 1, show that there is a good accordance between the ceramic final compositions after sintering and the starting nominal compositions. The Zn content in the ceramic final composition having its nominal composition $In_2O_3:Zn_{0.02}$ (IZO) reaches ~ 1.4 mol. %. Note that this value is consistent with the reported ZnO solubility limit into In_2O_3 (~ 1-2 mol. %) [24, 36]. A slight loss of SnO_2 varying from ~ 0.5-1 mol. % (which corresponds to ~0.27 to 0.54 weight %) is also observed for both ITZO and ITO ceramics (Table 1).

Sample identification	**Starting Mixture**	**Ceramic composition determined by EPMA ± 0.005**	**Bulk density (g/cm^3) ± 0.05**
$In_2O_3:Zn_{0.02}$	$(In_2O_3)_{0.99}+(ZnO)_{0.02}$	$In_{1.986}Zn_{0.014}O_{2.993-\delta/2}$	3.03
$In_2O_3:Sn_{0.10}$ (ITO)	$(In_2O_3)_{0.95}+(SnO_2)_{0.1}$	$In_{1.910}Sn_{0.090}O_3$	2.52
$[In_2O_3:Sn_{0.10}]:Zn_{0.04}$	$[(In_2O_3)_{0.95}+(SnO_2)_{0.1}]_{0.98}+(ZnO)_{0.04}$	$In_{1.866}Sn_{0.089}Zn_{0.045}O_{3-\delta/2}$	3.50
$[In_2O_3:Sn_{0.10}]:Zn_{0.06}$	$[(In_2O_3)_{0.95}+(SnO_2)_{0.1}]_{0.97}+(ZnO)_{0.06}$	$In_{1.847}Sn_{0.091}Zn_{0.063}O_{3-\delta/2}$	3.92
$[In_2O_3:Sn_{0.10}]:Zn_{0.08}$	$[(In_2O_3)_{0.95}+(SnO_2)_{0.1}]_{0.96}+(ZnO)_{0.08}$	$In_{1.827}Sn_{0.090}Zn_{0.083}O_{3-\delta/2}$	4.87
$[In_2O_3:Sn_{0.10}]:Zn_{0.10}$	$[(In_2O_3)_{0.95}+(SnO_2)_{0.1}]_{0.95}+(ZnO)_{0.10}$	$In_{1.812}Sn_{0.090}Zn_{0.098}O_{3-\delta/2}$	6.57

Table 1: Ceramic chemical composition and bulk density for $[In_2O_3:Sn_{0.10}]:Zn_y$ ceramics (ITZO), $0 \leq y \leq 0.10$. The reported bulk densities were deduced by measuring pellet dimensions and weights. Note that the pellets are prepared by hand-pressing powder mixture in an alumina crucible. In_2O_3:Zn data were given here only for comparison. $\delta/2$ indicates the neutral oxygen vacancy created by doping with Zn, the value of $\delta/2$ varying with Zn content.

These results are confirmed by TGA analysis achieved on both ITO and ITZO ceramics (Fig. 1). A low weight loss (0.28 weight % for $[In_2O_3:Sn_{0.10}]:Zn_{0.10}$ and 0.35 weight % for $In_2O_3:Sn_{0.10}$) is observed between 340 °C and 800°C corresponding to Sn departure. Moreover, a weight loss (~ 0.6 weight %) is observed between room temperature and ~ 340°C which is related to the release of water (adsorbed water and hydroxyl groups). Finally, the slight weight loss observed for temperatures higher than 820 °C can be assigned for some oxygen departure. However, a small weight gain is observed, mainly for ITO, while cooling the ceramics; probably due to a partial re-oxidation (Fig. 1).

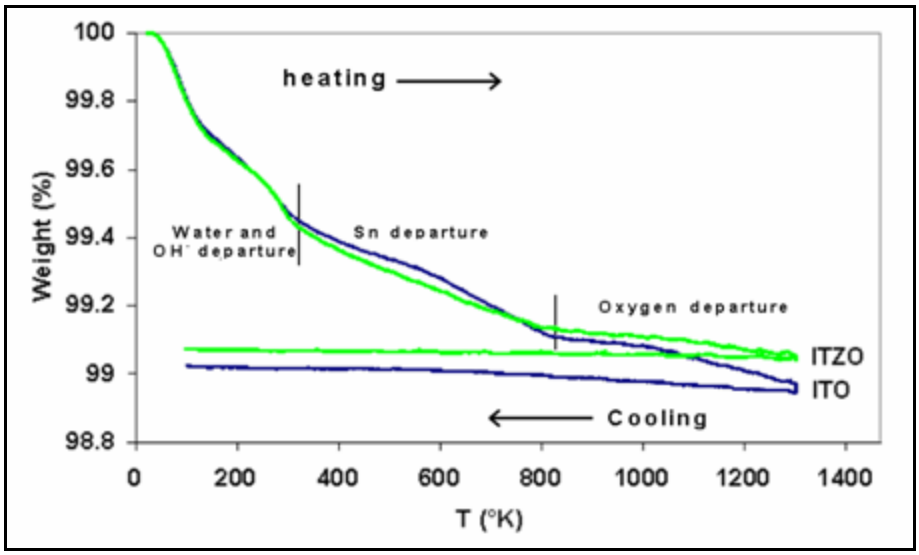

Fig. 1: TGA data for In_2O_3:$Sn_{0.10}$ (ITO) and [In_2O_3:$Sn_{0.10}$]:$Zn_{0.10}$ (ITZO) (nominal composition).

The IZO ceramic having the nominal composition In_2O_3:$Zn_{0.02}$ (Table 1) has a low density : ~ 3.03 g/cm^3; it corresponds only to 42 % of the theoretical density of In_2O_3.This indicates that the Zn content in IZO, corresponding to the solubility limit of Zn into In_2O_3, is not enough to induce a high densification when the pellet is prepared by our method (hand pressed) [36]. However for ITZO ceramics, the bulk density was found to increase from 2.52 to 6.57 g/cm^3 (reaching 92 % of the theoretical density), when y increases from 4-10 mol. % [37]. From Table 1 and Fig. 2, the highest density is observed for the ceramic co-doped with quasi equal amounts of Zn and Sn (around 10 mol. %). The density enhancement must be correlated to the presence of Zn^{2+} in substitutional position (as it occurred for AZTO ceramics [38]), which leads to the formation of neutral oxygen

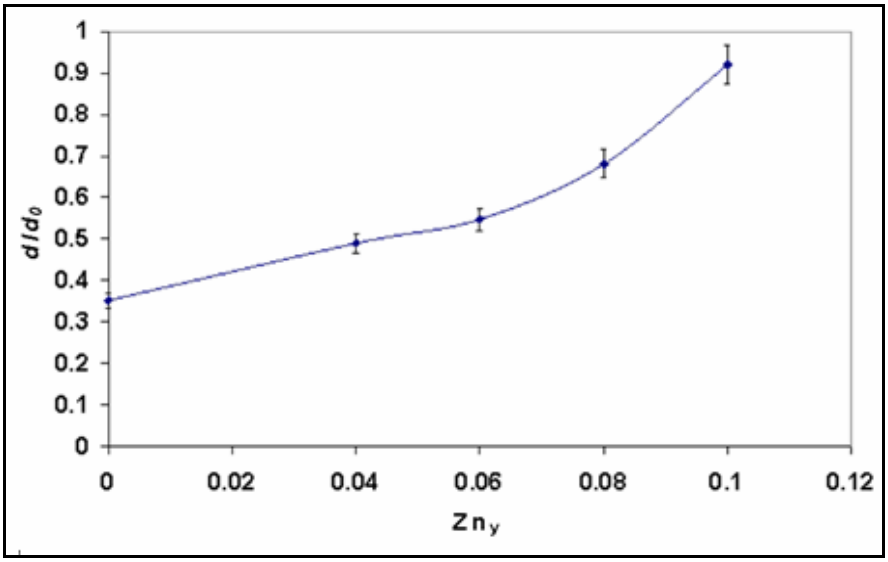

Fig. 2: Relative bulk density (d/d_0) variation with Zn_y for [In_2O_3:$Sn_{0.10}$]:Zn_y ceramics.

vacancies ($\delta/2$) according to:

$$In_{2-x-y-\delta}^{3+} Sn_x^{4+} Zn_{y+\delta}^{2+} O_{3-(\delta/2)}^{2-} \square_{\delta/2} \left[(x-y)e_{C.B.}^{-}\right] \quad \text{(a)}$$

Indeed, as observed for AZTO (Chapter II), the neutral oxygen vacancies promote mass transport at the grain boundary resulting in ceramic densification. However, the presence of Zn^{2+} in substitution position will compensate for the free carriers produced by doping with Sn^{4+} [according to formula (a)] resulting in net charge content per formula unit equal to "*x*-*y*".

1-3. Structural characterization

Indium oxide has the cubic bixbyite structure (also called c-type rare earth oxide structure) which has a 80 atoms unit cell ($In_{32}O_{48}$) with the Ia3 space group and a lattice parameter equal to 10.117 Å [39]. This structure can be derived from the related fluorine structure (CaF_2) by removing one fourth of the anions, and allowing for small shifts of the ions [40]. Indium cations are located at two non-equivalent six-fold positions, referred to 'b' and 'd' (Fig. 3). The b-site cations (8) are bound by two structural vacancies along a body-diagonal. The d-site cations (24) are bound by two structural vacancies along a face-diagonal. It should be noted that these structural vacancies (16) are actually empty oxygen interstitial positions.

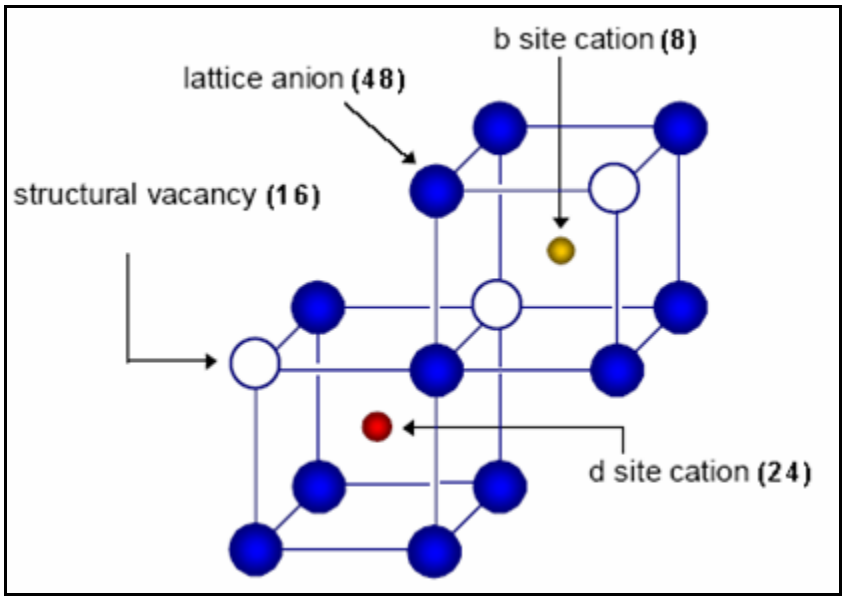

Fig. 3: Schematic representation of b and d cation sites in the bixbyite structure

1-3-a. ITO (In_2O_3:Sn)

X-Ray Diffraction patterns for In_2O_3 and ITO (In_2O_3:$Sn_{0.10}$ nominal composition) powders annealed at 1300°C are shown in Fig. 4. For ITO, some extra low intensity peaks corresponding to the rutile SnO_2 are observed, in addition to the peaks characteristic of the ITO bixbyite structure (JCPDS reference pattern 89-4596). The ratio between the highest intensity ITO peak and the highest intensity SnO_2 peak is 1: ~ 0.03. This is due to the solubility limit of SnO_2 into In_2O_3 (6 mol. %) at 1300 °C as shown by Enoki et al. [35, 36]. In addition, a pronounced decrease of the peaks FWHM (full width at half maximum) for ITO powder compared to In_2O_3 (JCPDS reference pattern 71-2194) is observed, indicating an enhancement of the crystallinity for doped In_2O_3. For example, if we consider the (222) peak, which is the most intense peak, the FWHM was found to decrease from 0.278 ° for In_2O_3 to 0.083 ° for ITO. This crystallinity enhancement seems to be related to the enhancement of the carrier concentration for Sn doped In_2O_3. A similar observation was also previously reported for ATO (Chapter II, section 1-3-a). Finally, we have noticed a slight shift of the main diffraction peaks of ITO towards lower angles compared to pure In_2O_3 (Fig.4), which accounts for a slight increase of the unit cell parameter from 10.117 Å for In_2O_3 to 10.123 Å for ITO. This behavior is not expected if we consider the substitution

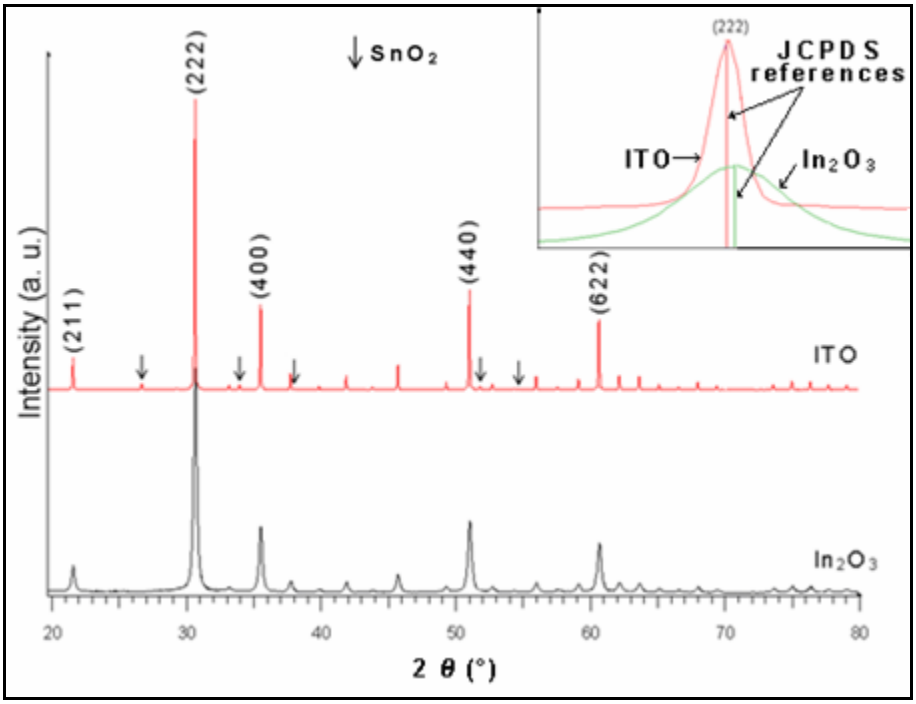

Fig.4: XRD data for (a) undoped In_2O_3 and (b) In_2O_3:$Sn_{0.01}$ (ITO) powders annealed at 1300 °C. The shift of the ITO (222) peak is shown in the insert. (↓) indicates peaks which correspond to the rutile SnO_2

of a part of In^{3+} by Sn^{4+} because Sn^{4+} has an ionic radius (0.69 Å) which is smaller than In^{3+} (0.80 Å) [41]. Thus, the enhancement of the cell parameter could be related to the high electronic carrier concentration in the conduction band and/or the presence of cations in interstitial positions.

1-3-b. ITZO (In_2O_3:Sn:Zn)

XRD patterns for ITZO powders annealed at 1300 °C (Fig. 5) show that they are very well crystallized and they adopted the bixbyite structure of ITO. No Extra peaks corresponding to ZnO_x or $Zn_kIn_2O_{3+k}$ structures are observed with increasing Zn content up to 10 mol. %. Nevertheless, the minor peaks characteristic of SnO_2 structure observed with those of ITO structure are found to gradually vanish with increasing Zn content up to y = 6 mol. %. This confirms the increase of solubility for both Zn and Sn when they are co-doped into In_2O_3 [25, 36]. Indeed, the increase of the solubility is attributed to the isovalent substitution of two In^{3+} by one Zn^{2+} and one Sn^{4+}. A slight increase of the FWHM is also observed while increasing Zn content. This evolution is most likely due to the decrease of the carrier concentration with increasing Zn (as it will be shown latter). Finally, we have

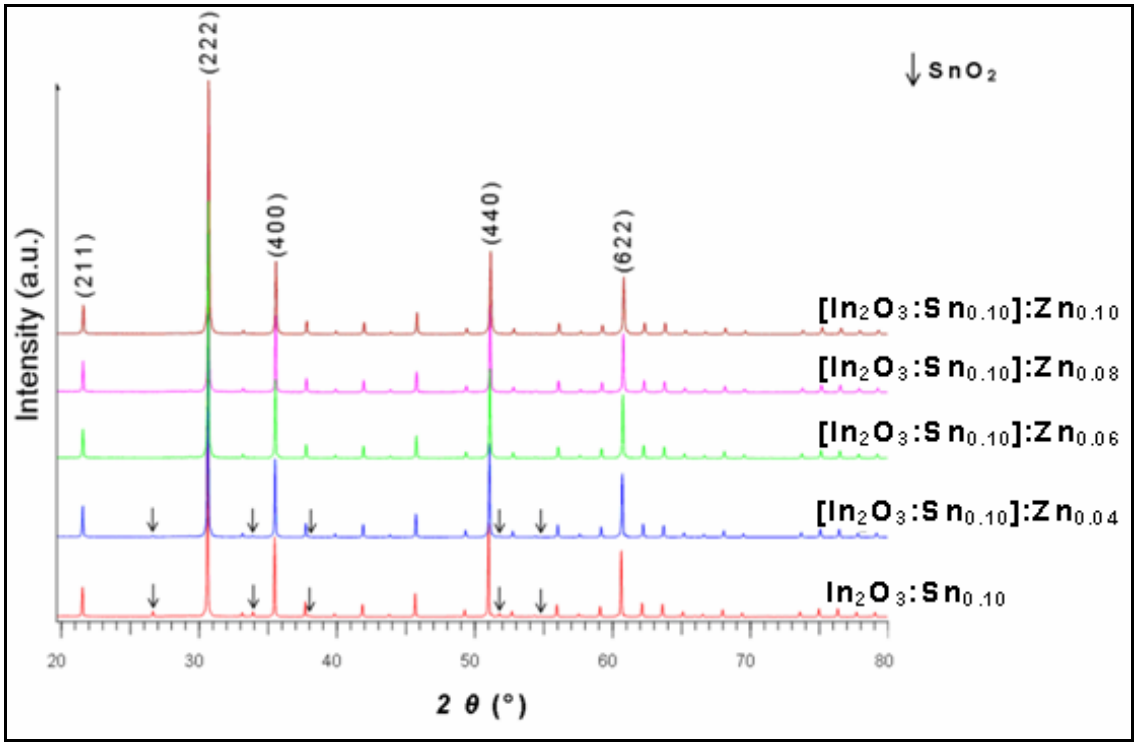

Fig. 5: XRD diagrams for ITZO sintered powders having the nominal composition $[In_2O_3:Sn_{0.10}]:Zn_y$, $0 \leq y \leq 0.10$. (↓) indicates peaks which correspond to the rutile SnO_2.

noted a shift of the main diffraction peaks towards higher angle that increases with Zn content (Fig. 6), inducing a decrease of the cell parameter 'a'(Table 2). This evolution should be attributed to the existence of Zn^{2+} in substitution positions (increasing with Zn contents) as we have already suggested in formula (a) ($In^{3+}_{2-x-y-\delta} Sn^{4+}_{x} Zn^{2+}_{y+\delta} O^{2-}_{3-(\delta/2)} \square_{\delta/2} \left[(x-y) e^{-}_{C.B.}\right]$). Indeed, the 6-fold coordinated Zn^{2+} has an ionic radius (0.74 Å) which is smaller than that of In^{3+} (0.80 Å) [41].

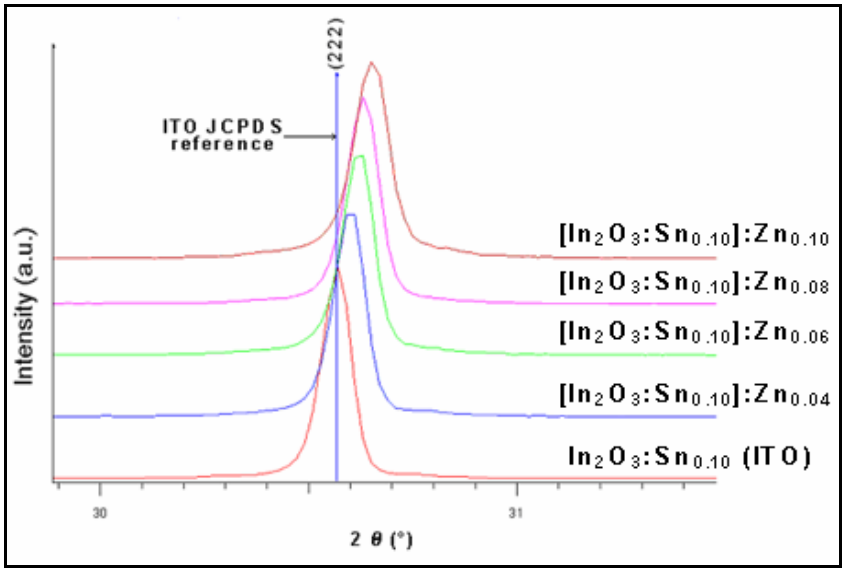

Fig.6: The shift of the x-ray (222) peak for ITZO sintered powders in comparison with ITO counterpart (JCPDS reference pattern 89-4596).

Sample identification	a (Å)
In_2O_3:$Sn_{0.10}$ (ITO)	10.123
[In_2O_3:$Sn_{0.10}$]:$Zn_{0.04}$	10.114
[In_2O_3:$Sn_{0.10}$]:$Zn_{0.06}$	10.107
[In_2O_3:$Sn_{0.10}$]:$Zn_{0.08}$	10.104
[In_2O_3:$Sn_{0.10}$]:$Zn_{0.10}$	10.097

Table 2: Cell parameter evolution with Zn content for ITZO sintered powders. ITO cell parameter is added as a reference.

The evolution of the morphology of ceramic surface with Zn content is presented on the SEM micrographs (Fig. 7). It was found that as Zn content increases in the ceramic, the grain percolation increases and porosity decreases. This confirms the gradual increase of density with Zn content (see Table 1 and Fig. 2). The highest density (~ 6.57) was observed for the ceramic containing a nominal Zn content of 10 mol. %

([In_2O_3:$Sn_{0.10}$]:$Zn_{0.10}$), which has almost a complete grain percolation (Fig. 7). Indeed, co-doping In_2O_3 with Zn and Sn leads to the presence of neutral oxygen vacancies (*δ/2*) according to $In^{3+}_{1-x-y-\delta} Sn^{4+}_{x} Zn^{2+}_{y+\delta} O^{2-}_{2-(\delta/2)} \square_{\delta/2} \left[(x-y)e^{-}_{C.B.}\right]$ (formula (a)), which allows mass transfer at the grain boundaries and hence grain percolation, leading to an enhancement of the ceramic density [37].

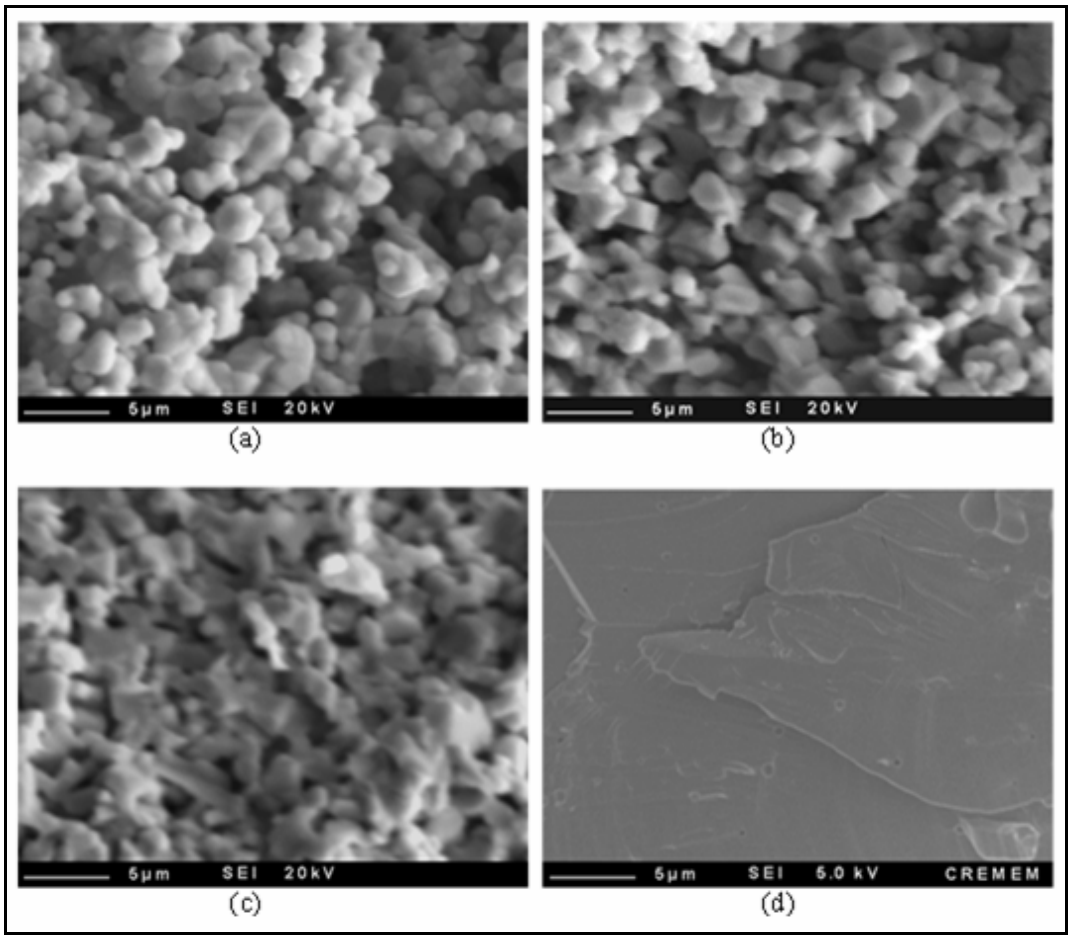

Fig. 7: SEM micrographs for ceramics having the following nominal compositions (a) In_2O_3:$Sn_{0.10}$, (b) [In_2O_3:$Sn_{0.10}$]:$Zn_{0.04}$, (c) [In_2O_3:$Sn_{0.10}$]:$Zn_{0.08}$, and (d) [In_2O_3:$Sn_{0.10}$]:$Zn_{0.10}$.

1-4. Electrical measurements

In_2O_3 is a non stoichiometric n-type, wide direct band-energy gap (≈ 3.5 eV), semiconductor or even semimetal for high doping rates. The origin of such conductivity is due to charged oxygen vacancy (V_O) and/or doping with Sn^{4+}. Fan and Goodenough [11] have developed a model showing that the bottom of the conduction band is mainly composed of In: 5s states and the valence band top is composed of O: 2p states (Fig. 8).

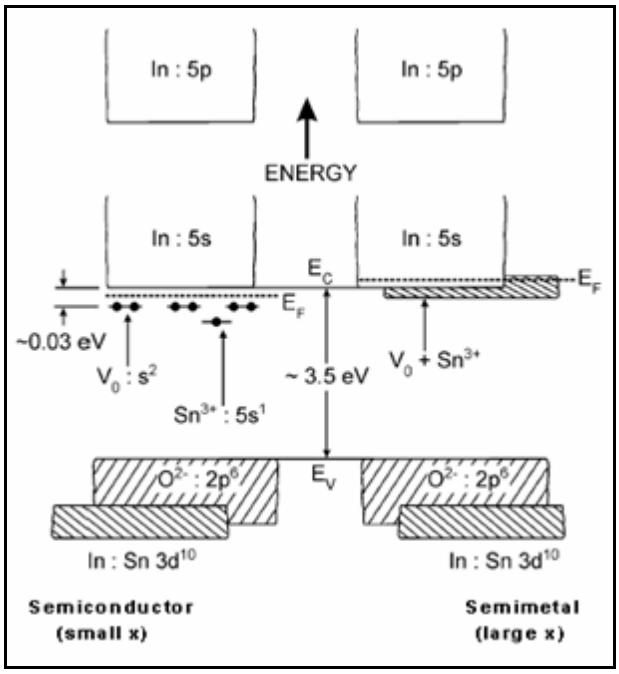

Fig. 8: Schematic energy-band model for Sn doped In_2O_3 for small and large doping concentration (x) (From [11]).

The ITZO ceramics exhibited lower electrical resistivities compared to the ITO one (Fig. 9). The resistivity decreases gradually with Zn content and reaches its minimum (~ 1.7×10^{-3} Ω.cm) for the ceramic that nominally contains 10 mol. % of Zn. This is partly due to difference in ceramic density, reported previously (Table 1). Indeed, we observe the

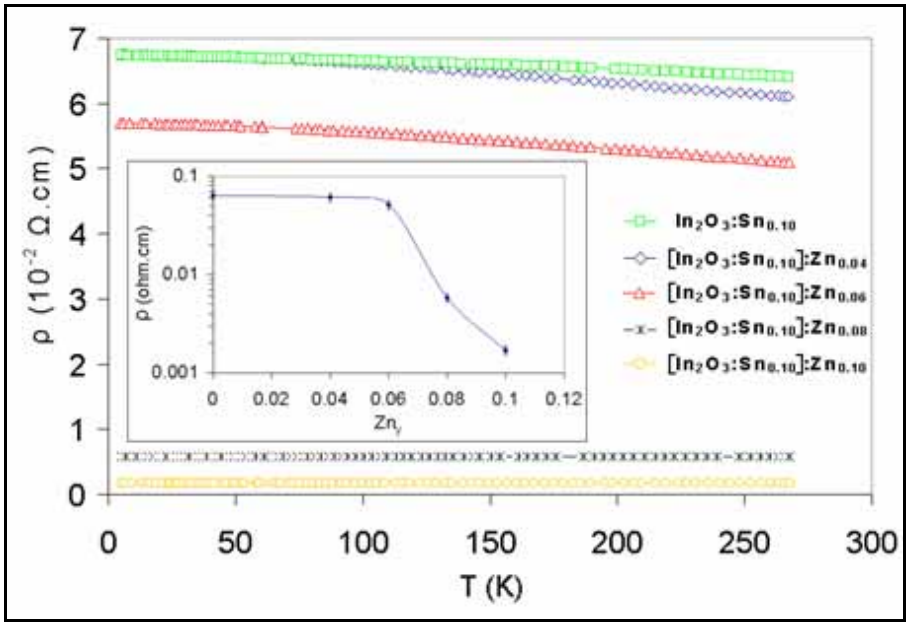

Fig. 9: Resistivity evolution with temperature for different nominal Zn contents (Zn_y) in the ITZO ($[In_2O_3:Sn_{0.10}]:Zn_y$) ceramic with $0 \leq y \leq 0.10$. The resistivity evolution at room temperature is shown in the insert.

lowest resistivity for the ceramic that has highest density. We have also observed a semiconducting behavior for the three ceramics having the highest resistivities, which could be related to the low density observed for these ceramics that probably induces a low mobility. The ceramic carrier concentrations were deduced from Seebeck measurements (Annex 7) which were done at low temperature (at the service de "Mesures de Transport Electronique" de l'ICMCB) (Fig. 10). We have first deduced the energy difference between the conduction band and the Fermi energy level $|E_F-E_C|$ from the slope (Fig. 10) using the following equation:

$$S \approx -\frac{k_B}{e}\frac{\pi^2}{|E_F - E_C|}k_B T \qquad (1)$$

where S is the Seebeck coefficient measured in V/K. The carrier concentration can then be deduced using the following equation for a degenerate semiconductor:

$$E_F - E_C = \frac{h^2}{2m^*}\left(\frac{3N}{8\pi}\right)^{2/3} \qquad (2)$$

N is the carrier concentration, and m^* is the electron effective mass (assuming m^* is equal to 0.4 m_e [42]). All the electrical data deduced from Seebeck and resistivity measurements are listed in Table 3. First, the carrier concentration decreases with Zn

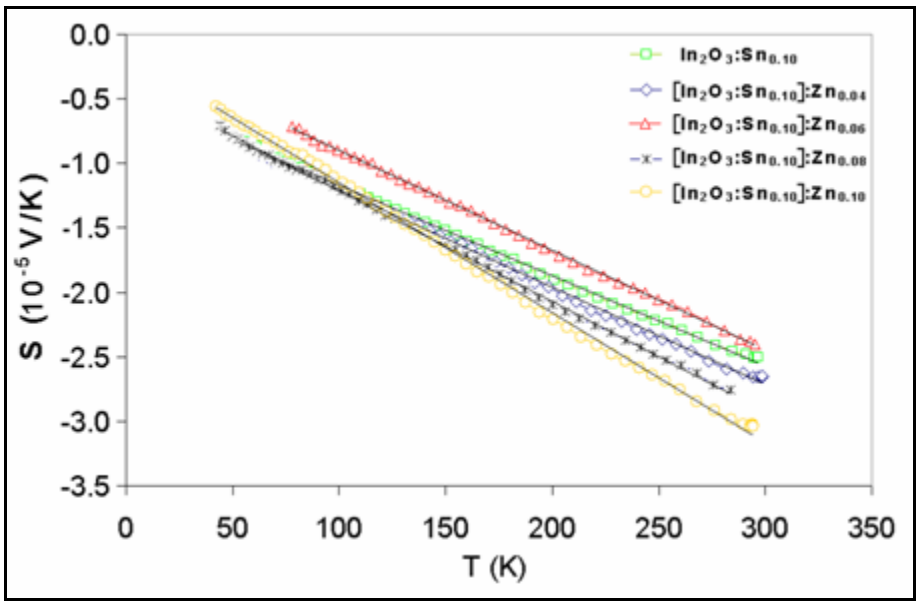

Fig. 10: Seebeck coefficient evolution with temperature for different nominal Zn contents (Zn_y) in the ITZO ($[In_2O_3:Sn_{0.10}]:Zn_y$) ceramic with $0 \le y \le 0.10$.

amount in the ceramic. This can be explained by the increasing substitution of In^{3+} by Zn^{2+} in the In_2O_3 structure, which is confirmed by the shift towards higher angle of the different peaks on the XRD diagrams (Fig. 6). However, a strong enhancement of the carrier mobility is observed when Zn content is higher. The enhancement of the mobility is correlated to the strong enhancement of the grain percolation (Fig. 7) and hence ceramic density [36, 37]. Consequently, a low mobility is obtained for ceramics having a semiconductor behavior (Fig. 9) while a high mobility (at least 10 times higher) is observed for the ceramic having metallic behavior (Fig. 9).

Sample identification	**E_F-E_C (eV)**	**Carrier mobility ($cm^2V^{-1}s^{-1}$) ± 5%**	**Carrier concentration (10^{20} e^- cm^{-3}) ± 5%**	**Resistivity (10^{-3} Ω.cm) ± 5%**
In_2O_3:$Sn_{0.10}$ (ITO)	0.67	0.16	6.30E+20	64
[In_2O_3:$Sn_{0.10}$]:$Zn_{0.04}$	0.62	0.18	5.63E+20	61
[In_2O_3:$Sn_{0.10}$]:$Zn_{0.06}$	0.61	0.23	5.42E+20	51
[In_2O_3:$Sn_{0.10}$]:$Zn_{0.08}$	0.55	2.30	4.68E+20	5.8
[In_2O_3:$Sn_{0.10}$]:$Zn_{0.10}$	0.47	10.09	3.65E+20	1.7

Table 3: E_F-E_C, mobility, carrier concentration and resistivity values for ITO and different ITZO ceramics. The carrier concentration was deduced using Seebeck coefficient measurements.

Using the EPMA results and electrical measurements, we can calculate the exact final formula for the ITO and ITZO ceramics. In the case of ITO ceramic, we have only a substitution of In^{3+} by Sn^{4+} in the In_2O_3 lattice producing free electron carriers in the conduction band according to:

$$In_{2-x}^{3+} Sn_x^{4+} O_3^{2-} \left[x e_{C.B.}^- \right] \quad \text{(b)}$$

x was deduced from the carrier concentration (Table 3) and found to be equal to ~ 0.04 per formula unit. Hence, one should normally write the following formula for ITO:

$$In_{1.96}^{3+} Sn_{0.04}^{4+} O_3^{2-} \left[0.04 e_{C.B.}^- \right] \quad \text{(c)}$$

However, formula (c) differs from that determined using EPMA: $In_{1.91}Sn_{0.09}O_3$ which is more accurate. In fact, let us recall that the 0.09 Sn content is divided into three parts: (i) a part goes to form the rutile SnO_2 additional phase as previously shown by XRD analysis

(paragraph 1-3-a), (ii) another part substitutes In^{3+} producing free electrons in the conduction band according to Formula (c), and (iii) the remaining Sn are most probably segregated at the grain boundaries where structural disorder predominates.

For ITZO, both Sn^{4+} and Zn^{2+} substitute In^{3+} in the In_2O_3 according to formula (a) ($In^{3+}_{2-x-y-\delta}Sn^{4+}_{x}Zn^{2+}_{y+\delta}O^{2-}_{3-(\delta/2)}\square_{\delta/2}\left[(x-y)e^{-}_{C.B.}\right]$). The calculated parameters (x, y and δ) and the corresponding final formula for ITZO ceramics are listed in Table 4.

Sample identification	x	y	δ	Final formula
$[In_2O_3:Sn_{0.10}]:Zn_{0.06}$	0.091	0.057	0.006	$In^{3+}_{1.847}Sn^{4+}_{0.091}Zn^{2+}_{0.063}O^{2-}_{2.997}\square_{0.003}\left[(0.034)e^{-}_{C.B.}\right]$
$[In_2O_3:Sn_{0.10}]:Zn_{0.08}$	0.092	0.062	0.020	$In^{3+}_{1.826}Sn^{4+}_{0.092}Zn^{2+}_{0.082}O^{2-}_{2.990}\square_{0.010}\left[(0.030)e^{-}_{C.B.}\right]$
$[In_2O_3:Sn_{0.10}]:Zn_{0.10}$	0.090	0.066	0.032	$In^{3+}_{1.812}Sn^{4+}_{0.090}Zn^{2+}_{0.098}O^{2-}_{2.984}\square_{0.016}\left[(0.024)e^{-}_{C.B.}\right]$

Table 4: ITZO parameters and final formulas calculated using EPMA results and carrier concentration determined by Seebeck measurements.

1-5. Conclusions

ITO, IZO and ITZO ceramic pellets have been prepared without using any cold or hot pressing procedure. They are done simply by lightly pressed powder mixture (hand pressed) in cylindrical alumina crucible and then by sintering at 1300 °C. The idea was to be able to prepare large scale targets that could be used for industrial applications in a PVD process.

IZO ceramic final composition was found to have Zn content of ~ 1.4 mol. % which corresponds to the Zn solubility limit into In_2O_3. The density of our IZO ceramic is low (~ 3.03 g/cm^3) compared with the theoretical density of In_2O_3 (7.16 g/cm^3). For ITO ceramic, a good accordance between the ceramic final composition and the starting mixture was observed with tiny loss of Sn^{4+} (~ 1 mol. %) and its density is low (35 % of the theoretical density). For ITZO, the ceramic final compositions are also in good accordance with their starting mixtures with also a tiny loss of Sn^{4+} (~ 0.5-1 mol. %). However, the density of the prepared ITZO ceramic increases gradually as Zn content increases, due to the increase of the neutral oxygen vacancies which promote mass transport at the grain boundaries and, thereby, facilitates the grain percolation. The highest

density (~ 92 % of the theoretical density) is observed for the ceramic having the nominal composition $[In_2O_3:Sn_{0.10}]:Zn_{0.10}$.

Compatible with literature [35], SnO_2 solubility into In_2O_3 reached ~ 6 mol. % as shown by XRD. However, the solubility of Sn and Zn was found to increase when they co-substituted In into In_2O_3. Indeed, as shown by XRD analysis, no additional peak corresponding to Sn or Zn oxide phases is observed for ceramics having Zn content ≥ 6 mol. %. In addition, the small shift of the XRD peaks towards higher angles accounts for cell parameter decreasing due to the substitution of some In^{3+} by Zn^{2+}.

Most interestingly, the electrical resistivities of ITZO ceramics are lower than that of ITO counterpart due to higher density and lower porosity and hence higher mobility. The lowest resistivity (~ 1.7×10^{-3} Ω.cm) was observed for the one having the nominal composition $[In_2O_3:Sn_{0.10}]:Zn_{0.10}$. To conclude, using simple sintering of lightly pressed ITZO mixed powder, we success to prepare a highly dense and conductive ceramic suitable for sputtering. Let us recall that the nominal composition $[In_2O_3:Sn_{0.10}]:Zn_{0.10}$ corresponds to the starting powder mixture:

$$[(In_2O_3)_{0.95} + (SnO_2)_{0.1}]_{0.95} + (ZnO)_{0.10}.$$

This mixture will be used to prepare a ceramic target suitable for thin film deposition by sputtering technique.

2. Thin films

ITZO thin films were deposited using the RF sputtering deposition technique. We have used the sputtering machine (Leybold L560, Fig. 18, Chapter II) that was previously used for ATO and AZTO thin films deposition. This work was done in collaboration with J. P. MANAUD, from "Centre de Ressources Couches Minces de l'ICMCB".

2-1. Preparation of the target

A 50 mm diameter ITZO ceramic target was prepared using the optimized ceramic composition (see paragraph 1-5 of Chapter III). A 50 g batch of appropriate amounts of In_2O_3, SnO_2 and ZnO powders were ball milled for 3 h in agate bowl containing agate balls and ethanol. Then, after evaporating the ethanol, the powder was ground in an agate mortar, and then filled in 82.56 mm diameter cylindrical alumina crucible (see Fig. 11).

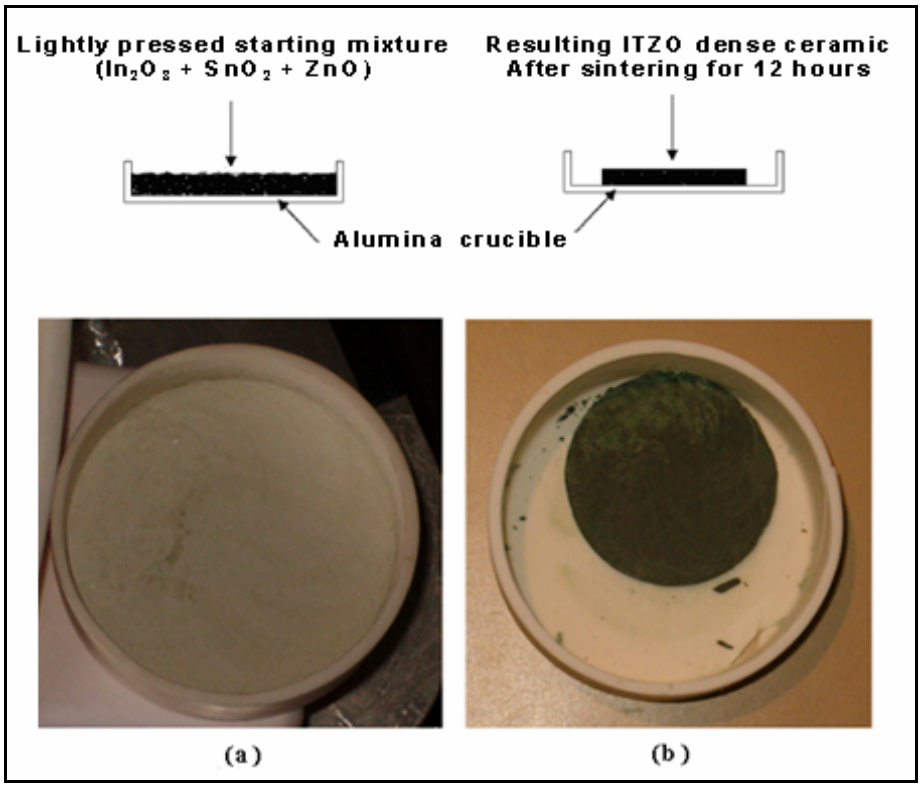

Fig. 11: A schematic representation of the preparation of the ITZO dense ceramic, (a) photograph for lightly pressed powder mixture in the alumina crucible and (b) photograph of resulting dense ITZO ceramic showing the shrinkage.

The powder mixture in the crucible was lightly pressed (by hand) and then sintered at 1300 °C under air for 12 hours. ITZO ceramic target having a relative density ~ 0.92 was then obtained. The target diameter was found to be ~ 52.5 mm after thermal treatment which corresponds to ~ 36.4 % shrinkage in diameter due to the densification process. The final 50 mm diameter target was achieved after polishing.

2-2. Sputtering parameters optimization

Using the as prepared target, ITZO thin films were deposited by RF magnetron sputtering in a turbo-pumped sputtering chamber (Leybold L560). Before film deposition, the residual gases pressure was about 5-9×10^{-5} Pa. Before each deposition process, a pre-sputtering has been made systematically for 20 min in order to clean the target surface. The film deposition was done at room temperature without heating the substrate. They were deposited on glass and PET (polyethylene terephthalate)T substrates, during various deposition times. The deposition RF power density was varied from 0.5 to 2.5 W/cm^2. It was done at a fixed total gas pressure of 1 Pa under a mixture of argon (99.999 %) and oxygen (99.99 %), with oxygen partial pressure varying between 0-2 %.

In order to have films with good opto-electronic properties, we have first optimized the sputtering conditions. Hence, we have studied the influence of the power density (P) and the oxygen partial pressure (p_{O_2}) on deposition rate, optical and electrical properties of the ITZO thin films [43]. In order to have low energy sputtered particles (suitable for PET substrate), the target to substrate distance ($d_{t\text{-}s}$) was fixed at 7 cm, which is the maximum distance allowing to maintain the plasma in the sputtering chamber at low sputtering power density of 0.5 W/cm^2.

2-2-a. Influence of the sputtering parameters on the deposition rate

The determination of the deposition rate was done, as usual, by depositing a film for a certain period of time on glass substrate and then by measuring the film thickness using a profilometer. As found on Fig. 12, increasing the power density from 0.5 to 2.5 W/cm^2 almost linearly increases the deposition rate from 4.3 to 37.2 nm/min. Indeed, higher power density induces higher plasma density and momentum transfer to the target.

However, we choose not to exceed higher power densities because the main objective of this study is to deposit ITZO films on plastic substrates.

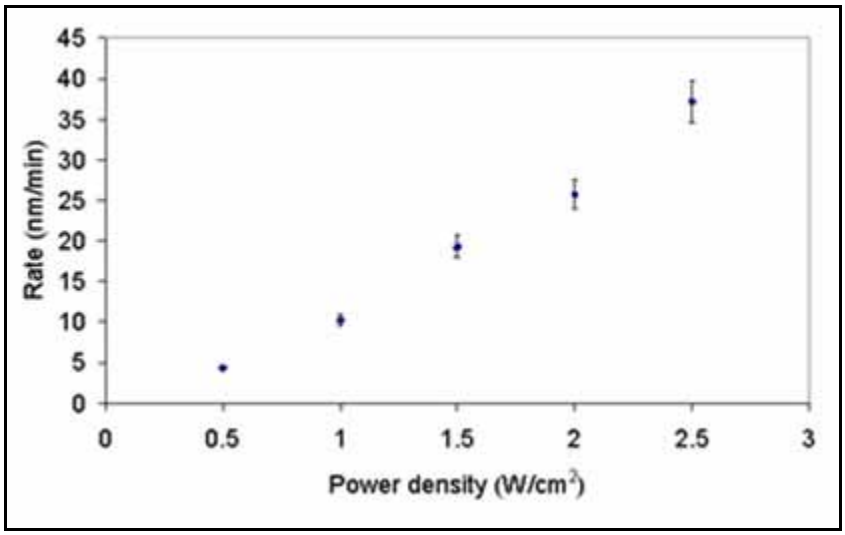

Fig. 12: Influence of the sputtering power density on deposition rate of ITZO thin films (p_{O_2} = 0.2 %).

As expected, contrary to the power density, the deposition rate decreases with increasing oxygen amount in the plasma (Fig. 13). This can be related either to the nature of the molecular ions present in the mixed plasma that have a lower mean free path inducing a lower probability for particles to reach the substrate, or to the target extreme surface composition that varies according to the nature of plasma and can influence the deposition rate.

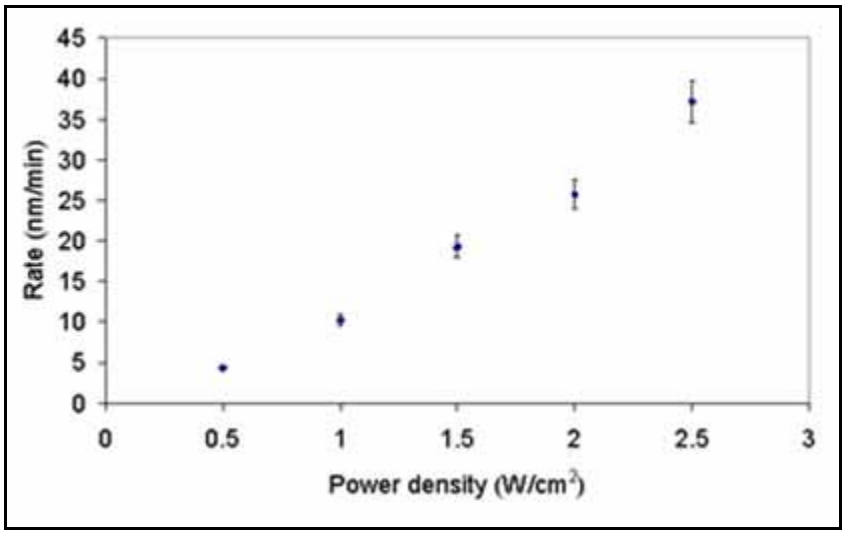

Fig. 13: Influence of the oxygen partial pressure on the deposition rate of ITZO thin films (P = 1 W/cm^2).

2-2-b. Influence of the sputtering parameters on the optical properties

The Fig. 14 shows the evolution of the transmittance between 200 and 2500 nm as a function of the power density. The highest visible transparency (~ 86 %) is obtained for thin films deposited on glass substrate at a power density of 0.5 W/cm^2. However, the lowest transparency (~ 71%) is observed for the samples deposited at the highest sputtering power density (2.5 W/cm^2). Indeed, at high power density, a back sputtering phenomenon may occur causing structural defects in the film; the later introduce sub-band gap energy states leading to a decrease of the film transparency.

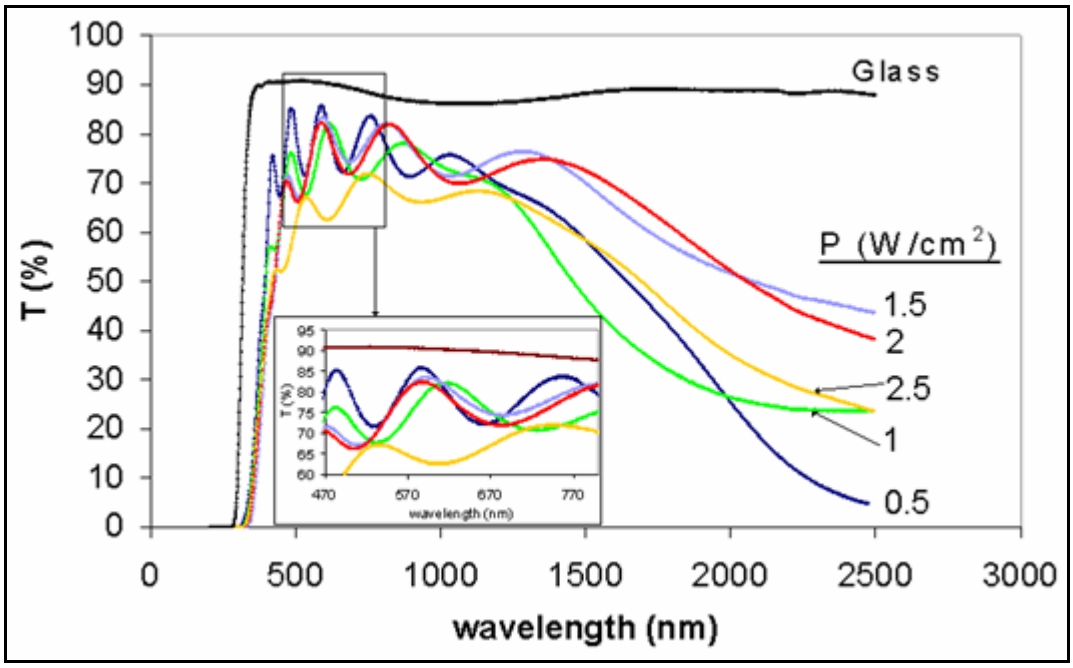

Fig. 14: Transparency spectrum for ITZO thin films deposited at different power densities. (p_{O_2} = 0.2 %). Film thickness was fixed around 400 nm for all films. Inset shows the expanded visible region showing the transparency.

The optical energy band-gap (E_g) has been determined by extrapolating the linear portion of the plotted curves (Fig. 15) to zero absorption. E_g of the deposited ITZO films first decreases from ~ 3.88 to ~ 3.57 eV when the power density goes from 0.5 to 1.5 W/cm^2 (Fig. 15). For power densities higher than 1.5 W/cm^2, we observe an increase of E_g. The latter evolution is related to the evolution of the carrier concentration (Burstein-Moss effect [44, 45]), as will be shown in the next paragraph (2-2-c).

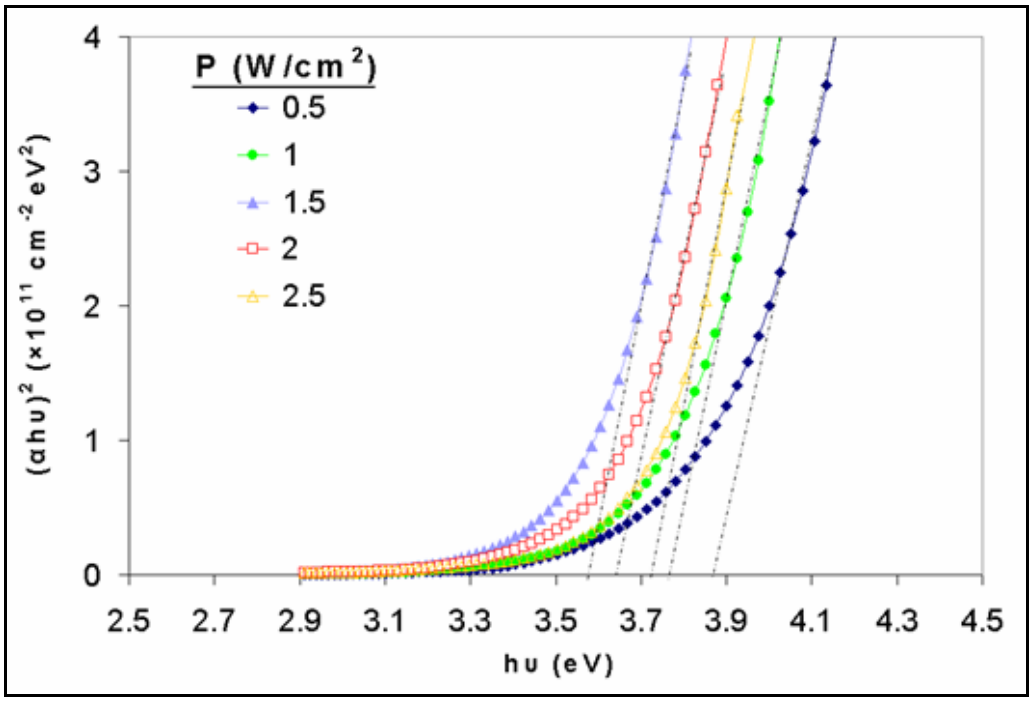

Fig. 15: Determination of the optical energy band-gap for ITZO thin film deposited at various power densities

The influence of the oxygen partial pressure (p_{O_2}) on the transmission was studied for thin films prepared under the lowest power density (0.5 W/cm^2) which give the best transparency in the visible range. A low visible transparency (~ 77 %) was observed for film deposited at p_{O_2} = 0.1 % (inset of Fig. 16), brown in color. However, for films

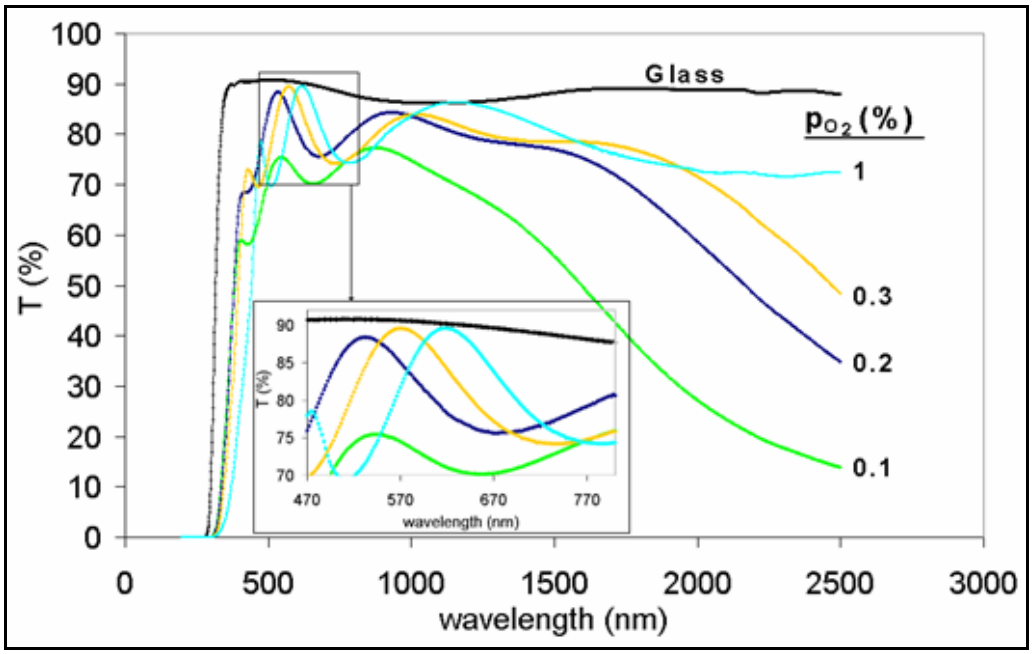

Fig. 16: Optical transmission for different ITZO thin films prepared under various oxygen partial pressure (P = 0.5 W/cm^2). Films thicknesses ranged between 250 and 280 nm.

deposited at a p_{O_2} higher than 0.1 %, a high transparency is obtained, ranging from ~88.5 to ~89.5 % for an oxygen partial pressure ranging between 0.2 and 1 % and the films are nearly colorless.

E_g decreases from about ~ 3.89 to ~ 3.66 eV when the oxygen partial pressure in the sputtering chamber evolutes from 0.1 to 1 % (Fig. 17). Increasing the oxygen partial pressure favors the decrease of the oxygen vacancies (δ) leading to a decrease of the carrier concentration [as will be seen later on formula (d)].

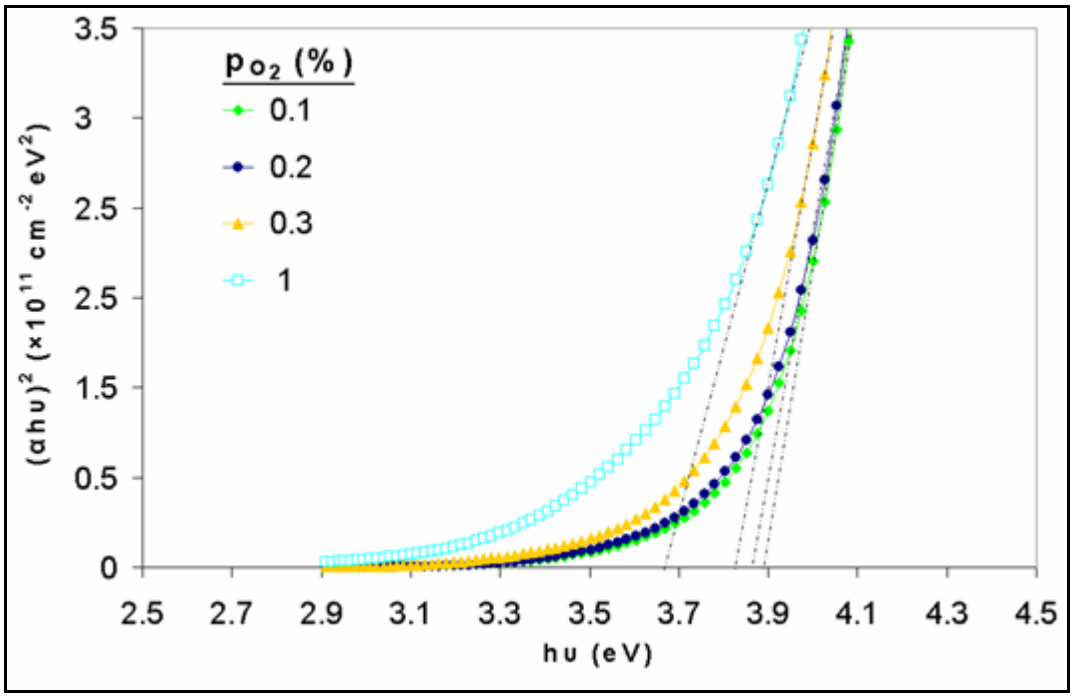

Fig. 17: Determination of the optical energy band-gap for ITZO thin film deposited under different oxygen partial pressure.

2-2-c. Influence of the sputtering parameters on the electrical properties

The Table 5 indicates the evolution of the carrier concentration, the mobility and the resistivity as a function of the power density. The resistivity of ITZO thin films gradually increases, from ~ 4.6×10^{-4} Ω.cm to ~ 5.1×10^{-3} Ω.cm, when the power density goes from 0.5 W/cm^2 to 1.5 W/cm^2 (Fig. 18) and then decreases for higher power density. Indeed, the resistivity is inversely proportional to the carrier concentration. However, as expected, the mobility evolution shows an inverse trend to the carrier concentration even if

the mobility has a minor contribution to the resistivity. Note that the lowest resistivity is obtained for a power density of 0.5 W/cm^2.

Power density (W/cm^2)	Carrier conc. (e^- cm^{-3}) ± 5%	Mobility (cm^2/V.s) ± 5%	Resistivity (Ω.cm) ± 5%
0.5	5.54×10^{20}	24.1	4.6×10^{-4}
1	2.82×10^{20}	29.1	7.6×10^{-4}
1.5	3.31×10^{19}	36.8	5.1×10^{-3}
2	6.7×10^{19}	21.6	4.2×10^{-3}
2.5	2.11×10^{20}	18.7	1.6×10^{-3}

Table 5: Carrier concentration (determined from Hall measurement), mobility, and resistivity for different ITZO thin films deposited at different power densities.

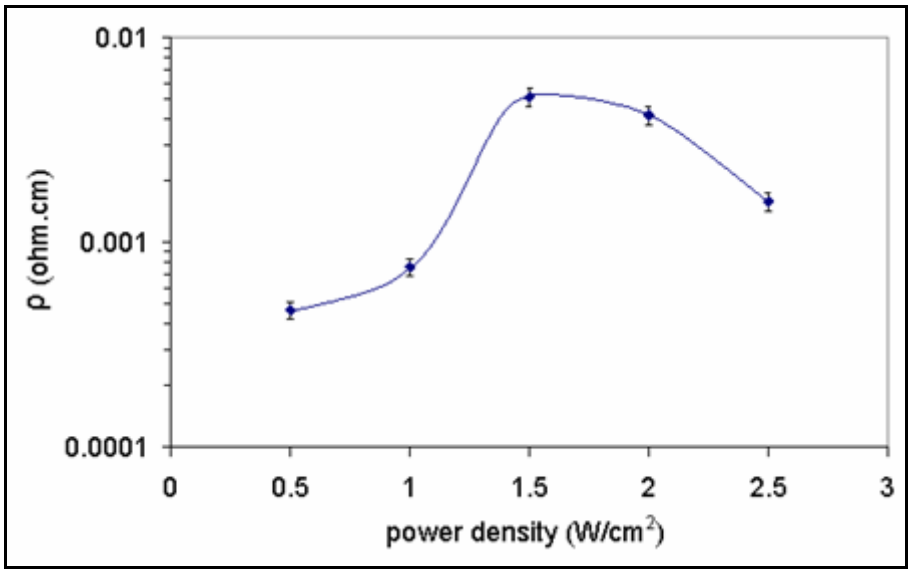

Fig. 18: Evolution of resistivity with power density (p_{O_2} = 0.2 %).

We have also followed the evolution of resistivity as a function of the oxygen partial pressure for ITZO thin films deposited at a power density of 0.5 W/cm^2.

The values of carrier concentration, mobility and resistivity for different oxygen partial pressures are listed in Table 6. The lowest resistivity (~ 4.4×10^{-4} Ω.cm) is obtained for films deposited at p_{O_2} = 0.2 % (Fig. 19). For films deposited at lower p_{O_2} (0.1 %), the carrier concentration corresponds to the highest value (Table 6) that explains the low transparency (Fig. 16) and the highest E_g (Fig. 17). Nevertheless, the mobility is lower than that of films deposited at p_{O_2} = 0.2 % (Table 8), which explains the higher resistivity. For

films deposited at p_{O_2} higher than 0.2 %, the carrier concentration decreases with p_{O_2}. In addition, the mobility was also decreased with p_{O_2}, which may be due to structural disorder induced by oxygen insertion into the amorphous structure that will be evidenced in the next paragraph (2-2-d). Consequently, the film resistivity drastically increases (~ 1.7×10^{-1} Ω.cm) when it is deposited at high p_{O_2}(1 %).

Oxygen partial pressure (%)	Carrier conc. ($e^- cm^{-3}$) ± 5%	Mobility ($cm^2/V.s$) ± 5%	Resistivity (Ω.cm) ± 5%
0.1	5.36×10^{20}	17.8	6.55×10^{-4}
0.2	4.89×10^{20}	28.8	4.44×10^{-4}
0.3	3.41×10^{20}	23.3	7.85×10^{-4}
1	9.23×10^{19}	0.40	1.70×10^{-1}

Table 6: Carrier concentration determined by Hall measurement, calculated mobility, and measured resistivity for different ITZO thin films deposited at different oxygen partial pressures.

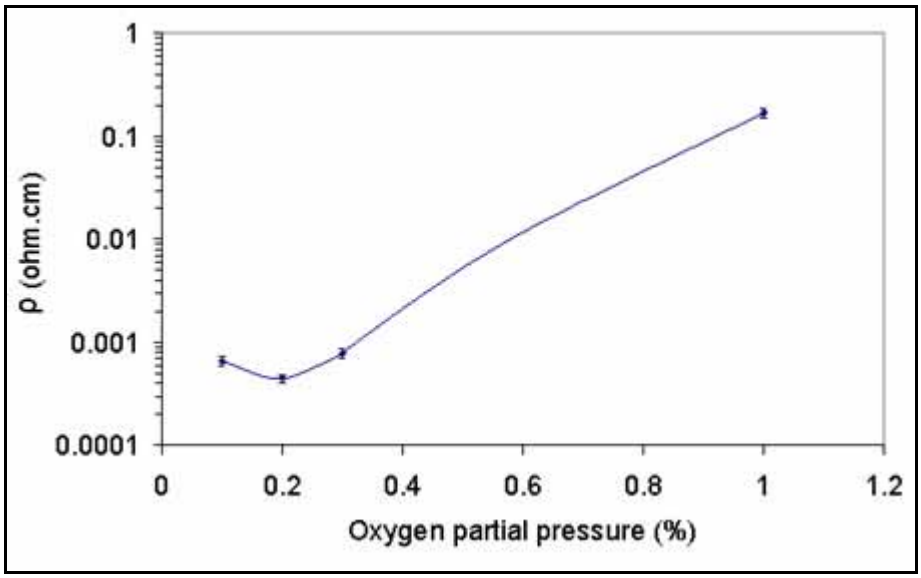

Fig. 19: Evolution of the resistivity as a function of the oxygen partial pressure for ITZO thin films (P = 0.5 W/cm^2).

2-2-d. Influence of the sputtering parameters on the structure and the morphology.

The evolution of the X-ray diffractograms (Fig. 20) shows that the film deposited at 0.5 W/cm^2 has an x-ray amorphous structure, which is attributed to the low energy particles arriving to the substrate surface. In addition, as the RF power density increases (1

and 1.5 W/cm^2), higher energy particles arrive to the substrate, and hence, lead to a better crystallinity. However, for power densities higher than 1.5 W/cm^2, the crystallinity of the film gradually decreases with the power density and we observe peak broadening. The disorder associated with higher power densities is probably due to the back sputtering phenomenon that induces structural defects in the deposited film. The Zn^{2+} ions may occupy two types of sites (substitutional or interstitial) in the structure, as indicated in the following formula:

$$In_{2-x-y-\delta}^{3+} Sn_x^{4+} Zn_{y+\delta}^{2+} Zn_z^{2+} O_{3-(\delta/2)}^{2-} \square_{\delta/2} \left[(x - y + 2z) e_{C.B.}^{-} \right] \qquad \text{(d)}$$

To have a high carrier concentration, it is better to have preferentially Zn^{2+} in interstitial position (z).

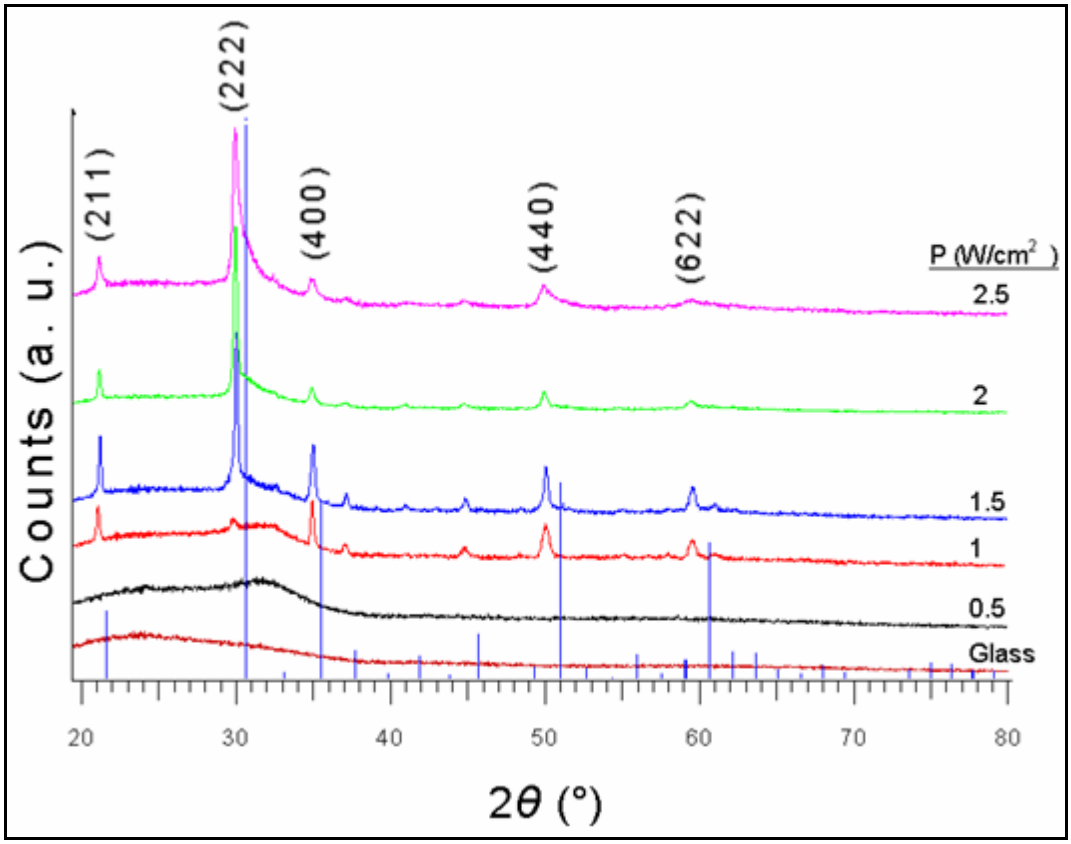

Fig. 20: X-ray diffraction diagram of ITZO thin films deposited on glass substrate at different power densities. The XRD pattern of ITO (JCPDS no. 89-4596) is given for comparison (vertical lines).

In a crystallized structure, Zn^{2+} will preferentially occupy substitutional position in order to minimize the energy and to reduce the steric effects while the creation of the interstitials will be favored in the case of disordered structure (amorphous). In addition, Park et al. [24] have shown that the existence of Zn in interstitial position into In_2O_3

structure leads to an increase in the cell parameter. If we compare the peak positions of our thin films with those characteristic of ITO, we always observe a shift towards lower angles, which indicates an increase in the cell parameter. This shift is minimized in the case of the best crystallized compound (corresponding to the power of 1.5 W/cm^2). So, we can expect to have a higher proportion of interstitials into disordered structure, resulting in a higher carrier concentration. The SEM photographs prepared at different power densities are presented in Fig. 21. The film deposited at low power density (0.5 W/cm^2) is dense and smooth [Fig. 21 (a)]. However, a continuous change of morphology is observed form (a) to (c) when we increase the power density. On Fig. 21 (c), the occurrence of grains is clearly visible on the surface with grain size ~ 130 nm. In addition, some zones (dark gray), which may correspond to back sputtering phenomenon are visible.

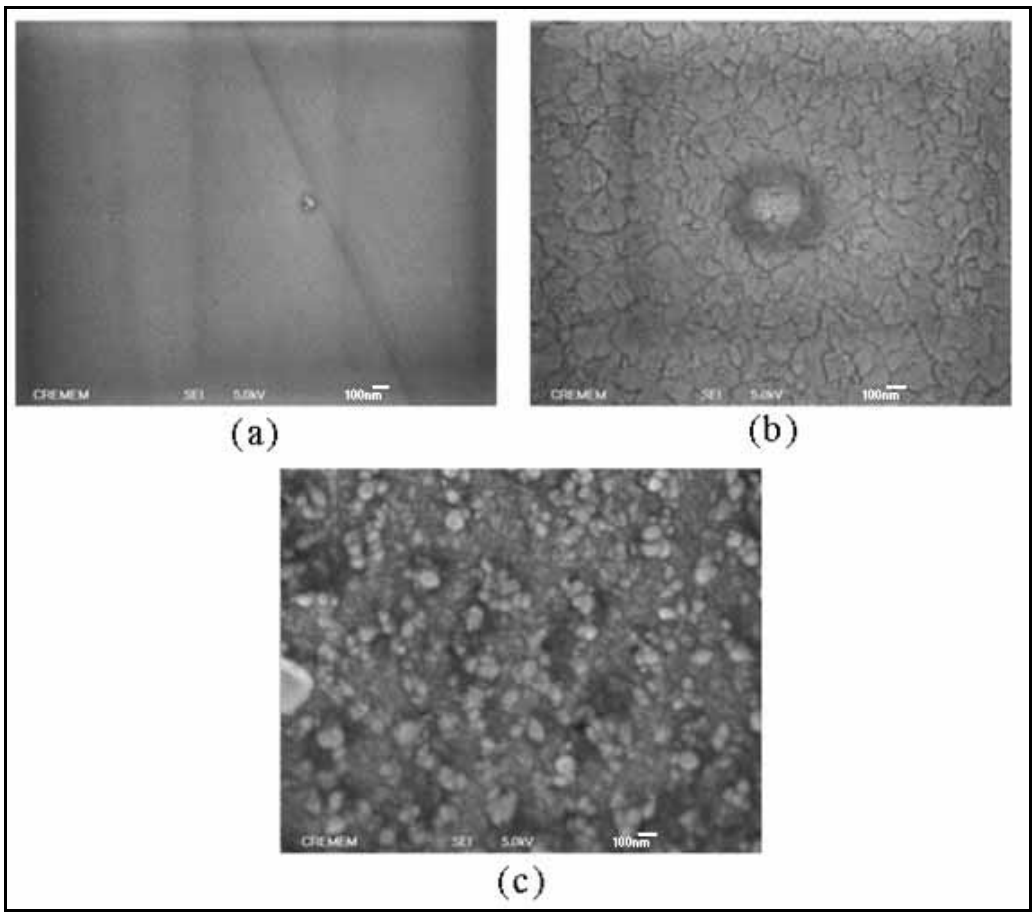

Fig. 21: SEM micrographs for ITZO thin film deposited at RF sputtering power of (a) 0.5 W/cm^2, (b) 1.5 W/cm^2 and (c) 2.5 W/cm2.

We have also studied the surface roughness using AFM (Fig. 22). The ITZO film deposited at 0.5 W/cm^2 revealed a very smooth surface which is in good agreement with SEM results. However, the surface roughness is enhanced with power density due to the

film crystallization. In fact, for higher deposition power, a pronounced increase in the R_a (see Chapter II, page 77) is found due to the back sputtering phenomenon (Table 7).

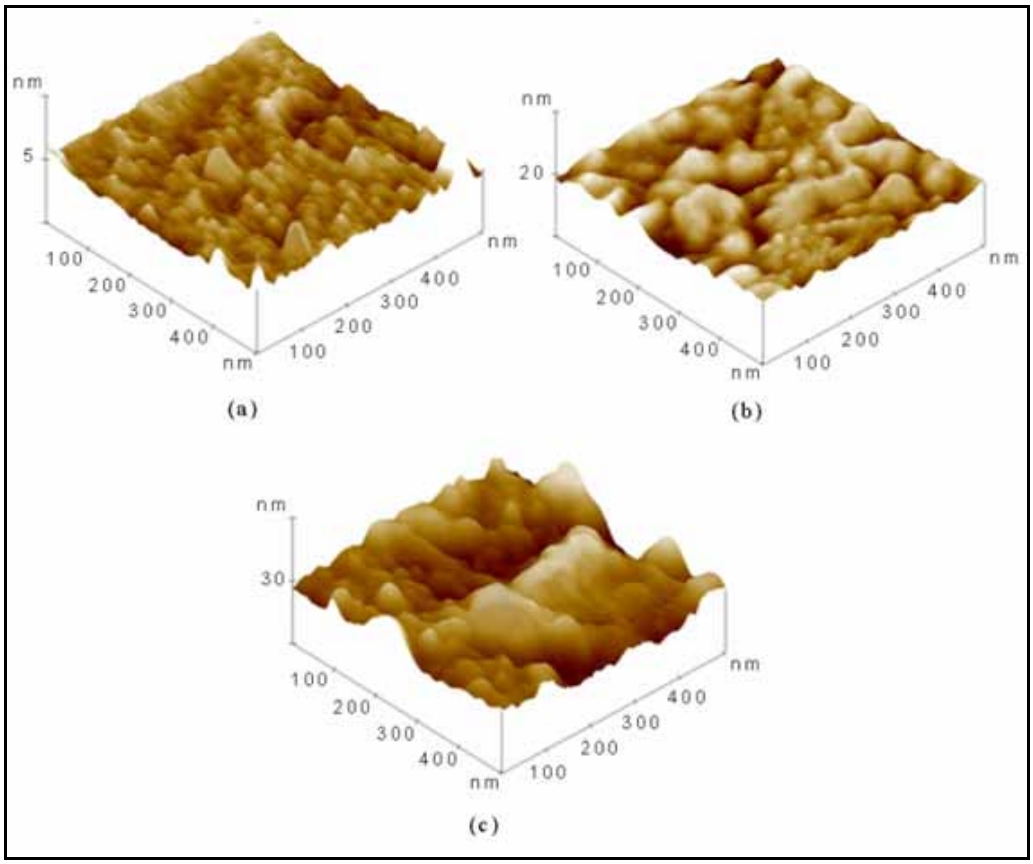

Fig. 22: AFM images for ITZO thin film deposited at different sputtering powers (a) 0.5 W/cm^2, (b) 1.5 W/cm^2 and (c) 2.5 W/cm^2. Note the different z-axis scales.

Power density (W/cm^2)	R_a (nm)
0.5	0.24
1.5	0.87
2.5	3.42

Table 7: Evolution of average surface roughness with power density

2-2-e. Optimized sputtering parameters

If we take into account all the previous results concerning the influence of the sputtering parameters on the thin films, we can conclude that:

i) The lowest resistivity in addition to the highest transparency was observed for thin film deposited at sputtering power density (P) of 0.5 W/cm^2.

ii) The highest transparency was observed for films deposited at $p_{O_2} > 0.1$ %.

iii) The lowest resistivity was obtained for films deposited at $p_{O_2} = 0.2$ %.

Hence, the optimized sputtering conditions for ITZO thin films leading to a high transparency and lowest resistivity are the following:

$P = 0.5$ W/cm^2, $p_{tot} = 1$ Pa, $p_{O_2} = 0.2$ % and $d_{t-s} = 7$ cm.

Indeed, these sputtering parameters lead to films with an x-ray amorphous structure where Zn^{2+} preferentially occupies interstitial position, enhancing, thereby, the carrier concentration [43].

2-3. ITZO thin films prepared under optimum conditions

We have applied the optimized sputtering conditions to deposit our ITZO thin films on glass (ITZO-Glass) or plastic substrates (ITZO-PET). Then, we have thoroughly studied the composition, the structure, the roughness, as well as the optical and the electrical properties of our thin films.

2-3-a. Composition

As usual, we have used the EPMA to determine the composition of our thin films. The composition of the ITZO thin films deposited under optimized sputtering conditions on glass and plastic substrates as well as the composition of the ceramic target used for deposition are indicated in Table 8. The final composition of films deposited on glass or plastic substrates is the same. However, there is some small loss of both Sn and Zn compared to ceramic target composition. This difference may be due to the different sputtering yields of the different species existing in the target [43].

Ceramic and thin film identification	**Ceramic final composition ± 0.005**	**Thin film (on glass) composition ± 0.005**	**Thin film (on plastic) composition ± 0.005**
ITZO	$In_{1.821}Sn_{0.090}Zn_{0.098}O_{3-\delta}$	$In_{1.838}Sn_{0.084}Zn_{0.078}O_{3-\delta}$	$In_{1.839}Sn_{0.082}Zn_{0.079}O_{3-\delta}$

Table 8: ITZO ceramic and thin film compositions determined by EPMA.

2-3-b. Morphology and structure

The Fig. 23 shows that the ITZO-PET film has a higher surface roughness (R_a = 1.46 nm) than the ITZO-Glass film (R_a = 0.24 nm). This is due to the higher roughness of the starting plastic substrate surface.

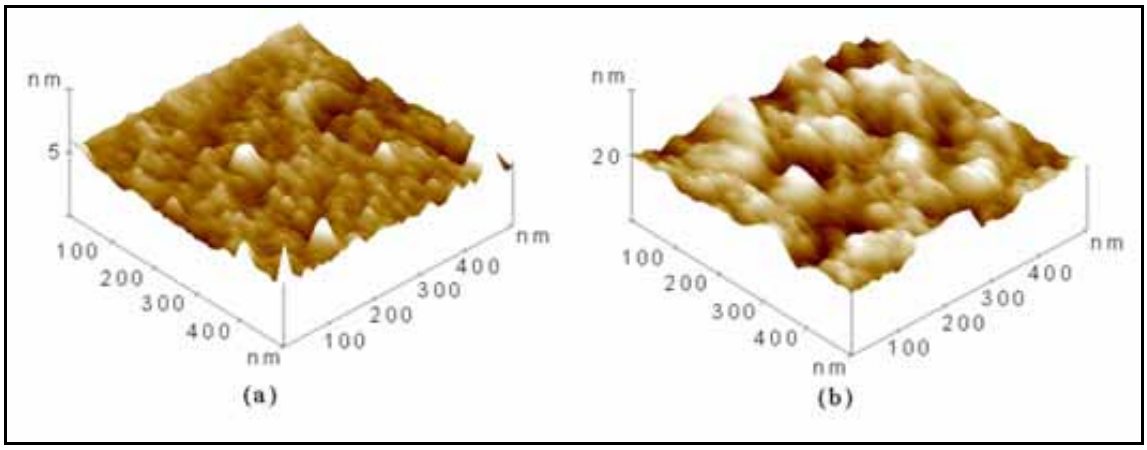

Fig. 23: AFM images for (a) ITO-Glass film and (b) ITZO-PET film. Note the different z-axis scales.

Both ITZO-Glass and ITZO-PET show an x-ray amorphous structure (Fig. 24). As was previously shown [paragraph (2-2-d)], this is due to the film deposition occurring at low power density (0.5 W/cm^2); the peaks observed are characteristic of the plastic (PET) substrate.

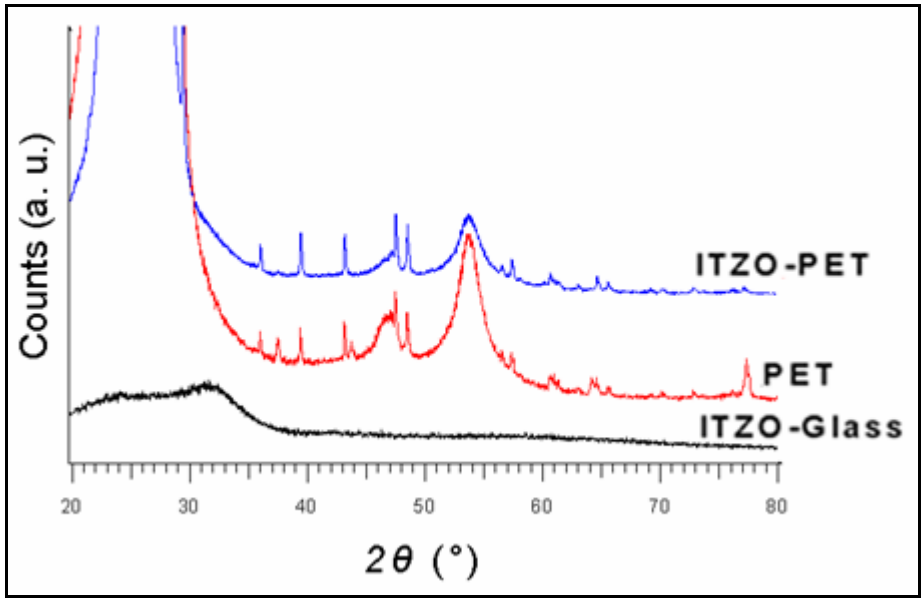

Fig. 24: XRD patterns for ITZO thin films deposited on glass substrate (ITZO-Glass), or on plastic substrate (ITO-PET). The XRD pattern of the PET substrate is given for comparison.

2-3-c. Optical properties

The evolution of the transmittance with the wavelength for ITZO films deposited on glass and plastic substrates is respectively shown on Figures 25 and 26.

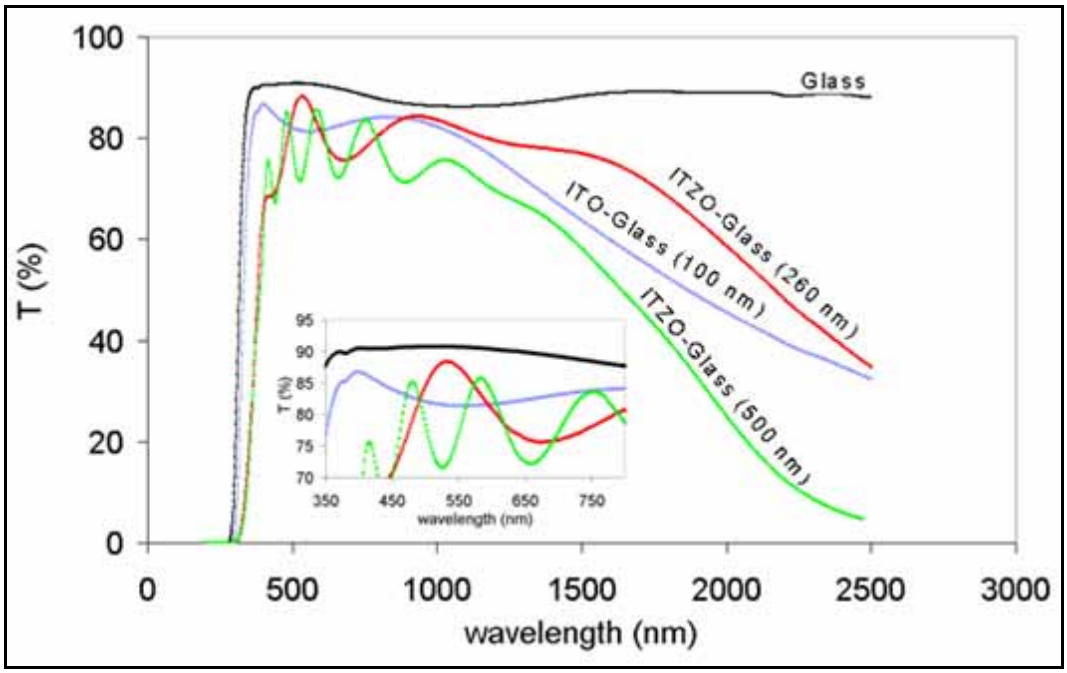

Fig. 25: Optical transmission for ITZO-Glass thin films having different thicknesses. The transparency of ITO-Glass is given for comparison.

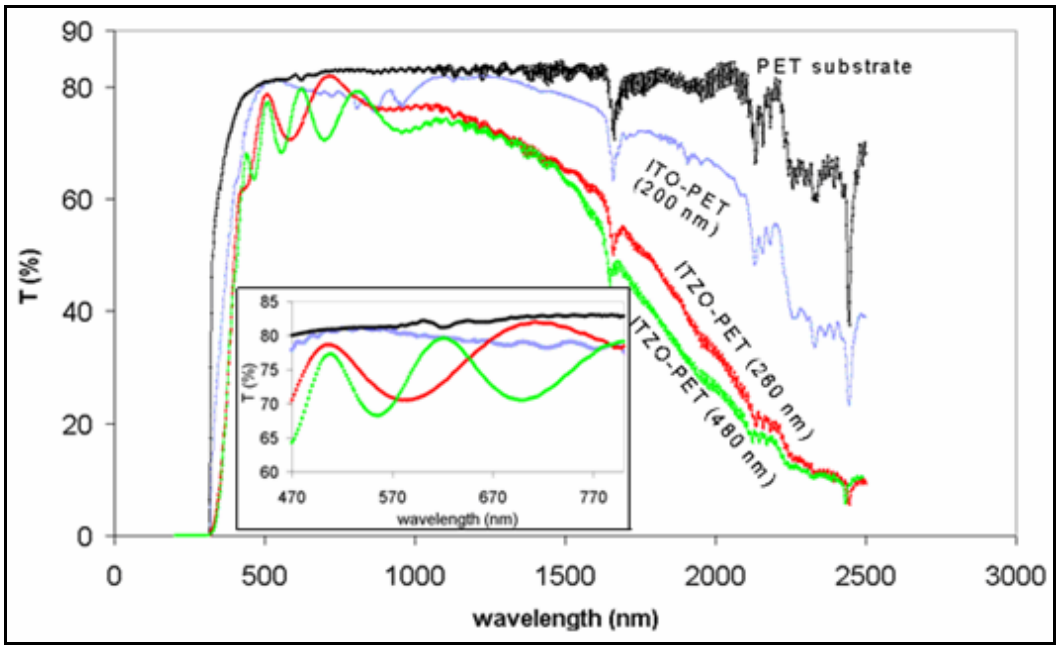

Fig. 26: Optical transmission for ITZO-PET thin films having different thicknesses. The transparency of ITO-PET is given for comparison.

For ITZO-glass (inset of Fig. 25), a high transparency (~ 88.5%) is observed for films having a thickness of ~ 260 nm, which is close to the value obtained for the commercial ITO deposited on glass (ITO-Glass). However, as expected, the transparency slightly decreased (~ 3 %) when the film thickness increased up to ~ 500 nm. In the case of ITZO-PET films (260 nm thick)(inset of Fig. 26), the transparency is of the same order than that observed for the commercial ITO which is deposited on PET. Transparencies of ~ 82 % and ~ 80 % are obtained for ITZO-PET films having respectively a thickness of ~ 260 nm and ~ 480 nm. Indeed, the transparency values are considered to be very high with respect to the plastic (PET) substrate transparency (~ 83 %) which of course limits the films transparency.

High IR reflectivity has been obtained for both ITZO-Glass and ITZO-PET thin films (Fig. 27). It reaches ~ 79 % for films deposited on glass, whereas ~ 87 % is attained for films deposited on plastic substrates. This is due to higher carrier concentration [as will be shown below (Table 9)], and hence, higher plasma frequency (ω_P), according to $\omega_P = (Ne^2 / \varepsilon_0 \varepsilon_\infty m_e^*)^{1/2}$ (equation 31, Chapter I), that induces higher IR reflectivity according to $R = 1 - \frac{2}{\omega_P \tau \varepsilon_\infty^{1/2}}$ (equation 42, Chapter I). ITZO films have always higher reflectivity in the IR range than the commercial ITO films because of higher values of carrier mobility (Table 9).

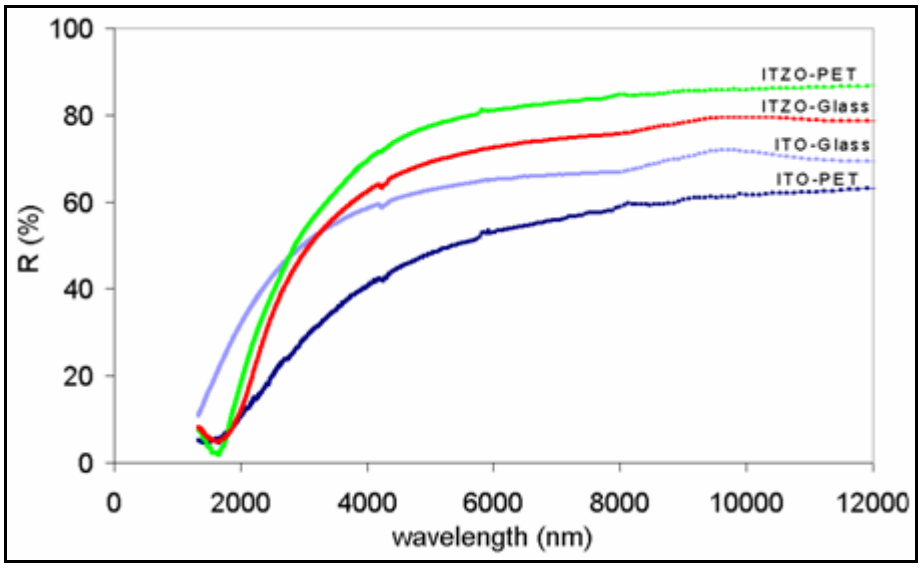

Fig. 27: Optical IR reflection for ITZO thin films deposited on glass (ITZO-Glass (260 nm) and plastic (ITZO-PET (260 nm)) substrates. The reflectivity curves of the commercial ITO-Glass (100 nm) and ITO-PET (200 nm) are given for comparison.

2-3-d. Electrical properties

Although we have a higher carrier concentration for ITZO-PET films than for ITZO-Glass having the same thickness (Table 9), the resistivity of ITZO-PET films is slightly higher (Table 9 and Fig. 28). Same tendency was also observed for sheet resistance. This behavior is due to the lower carrier mobility for the ITZO-PET thin films.

Sample	Thickness (nm) ± 20	Carrier conc. ($e^- cm^{-3}$) ± 5%	Mobility ($cm^2/V.s$) ± 5%	Resistivity (Ω.cm) ± 5%	Sheet resistance (Ω/□) ± 5%
ITZO-PET	260	5.30×10^{20}	25.2	4.68×10^{-4}	18.1
ITZO-PET	480	5.41×10^{20}	16.2	5.62×10^{-4}	14.0
ITZO-Glass	260	4.89×10^{20}	28.8	4.44×10^{-4}	17.2
ITZO-Glass	500	5.04×10^{20}	26.5	4.67×10^{-4}	9.1
Commercial					
ITO-PET	200	5.00×10^{20}	10.7	1.17×10^{-3}	58.5
ITO-Glass	100	8.43×10^{20}	18.6	3.99×10^{-4}	39.9

Table 9: Carrier concentration, mobility and resistivity for different thicknesses ITZO-PET and ITZO-Glass. The data of commercial ITO thin films (ITO-PET and ITO-Glass) are given for comparison.

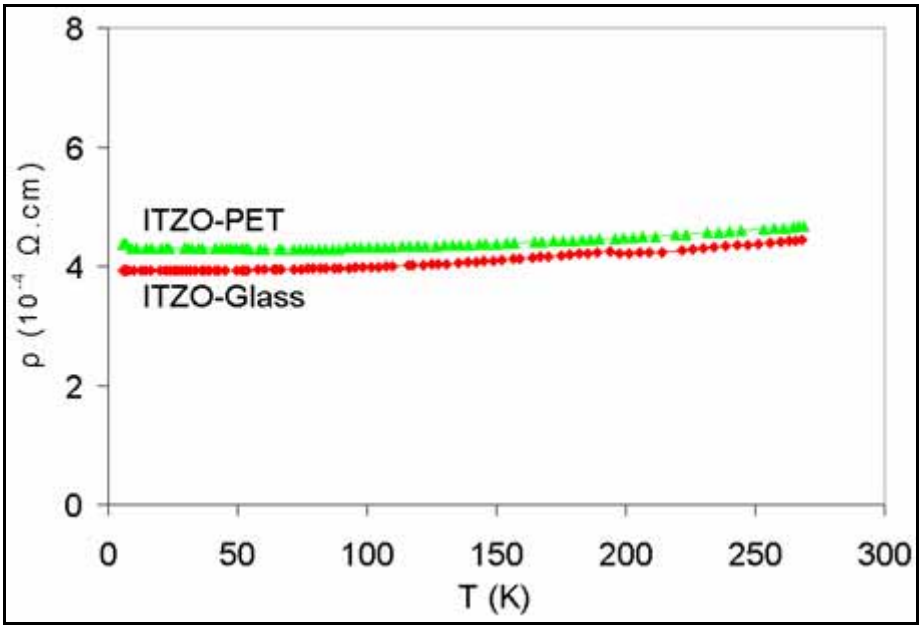

Fig. 28: Resistivity evolution with temperature for ITZO thin films deposited on plastic (ITZO-PET) and glass (ITZO-PET) substrate. Film thickness is 260 nm.

Table 9 also shows that the resistivity for ITZO films (260 nm) deposited on unheated-glass and/or plastic substrates is close to that observed for commercial ITO thin films which were deposited at ~ 200 °C on glass substrate (ITO-Glass), this temperature leading to well-crystallized films. The carrier concentration of our ITZO films is lower than that of ITO-Glass, but, they have higher mobility (Table 9). Most interestingly, the ITZO-PET thin films highlight lower resistivities, and therefore lower sheet resistances, than the commercial ITO-PET thin films which were similarly deposited at room temperature. This can be explained by the higher carrier concentration and mainly by the higher carrier mobility occurring in the ITZO-PET films [43].

2-4. Conclusions

We have prepared by RF magnetron sputtering ITZO thin films, deposited from optimized ITZO ceramic target. Most interestingly, the ITZO films deposited on polymer PET substrates have optoelectronic performances higher than their commercial ITO counterparts. Their amorphous character allows the occurrence of Zn^{2+} in interstitial positions leading to an increase of the carrier concentration, and therefore, of the conductivity. In crystallized ITZO films, the Zn^{2+} is in substitutional positions leading to a decrease of the conductivity. This behavior is different from that observed for ITO for which the conductivity increases as the crystallinity increases. This study shows the interest of such thin films on plastic substrates.

The optimized sputtering parameters in order to have high optoelectronic performances are the following:

$$P = 0.5\ W/cm^2,\ p_{O_2} = 0.2\ \%,\ P_{tot} = 1\ Pa,\ \text{and}\ d_{t\text{-}s} = 7\ cm.$$

The obtained amorphous films on both glass and plastic substrates have the same chemical composition and they have good accordance with the composition of the target. We have only observed a slight loss of Sn and Zn in the films due to the different sputtering yields of the different elements existing in the target. The morphology of thin films is dense with a very smooth surface

In term of optical properties, ITZO thin films highlighted a high visible transparency. It is ≥ 86 % for ITZO-Glass and ≥ 80 % for ITZO-PET; these values are

close to the transmittance value observed for the commercial ITO. Due to their high carrier-mobilities, the resistivity of ITZO films, deposited on glass and plastic substrate, is as low as that observed for commercial ITO-Glass. The lowest resistivity value reached $\sim 4.4 \times 10^{-4}$ Ω.cm for ITZO-Glass, while it reached $\sim 4.7 \times 10^{-4}$ Ω.cm for ITZO-PET. Interestingly, the ITZO thin films have lower resistivities, and therefore lower sheet resistances, than the commercial ITO-PET thin films due to the higher carrier concentration and mainly to the higher carrier-mobility of the ITZO-PET films. Moreover, the IR reflectivity of the ITZO films is always higher than that observed for the commercial ITO films because of the higher carrier-mobility occurring in ITZO.

Since our ITZO thin films deposited on plastic (ITZO-PET) substrates have higher performances than their commercial ITO counterpart (ITO-PET), they are good candidate for polymer-based optoelectronic devices, such as flexible ECD (ElectroChromic Devices), OLED, flexible solar cells etc. They are actually being tested for such device applications.

3. References

[1] J. I. Hamberg, C. G. Granqvist, *J. Appl. Phys.* **60** (1986) R123.

[2] C. G. Granqvist, *Appl. Phys. A* **52** (1991) 83.

[3] C. G. Granqvist, A. Hultaker, *Thin Solid Films* **411** (2002) 1.

[4] J. M. Phillips, R. J. Cava, G. A. Thomas, S. A. Carter, J. Kwo, T. Siegrist, J. J. Krajewski, J. H. Marshall, W. F. Peck, Jr., D. H. Rapkine, *Appl. Phys. Lett.* **67** (1995) 2246.

[5] B. G. Lewis, D. C. Paine, *MRS Bull*. **25** (2000) 22.

[6] A. J. Freeman, K. R. Poeppelmeier, T. O. Mason, R. P. H. Chang, T. J. Marks, *MRS Bull*. **25** (2000) 45.

[7] R. Wang, L. L. H. King, A. W. Sleight, *J. Mater. Res.* **11** (1996) 1659.

[8] C. Ktlic, A. Zunger, *Phys. Rev. Lett.* **88** (2002) 95501.

[9] K. Nomura, H. Ohta, K. Ueda, T. Kamiya, M. Hirano, H. Hosono, *Science* **300** (2003) 1269.

[10] B. Yaglioglu, Y. Huang, Hy. Y. Yeom, D. C. Paine, *Thin Solid Films* **496** (2006) 89.

[11] J. C. C. Fan, J. B. Goodenough, *J. Appl. Phys.* **48** (1977) 3524.

[12] E. Fortunato, A. Pimentel, A. Gonçalves, A. Marques, R. Martins, Thin Solid Films **502** (2006) 104.

[13] T. Minami, T. Kakumu, Y. Takeda, S. Takata, *Thin Solid Films* **290-291** (1996) 1.

[14] N. Naghavi, A. Rougier, C. Marcel, C. Guéry, J. B. Leriche, J .M. Tarascon, *Thin Solid Films* **360** (2000) 233.

[15] N. Naghavi, C. Marcel, L. Dupont, A. Rougier, J. B. Leriche, C. Guéry, *J. Mater. Chem.* **10** (2000) 2315.

[16] N. Naghavi, C. Marcel, L. Dupont, C. Guéry, C. Maugy, J.M. Tarascon, *Thin Solid Films* **419** (2002) 160.

[17] T. Sasabayashi, N. Ito, E. Nishimura, M. Kon, P.K. Song, K. Utsumi, A. Kaijo, Y. Shigesato, *Thin Solid Films* **445** (2003) 219.

[18] Y. S. Jung, J. Y. Seo, D. W. Lee, D. Y. Jeon, *Thin Solid Films* **445** (2003) 63.

[19] N. Ito, Y. Sato, P. K. Song, A. Kaijio, K. Inoue, Y. Shigesato, *Thin Solid Films* **496** (2006) 99.

[20] D. Y. Ku, I. H. Kim, I. Lee,K. S. Lee, T. S. Lee, J. H. Jeong, B. Cheong, Y. J. Baik, W. M. Kim, *Thin Solid Films* **515** (2006) 1364.

[21] T. Minami, T. Kakumu, S. Takata, J. Vac. Sci. Technol., A 14 (3) (1996) 1704.

[22] N. Naghavi, L. Dupont, C.Marcel, C. Maugy, B. Laïk, A. Rougier, C.Guéry, J.M. Tarascon, Electrochim. Acta 46 (2001) 2007.

[23] T. Moriga, D. D. Edwards, T. O. Mason, *J. Am. Ceram. Soc.* **81** (1998) 1310.

[24] D. H. Park, K. Y. Son, J. H. Lee, J. J. Kim, J. S. Lee, *Solid State Ionics* **172** (2004) 431.

[25] G. B. Palmer, K. R. Poeppelmeier, T. O. Mason, *Chem. Mater.* **9** (1997) 3121.

[26] A. Ambrosini, G. B. Palmer, A. Maignan, , K. R. Poeppelmeier, M. A. Lane, P. Brazis, C. R. Kannewurf, T. Hogan, T. O. Mason, *Chem. Mater.* **14** (2002) 52.

[27] A. Ambrosini, S. Malo, K. R. Poeppelmeier, M. A. Lane, C. R. Kannewurf, T. O. Mason, *Chem. Mater.* **14** (2002) 58.

[28] T. Minami, T. Kakumu, K. Shimokawa, S. Takata, *Thin Solid Films* **317** (1998) 318.

[29] T. Minami, T. Yamamoto, Y. Toda, T. Miyata, *Thin Solid Films* **373** (2000) 189.

[30] H. M. Ali, *phys. stat. sol. a* **202** (2005) 2742.

[31] M. Russak, J. De Carlo, *J. Vac. Sci. Technol.* **1** (1983) 1563.

[32] H. Kim A. Piqué, J. S. Horwitz, H. Mattoussi, H. Murata, Z. H. Kafafi, D. B. Chrisey, *Appl. Phys. Lett.* **74** (1999) 3444.

[33] T. O. Mason,a G. B. Gonza´lez,a J.-H. Hwangb, D. R. Kammler, *Phys. Chem. Chem. Phys.* **5** (2003) 2183.

[34] H. Kim, C. M. Gilmore, *J. Appl. Phys.* **86** (1999) 6451.

[35] H. Enoki, J. Echogoya, H. suto, *J. Mater. Sci.* **26** (1991) 4110.

[36] I. Saadeddin, B. Pecquenard, G. Campet," Zn and Sn doped In_2O_3 ceramics: structural and electrical characterization", *to be published.*

[37] Patent under deposition (demand no. 2,547,091)

[38] I. Saadeddin, H. S. Hilal, B. Pecquenard , J. Marcus, A. Mansouri, C. Labrugere, M. A. Subramanian, G. Campet, *Solid state Sci.* **8** (2006) 7.

[39] M. Marezio, *Acta Cryst.* **20** (1966) 723.

[40] J. H. W. De Witt, *J. Solid State Chem.* **20** (1977) 143.

[41] R D. Shannon, *Acta Cryst. A* **32** (1976) 751.

[42] C. Marcel, *Ph.D. thesis*, Bordeaux 1 University, Bordeaux, France (1998).

[43] I. Saadeddin, B. Pecquenard, J. P. Manaud, G. Campet, "Synthesis and characterization of Zn and Sn doped In_2O_3 thin films deposited on glass and plastic PET substrates" *to be published.*

[44] E. Burstein, *Phys. Rev.* **93** (1954) 632.

[45] T. S. Moss, *Proc. Phys. Soc. London Sect.* B **67** (1954) 775.

General conclusions and perspectives

❖ As we have already stated in the general introduction, although using sputtering techniques allow us to obtain high quality thin films (homogeneous and smooth surface), no commercial ATO (SnO_2:Sb) targets for RF or DC sputtering exist, which was attributed to antimony departure during target sintering. In this thesis, we have shown that it is possible to prepare dense and conductive ATO ceramic targets, suitable for sputtering, without antimony departure. This is achieved for an initial antimony content not exceeding 0.012 at. %. However, co-doping SnO_2 with quasi equal amounts of Sb and Zn, forming AZTO (SnO_2:Sb:Zn) ceramics, allowed us to introduce higher amounts of antimony due to the isovalent substitution of three Sn^{4+} by two Sb^{5+} and one Zn^{2+}. The latter reduces the number of free electrons produced by doping SnO_2 with Sb^{5+}, allowing thereby a modulation of their concentration. In addition, the presence of neutral oxygen vacancies ($\square_\delta$) due to Sn^{4+} substitution by Zn^{2+} promotes mass transport at the grain boundaries during the ceramic sintering and thereby enhances the density (~ 92 % of the SnO_2 theoretical density). That led to an enhancement of the carrier mobility. Consequently, the highest conductivity is observed for AZTO ceramics.

The sputtered ATO and AZTO thin films have a good accordance in term of composition with their corresponding ceramic targets. They have a dense morphology with a smooth surface and they are polycrystalline with the rutile structure of SnO_2. For both thin films, the transmittance in the visible reaches ~ 90%.

In the case of ATO thin films, PD-annealing allowed an increase of Sb^{5+} content (oxidation of part of Sb^{3+}) enhancing therefore the carrier concentration. That induces the occurrence of a high reflectivity (reaching ~ 60%) in the infrared range and a low resistivity (2.1×10^{-3}). Due to these characteristics, our ATO thin films were successfully used as transparent heat reflectors (transparent in the visible and reflective in the infrared) in high temperature insert (HTI) cell, to study materials having high temperature critical points.

Even if Sb amount in the AZTO thin films is higher than in ATO (5 % instead of 1 %), we were able to modulate the conductivity by co-doping with Zn^{2+}. This leads to a carrier concentration one order of magnitude lower than that for ATO. The ability to modulate the conductivity in ATZO films allowed us to produce transparent and resistive AZTO layers for specific applications. In particular, the AZTO thin films were

successfully used as transparent micro-furnaces in Alice Like Insert (ALI) cells to study materials having near ambient critical points (like CO_2 and SF_6).

❖ Commercial ITO based target are usually prepared by using hot pressing procedure, which is known to be highly expensive. However, following a similar strategy than that used for SnO_2, co-doping In_2O_3 with Sn^{4+} and Zn^{2+}, forming ITZO ceramic (In_2O_3:Sn:Zn), allowed us to achieve a straightforward target preparation by direct sintering the lightly pressed (hand pressed) powder mixture in an appropriate alumina crucible, without using any cold or hot pressing procedure [patent under deposition, demand no. 2,547,091]. This will markedly reduce the manufacturing cost of commercial ITO based targets and particularly of large area targets intended for industrial coatings. The obtained ITZO ceramic targets have a density as high as ~ 92 % of the In_2O_3 theoretical density.

From optimized ITZO ceramic target, we have prepared by RF magnetron sputtering ITZO thin films, deposited on glass and PET substrates. Most interestingly, the ITZO films deposited on polymer PET have opto-electronic performances higher than their commercial ITO counterparts. Their amorphous character allowed the occurrence of Zn^{2+} in interstitial position leading to an increase of the carrier concentration, and therefore, of the conductivity. In crystallized ITZO film, Zn^{2+} preferentially occupy substitutional positions leading to a decrease of the conductivity. This behavior is different from that observed for ITO for which the conductivity increases as the crystallinity increases. This study shows the interest of such thin films on plastic substrates.

Since our ITZO thin films deposited on plastic PET substrates have higher performances than their commercial ITO counterpart (ITO-PET), they are good candidate for polymer-based opto-electronic devices, such as flexible ECD (ElectroChromic Devices), flexible solar cells etc. They are actually being tested for such device applications.

Further additional studies will be achieved in order to complete this work. For instance EXAFS and Raman spectroscopy, on the one hand, and Mössbauer spectroscopy, on the other hand, will allow us to identify the local structure in the amorphous ITZO films (sites of Zn) and to confirm the presence of both Sb^{3+} and Sb^{5+} in ATO, respectively.

Annexes

Annex 1

General review of electrical and optical properties for main TCOs

The electrical and optical properties of TCOs films are strongly dependent on dopant concentration and different growth parameters, commonly considered in different deposition techniques, such as: substrate temperature, film thickness, post-deposition annealing, gas flow rates, composition of spray solutions, sputtering power, etc. Table 1 summarizes the electrical and optical properties of some prominent TCOs films. It shows how electrical and optical properties, of these films, are affected by deposition techniques employed under otherwise optimal conditions.

Material	**Deposition technique**	**Electrical conductivity (Ω^{-1} cm^{-1})**	**Carrier concentration (cm^{-3})**	**Hall mobility (cm^2 V^{-1} s^{-1})**	**Transmission (visible region)**	**Reflection (infrared region)**	**Reference**
Cd_2SnO_{4-x}	Sputtering	1.1×10^2	2.0×10^{19}	—	83	—	[1]
Cd_2SnO_{4-x}	Sputtering	2.0×10^3	5.0×10^{20}	40	>80	80	[2]
Cd_2SnO_{4-x}	Sputtering	1.5×10^3	—	20	—	—	[3]
Cd_2SnO_{4-x}	Sputtering	2.0×10^3	5.0×10^{20}	22	93	—	[4]
Cd_2SnO_{4-x}	Sputtering	—	5.0×10^{19}	40	90	—	[5]
Cd_2SnO_{4-x}	Sputtering	6.5×10^3	1.0×10^{21}	—	85	90	[6, 7]
Cd_2SnO_{4-x}	Sputtering	—	—	—	90	60	[8]
Cd_2SnO_{4-x}	Sputtering	—	—	—	>80	—	[9]
In_2O_3:F	CVD	3.5×10^3	—	—	>85	—	[10]
In_2O_3:F	Ion plating	5.7×10^3	3.2×10^{21}	11	—	—	[11]
In_2O_3:Zn	Sputtering	2.9×10^3	7.65×10^{20}	—	—	—	[12]
In_2O_{3-x}	Thermal evaporation	5.0×10^3	4.0×10^{20}	70	>90	—	[13]
In_2O_{3-x}	Spray	6.0×10^3	4.2×10^{19}	89.7	—	—	[14]
ln_2O_{3-x}	Spray				>90	—	[15]
In_2O_{3-x}	Sputtering	3.0×10^3	3.6×10^{20}	—	—	—	[16]

Material	Deposition technique	Electrical conductivity (Ω^{-1} cm^{-1})	Carrier concentration (cm^{-3})	Hall mobility (cm^2 V^{-1} s^{-1})	Transmission (visible region)	Reflection (infrared region)	Reference
In_2O_{3-x}	Sputtering	—	—	—	80	—	[17]
In_2O_{3-x}	Reactive evaporation	5.0×10^{2}	3.5×10^{19}	25-60	—	—	[18]
In_2O_{3-x}	Reactive evaporation	3.0×10^{3}	1.0×10^{20}	—	—	—	[19]
In_2O_{3-x}	Ion plating	6.7×10^{3}	7.0×10^{20}	70	—	—	[20]
ITO	e-beam evaporation	2.0×10^{3}	5.8×10^{20}	16.8	>90	—	[21]
ITO	e-beam evaporation	4.1×10^{3}	8.0×10^{20}	30	90	>80	[22]
ITO	e-beam evaporation	5.0×10^{3}	7.0×10^{20}	24	—	—	[23]
ITO	e-beam evaporation	2.3×10^{4}	1.4×10^{21}	103	—	—	[24]
ITO	Reactive evaporation	1.6×10^{3}	7.0×10^{20}	15	—	—	[25]
ITO	e-beam evaporation	—	—	—	95	>90	[26]
ITO	e-beam evaporation	—	—	—	90	—	[27]
ITO	Post-oxidized	5.0×10^{2}	1.0×10^{20}	20	—	—	[28]
ITO	CVD	5.0×10^{3}	1.0×10^{21}	10	90	—	[29]
ITO	Spray	—	1.0×10^{21}	70	>85	>85	[30]
ITO	Spray	5.5×10^{3}	1.0×10^{21}	30	—	—	[14]
ITO	Spray	2.0×10^{3}	5.0×10^{20}	30	—	—	[18]
ITO	Spray	1.0×10^{4}	2.0×10^{20}	33	82	—	[31]
ITO	Spray	4.0×10^{3}	6.0×10^{20}	36	—	—	[32]
ITO	Spray	—	—	—	92	—	[33]
ITO	Spray	—	—	—	90	—	[34]
ITO	Spray	—	—	—	>85	85	[35]
ITO	Spray	—	—	—	88	90	[36]

Material	Deposition technique	Electrical conductivity (Ω^{-1} cm^{-1})	Carrier concentration (cm^{-3})	Hall mobility (cm^2 V^{-1} s^{-1})	Transmission (visible region)	Reflection (infrared region)	Reference
ITO	Spray	—	—	—	>85	—	[37]
ITO	Sputtering	—	1.0×10^{20}	12	—	—	[38]
ITO	Sputtering	2.7×10^{3}	7.0×10^{20}	24.5	—	—	[39]
ITO	Sputtering	8.0×10^{3}	1.0×10^{21}	43	—	—	[40]
ITO	Sputtering	2.5×10^{3}	1.0×10^{21}	35	—	—	[41]
ITO	Sputtering	1.5×10^{3}	8×10^{20}	12	—	—	[42]
ITO	Sputtering	1.4×10^{3}	7.0×10^{20}	16	—	—	[43]
ITO	Sputtering	5.0×10^{3}	6.2×10^{20}	48.6	—	—	[44]
ITO	Sputtering	—	—	—	90	—	[45]
ITO	Sputtering	—	—	—	80	—	[46]
ITO	Sputtering	—	—	—	90	90	[47]
ITO	Sputtering	—	—	—	90	84	[48]
ITO	Sputtering	—	—	—	95	90	[49]
ITO	Sputtering	—	—	—	85	80	[8]
ITO	Sputtering	—	—	—	95	—	[50]
ITO	Sputtering	—	—	—	92	—	[51]
ITO	Sputtering	—	—	—	—	—	[52]
ITO	Sputtering	—	—	—	85	>80	[53]
ITO	CVD	6.0×10^{3}	8.8×10^{20}	43	90-95	90	[54]
ITO	Ion plating	5.0×10^{3}	9.1×10^{20}	53.6	—	—	[55]
ITO	Ion plating	1.0×10^{3}	—	—	—	—	[56]
ITO	Sol-gel	3.0×10^{1}	—	—	—	—	[57]
ITO:F	Sputtering	1.5×10^{3}	6.0×10^{20}	16	>80	70	[58]
SnO_2:As	CVD	6.0×10^{3}	9.0×10^{20}	45	90	—	[59]
SnO_2:F	Spray	2.0×10^{3}	1.5×10^{21}	17	—	—	[60]
SnO_2:F	Spray	2.0×10^{3}	4.6×10^{20}	27.7	>80	90	[61]
SnO_2:F	Spray	—	3.5×10^{20}	46	>90	85	[62]

Material	Deposition technique	Electrical conductivity (Ω^{-1} cm^{-1})	Carrier concentration (cm^{-3})	Hall mobility (cm^2 V^{-1} s^{-1})	Transmission (visible region)	Reflection (infrared region)	Reference
SnO_2:F	Spray	1.0×10^{5}	1021	20	—	—	[63]
SnO_2:F	Spray	—	5.0×10^{20}	50	—	—	[64]
SnO_2:F	Spray	2.0×10^{3}	4.4×10^{20}	30	—	—	[65]
SnO_2:F	Spray	2.0×10^{3}	1.2×10^{21}	10	—	—	[66]
SnO_2:F	Spray	—	—	—	91	80	[67]
SnO_2:F	Spray	—	—	—	>90	90	[62]
SnO_2:F	Spray	—	—	—	90	—	[68]
SnO_2:F	Spray	—	—	—	88	85	[69]
SnO_2:F	Spray	—	—	—	80-90	—	[70]
SnO_2:Sb	Spray	5.0×10^{2}	2.0×10^{20}	15	80	—	[71]
SnO_2:Sb	Spray	1.0×10^{3}	4.0×10^{20}	17	—	—	[14]
SnO_2:Sb	Spray	1.0×10^{3}	7.0×10^{20}	10	85	—	[72]
SnO_2:Sb	Spray	—	—	—	80	84	[69]
SnO_2:Sb	Spray	—	—	—	88	80	[36]
SnO_2:Sb	Sputtering	5.0×10^{2}	3.0×10^{20}	10	80	—	[73]
SnO_{2-x}	Sputtering	1.6×10^{2}	1.3×10^{20}	7.72	95	—	[74]
SnO_{2-x}	Sputtering	1.0×10^{2}	—	—	80	—	[75]
SnO_{2-x}	Sputtering	1.0×10^{2}	1.2×10^{20}	—	—	—	[76]
SnO_{2-x}	Sputtering	3.0×10^{2}	—	—	—	—	[77]
SnO_{2-x}	Sputtering	1.6×10^{0}	2.7×10^{18}	3.64	—	—	[78]
SnO_{2-x}	Sputtering	1.1×10^{4}	—	—	—	—	[79]
SnO_{2-x}	Sputtering	—	—	—	75	55	[80]
SnO_{2-x}	Spray	4.0×10^{1}	1.0×10^{20}	8	80	—	[71]
SnO_{2-x}	Spray	3.0×10^{2}	1.5×10^{20}	10	—	—	[60]
SnO_{2-x}	Spray	2.5×10^{2}	1.3×10^{20}	11	—	—	[81]
SnO_{2-x}	Spray	—	4.0×10^{19}	53	—	—	[82]
SnO_{2-x}	Spray	—	1.5×10^{20}	8.5	—	—	[83]

Material	Deposition technique	Electrical conductivity (Ω^{-1} cm^{-1})	Carrier concentration (cm^{-3})	Hall mobility (cm^2 V^{-1} s^{-1})	Transmission (visible region)	Reflection (infrared region)	Reference
SnO_{2-x}	Spray	—	—	—	90	—	[84]
SnO_{2-x}	Spray	—	—	—	82	—	[85]
SnO_{2-x}	Spray	—	—	—	97	—	[68]
SnO_{2-x}	CVD	2.6×10^{2}	1.3×10^{20}	12.8	—	—	[86]
SnO_{2-x}	Laser evaporation	3.3×10^{2}	—	—	—	—	[87]
$Zn_{1+x}O$	Reactive evaporation	1.0×10^{3}	1.0×10^{20}	10	88	—	[88]
$Zn_{1+x}O$	CVD	1.0×10^{3}	1.0×10^{21}	14	—	—	[89]
$Zn_{1+x}O$	CVD	—	—	—	>90	—	[90]
$Zn_{1+x}O$	Sputtering	5.0×10^{2}	5.0×10^{19}	8	—	—	[91]
$Zn_{1+x}O$	Reactive evaporation	2.9×10^{2}	$4\text{-}12\times10^{19}$	oct-40	—	—	[92]
$Zn_{1+x}O$	Spray	—	—	—	70	—	[93]
ZnO:Al	Sputtering	1.0×10^{2}	4.7×10^{20}	1.47	90	—	[94]
ZnO:Al	Sputtering	4×10^{3}	8.0×10^{20}	20	—	—	[95]
ZnO:Al	Sputtering	4×10^{3}	1.0×10^{21}	30-40	—	—	[96]
ZnO:Al	Sputtering	7×10^{3}	1.0×10^{21}	25	—	—	[97]
ZnO:Al	CVD	3.0×10^{3}	8.0×10^{20}	35	85	90	[98]
ZnO:Ga	Sputtering	1.0×10^{3}	1.0×10^{21}	10	>85	—	[99]
ZnO:In.	Spray	1.0×10^{3}	2.2×10^{20}	24	—	—	[100]
ZnO:In	Sputtering	5.0×10^{1}	7.0×10^{19}	1.9	>80	—	[101]
ZnO:In	Sputtering	3.0×10^{2}	1.0×10^{20}	12.6	—	—	[94]

Table 1: Electrical and optical properties of the main prominent TCO thin films.

By taking into account the results summarized on Table 1, the following considerations and conclusions on electrical and optical properties may be mentioned:

i) concerning electrical properties:

1) All main TCO films are n-type semiconductors.
2) Electrical properties are significantly affected by substrate temperature (during deposition or post annealing). With higher substrate temperature, the grain size increases. The carrier (i.e. electron) mobility and conductivity are consequently enhanced. Moreover, by post annealing in reducing atmospheres, more oxygen vacancies are created, enhancing even more the conductivity [1, 6, 33, 34, 60, 95].
3) Doping of transparent conducting oxide films with suitable impurities (e.g. $Sb5^{+}$ [61] and F^{-}[67] for SnO_2 and Sn^{4+} [22, 25, 28, 29, 34] and F^{-}[10] for In_2O_3), markedly improves the electrical properties of these oxide films. Indeed, this improvement is due to the expected increase of the concentration of the mobile electrons in the conduction band.
4) The fact that the carrier mobility depends on type of dopant used and its concentration is exhibited in Table 1.
5) As the carries concentration increases, the mobility increases initially and rapidly decreases due to electron-electron scattering [61, 71].
6) As expected, the upper limit of electron density is determined by dopant solubility. When solubility limit is overtaken, the dopants form clusters in the lattice. Such clusters act as additional scattering centers which also reduce the carrier mobility and, therefore, the conductivity.
7) In dense films having carrier concentrations higher than 10^{20} cm^{-3}, both carrier concentration and mobility are nearly independent of temperature especially at lower temperature ranges [22, 71], indicating a degenerate semiconductor behavior. The conduction mechanism is governed by carrier concentration (i.e. the concentration of the mobile electrons in the conduction band, as quoted above). In general, when carrier concentration is lower than 10^{18} cm^{-3}, the conduction is mainly limited by grain boundary scattering. On the other hand, when carrier concentration is higher than 10^{20} cm^{-3}, ionized donor-center scattering may become the dominant scattering mechanism.

8) A number of different conduction mechanisms have been proposed for films having carrier concentrations between 10^{18} and $10^{21,}$ cm^{-3}. Much work is still needed to fully understand the different scattering mechanisms involved in the conduction process in these oxide films.

9) The film properties are influenced by oxygen diffusion process either into the film or out of it [13, 73, 74, 77]. Post-deposition annealing in different atmosphere such as air, vacuum, nitrogen, hydrogen, formatting gas of H_2 and N_2, etc. may further improve film electrical properties [35, 38-40, 81, 84].

ii) <u>concerning optical properties:</u>

1) Both direct and indirect allowed transitions exist in these materials. The values of the corresponding energy band gaps strongly depend on the carrier concentration, which in turn depends on the deposition conditions [46, 71, 101]. The absorption edge shifts towards higher energy with an increase in the carrier concentration. The shift in band edge was generally explained on the basis of the Burstein-Moss model [102, 103], for materials where the electron density, *N*, far exceeds the Mott critical density [104], which is given by

$$N >> (0.25\, m_e^* e^2 / \varepsilon_0 \hbar^2)^3 \qquad (1)$$

where m_e^* is the electron effective mass, e is the electron charge, ε_0 is the permittivity of free space and $\hbar = h/2\pi$ is Planck's constant.

2) The substrate temperature, applied during films growth, significantly affects the optical properties [1, 25, 33, 73].

3) Tin-doped indium oxide and fluorine or antimony-doped tin oxide films are widely recommended for practical device applications. ITO films are usually preferred for high grade applications, i.e. opto-electronics, while fluorine or antimony-doped tin oxide films are normally used to coat large surfaces, e.g. heat mirrors, because of the lower cost of the tin oxide. Transmission characteristics of doped SnO_2 films are comparable to these of ITO films in the visible region. However, the reflection properties of ITO films are superior to those of doped SnO_2 films in the infrared region. Moreover, transmission

properties of ITO films are less sensitive to film thickness. This means that thicker films of ITO with lower sheet resistances can be used without significantly affecting the optical quality of these films. The better features of ITO films are mainly due to the fact that these films can be prepared with higher carrier concentrations and mobilities.

4) Aluminum-doped ZnO films are emerging as an alternative candidate for transparent conducting applications. These films have shown extremely promising results in term of transmission and reflection values of the order of 85 and 90% [94, 98]. These results resemble are close to those obtained with best ITO and SnO_2:F films, currently used in a variety of applications.

Annex 2

Determination of thin film resistivity using four probe technique

For a rectangular shaped sample (Fig. 1), the resistance R expressed in Ω is given by

$$R = \rho(l/bt) \tag{2}$$

where l is the length, b is the width and t *is* the thickness of the sample. If $l=b$, equation (2) becomes

$$R = \rho/t = R_s \tag{3}$$

The quantity R_s is known as the sheet resistance and it is the resistance of one square of the film and is independent of the size of the square. The sheet resistance is expressed in ohms/square (Ω/□). The most commonly used method for measuring the sheet resistance R_s is a four-point probe technique. A typical schematic setup is shown in Fig. 1 (b). When the probes are placed on a material of semi-infinite volume, the resistivity is given by [105]

$$\rho = \frac{V}{I}\frac{2\pi}{1/d_1 + 1/d_2 - 1/(d_1+d_2) - 1/(d_2+d_3)}.$$

When $d_1 = d_2 = d_3 = d$,

$$\rho = \frac{V}{I}2\pi d\,. \tag{4}$$

If the material is in the form of an infinitely thin film resting on an insulating support, equation (4) leads to [105]:

$$\rho = \frac{V}{I}\frac{\pi t}{\ln 2}$$

or

$$\frac{\rho}{t} = R_s = 4.53V/I\ . \tag{5}$$

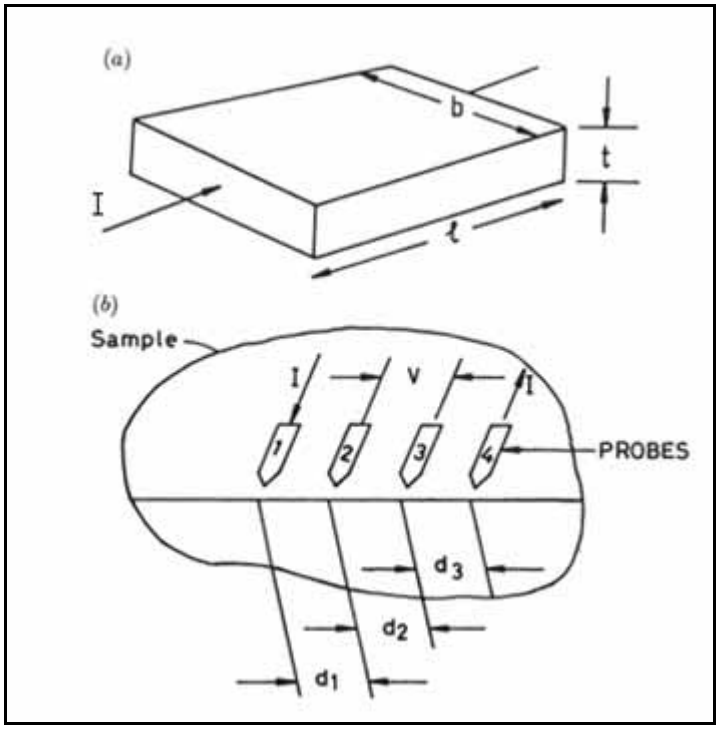

Fig. 1: Schematic diagram showing: (a) Definition of resistivity and sheet resistance. (b) the four-point probe technique.

Annex 3

Hall Effect basic concept

When a current is passed through a slab of a material in the presence of a transverse magnetic field ***B*** (Fig. 2), the electrons run in the negative x-direction with a speed ***v*** and experience a force (the *Lorentz* force) $\boldsymbol{F} = -q\boldsymbol{v}\times\boldsymbol{B}$ in the negative *y*-direction. Due to this event, a small potential difference, known as the Hall voltage (V_H), is developed (between face 1 and face 2), in a direction perpendicular to both the current and the magnetic field. Face 1 is positive for p-type samples and negative for n-type samples. The Hall voltage is expressed as:

$$V_H = R_H I(B/t) \tag{6}$$

where V_H is the Hall voltage, B is the magnetic field and I is the current through the

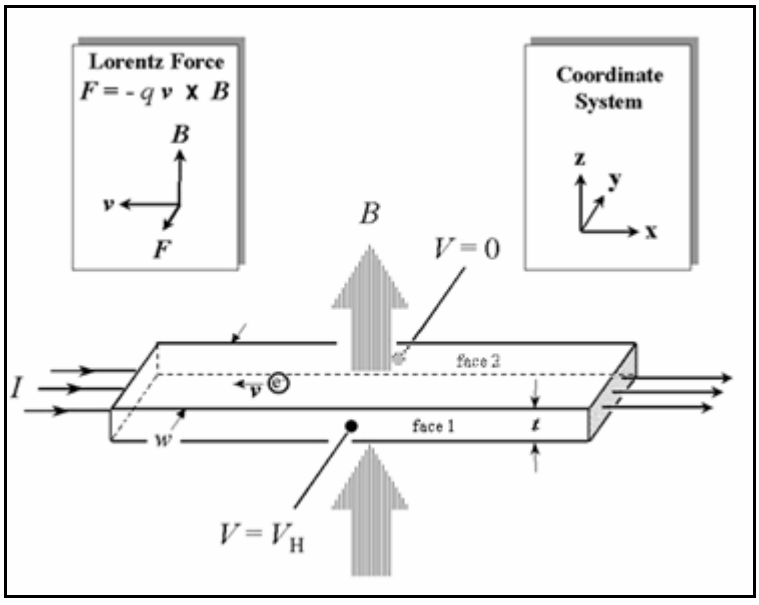

Fig. 2: Hall Effect Phenomena.

sample. R_H is the Hall coefficient and is related to the carrier density, N, according to the relation

$$R_H = r_H(1/Ne) \tag{7}$$

where r_H is the Hall scattering factor and e the charge of carriers; e is negative (positive) if the carriers are electrons (holes). The value of r_H mainly depends on the geometry of the scattering surface. Normally, r_H does not depart very significantly from unity. For n-type semiconductors, R_H is negative while for p-type it is positive. Hall Effect measurements, combined with conductivity measurement, enable calculation of mobility of charge carriers. Indeed, the well known relation $\mu = \sigma / Ne$ and relation (7) lead to

$$\mu = R_H \sigma . \tag{8}$$

The mobility of charge carriers determined by Hall measurements is known as Hall mobility (μ_H).

Annex 4

Electrical conduction in different TCO thin film materials

a. Electrical conduction in polycrystalline semiconducting materials.

The expression for mobility of charge carriers ($\mu = \frac{e\tau}{m^*}$) depends on the relaxation time, τ, which in turn depends on the drift velocity and the mean free path of the charge carriers. These parameters depend on the mechanism by which the carriers are scattered by lattice imperfections.

The total mobility μ_t is written as

$$\frac{1}{\mu_t} = \sum_i \frac{1}{\mu_i} \tag{9}$$

where μ_i is related to the *i*th scattering mechanism. A brief account of various scattering mechanisms for electron (hole) carriers involved in n-type (p-type) semiconducting materials is given here.

(i) Phonon scattering.

In addition to the various imperfections (lattice distortions induced by doping, grain boundaries, etc.), phonons (i.e. lattice vibrations) also distort lattice periodicity. However, in this work, we will neglect this effect which is predominant in the far infrared region only, in which we will not focus on.

(ii) Neutral impurity scattering.

The carrier scattering, by neutral impurity atoms, in the crystal lattice resembles low-energy electron scattering in a gas. According to Erginsoy [106], the mobility due to neutral impurity scattering is given by

$$\mu_N = \frac{m^* e^3}{20\hbar^3 \varepsilon_0 \varepsilon_s N_n} \tag{10}$$

Where N_n *is* the concentration of neutral impurities, ε_0 is the static dielectric constant or permittivity of free space, and ε_s is the permittivity of the semiconductor. In our case, this scattering effect can be reasonably neglected.

(iii) Electron-electron scattering.

This effect will also be neglected in this study. Indeed, electron-electron scattering has little influence on mobility because in this process the total momentum of the electron gas is not changed. Typically, for a non-degenerate semiconductor, dominated by ionized impurity scattering, the mobility is reduced by 60%, whereas in the case of degenerate semiconductors, such as the TCOs, there is no reduction [107, 108].

(iv) Ionized donor center scattering.

We will show in this thesis that for our films, one of the greatest effect on the scattering of the carriers is produced by the ionized donor centers (i.e. Sb^{5+} in ATO for instance). This is because the electrostatic field due to such impurities remains effective even for degenerate n-type semiconductors, such as the above quoted TCOs. In fact, for such cases, the contribution of ionized impurity scattering is given by [109]:

$$\mu_{IS} = \frac{4e}{h}\left(\frac{\pi}{3}\right)^{1/3} N^{-2/3} \tag{11}$$

(v) Grain boundary scattering.

In addition to ionized donor center scattering, shown above, grain-boundary scattering is another important scattering mechanism that has to be taken into consideration in polycrystalline ceramics and thin films. Undoubtedly, conduction mechanism should be influenced by the inherent inter-crystalline boundaries (grain boundaries). These boundaries generally contain fairly high densities of interface states which can trap part of the free carriers from the core of the grain and scatter the remaining free carriers by virtue of the inherent disorders and the presence of trapped charges. These phenomena result in a potential gradient in the grain boundaries leading to a so-called 'space charge region'. Due to the potential gradient, band bending occurs in the space charge region, resulting in

potential barriers to charge transport. The most commonly used model, to explain the transport phenomenon in polycrystalline films, was proposed by Petritz [110]. According to this model, the conductivity of charge carriers dominated by grain boundaries (σ_g) is given by the relation

$$\sigma_g = eN\mu_0 \exp\left(\frac{-e\phi_b}{k_B T}\right) \tag{12}$$

In this relation, ϕ_b is potential barrier height, N is carrier density in the crystallite cores (i.e. density of conduction-band electrons in the above quoted TCOs, which is generally temperature independent); $\mu_0 = (M / n_c k_B T)$ where n_c is the number of crystallites per unit length along the film, and M is a factor that is barrier dependent (grain-percolation and pore-size dependent etc.).

Thus from equation (12) the grain boundary limited mobility can be written as

$$\mu_g = \mu_0 \exp\left(\frac{-e\phi_b}{k_B T}\right) \tag{13}$$

The pre-exponential term in equation (13) is modified by Seto [111] resulting in the following equation:

$$\mu_g = el'(2\pi m * k_B T)^{-1/2} \exp\left(\frac{-e\phi_b}{k_B T}\right) \tag{14}$$

where l' is the grain size.

b. Conduction mechanism in amorphous materials.

In amorphous materials, the hopping process, often so-called Variable Range Hopping (VRH) is the most dominant conduction mechanism. Such conductivity is generally expressed as

$$\sigma = \frac{\sigma_0'}{T^{1/2}} \exp\left[-\left(\frac{T_0}{T}\right)^x\right] \tag{15}$$

where the value of x varies between *0.25* and *0.5* depending upon the nature of the amorphous semiconductor, and the model used [112, 113]. The most commonly used model for variable range hopping is due to Mott [113]. According to Mott's theory, that is based on a number of assumptions, such as the energy independence of the density of states, one gets:

$$\sigma = \frac{\sigma_0'}{T^{1/2}} \exp\left[-\left(\frac{T_0}{T} \right)^{1/4} \right] \tag{16}$$

where

$$\sigma_0' = 3e2\nu_{ph} \left[\frac{N(E_F)}{8\pi\alpha k_B} \right]^{1/2} \tag{17}$$

and where

$$T_0 = \frac{\lambda_c \alpha^3}{k_B N(E_F)} \tag{18}$$

where $N(E_F)$ is the density of states near the Fermi level, λ_c is a dimensionless constant (≈ 18), ν_{ph} is a frequency factor taken here as Debye frequency (≈ 3.3×10^{12} Hz), and α is the decay constant of the wave function of the localized states near the Fermi level.

c. Conduction in nanocrystalline materials.

In nanocrystalline materials, for which the average elementary-particle size is lower than ~10 nm, the occurrence of structural defects that are predominant at the particle surfaces must be taken into consideration. Therefore, for these materials, there should be a distinction between particle ‘surface region’, where hopping conduction occurs in a similar way as for amorphous semiconductors, and particle ‘core region’, where the carriers are more delocalized [114].

Annex 5

Reflectance and transmittance of TCO thin films

For a layer of index $n^* = n - ik$, thickness t deposited on a substrate of index $n_1^* = n_1 - ik_1$ (Fig. 3), the reflectance and transmittance can be written as [115, 116]:

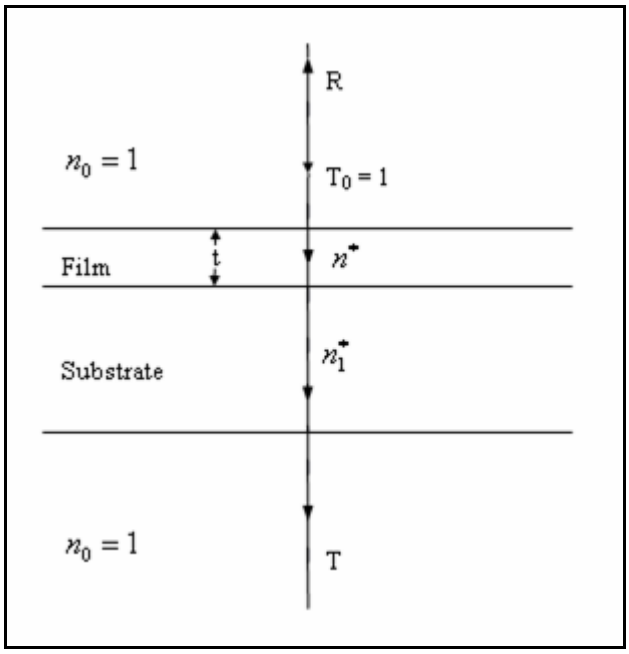

Fig. 3: System made of an absorbing thin film on a thick finite transparent substrate.

$$R = \frac{(g_1^2 + h_1^2)e^{2x_1} + (g_2^2 + h_2^2)e^{-2x_1} + A\cos 2\gamma_1 + B\sin 2\gamma_1}{e^{2x_1} + (g_1^2 + h_1^2)(g_2^2 + h_2^2)e^{-2x_1} + C\cos 2\gamma_1 + D\sin 2\gamma_1} \tag{19}$$

and

$$T = \left(\frac{n_1}{n_0}\right)\frac{\left[(1+g_1)^2 + h_1^2\right]\left[(1+g_2)^2 + h_2^2\right]}{e^{2x_1} + (g_1^2 + h_1^2)(g_2^2 + h_2^2)e^{-2x_1} + C\cos 2\gamma_1 + D\sin 2\gamma_1} \tag{20}$$

where

$$g_1 = \frac{n_0^2 - n^2 - k^2}{(n_0 + n)^2 + k^2} \qquad g_2 = \frac{n^2 - n_1^2 + k^2 - k_1^2}{(n - n_1)^2 + (k + k_1)^2}$$

$$h_1 = \frac{2n_0 k}{(n_0 + n)^2 + k^2} \qquad h_2 = \frac{2(nk_1 - n_1 k)}{(n + n_1)^2 + (k + k_1)^2}$$

$$x_1 = \frac{2\pi kt}{\lambda} = \frac{\alpha t}{2} \qquad \gamma_1 = \frac{2\pi nt}{\lambda}$$

$$A = 2(g_1 g_2 + h_1 h_2) \qquad B = 2(g_1 h_2 - g_2 h_1)$$

$$C = 2(g_1 g_2 - h_1 h_2) \qquad D = 2(g_1 h_2 + g_2 h_1)$$

where n_0 is the refractive index of air, λ is the wavelength of the incident light, and $\alpha = \frac{4\pi k}{\lambda}$ is the absorption coefficient.

Annex 6

Determination of the refractive index, *n*, and extinction coefficient, *k* in the interference transmission

For weakly and medium absorbing films (Fig. 4), the measurement of transmission of light through a film in the region of transparency is sufficient to determine the real and imaginary parts of the complex refractive index $n^* = n - ik$.

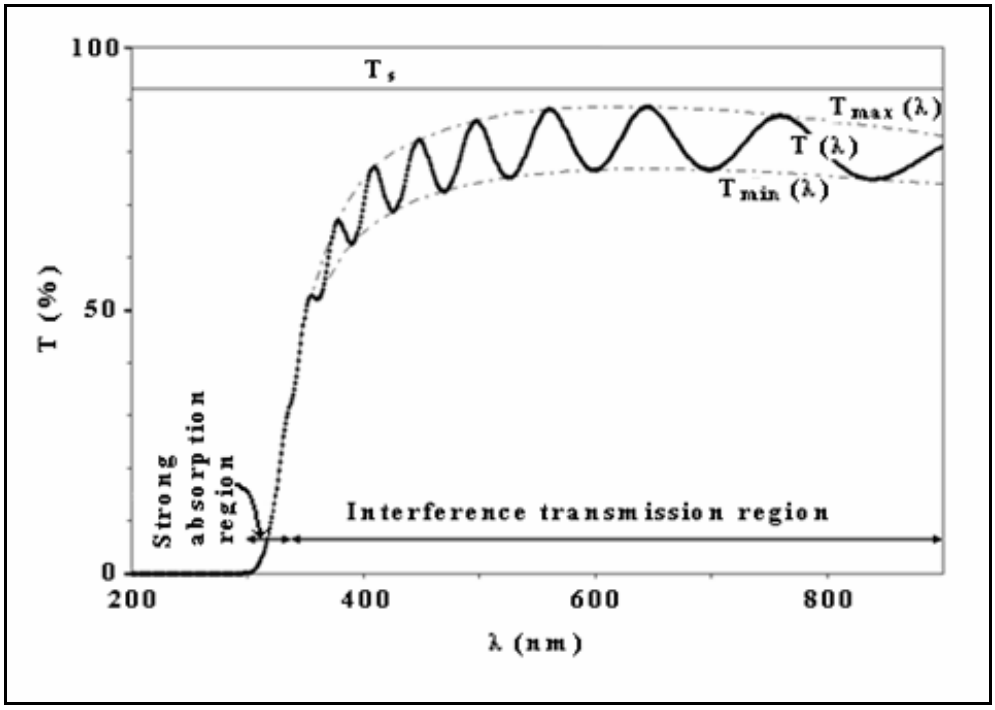

Fig. 4: Typical transmission spectrum for a uniform TCO thin film.

A simple method was developed to calculate these constants [116, 117]. If the incident light has unit amplitude, then the amplitude of the transmitted wave would be

$$A' = \frac{t_1 t_2 \exp(-2\pi i n^* t / \lambda)}{1 + r_1 r_2 \exp(-4\pi i n^* / \lambda)} \tag{21}$$

where, t_1, t_2, r_1, and r_2 are the transmission and reflection coefficients of the front and rear surfaces, respectively, and are given by

$$t_1 = \frac{2n_0}{n_0 + n} \qquad t_2 = \frac{2n}{n + n_1}$$

$$r_1 = \frac{n_0 - n}{n_0 + n} \qquad r_2 = \frac{n - n_1}{n + n_1}$$

where n_0 and n_1 are the real part of the refractive index of the air and substrate respectively.

The transmission of the layer is given by

$$T = \frac{n_1}{n_0}|A'|^2 \tag{22}$$

In the case of weak absorption, $k^2 << (n - n_0)^2$ and $k^2 << (n - n_1)^2$ so that T is given as

$$T = \frac{16 n_0 n_1 n^2 x}{C_1^2 + C_2^2 x^2 + 2C_1 C_2 x \cos(4\pi nt/\lambda)} \tag{23}$$

where $C_1 = (n + n_0)(n_1 + n), C_2 = (n - n_0)(n_1 - n),$ and

$$x = \exp\frac{-4\pi kt}{\lambda} = \exp -\alpha t \tag{24}$$

The maxima and minima of T in equation (21) occurs for

$$2nd = m\lambda \tag{25}$$

where m (the order number) is an integer for maxima and half integer for minima. The extreme values of transmission then can be calculated and given by the formulae

$$T_{\max} = 16 n_0 n_1 n^2 x/(C_1 + C_2 x)^2 \tag{26}$$

$$T_{\min} = 16 n_0 n_1 n^2 x/(C_1 - C_2 x)^2 \tag{27}$$

$T_{\max}$ and $T_{\min}$ can be considered as a continuous function of λ (Fig. 4) through $n(\lambda)$ and $x(\lambda)$. These functions are the envelopes of the maxima $T_{\max}(\lambda)$ and minima $T_{\min}(\lambda)$ in the transmission spectrum. The ratio $T_{\max}/T_{\min}$ can be used to find the value of x, thus:

$$x = \frac{\mathrm{C1}\left[1 - (\mathrm{T_{max}}/\mathrm{T_{min}})^{1/2}\right]}{\mathrm{C_2}\left[1 + (\mathrm{T_{max}}/\mathrm{T_{min}})^{1/2}\right]} \tag{28}$$

From equations (27) and (28)

$$n = \left[N + (N^2 - n_0^2 n_1^2)^{1/2} \right]^{1/2} \tag{29}$$

where

$$N = \frac{n_0^2 + n_1^2}{2} + 2 n_0 n_1 \frac{T_{\max} - T_{\min}}{T_{\max} T_{\min}} .$$

Equation (29) shows that n is explicitly determined from $T_{\max}$, $T_{\min}$, with n_1 and n_0 being measured at the same wavelength. Knowing n, one can also determine α from equation (28). Using this method, one can also find the film thickness, which can be calculated from the two successive maxima or minima using the relation (25), and is given by

$$t = \frac{\lambda_1 \lambda_2}{2[n(\lambda_1)\lambda_2 - n(\lambda_2)\lambda_1]} \tag{30}$$

Knowing t and x, one may calculate k using equation (24).

Annex 7

Seebeck Effect basic concept

When an external temperature gradient ΔT is present an electromotive force $\Delta(\varphi - \frac{\eta}{e})$ is generated [118, 119]. The Seebeck coefficient S or thermoelectric power is so defined by the relation

$$S = \frac{\Delta(\varphi - \frac{\eta}{e})}{\Delta T} \tag{31}$$

with φ electrostatic potential and η position of Fermi leve with respect to E_C (n-type carriers) or to E_V (p-type carriers).

The schema below shows that, In the presence of a temperature gradient ΔT imposed between two junction a and b made from two contacts of material A with material B, a potential difference ΔV between the opened circuit ends C and D is created. The carriers flow in the presence of the thermal gradient (from hot side to cold side) causes the appearance of electrostatic potential gradient, opposing to the carrier's flow in order to equilibrate the temperature gradient.

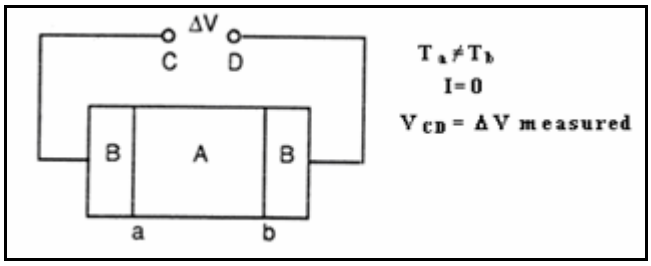

The Seebeck coefficient is defined as the open circuit voltage produced between two points on a conductor, where a uniform temperature difference of 1K exists between those points.

The coefficient S_{AB}, which characterized the thermoelectric power of material A with respect to material B, and is defined by the relation: $S_{AB} = \lim_{\Delta T \to 0} \frac{\Delta V}{\Delta T} = \frac{dV}{dT}$.

By convention, the Seebeck coefficient is taken as positive if the positive end of equivalent generator is situated at the sample cold end. In the case of n-type majority carriers which is ours, α will so be negative.

For degenerate semiconductor, even at low temperature ranges (below 100-150 K), the predominant scattering mechanism for conduction band electrons arises from the ionized impurities (ionized electron donor center). Taking this into account, the Seebeck coefficient can then be written as [119]

$$S = -\frac{k_B}{e}\frac{\pi^2 \eta^*}{\pi^2 + (\eta^*)^2} \tag{32}$$

where

$$\eta^* = \frac{|E_F - E_C|}{k_B T} \tag{33}$$

For n-type semiconductor, the Fermi level in the band gap is close to the conduction band edge, in this case $\pi^2 >> (\eta^*)^2$, we can approximate equation (32) to be

$$S \approx -\frac{k_B}{e}\frac{|E_F - E_C|}{k_B T} \tag{34}$$

At base temperatures and high doping rates, $(\eta^*)^2 >> \pi^2$, equation (32) can then be approximated to

$$S \approx -\frac{k_B}{e}\frac{\pi^2}{|E_F - E_C|}k_B T \tag{35}$$

For degenerate semiconductors, the only electrons participates to transport are those at the Fermi level, the Fermi energy level does not depend on the temperature, but only the charged impurity concentration, according to:

$$\eta = E_F - E_C = \frac{h^2}{2m^*}\left(\frac{3N}{8\pi}\right)^{2/3} \tag{36}$$

Substituting equation (36) into (35) we get

$$S = -\left[\frac{2}{e}\left(\frac{\pi}{3}\right)^{2/3}\left(\frac{k_B}{\hbar}\right)\right]\frac{m^*}{N^{3/2}}T \tag{37}$$

So, measuring the thermoelectric power evolution with temperature allows the deduction of the Fermi level with respect to the conduction band energy, and hence calculating m^* by knowing N from Hall Effect and vice versa.

References of annexes.

[1] R. A. Ortiz, *J. Vac. Sci. Technol.* **20** (1982) 7.

[2] S. Schiller, G. Beister, E. Buedke, H. J. Becker, H. Schicht, *Thin Solid Films* **96** (1982) 113.

[3] E. Leja, K. Budzynska, T. Pisarkiewicz, T. Stapinski, *Thin Solid Films* **100** (1983) 203.

[4] N. Miyata, K. Miyake, K. Koga, T. Fukushima, *J. Electrochem. Soc.* **127** (1980) 918.

[5] T. Pisarkiewicz, K. Zakrzewska, E. Leja, *Thin Solid Films* **153** (1987) 479.

[6] G. Haacke, *Appl. Phys. Lett.* **30 (**1977) 380.

[7] G. Haacke, *Appl. Phys. Lett.* **28** (1976) 622.

[8] R. P. Howson, M. I. Ridge, *Thin Solid Films* **77** (1981) 119.

[9] E. Leja, T. Stapinski, K. Marszalek, *Thin Solid Films* **125** (1985) 119.

[10] T. Maruyama, K. Fukui, *Japan. J. Appl. Phys.* **29** (1990) L1705.

[11] J. N. Avaritsiotis, R. P. Howson *Thin Solid Films* **77 (**1981) 351.

[12] N. Ito, Y. Sato, P.K. Song, A. Kaijio, K. Inoue,Y. Shigesato, *Thin Solid Films* **496** (2006) 99.

[13] C. A. Pan, T. P. Ma, *J. Electron. Mater.* **10** (1981) 43.

[14] W. Siefert, *Thin Solid Films* **121** (1984) 275.

[15] C. H. Lee, C. S. Huang, *Mater. Sci. Eng. B* **22** (1994) 233

[16] J. R. Bellingham, W. A. Phillips, C. J. Adkins, *Thin Solid Films* **195** (1991) 23.

[17] J. Szczyrbowski, A. Dietrich, H. Hoffmann, *Phys. Status Solidi* a **69** (1982) 217.

[18] S. Noguchi, H. Sakata, *J. Phys. D: Appl. Phys.* **13** (1980) 1129.

[19] A. Golan, J. Bragman, Y. Shapira, *Appl. Phys. Lett.* **57** (1990) 2205.

[20] J. I. Leong, J. H. Moon, J. H. Hong, J. S. Kang, Y. P. Lee, *Appl. Phys. Lett.* **64** 1994) 1215

[21] R. Banerjee, D. Das, S. Ray, A. K. Batabyal, A. K. Barua, *Solar Energy Mater.* **13** (1986) 11.

[22] S. A. Agnihotry, K. K. Saini, T. K. Saxena, K. C. Nagpal, S. Chandra, *J. Phys. D: Appl. Phys.* **18** (1985) 2087.

[23] P. F. Robosto, R. Braunstein, *Phys. Status Solidi a* **119** (1990) 155.

[24] I. A. Rauf, *Mater. Lett.* **18** (1993) 123.

[25] S. Noguchi, H. Sakata, *J. Phys. D: Appl. Phys.* **114** (1981) 1523.

[26] I. Hamberg, C. G. Granqvist, *Solar Energy Mater.* **11** (1984) 239.

[27] P. F. Robusto, R. Braunstein, *Phys. Status Solidi* a **119** (1990) 155.

[28] M. Mizuhashi, *Thin Solid Films* **76** (1981) 9.

[29] T. Maruyama, K. Fukui, *J. Appl. Phys*. **70** (1991) 3848.

[30] G. Frank, E. Kauer H. Kostlin, *Thin Solid Films* **77** (1981)107.

[31] S. Kulaszewicz, W. Jarmoc, I. Lasocka, Z. Lasocki, K. Turowska, *Thin Solid Films* **117** (1984) 157.

[32] A. K. Saxena, S. P. Singh, R. Thangaraj, O. P Agnihotri, *Thin Solid Films* **117** (1984) 95.

[33] R. Pommier, C. Gril, J. Marucchi, *Thin Solid Films* **77** (1981) 91.

[34] V. Vasu, A. Subrahmanyam, *Thin Solid Films* **193/194** (1990) 696.

[35] G. Frank, E. Kauer, H. Kostlin, F. J. Schmitte, *Solar Energy Mater.* **8** (1983) 387.

[36] W. Siefert, *Thin Solid Films* **120** (1984) 275.

[37] L. Gouskov, J. M. Saurel, C. Gril, M. Boustani, A. Oemry, *Thin Solid Film* **9** (1983) 365.

[38] K. Sreenivas, T. Sudersena Rao, A. Mansingh, *J. Appl. Phys.* **57** (1985) 384.

[39] C. H. L. Weijtens, *J. Electrochem Soc.* **138** (1991) 3432.

[40] Y. Shigesato, S. Takaki, T. Haranon, *J. Appl. Phys.* **71** (1992) 3356.

[41] M. Buchanan, J. B. Webb, D. F. Williams, *Thin Solid Films* **80** (1981) 373.

[42] M. Jachimowski, A. Brudnik, H. Czternastek, *J. Phys. D: Appl. Phys.* **18** (1985) L145.

[43] S. Ishibashi, Y. Higuchi, Y. Ota, K. Nakamura, *J. Vac. Sci. Technol. A* **8** (1990) 1399, 1403.

[44] Y. Shigesato, Y. Hayashi, A. Masui, T. Haranou, *Japan. J. Appl. Phys.* **30** (1991) 814.

[45] A. P. Theuwissen, G. J. Declerck, *Thin Solid Films* **121** (1984) 109.

[46] J. R. Bellingham, W. A. Phillips, C. J. Adkins, *J. Phys.: Condens. Matter* **2** (1990) 6207.

[47] N. Croitoru, E. Bannett, *Thin Solid Films* **82** (1981) 235.

[48] J. C. C. Fan, *Thin Solid Films* **80** (1981) 125.

[49] S. S. Bawa, S. S. Sharma, S. A. Agnihotry, A. M. Biradar, S. Chandra, *Proc. SPIE* **428** (1983) 22.

[50] K. Sreennivas, T. Sudersena Rao, A. Mansingh, *J. Appl. Phys.* **57** (1985) 384.

[51] G. Sberveglieri, P. Benussi, G. Coccoli, S. Groppelli, P. Nelli, *Thin Solid Films* **186** (1990) 349.

[52] C. H. L. Weijtens, P. A. C. Vanloon, *Thin Solid Films* **196** (1991) 1.

[53] W. Wen-Fa, C. Bi-Shiou, *Thin Solid Films* **247** (1994) 201.

[54] L. A. Ryabova, V. S. Salun, I. A. Serbinov, *Thin Solid Films* **92** (1982) 327.

[55] C. Yuanri, X. Xinghao, J. Zhaoting, P. Chuancai, X. Shuyun, *Thin Solid Films* **115** (1984) 195.

[56] J. Machet, J. Guille, P. Saulnier,S. Robert, *Thin Solid Films* **80** (1981) 149.

[57] D. M. Mattox, *Thin Solid Films* **204** (1991) 25.

[58] C. Geoffroy, G. Campet, J. Portier, J. Salardenne, G. Couturier, M. Baourrel, J. M. Chabagno, D. Ferry, C. Ouet, *Thin Solid Films* **202** (1991) 77.

[59] S. R. Vishwakarma, J. P. Upadhyay, H. O. Prasad, *Thin Solid Films* **176** (1989) 99.

[60] B. Gottlieb, R. Koropecki, R. Arce, R. Crisalle, J. Ferron, *Thin Solid Films* **199** (1991) 13.

[61] E. Shanthi, A. Banerjee, V. Dutta, K. L. Chopra, *J. Appl. Phys.* **53** (1982) 1615.

[62] F. Simonis, M. V. Leij, C. J. Hoogendoom, *Solar Energy Mater.* **1** (1979) 221.

[63] C. Agashe, M. G. Takwale, B. R. Marathe, V. G. Bhide, *Solar Energy Mater.* **17** (1988) 99.

[64] G. Mavrodiev, M. Gajdardziska, N. Novkovski, *Thin Solid Films* **113** (1984) 93.

[65] J. Bruneaux, H. Cachet, M. Froment, A. Messad, *Thin Solid Films* **197** (1991) 129.

[66] J. Dutta, P. Roubeau, T. Emeraud, J. M. Laurent, A. Smith, F. Lebelanc, J. Perrin, *Thin Solid Films* **239** (1994) 150.

[67] J. C. Manifacier, *Thin Solid Films* **90** (1982) 297.

[68] H. H. Afify, R. S. Momtaz, W. A. Badawy, S. A. Nasser, *J. Mater. Sci.: Mater. Electron.* **2** (1991) 40.

[69] T. Karlsson, A. Roos, C. G. Rilebing, *Solar Energy Mater.* **11** (1985) 469.

[70] J. Calderer, J. Esta, H. Luquet, M. Savelli, *Solar Energy Mater.* **5** (1981) 337.

[71] E. Shanthi, V. Dutta, A. Banerjee, K. L. Chopra, *J. Appl. Phys.* **51** (1980) 6243.

[72] H. Kaneko, K. Miyake, *J. Appl. Phys.* **53** (1982) 3629.

[73] K. Suzuki, M. Mizuhashi, *Thin Solid Films* **97** (1982) 119.

[74] A. De, S. Ray, *J. Phys. D: Appl. Phys.* **24** (1991) 719.

[75] R. P. Howson, H. Barankova, A. G. Spencer, *Proc. SPIE* **1275** (1990) 75.

[76] B. Stjerna, C. G. Granqvist, *Thin Solid Films* **193/194** (1990) 704.

[77] B. Stjerna, C. G. Granqvist, *Solar Energy Mater.* **20** (1990) 225.

[78] R. Sanjines, V. Damarne and F. Levy, *Thin Solid Films* **193/194** (1990) 935.

[79] R. P. Howson, H. Barankova, A. G. Spencer, *Thin Solid Films* **196** (1991) 315.

[80] B. Stejerna, C. G. Granqvist, *Thin Solid Films* **193/194** (1990) 704.

[81] M. N. Islam, M. O. Hakim, *J. Phys. D: Appl. Phys.* **19** (1986) 615.

[82] A. Antonaia, P. Menna, M. L. Addonizio, M. Crocchiolo, *Solar Energy Mater. and Solar Cells* **28** (1992) 167.

[83] V. Vasu and A. Subrahmanyam, *Thin Solid Films* **193/194** (1990) 973.

[84] J. Melsheimer, D. Zifgler, *Thin Solid Films* **109** (1983) 71.

[85] V. Vasu, A. Subrahmanyam, *Thin Solid Films* **202** (1991) 283.

[86] G. Sanon, R. Rup, A. Mansingh, *Thin Solid Films* **190** (1990) 287.

[87] C. M. Dai, C. S. Su, D. S. Chuu, *Appl. Phys. Lett.* **57** (1990) 1879.

[88] H. G. Swamy, P. J. Reddy, *Semicond. Sci. Technol.* **5** (1990) 980.

[89] M. Shimizu, T. Horu, T. Shiosaki, A. Kawabata, *Thin Solid Films* **96** (1982) 149.

[90] M. F. Ogawa, Y. Natsume, T. Hirayama, H. Sakata, *J. Mater. Sci. Lett.* **9** (1990) 1354.

[91] J. B. Webb, D. F. Williams, M. Buchanan, *Appl. Phys. Lett.* **39** (1981) 640.

[92] J. Ma, S. Y. Li, *Thin Solid Films* **237** (1994) 16.

[93] M. S. Tomar, F. J. Garcia, *Thin Solid Films* **90** (1982) 419.

[94] S. Ghosh, A. Sarkar, S. Bhattacharya, S. Chaudhury, A. K. Pal, *J. Cryst. Growth* **108** (1991) 534.

[95] T. Minami, K. Oohashi, S. Takata, T. Mouri, N. Ogawa, *Thin Solid Films* **193/194** (1990) 721.

[96] T. Minami, H. Nanto, S. Takata, *Thin Solid Films* **124** (1985) 43.

[97] Y. Igasaki, H. Saito, *J. Appl. Phys.* **70** (1991) 3613.

[98] J. Hu, R. G. Gordon, *J. Appl. Phys.* **71** (1992) 880.

[99] B. H. Choi, H. B. Im, J. S. Song, K. H. Yoon, *Thin Solid Films* **193/194** (1990) 712.

[100] S. Major, A. Banerjee, K. L. Chopra, *Thin Solid Films* **125** (1985) 179.

[101] A. Sarkar, S. Ghosh, S. Chaudhury, A. K. Pal, *Thin Solid Films* **204** (1991) 255.

[102] E. Burstein, *Phys. Rev.* **93** (1954) 632.

[103] T. S. Moss, *Proc. Phys. Soc. London Sect. B* **67** (1954) 775.

[104] N. F. Mott, *Metal Insulator Transitions*, London, Taylor and Francis, 1974.

[105] L. B. Valdes, *Proc. IRE* **42** (1954) 420

[106] C. Erginsoy *Phys. Rev.* **79** (1950) 1013.

[107] J. Appel, *Phys. Rev.* **122** (1961) 1760.

[108] R. T. Bate, R. D. Baxter, F. J. Reid, A. C. Beer, *J. Phys. Chem. Solids* **26** (1965) 1205.

[109] V. A. Johnson, K. Lark-Horovitz, *Phys. Rev.* **71** (1947) 374.

[110] R. L. Petritz, *Phys. Rev.* **104** (1956) 1508.

[111] J. Seto, *J. Appl. Phys*. **104** (1975) 5247.

[112] A. L. Efror B. I. Shklovskii, *J. Phys. C: Solid State Phys.* **8** (1975) L 49.

[113] N. F. Mort, *Phil. Mag.* **19** (1969) 835.

[114] C. Geoffroy, G. Campet, J. Portier, *Mat. Sci. Eng. B* **8** (1991) 45.

[115] O. S. Heavens, *Optical Properties of Thin Solid Films*, London, Butterworth 1955.

[116] R. Swanepoel, *J. phys. E: Sci. Instrum*. **16** (1983) 1214.

[117] J. C. Manifacier, J. Gasiot, J. P. Fillard, *J. Phys. E: Sci. Instrum.* **9** (1976) 1002.

[118] J. Bhattacharyya, S. Chaudhuri, D. De, A. K. Pal, *thin solid films* **128** (1985) 231.

[119] C. Marcel, *Ph. D. Thesis*, Bordeaux 1 University, Bordeaux, Fr

Summary:

Transparent conducting oxides (TCOs) have the unique feature of combining optical transparency in the visible region (colorless state) with metal type electrical conductivity. In spite of all the intensive investigations during these last 35 years, there is still a need to have TCOs with better optimized opto-electronic properties. That led us to carry out studies on the following TCOs, in both ceramic and thin film forms: (i) ATO and AZTO (tin dioxide co-doped with antimony and zinc); (ii) IO (indium trioxide) doped with new specific elements (confidential results) which significantly enhance the electronic conductivity. Co-doping SnO_2 with Sb and Zn (forming AZTO) allowed us to obtain highly dense and conductive ceramics without antimony departure. ATO and AZTO thin films, deposited from ceramic targets with optimized compositions, have high transparency in the visible range. The electronic conductivity of AZTO thin films can be modulated, thanks to the co-doping.

Thus, we could propose new doping elements, and correlatively, new efficient TCO electrodes.

Keywords:

- Ceramic - Thin film - Sputtering - SnO_2 - In_2O_3 - Doping -Opto-electronic properties

Résumé:

Les ”Oxydes Transparents et Conducteurs” (TCOs) possèdent une conductivité de type métallique tout en conservant, à l’état de films minces, une absorption négligeable dans tout le domaine visible. Malgré les recherches intensives menées durant ces 35 dernières années, il est nécessaire d’obtenir des TCOs avec de meilleures performances afin de répondre aux exigences des nouveaux dispositifs opto-électroniques. C’est dans cette optique que nous avons étudié les TCOs suivants sous forme de céramiques et de couches minces : (i) ATO et AZTO (symbolisant respectivement l’oxyde d’étain dopé à l’antimoine et l’oxyde d’étain co-dopé à l'antimoine et au zinc); (ii) IO (symbolisant l’oxyde d’indium) dopé avec des éléments spécifiques (résultats confidentiels) qui confèrent un conductivité électronique remarquable même lorsque le dépôt est réalisé sur substrat plastique. Dans le cas de AZTO, le co-dopage nous a permis d’obtenir des céramiques très denses et conductrices, sans perte d’antimoine lors du frittage. Par ailleurs, la conductivité électronique des films minces AZTO peut être modulée grâce au co-dopage.

Ainsi, nous pouvons proposé de nouveaux TCOs présentant des performances adaptées aux besoins d’applications spécifiques.

Mots-clefs:

- Céramique - Couche mince - Pulvérisation cathodique - SnO_2 - In_2O_3 - Dopage - Propriétés opto-électroniques